

Ministry of Science and Higher Education of the Russian Federation  
ITMO University

ISSN 2220-8054

***NANOSYSTEMS:***  
***PHYSICS, CHEMISTRY, MATHEMATICS***

**2023, volume 14(4)**

**Наносистемы: физика, химия, математика**

**2023, том 14, № 4**



# NANOSYSTEMS:

PHYSICS, CHEMISTRY, MATHEMATICS

## ADVISORY BOARD MEMBERS

**Chairman:** V.N. Vasiliev (*St. Petersburg, Russia*),  
V.M. Buznik (*Moscow, Russia*); V.M. Ievlev (*Voronezh, Russia*), P.S. Kop'ev (*St. Petersburg, Russia*), N.F. Morozov (*St. Petersburg, Russia*), V.N. Parmon (*Novosibirsk, Russia*),  
A.I. Rusanov (*St. Petersburg, Russia*),

## EDITORIAL BOARD

**Editor-in-Chief:** I.Yu. Popov (*St. Petersburg, Russia*)

### Section Co-Editors:

Physics – V.M. Uzdin (*St. Petersburg, Russia*),

Material science – V.V. Gusarov (*St. Petersburg, Russia*); O.V. Al'myasheva (*St. Petersburg, Russia*);

Chemistry – V.K. Ivanov (*Moscow, Russia*),

Mathematics – I.Yu. Popov (*St. Petersburg, Russia*).

### Editorial Board Members:

V.M. Adamyan (*Odessa, Ukraine*); A.P. Alodjants (*St. Petersburg, Russia*); S. Behta (*Stockholm, Sweden*); J. Behrndt (*Graz, Austria*); M.B. Belonenko (*Volgograd, Russia*); A. Chatterjee (*Hyderabad, India*); A.V. Chizhov (*Dubna, Russia*); A.N. Enyashin (*Ekaterinburg, Russia*), P.P. Fedorov (*Moscow, Russia*); E.A. Gudilin (*Moscow, Russia*); H. Jónsson (*Reykjavik, Iceland*); A.A. Kiselev (*Durham, USA*); Yu.S. Kivshar (*Canberra, Australia*); S.A. Kozlov (*St. Petersburg, Russia*); P.A. Kurasov (*Stockholm, Sweden*); A.V. Lukashin (*Moscow, Russia*); I.V. Melikhov (*Moscow, Russia*); G.P. Miroshnichenko (*St. Petersburg, Russia*); I.Ya. Mittova (*Voronezh, Russia*); Nguyen Anh Tien (*Ho Chi Minh, Vietnam*); V.V. Pankov (*Minsk, Belarus*); K. Pankrashkin (*Orsay, France*); A.V. Ragulya (*Kiev, Ukraine*); V. Rajendran (*Tamil Nadu, India*); A.A. Rempel (*Ekaterinburg, Russia*); V.Ya. Rudyak (*Novosibirsk, Russia*); H.M. Sedighi (*Ahvaz, Iran*); D Shoikhet (*Karmiel, Israel*); P Stovicek (*Prague, Czech Republic*); V.M. Talanov (*Novocherkassk, Russia*); A.Ya. Vul' (*St. Petersburg, Russia*); A.V. Yakimansky (*St. Petersburg, Russia*), V.A. Zagrebnov (*Marseille, France*).

### Editors:

I.V. Blinova; A.I. Popov; A.I. Trifanov; E.S. Trifanova (*St. Petersburg, Russia*),  
R. Simoneaux (*Philadelphia, Pennsylvania, USA*).

**Address:** ITMO University, Kronverkskiy pr., 49, St. Petersburg 197101, Russia.

**Phone:** +7(812)607-02-54, **Journal site:** <http://nanojournal.ifmo.ru/>,

**E-mail:** [nanojournal.ifmo@gmail.com](mailto:nanojournal.ifmo@gmail.com)

## AIM AND SCOPE

The scope of the journal includes all areas of nano-sciences. Papers devoted to basic problems of physics, chemistry, material science and mathematics inspired by nanosystems investigations are welcomed. Both theoretical and experimental works concerning the properties and behavior of nanosystems, problems of its creation and application, mathematical methods of nanosystem studies are considered.

The journal publishes scientific reviews (up to 30 journal pages), research papers (up to 15 pages) and letters (up to 5 pages). All manuscripts are peer-reviewed. Authors are informed about the referee opinion and the Editorial decision.

# CONTENT

## MATHEMATICS

S. Kanemitsu, Jay Mehta, Y. Sun  
**Irreducible characters of the icosahedral group** 405

I.V. Blinova, E.N. Grishanov, A.I. Popov, I.Y. Popov, M.O. Smolkina  
**On spin flip for electron scattering by several delta-potentials for 1D Hamiltonian with spin-orbit interaction** 413

I.Y. Popov  
**A model of charged particle on the flat Möbius strip in a magnetic field** 418

## PHYSICS

J. Matrasulov, J.R. Yusupov, A.A. Saidov  
**Fast forward evolution in heat equation: Tunable heat transport in adiabatic regime** 421

J. Dweik, H. Farhat, J. Younis  
**The Space Charge Model. A new analytical approximation solution of Poisson-Boltzmann equation: the extended homogeneous approximation** 428

Asma N. Naqash, Khurshed A. Shah, J. Sheikh, B. Kumbhani  
**Transport Properties of GaAs Co-Doped H-passivated Low-buckled and High-buckled Zigzag Silicene Nanoribbon Two Probe Devices** 438

## CHEMISTRY AND MATERIAL SCIENCE

I.B. Dorosheva, A.S. Vokhmintsev, I.A. Weinstein, A.A. Rempel  
**Induced surface photovoltage in TiO<sub>2</sub> sol-gel nanoparticles** 447

K. Abinaya, P. Sharvanti, N. Rajeswari Yogamalar  
**Solution processed Ag–In–S nanoparticles as light adsorber in ZnO for photovoltaic application** 454

J. Abimalar, V. Anslin Ferby  
**Structural, electrical, optical and phase investigation of perovskite barium zirconate nano-particles prepared through auto-combustion technique** 467

Boni Samuel, Adarsh K. J, V P N Nampoore, A Mujeeb <b>Optimization of certain synthesis parameters for CdSe quantum dots and synthesis of CdSe-ZnSe nano-tetrapods through facile hot injection method</b>	<b>479</b>
N.K. Thach, I.S. Krechetov, V.V. Berestov, O.I. Kan, I.V. Maslochenko, T.L. Lepkova, S.V. Stakhanova <b>The role and effect of CO<sub>2</sub> flow rate on the structure formation of ultrahigh porous activated carbon from H<sub>3</sub>PO<sub>4</sub>-impregnated waste cotton used as supercapacitor electrode material</b>	<b>489</b>
<b>Information for authors</b>	<b>498</b>

## Irreducible characters of the icosahedral group

S. Kanemitsu<sup>1,a</sup>, Jay Mehta<sup>2,b</sup>, Y. Sun<sup>3,c</sup>

<sup>1</sup>Sanmenxia SUDA New Energy Research Institute, Sanmenxia, Henan, P. R. China

<sup>2</sup>Department of Mathematics, Sardar Patel University, Vallabh Vidyanagar, Gujarat, India

<sup>3</sup>Graduate School of Engrg., Kyushu Inst. Tech., 1-1 Sensuicho Tobata, Kitakyushu, Japan

<sup>a</sup>omnikanemitsu@yahoo.com, <sup>b</sup>jay\_mehta@spuvvn.edu, <sup>c</sup>sun@ele.kyutech.ac.jp

Corresponding author: Jay Mehta, jay\_mehta@spuvvn.edu

PACS 02.20.Bb

Dedicated to Professor Dr. Vladimir N. Chubarikov

**ABSTRACT** To study point groups, their irreducible characters are essential. The table of irreducible characters of the icosahedral group  $A_5$  is usually obtained by using its duality to the dodecahedral group. It seems that there is no literature which gives a routine computational way to complete it. In the works of Harter and Allen, a computational method is given and the character table up to the tetrahedral group  $A_4$  using the group algebra table and linear algebra. In this paper, we employ their method with the aid of computer programming to complete the table. The method is applicable to any other more complicated groups.

**KEYWORDS** icosahedral group, irreducible representation, simple characters, regular representation, eigenvalues.

**FOR CITATION** S. Kanemitsu, Jay Mehta, Y. Sun Irreducible characters of the icosahedral group. *Nanosystems: Phys. Chem. Math.*, 2023, **14** (4), 405–412.

### 1. Introduction and irreducible characters of $S_3$

The icosahedral group  $A_5$  also denoted  $C_{60}$  is important in the light of recent developments of fullerene structures, cf. [1–4]. The character table of the icosahedral group  $A_5$  is usually obtained by using its duality to the dodecahedral group [5](pp. 216–219). Alternatively, it is simply stated without any indication of proof, cf. e.g. [6, 7]. It seems that there is no literature which gives a routine computational way to find it with the aid of computers. We describe the method of Harter [8, 9] and Allen [10] and determine the character table of the icosahedral group. The method is rather a light-hearted one and without much knowledge, one can construct character tables. The procedure is described in the following subsections. For some algebraic preliminaries, see, e.g. [11].

#### 1.1. Algebra table and regular representation matrices

[10](p. 27) gives one the table of irreducible characters up to the tetrahedral group  $T_d$  and we shall give one for the icosahedral group. We need to form the table of conjugate classes and their algebra table. We illustrate the procedure by the 3rd symmetric group (Table 1).

TABLE 1. Conjugate classes of  $S_3$

label	representative	type	cardinality
$C_1$	(1)(2)(3)	(1, 0, 0)	1
$C_2$	(1, 2)(3)	(0, 1, 0)	3
$C_3$	(1, 2, 3)	(0, 0, 1)	2

Here  $C_i^{-1}$  is the conjugate class consisting of all the inverses of elements of  $C_i$  (Table 2).

The (right) regular representation matrix  $R(C_\alpha)$  has the  $(i, j)$ -entry  $c_{i\alpha}^j$ , which are the structure constants defined by

$$C_i C_\alpha = \sum_{j=1}^n c_{i\alpha}^j C_j, \quad (1)$$

where  $n$  is the number of conjugate classes of  $G$ .

TABLE 2. Class algebra table for  $S_3$

classes	$C_1$	$C_2$	$C_3$
$C_1$	$C_1$	$C_2$	$C_3$
$C_2^{-1} = C_2$	$C_2$	$3C_1 + 3C_3$	$2C_2$
$C_3^{-1} = C_3$	$C_3$	$2C_2$	$2C_1 + C_3$

Looking at each column in Table 2, we see immediately that

$$R(C_2) = \begin{pmatrix} 0 & 1 & 0 \\ 3 & 0 & 3 \\ 0 & 2 & 0 \end{pmatrix}, \quad R(C_3) = \begin{pmatrix} 0 & 0 & 1 \\ 0 & 2 & 0 \\ 2 & 0 & 1 \end{pmatrix}. \tag{2}$$

Note that we always have  $R(C_1) = E$ , where  $E$  is the identity matrix.

**1.2. Eigenvalues and eigenspaces of regular representations**

$R(C_2)$  has eigenvalues  $0, \pm 3$  with the following eigenspaces

$$E_{R(C_2)}(0) = \mathbb{R} \begin{pmatrix} 1 \\ 0 \\ -1 \end{pmatrix}, \quad E_{R(C_2)}(\pm 3) = \mathbb{R} \begin{pmatrix} 1 \\ \pm 3 \\ 2 \end{pmatrix} \tag{3}$$

and  $R(C_3)$  has eigenvalues  $-1, 2, 2$  with the following eigenspaces

$$E_{R(C_3)}(-1) = \mathbb{R} \begin{pmatrix} 1 \\ 0 \\ -1 \end{pmatrix} \quad E_{R(C_3)}(2) = \mathbb{R} \begin{pmatrix} 1 \\ 0 \\ 2 \end{pmatrix} \oplus \mathbb{R} \begin{pmatrix} 0 \\ 1 \\ 0 \end{pmatrix} = \mathbb{R} \begin{pmatrix} 1 \\ 3 \\ 2 \end{pmatrix} \oplus \mathbb{R} \begin{pmatrix} 1 \\ -3 \\ 2 \end{pmatrix}. \tag{4}$$

**Remark 1.** To find eigenvalues of  $R(C_j)$ ,  $j = 2, 3$  Allen uses the method of raising-to-powers.

$$C_2^0 = C_1, \quad C_2^1 = C_2, \quad C_2^2 = 3C_1 + 3C_3, \quad C_2^3 = 3C_1 + 3C_3 = 3C_2 + 3C_3C_2 = 3C_2 + 6C_2 = 9C_2, \tag{5}$$

whence the Cayley-Hamilton equation resp. the characteristic equation

$$C_2^3 - 9C_2 = 0, \quad \lambda^3 - 9\lambda = 0 \tag{6}$$

and the eigenvalues are  $0, \pm 3$ .

$$C_3^0 = C_1, \quad C_3^1 = C_3, \quad C_3^2 = 2C_1 + C_3, \quad C_3^3 = 2C_1 + 3C_3, \tag{7}$$

whence the Cayley-Hamilton equation  $C_3^3 - 4C_3^2 + 4C_2 = 0$ , But we already have a lower order equation resp. the characteristic equation

$$C_3^2 - C_3 - 2C_1 = 0, \quad \lambda^2 - \lambda - 2 = 0 \tag{8}$$

and the eigenvalues are  $2, -1$ . But this is practical only for lower degree matrices. This process may be automated.

**1.3. Matching the eigenvalues**

This process may remain manual and depends on inspection.

A character table (CT) is in effect a collection of traces of IR's (Irreducible representation) of the group. As such, all of the entries in a given row of a CT belong to the same IR. Up to now the eigenvalues are arranged in sets according to classes  $C_i$ . For a specific IR,  $\mathcal{P}$ , say, the character  $\chi_i^{(\alpha)}$  assigned to class  $C_i$  is associated with a specific member of the set  $\{\lambda_i\}$ . It is therefore required that for a given  $\mathcal{P}^{(\alpha)}$ , a single eigenvalue be picked from each of the  $n$  sets  $\lambda_i$  and that these eigenvalues be arranged in a new set

$$\{\lambda^{(\alpha)}\} = \lambda_1^{(\alpha)}, \dots, \lambda_n^{(\alpha)} \tag{9}$$

all of which are associated with the given  $\mathcal{P}^{(\alpha)}$ . This procedure is called *matching the eigenvalues*.

The collection of eigenvalues  $\lambda^{(\alpha)}$  has a single column vector  $\mathbf{v}^{(\alpha)}$  associated with it, which has the property

$$R[C_i]\mathbf{v}^{(\alpha)} = \lambda_i^{(\alpha)}\mathbf{v}^{(\alpha)}, \quad i = 1, \dots, n. \tag{10}$$

The vector  $\mathbf{v}^{(\alpha)}$  is, simultaneously, an eigenvector of every  $R(C_i)$ . When this property is used in conjunction with (3) and (4), we see that  $\lambda = -1$  from  $R(C_2)$ , and  $\lambda = 0$  from  $R(C_3)$  belong to the same set  $\{\lambda^{(1)}\}$ , where the common eigenvectors are

$$\mathbf{v}^{(1)} = \begin{pmatrix} 1 \\ 0 \\ -1 \end{pmatrix}, \quad \mathbf{v}^{(2)} = \begin{pmatrix} 1 \\ 3 \\ 2 \end{pmatrix}, \quad \mathbf{v}^{(3)} = \begin{pmatrix} 1 \\ -3 \\ 2 \end{pmatrix}. \tag{11}$$

Here  $\mathbf{v}^{(2)}$  is a common eigenvector of  $R(C_2)$  and  $R(C_3)$  belonging to the eigenvalue  $\lambda_2^{(2)} = 3$  resp.  $\lambda_3^{(2)} = 2$ . Similarly,  $\mathbf{v}^{(3)}$  is a common eigenvector belonging to the eigenvalue  $\lambda_2^{(2)} = -3$  resp.  $\lambda_3^{(3)} = 2$ . Every set  $\{\lambda^{(\alpha)}\}$  contains the  $n$ -fold multiple eigenvalues  $\lambda = 1$  from  $R(C_1)$ , so that the complete set found is represented in Table 3.

TABLE 3. Eigenvalues arranged

eigenvalue set	$C_1$	$C_2$	$C_3$	eigenvector
$\{\lambda^{(1)}\}$	$\lambda_1^{(1)} = 1$	$\lambda_2^{(1)} = 0$	$\lambda_2^{(1)} = -1$	$\mathbf{v}^{(1)}$
$\{\lambda^{(2)}\}$	$\lambda_1^{(2)} = 1$	$\lambda_2^{(2)} = 3$	$\lambda_3^{(2)} = 2$	$\mathbf{v}^{(2)}$
$\{\lambda^{(3)}\}$	$\lambda_1^{(3)} = 1$	$\lambda_2^{(3)} = -3$	$\lambda_3^{(3)} = 2$	$\mathbf{v}^{(3)}$

**1.4. Finding values of irreducible characters**

To find CT we accommodate the values of  $\lambda_i^{(\alpha)}$  and arrange the characters in the order of increasing dimension of IR. The following formula appears as the coefficients of (49') in [9](p. 747, l. 2):

$$\chi_j^{(\alpha)} = \frac{\ell^{(\alpha)}}{\text{card}(C_j)} \lambda_j^{(\alpha)}, \tag{12}$$

where  $\chi_i^{(\alpha)}$  is the character value  $\chi^{(\alpha)}(\text{ord}(C_j))$  of the  $j$ th class in the  $\alpha$ th irreducible representation (IR),  $\ell^{(\alpha)}$  the dimension of the  $\alpha$ th IR and  $\text{ord}(C_j)$  is the order of the  $j$ th class.

We appeal to the formula ([9](p. 747))

$$\frac{1}{|G|} \sum_j \frac{(\lambda_j^{(\alpha)})^2}{\text{card}(C_j)} = \frac{1}{(\ell^{(\alpha)})^2}. \tag{13}$$

It follows that  $\ell^{(2)} = 2$  and other two are 1. We rearrange Table 3 in the order of dimensions and label them as follows (Table 4) (so as to compare with [10](p. 23)).

TABLE 4. Eigenvalues arranged

IR	$C_1$	$C_2$	$C_3$	dim
$\mathcal{P}^{(0)}$	$\lambda_1^{(0)} = 1$	$\lambda_2^{(0)} = 3$	$\lambda_3^{(0)} = 2$	$\ell^{(0)} = 1$
$\mathcal{P}^{(1)}$	$\lambda_1^{(1)} = 1$	$\lambda_2^{(1)} = -3$	$\lambda_2^{(1)} = 2$	$\ell^{(1)} = 1$
$\mathcal{P}^{(2)}$	$\lambda_1^{(2)} = 1$	$\lambda_2^{(2)} = 0$	$\lambda_3^{(2)} = -1$	$\ell^{(2)} = 2$

We stretch the interpretation of (12) to mean

$$\chi_j^{(\alpha)} = \ell^{(\alpha)} \left( \frac{\lambda_j^{(\alpha)}}{\text{card}(C_j)} \right). \tag{14}$$

Then

$$\chi_j^{(2)} = 2 \left( \frac{1}{\text{card}(C_1)}, \frac{0}{\text{card}(C_2)}, \frac{-1}{\text{card}(C_3)} \right) = \left( \frac{2}{1}, \frac{0}{3}, -\frac{2}{2} \right) = (2, 0, -1). \tag{15}$$

Similarly,

$$\chi_j^{(0)} = \left( \frac{1}{\text{card}(C_1)}, \frac{3}{\text{card}(C_2)}, \frac{2}{\text{card}(C_3)} \right) = (1, 1, 1), \quad \chi_j^{(1)} = (1, -1, 1). \tag{16}$$

TABLE 5. Values of irreducible characters

IR	$C_1$	$C_2$	$C_3$
$\mathcal{P}^{(0)}$	$\chi_1^{(0)} = 1$	$\chi_2^{(0)} = 1$	$\chi_3^{(0)} = 1$
$\mathcal{P}^{(1)}$	$\chi_1^{(1)} = 1$	$\chi_2^{(1)} = -1$	$\chi_3^{(1)} = 1$
$\mathcal{P}^{(2)}$	$\chi_1^{(2)} = 2$	$\chi_2^{(2)} = 0$	$\chi_3^{(2)} = -1$

TABLE 6. Conjugate classes of  $S_5$

label	representative	type	cardinality
$C_1$	(1)(2)(3)(4)(5)	(5, 0, 0, 0, 0)	1
$C_2$	(1, 2)(3)(4)(5)	(3, 1, 0, 0, 0)	10
$C_2$	(1, 2)(3, 4)(5)	(1, 2, 0, 0, 0)	15
$C_4$	(1, 2, 3)(4)(5)	(2, 0, 1, 0, 0)	20
$C_5$	(1, 2, 3)(4, 5)	(0, 1, 1, 0, 0)	20
$C_6$	(1, 2, 3, 4)(5)	(1, 0, 0, 1, 0)	30
$C_7$	(1, 2, 3, 4, 5)	(0, 0, 0, 0, 1)	24

TABLE 7. Conjugacy classes of  $A_5$

class	type	representative	$k_j$
$C_1$	(5, 0, 0, 0, 0)	(1)	1
$C_2$	(2, 0, 1, 0, 0)	(1, 2, 3)	20
$C_3$	(1, 2, 0, 0, 0)	(1, 2)(3, 4)	15
$C_4$	(0, 0, 0, 0, 1)	(1, 2, 3, 4, 5)	12
$C_5$	(0, 0, 0, 0, 1)	(2, 1, 3, 4, 5)	12

2. Irreducible characters of  $A_5$

This will be much harder. We need to prepare the class algebra table (Table 6).

The goal is to establish the following theorem.

**Theorem 1.** All simple characters of  $A_5$  are given by Table 8:

TABLE 8. All simple characters of  $A_5$  ( $\tau$  indicates  $\frac{1 + \sqrt{5}}{2}$  – the golden ratio)

	$C_1$	$C_2$	$C_3$	$C_4$	$C_5$
$\chi_1$	1	1	1	1	1
$\chi_2$	3	0	-1	$\tau$	$-\tau^{-1}$
$\chi_3$	3	0	-1	$-\tau^{-1}$	$\tau$
$\chi_4$	4	1	0	-1	-1
$\chi_5$	5	-1	1	0	0

2.1. Class algebra table and regular representation matrices

For this, we need the class algebra table (Table 9)

TABLE 9. Class algebra table for  $A_5$

classes	$C_1$	$C_2$	$C_3$	$C_4$	$C_5$
$C_1$	$C_1$	$C_2$	$C_3$	$C_4$	$C_5$
$C_2^{-1}=C_2$	$C_2$	$20C_1+7C_2+8C_3+5C_4+5C_5$	$6C_2+4C_3+5C_4+5C_5$	$3C_2+4C_3+5C_4+5C_5$	$3C_2+4C_3+5C_4+5C_5$
$C_3^{-1}=C_3$	$C_3$	$6C_2+4C_3+5C_4+5C_5$	$15C_1+3C_2+2C_3+5C_4+5C_5$	$3C_2+4C_3+5C_5$	$3C_2+4C_3+5C_4$
$C_4^{-1}=C_4$	$C_4$	$3C_2+4C_3+5C_4+5C_5$	$3C_2+4C_3+5C_5$	$12C_1+3C_2+5C_4+C_5$	$3C_2+4C_3+C_4+C_5$
$C_5^{-1}=C_5$	$C_5$	$3C_2+4C_3+5C_4+5C_5$	$3C_2+4C_3+5C_4$	$3C_2+4C_3+C_4+C_5$	$12C_1+3C_2+C_4+5C_5$

$$R(C_2) = \begin{pmatrix} 0 & 1 & 0 & 0 & 0 \\ 20 & 7 & 8 & 5 & 5 \\ 0 & 6 & 4 & 5 & 5 \\ 0 & 3 & 4 & 5 & 5 \\ 0 & 3 & 4 & 5 & 5 \end{pmatrix}. \tag{17}$$

$$R(C_3) = \begin{pmatrix} 0 & 0 & 1 & 0 & 0 \\ 0 & 6 & 4 & 5 & 5 \\ 15 & 3 & 2 & 5 & 5 \\ 0 & 3 & 4 & 0 & 5 \\ 0 & 3 & 4 & 5 & 0 \end{pmatrix}. \tag{18}$$

$$R(C_4) = \begin{pmatrix} 0 & 0 & 0 & 1 & 0 \\ 0 & 3 & 4 & 5 & 5 \\ 0 & 3 & 4 & 0 & 5 \\ 12 & 3 & 0 & 5 & 1 \\ 0 & 3 & 4 & 1 & 1 \end{pmatrix}. \tag{19}$$

$$R(C_5) = \begin{pmatrix} 0 & 0 & 0 & 0 & 1 \\ 0 & 3 & 4 & 5 & 5 \\ 0 & 3 & 4 & 5 & 0 \\ 0 & 3 & 4 & 1 & 1 \\ 12 & 3 & 0 & 1 & 5 \end{pmatrix}. \tag{20}$$

**2.2. Finding eigenvalues and eigenvectors by a computer**

(1) The eigenvalues of the matrix  $R(C_2)$  are obtained by a python program:

$$20, 5, -4, 0, 0$$

. Their corresponding eigenvectors are as follows

$$\begin{aligned} v_1 &= (0.03, -0.15, -0.196, -0.012, -0.016) \\ v_2 &= (0.661, -0.753, -0.784, 0, 0) \\ v_3 &= (0.496, 0, 0.588, 0.063, 0.849) \\ v_4 &= (0.396, 0.452, 0, -0.73, -0.437) \\ v_5 &= (0.396, 0.452, 0, 0.679, -0.241) \end{aligned}$$

and the polynomial is

$$\lambda^5 - 21\lambda^4 + 400\lambda^2.$$

(2) The eigenvalues of the matrix  $R(C_3)$  obtained by a python program are:

$$15, -5, 3, 0, -5$$

and the their corresponding eigenvectors are

$$\begin{aligned} v_1 &= (-0.033, -0.171, 0.196, 0.15, 0.016) \\ v_2 &= (-0.661, 0, -0.784, 0.753, 0) \\ v_3 &= (-0.496, 0.857, 0.588, 0, -0.08) \\ v_4 &= (-0.396, -0.342, 0, -0.452, -0.671) \\ v_5 &= (-0.396, -0.342, 0, -0.452, 0.736) \end{aligned}$$

and the polynomial is

$$\lambda^5 - 8\lambda^4 - 110\lambda^3 + 1125\lambda.$$

(3) The eigenvalues of the matrix  $R(C_4)$  obtained by a python program are:

$$12, 6.47, 0, -3, -2.47$$

and the their corresponding eigenvectors are

$$\begin{aligned} v_1 &= (0.033, 0.116, -0.196, -0.15, 0.116) \\ v_2 &= (0.661, 0, 0.784, -0.753, 0) \\ v_3 &= (0.496, -0.581, -0.588, 0, -0.581) \\ v_4 &= (0.396, 0.752, 0, 0.452, -0.287) \\ v_5 &= (0.396, -0.287, 0, 0.452, 0.752) \end{aligned}$$

and the polynomial is

$$\lambda^5 - 13\lambda^4 - 16\lambda^3 + 288\lambda^2 + 576\lambda.$$

(4) The eigenvalues of the matrix  $R(C_5)$  obtained by a python program are:

$$12, 6.47, 0, -3, -2.47$$

and the their corresponding eigenvectors are

$$\begin{aligned} v_1 &= (0.033, 0.116, -0.196, 0.15, 0.116) \\ v_2 &= (0.661, 0, 0.784, 0.753, 0) \\ v_3 &= (0.496, -0.581, -0.588, 0, -0.581) \\ v_4 &= (0.396, -0.287, 0, -0.452, 0.752) \\ v_5 &= (0.396, 0.752, 0, -0.452, -0.287) \end{aligned}$$

and the polynomial is

$$\lambda^5 - 13\lambda^4 - 16\lambda^3 + 288\lambda^2 + 576\lambda = \lambda(\lambda - 12)(\lambda + 3)(\lambda^2 - 4\lambda - 16)$$

The eigenvalues of  $R(C_5)$  are:

$$12, 4\tau, 0, -3, -4\tau^{-1}.$$

### 2.3. Matched eigenvalues

This section combines §1.2 and §1.3 to give the table corresponding to Table 4.

TABLE 10. Eigenvalues arranged

	$C_1$	$C_2$	$C_3$	$C_4$	$C_5$	eigenvectors	dim
$\{\lambda^{(1)}\}$	1	20	15	12	12	$\mathbf{v}^{(1)}$	$\ell^{(1)} = 1$
$\{\lambda^{(2)}\}$	1	0	-5	$4\tau$	$-4\tau^{-1}$	$\mathbf{v}^{(2)}$	$\ell^{(2)} = 3$
$\{\lambda^{(3)}\}$	1	0	-5	$-4\tau^{-1}$	$4\tau$	$\mathbf{v}^{(3)}$	$\ell^{(3)} = 3$
$\{\lambda^{(4)}\}$	1	5	0	-1	-3	$\mathbf{v}^{(4)}$	$\ell^{(4)} = 4$
$\{\lambda^{(2)}\}$	1	-4	3	0	0	$\mathbf{v}^{(5)}$	$\ell^{(5)} = 5$

Here

$$\mathbf{v}^{(1)} = {}^t(0.03, -0.15, -0.196, -0.012, -0.016)$$

$$\mathbf{v}^{(2)} = {}^t(0.396, 0.452, 0, 0.679, -0.241)$$

$$\mathbf{v}^{(3)} = {}^t(0.661, -0.753, -0.784, 0, 0)$$

$$\mathbf{v}^{(4)} = {}^t(0.396, 0.452, 0, -0.73, -0.437)$$

$$\mathbf{v}^{(5)} = {}^t(0.496, 0, 0.588, 0.063, 0.849).$$

## 2.4. Proof of Theorem 1

Using the method in §1.4, we find the values of all ICs.

$$\begin{aligned} \chi_j^{(1)} &= 1 \left( \frac{1}{\text{card}(C_1)}, \frac{20}{\text{card}(C_2)}, \frac{15}{\text{card}(C_3)}, \frac{12}{\text{card}(C_4)}, \frac{12}{\text{card}(C_5)} \right) \\ &= \left( \frac{1}{1}, \frac{20}{20}, \frac{15}{15}, \frac{12}{12}, \frac{12}{12} \right) = (1, 1, 1, 1, 1). \end{aligned} \quad (21)$$

$$\begin{aligned} \chi_j^{(2)} &= 3 \left( \frac{1}{\text{card}(C_1)}, \frac{0}{\text{card}(C_2)}, \frac{-5}{\text{card}(C_3)}, \frac{4\tau}{\text{card}(C_4)}, \frac{-4\tau^{-1}}{\text{card}(C_5)} \right) \\ &= (1, 0, -1, \tau, -\tau^{-1}). \end{aligned} \quad (22)$$

$$\begin{aligned} \chi_j^{(3)} &= 3 \left( \frac{1}{\text{card}(C_1)}, \frac{0}{\text{card}(C_2)}, \frac{-5}{\text{card}(C_3)}, \frac{-4\tau^{-1}}{\text{card}(C_4)}, \frac{4\tau}{\text{card}(C_5)} \right) \\ &= (1, 0, -1, -\tau^{-1}, \tau). \end{aligned} \quad (23)$$

$$\begin{aligned} \chi_j^{(4)} &= 4 \left( \frac{1}{\text{card}(C_1)}, \frac{5}{\text{card}(C_2)}, \frac{0}{\text{card}(C_3)}, \frac{-1}{\text{card}(C_4)}, \frac{-3}{\text{card}(C_5)} \right) \\ &= (4, 1, 0, -1, -1). \end{aligned} \quad (24)$$

$$\begin{aligned} \chi_j^{(5)} &= 5 \left( \frac{1}{\text{card}(C_1)}, \frac{-4}{\text{card}(C_2)}, \frac{3}{\text{card}(C_3)}, \frac{0}{\text{card}(C_4)}, \frac{0}{\text{card}(C_5)} \right) \\ &= 5 \left( \frac{1}{1}, \frac{-4}{20}, \frac{3}{15}, 0, 0 \right) = (5, -1, 1, 0, 0). \end{aligned} \quad (25)$$

as in Table 7. This proves Theorem 1. □

## 3. Conclusion

The method described here of Harter and Allen may be applied to any other interesting finite groups which will be conducted elsewhere.

## References

- [1] Andova V., Kardos F., Skrekovski R. Mathematical aspects of fullerenes. *Ars Mathematica Contemporanea*, 2016, **11**, P. 353–379.
- [2] Dresselhaus M.S. Dresselhaus D. and Saito Sh. Group-theoretical concepts for  $C_{60}$  and other fullerenes., *Material Sci. Engrg.*, 1993, **B19**, P. 122–128.
- [3] Nikolaev A.V., Plakhutin B.N.  $C_{60}$  fullerene as a pseudoatom of the icosahedral symmetry. *Russian Chemical Reviews*, 2010, **79**(9), P. 729–755.
- [4] Pleshakov I.V., Proskurina O.V., Gerasimov V.I., Kuz'min Yu.I. Optical anisotropy in fullerene-containing polymer composites induced by magnetic field. *Nanosystems: Phys. Chem. Math.*, 2022, **13**(5), P. 503–508.
- [5] Akizuki Y. *Abstract Algebra*, Kyoritsu-shuppan, Tokyo, 1956.
- [6] Conway J.H. *Atlas of Finite Groups: Maximal Subgroups and Ordinary Characters for Simple Groups*, Cambridge UP, Cambridge, 1985.
- [7] Lomont J.S. *Applications of finite groups*, Academic Press, New York, 1959.
- [8] Harter W.G. *Applications of algebraic representation theory*. PhD Thesis, Univ. of Calif., Irvine, 1967.
- [9] Harter W.G. *Algebraic theory of ray representations of finite groups*. *J. Math. Phys.*, 1968, **10**, P. 739–752.
- [10] Allen G. An efficient method for computation of character tables of finite groups. *NASA Techn. Rept.* (TN D-4763), Nat. Aerodyn. & space adm., Washington, 1968.
- [11] Kanemitsu S., Kuzumaki T. and Liu J.Y. *Intermediate abstract algebra*, Preprint 2024.

*Information about the authors:*

*S. Kanemitsu* – Sanmenxia SUDA New Energy Research Institute, No. 1, Taiyang Road, Sanmenxia Economic Development Zone, Sanmenxia, Henan, 472000, P. R. China; ORCID 0000-0002-8489-7665; omnikanemitsu@yahoo.com

*Jay Mehta* – Department of Mathematics, Sardar Patel University, Vallabh Vidyanagar, Gujarat 388 120, India; ORCID 0000-0003-1739-9639; jay\_mehta@spuvvn.edu

*Y. Sun* – Graduate School of Engrg., Kyushu Inst. Tech., 1-1Sensuicho Tobata, Kitakyushu 804-8555, Japan; ORCID 0000-0003-0433-8917; sun@ele.kyutech.ac.jp

*Conflict of interest:* the authors declare no conflict of interest.

## On spin flip for electron scattering by several delta-potentials for 1D Hamiltonian with spin-orbit interaction

Irina V. Blinova<sup>1,a</sup>, Evgeny N. Grishanov<sup>2,b</sup>, Anton I. Popov<sup>1,c</sup>, Igor Y. Popov<sup>1,d</sup>, Maria O. Smolkina<sup>1,e</sup>

<sup>1</sup>ITMO University, St. Petersburg, Russia

<sup>2</sup>Ogarev Mordovia State University, Saransk, Russia

<sup>a</sup>irin-a@yandex.ru, <sup>b</sup>evgenyng@mail.ru, <sup>c</sup>popov239@gmail.com, <sup>d</sup>popov1955@gmail.com, <sup>e</sup>vega14@mail.ru

Corresponding author: I. Y. Popov, popov1955@gmail.com

PACS 73.22.-f, 71.15.Dx, 71.70.Di, 81.05.Uw

**ABSTRACT** One-dimensional Rashba and Dresselhaus Hamiltonians with spin-orbit interaction are studied. It is assumed that there are point-like potentials on the line. The scattering problem is solved and the possibility of spin-flip is discussed.

**KEYWORDS** spin-orbit interaction; point-like potential; spin filtering; Schrödinger equation

**ACKNOWLEDGEMENTS** The work was supported by Russian Science Foundation (grant number 23-21-00096 (<https://rscf.ru/en/project/23-21-00096/>)).

**FOR CITATION** Blinova I.V., Grishanov E.N., Popov A.I., Popov I.Y., Smolkina M.O. On spin flip for electron scattering by several delta-potentials for 1D Hamiltonian with spin-orbit interaction. *Nanosystems: Phys. Chem. Math.*, 2023, **14** (4), 413–417.

### 1. Introduction

Conventional electronics is based on the charge transport. However, during last decades, a new branch of electronics, spintronics, was developing rapidly. In contrast to electronics which ignores the electron spin, spintronics deals with spinbased electron transport. It is not the electron charge but the electron spin that carries information [1]. The new wave of interest was inspired by the development of quantum computing and quantum computations (see, e.g., [2, 3]). Correspondingly, one needs electronic devices which can distinguish the spin orientation and can control it. The most popular theoretical idea for creating the background for such device is taking into account the spin-orbit interaction. There are two types of spin-orbit coupling: the Rashba Hamiltonian [4] and the Dresselhaus Hamiltonian [5]. The Rashba effect is a direct result of inversion symmetry breaking in the direction perpendicular to the two-dimensional plane. The Dresselhaus Hamiltonian describes the spin-orbit coupling in a two-dimensional semiconductor thin film grown with appropriate geometry. A number of works were devoted to spin-orbit coupling in different dimensions (see, e.g., [6–10]). Point-like potentials are rather useful in this situation [11–14]. As for one-dimensional models, quantum graph is very effective in this situation (see, e.g., [15–17]). Particularly, to ensure the spin filtering, spin flip, control of the spin transport one uses, usually, systems of coupled quantum rings (see, e.g., [14, 18–27]). In the present paper, we show an example of the spin-flip in 1D system without rings for the Hamiltonian with spin-orbit interaction.

### 2. Model construction

We start with the Schrödinger equation for the Rashba Hamiltonian in one-dimensional case. In the case of spin-orbit

interaction, we deal with 2-vector functions  $\psi = \begin{pmatrix} \psi_1 \\ \psi_2 \end{pmatrix}$ .

$$\begin{cases} i\hbar \frac{\partial \psi_1}{\partial t} = -\frac{\hbar^2}{2m} \frac{\partial^2 \psi_1}{\partial x^2} + \alpha_R \frac{\partial \psi_2}{\partial x}, \\ i\hbar \frac{\partial \psi_2}{\partial t} = -\frac{\hbar^2}{2m} \frac{\partial^2 \psi_2}{\partial x^2} - \alpha_R \frac{\partial \psi_1}{\partial x}, \end{cases} \quad (1)$$

where  $\hbar$  is the Plank constant,  $\alpha_R$  is the parameter of the Rashba spin-orbit interaction,  $|\psi|^2 = |\psi_1|^2 + |\psi_2|^2$ . Let us separate variables  $x, t$ . It means that  $\psi(x, t) = e^{i\omega t} \tilde{\psi}(x)$ . Correspondingly, the system (1) transforms to the following form:

$$\begin{cases} -\hbar\omega \tilde{\psi}_1 = -\frac{\hbar^2}{2m} \frac{\partial^2 \tilde{\psi}_1}{\partial x^2} + \alpha_R \frac{\partial \tilde{\psi}_2}{\partial x}, \\ -\hbar\omega \tilde{\psi}_2 = -\frac{\hbar^2}{2m} \frac{\partial^2 \tilde{\psi}_2}{\partial x^2} - \alpha_R \frac{\partial \tilde{\psi}_1}{\partial x}, \end{cases} \quad (2)$$

In the case of the Dresselhaus spin-orbit interaction, the corresponding system has the following form:

$$\begin{cases} -\hbar\omega\tilde{\psi}_1 = -\frac{\hbar^2}{2m}\frac{\partial^2\tilde{\psi}_1}{\partial x^2} - i\alpha_D\frac{\partial\tilde{\psi}_2}{\partial x}, \\ -\hbar\omega\tilde{\psi}_2 = -\frac{\hbar^2}{2m}\frac{\partial^2\tilde{\psi}_2}{\partial x^2} - i\alpha_D\frac{\partial\tilde{\psi}_1}{\partial x}, \end{cases} \quad (3)$$

where  $\alpha_D$  is the parameter of the Dresselhaus spin-orbit interaction.

As for the point-like potential at point  $x_0$ , it is determined by the coupling conditions at this point. There are many variants of such conditions (see, e.g., [14]). We choose the condition which corresponds to 1D delta-potential at the point:

$$\begin{cases} \tilde{\psi}(x_0+0) = \tilde{\psi}(x_0-0), \\ \tilde{\psi}'(x_0+0) - \tilde{\psi}'(x_0-0) = -\beta\tilde{\psi}(x_0+0). \end{cases} \quad (4)$$

Let us choose the atomic system of units with  $\hbar = 1, m = 1/2$ . Consider the case of finite number of point-like potentials at the line. Then, at each half-axis and at each segment between the potentials, one has the following system of differential equations:

$$\begin{cases} \tilde{\psi}_1'' + k^2\tilde{\psi}_1 + \alpha_R\tilde{\psi}_2' = 0, \\ \tilde{\psi}_2'' + k^2\tilde{\psi}_2 - \alpha_R\tilde{\psi}_1' = 0, \end{cases} \quad (5)$$

where  $k$  is the wavenumber. Taking  $\tilde{\psi}_j = C_j e^{\lambda x}$ ,  $j = 1, 2$ , one obtains the following characteristic equation

$$(\lambda^2 + k^2)^2 + \alpha_R^2 \lambda^2 = 0 \quad (6)$$

with the following four roots and the corresponding vectors  $\begin{pmatrix} C_1 \\ C_2 \end{pmatrix}$ :

$$\lambda = i\tilde{k}_1, \begin{pmatrix} 1 \\ -i \end{pmatrix}; \quad \lambda = -i\tilde{k}, \begin{pmatrix} 1 \\ -i \end{pmatrix}; \quad \lambda = i\tilde{k}, \begin{pmatrix} 1 \\ i \end{pmatrix}; \quad \lambda = -i\tilde{k}_1, \begin{pmatrix} 1 \\ i \end{pmatrix},$$

where

$$\tilde{k} = \frac{1}{2}(\sqrt{\alpha_R^2 + 4k^2} - \alpha_R), \quad \tilde{k}_1 = \frac{1}{2}(\sqrt{\alpha_R^2 + 4k^2} + \alpha_R).$$

Correspondingly, at each segment and half-axis, one has a solution in the form of linear combination of standard solutions. Coupling conditions (4) gives one a system for determination the coefficients of the linear combination.

### 3. Results and discussion

Consider the scattering problem for the case of one point-like potential at point  $x_0 = 0$ . System (5) has solution of the form

$$\begin{pmatrix} \tilde{\psi}_1 \\ \tilde{\psi}_2 \end{pmatrix} = e^{i\tilde{k}x} \begin{pmatrix} 1 \\ i \end{pmatrix} + B_1 e^{-i\tilde{k}x} \begin{pmatrix} 1 \\ -i \end{pmatrix} + D_1 e^{-i\tilde{k}_1 x} \begin{pmatrix} 1 \\ i \end{pmatrix}, \quad x < 0, \quad (7)$$

$$\begin{pmatrix} \tilde{\psi}_1 \\ \tilde{\psi}_2 \end{pmatrix} = A_2 e^{i\tilde{k}x} \begin{pmatrix} 1 \\ i \end{pmatrix} + C_2 e^{i\tilde{k}_1 x} \begin{pmatrix} 1 \\ -i \end{pmatrix}, \quad x > 0. \quad (8)$$

Coupling conditions (4) at point  $x_0 = 0$  gives one the following system for coefficients of (7), (8):

$$\begin{cases} 1 + B_1 + D_1 = A_2 + C_2, \\ 1 - B_1 + D_1 = A_2 - C_2, \\ \tilde{k} - \tilde{k}B_1 - \tilde{k}_1 D_1 = \tilde{k}A_2 + \tilde{k}_1 C_2 - i\beta A_2 - i\beta C_2, \\ -\tilde{k} - \tilde{k}B_1 + \tilde{k}_1 D_1 = -\tilde{k}A_2 + \tilde{k}_1 C_2 + i\beta A_2 - i\beta C_2. \end{cases} \quad (9)$$

We are interested in coefficients of the outgoing solution, which are as follows:

$$A_2 = \frac{\tilde{k} + \tilde{k}_1}{\tilde{k} + \tilde{k}_1 - i\beta}, \quad C_2 = 0,$$

i.e. the outgoing solution has the form:

$$\begin{pmatrix} \tilde{\psi}_1 \\ \tilde{\psi}_2 \end{pmatrix} = \frac{\tilde{k} + \tilde{k}_1}{\tilde{k} + \tilde{k}_1 - i\beta} e^{i\tilde{k}x} \begin{pmatrix} 1 \\ i \end{pmatrix}. \quad (10)$$

The second scattering problem with the solution of the following form

$$\begin{pmatrix} \tilde{\psi}_1 \\ \tilde{\psi}_2 \end{pmatrix} = e^{i\tilde{k}_1 x} \begin{pmatrix} 1 \\ -i \end{pmatrix} + B'_1 e^{-i\tilde{k} x} \begin{pmatrix} 1 \\ -i \end{pmatrix} + D'_1 e^{-i\tilde{k}_1 x} \begin{pmatrix} 1 \\ i \end{pmatrix}, \quad x < 0, \quad (11)$$

$$\begin{pmatrix} \tilde{\psi}_1 \\ \tilde{\psi}_2 \end{pmatrix} = A'_2 e^{i\tilde{k} x} \begin{pmatrix} 1 \\ i \end{pmatrix} + C'_2 e^{i\tilde{k}_1 x} \begin{pmatrix} 1 \\ -i \end{pmatrix}, \quad x > 0, \quad (12)$$

is solved analogously and gives one the following outgoing solution:

$$\begin{pmatrix} \tilde{\psi}_1 \\ \tilde{\psi}_2 \end{pmatrix} = \frac{\tilde{k} + \tilde{k}_1}{\tilde{k} + \tilde{k}_1 - i\beta} e^{i\tilde{k}_1 x} \begin{pmatrix} 1 \\ -i \end{pmatrix}. \quad (13)$$

Using the linearity of the problem, one can incorporate (10), (13) and obtain the solution for the general case:

$$\begin{pmatrix} \tilde{\psi}_1 \\ \tilde{\psi}_2 \end{pmatrix} = \begin{pmatrix} e^{i\tilde{k} x} + e^{i\tilde{k}_1 x} \\ i(e^{i\tilde{k} x} - e^{i\tilde{k}_1 x}) \end{pmatrix} + (B_1 + B'_1) e^{-i\tilde{k} x} \begin{pmatrix} 1 \\ -i \end{pmatrix} + (D_1 + D'_1) e^{-i\tilde{k}_1 x} \begin{pmatrix} 1 \\ i \end{pmatrix}, \quad x < 0, \quad (14)$$

$$\begin{pmatrix} \tilde{\psi}_1 \\ \tilde{\psi}_2 \end{pmatrix} = \frac{\tilde{k} + \tilde{k}_1}{\tilde{k} + \tilde{k}_1 - i\beta} \begin{pmatrix} e^{i\tilde{k} x} + e^{i\tilde{k}_1 x} \\ i(e^{i\tilde{k} x} - e^{i\tilde{k}_1 x}) \end{pmatrix}, \quad x > 0. \quad (15)$$

One can see that

$$\begin{pmatrix} e^{i\tilde{k} x} + e^{i\tilde{k}_1 x} \\ i(e^{i\tilde{k} x} - e^{i\tilde{k}_1 x}) \end{pmatrix} = e^{i\tilde{k} x} \begin{pmatrix} 1 + e^{i\alpha_R x} \\ i(1 - e^{i\alpha_R x}) \end{pmatrix}. \quad (16)$$

Here we took into account that  $\tilde{k}_1 - \tilde{k} = \alpha_R$ .

To obtain the spin flip, one should choose the proper input and output points. Namely, let the input point  $x_{in}$  be such that  $e^{i\alpha_R x_{in}} = 1$ . Then, keeping in mind (16), one obtains that the input wave function in (14) has the form  $\begin{pmatrix} 1 \\ 0 \end{pmatrix}$ . One can choose the output point  $x_{out}$  in such a way that

$$e^{i\alpha_R x_{out}} = -1. \quad (17)$$

We remember that  $\alpha_R$  does not depend on the electron energy (i.e. on  $k$ ). It means that the relation (17) is valid for all energies. Correspondingly, according to (15), the output state at this point has the form  $\begin{pmatrix} 0 \\ 1 \end{pmatrix}$ . Thus, one obtains the spin flip.

One observes the analogous situation for the case of several delta-potentials. It can be solved analytically, but the expressions are too large. It is more convenient to solve the equations numerically. Fig. 1 shows  $|\psi_1|$  and  $|\psi_2|$  at  $x = x_{out}$  as functions of  $k$  for fixed  $x_{in} = -5$  and  $x_{out} = 5$  (dimensionless units) for cases of 1, 3, 5, 9 point-like potentials posed at integer points symmetrically in respect to  $x = 0$ . One can see that in all cases the ratio  $\frac{|\psi_2|}{|\psi_1|}$  does not depend on  $k$  as has been obtained analytically (see (15) and (16)) for the case of one point-like potential at point  $x = 0$ . We mention that we deal with the diapason of  $k$  outside resonances induced by 1D resonators formed by several delta-potentials (see, e.g., [14]).

The case of the Dresselhaus spin-orbit interaction (3) can be considered analogously. Particularly, one obtains the following characteristic equation which is analogous to (6):

$$(\lambda^2 + k^2)^2 + \alpha_D^2 \lambda^2 = 0 \quad (18)$$

with the following four roots and the corresponding vectors  $\begin{pmatrix} C_1 \\ C_2 \end{pmatrix}$ :

$$\lambda = i\tilde{k}_1, \begin{pmatrix} 1 \\ 1 \end{pmatrix}; \quad \lambda = -i\tilde{k}, \begin{pmatrix} 1 \\ 1 \end{pmatrix}; \quad \lambda = i\tilde{k}, \begin{pmatrix} 1 \\ -1 \end{pmatrix}; \quad \lambda = -i\tilde{k}_1, \begin{pmatrix} 1 \\ -1 \end{pmatrix},$$

where

$$\tilde{k} = \frac{1}{2}(\sqrt{\alpha_D^2 + 4k^2} - \alpha_D), \quad \tilde{k}_1 = \frac{1}{2}(\sqrt{\alpha_D^2 + 4k^2} + \alpha_D).$$

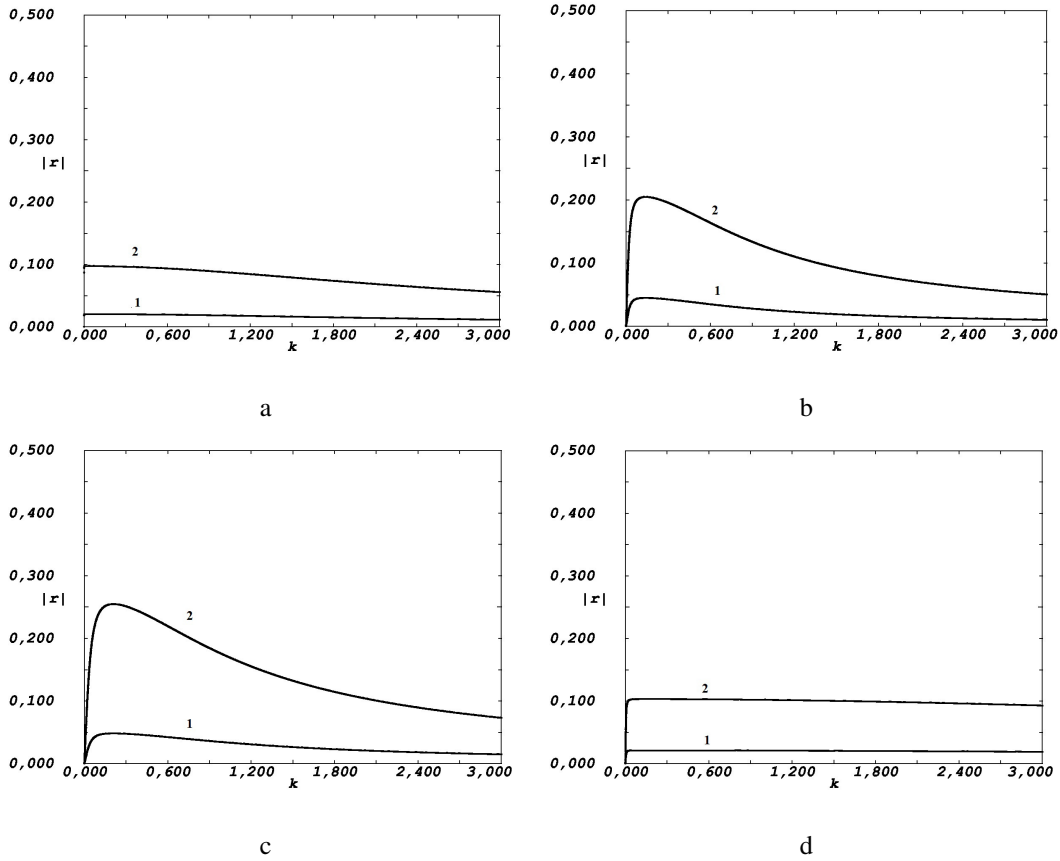


FIG. 1.  $r = |\psi_1|$  (curve 1) and  $r = |\psi_2|$  (curve 2) as functions of  $k$ : a - for one center, b - for 3 centers, c - for 5 centers, d - for 9 centers

Using the same procedure as in the Rashba case, one comes to the solution of the scattering problem for the Dresselhaus Hamiltonian:

$$\begin{pmatrix} \tilde{\psi}_1 \\ \tilde{\psi}_2 \end{pmatrix} = \frac{e^{i\tilde{k}x}}{\tilde{k}_1(\tilde{k} + \tilde{k}_1 - i\beta)} \times \begin{pmatrix} (\tilde{k} + \tilde{k}_1)(\tilde{k} + \tilde{k}_1 - i\beta - (\tilde{k} - i\beta)e^{i\alpha_D x}) + 2\tilde{k}\tilde{k}_1 e^{i\alpha_D x} \\ -(\tilde{k} + \tilde{k}_1)(\tilde{k} + \tilde{k}_1 - i\beta + (\tilde{k} - i\beta)e^{i\alpha_D x}) + 2\tilde{k}\tilde{k}_1 e^{i\alpha_D x} \end{pmatrix}, \quad x > 0.$$

One can see that there is no energy independent condition for spin flip as in the case of the Rashba spin-orbit interaction. Moreover, calculations show that the values of transmission coefficients is significantly smaller than in the Rashba case. Correspondingly, the Dresselhaus case is not good for spin-flip applications.

## References

- [1] Wolf S.A., Awschalom D.D., Buhrman R.A., Daughton J.M., S. von Molnar, Roukes M.L., Chtchelkanova A.Y., Treger D.M. Spintronics: A spin-based electronics vision for the future. *Science*, 2001, **294**, P. 1488–1495.
- [2] Nielsen M.A., Chuang I.L. *Quantum Computation and Quantum Information*. Cambridge University Press, Cambridge, 2010.
- [3] Lobanov I.S. Spin Boltzmann machine. *Nanosystems: Phys. Chem. Math.*, 2022, **13**(6), P. 593–607.
- [4] Bychkov Yu.A., Rashba E.I. Properties of a 2D electron gas with a lifted spectrum degeneracy. *Sov. Phys. - JETP Lett.*, 1984, **39**, P. 78–81.
- [5] Dresselhaus G. Spin-orbit coupling effects in Zinc blende structures. *Physical Review*, 1955, **100**(2), P. 580–586.
- [6] Magarill L.I., Romanov D.A., Chaplik A.V. Ballistic transport and spin-orbit interaction of two-dimensional electrons on cylindrical surface. *J. Exper. Theor. Phys.*, 1998, **113**(4), P. 1411–1428.
- [7] Ambrosetti A., Pederiva F., Lipparini E., Gandolfi S. Quantum Monte Carlo study of the two-dimensional electron gas in presence of Rashba interaction. *Phys. Rev. B*, 2009, **80**, P. 125306.
- [8] Ishizaka K., et.al. Giant Rashba-type spin splitting in bulk BiTeI, *Nature Materials*, 2011, **10**, P. 521–526.
- [9] Di Sante D., Barone P., Bertacco R., Picozzi S. Electric Control of the Giant Rashba Effect in Bulk GeTe. *Advanced Materials*, 2013, **25**, P. 509–513.
- [10] Brüning J., Geyler V., Pankrashkin K. Explicit Green functions for spin-orbit Hamiltonians. *J. Phys. A: Math. Theor.*, 2007, **40**, P. F697–F704.
- [11] Jursenas R. Spectrum of a family of spin-orbit coupled Hamiltonians with singular perturbation. *J. Phys. A: Math. Theor.*, 2016, **49**(6), P. 065202.
- [12] Boitsev A.A., Brasche J., Popov I.Y. Point-like perturbation of Rashba Hamiltonian. *Complex Variables and Elliptic Equations*, 2021, **66**(1), P. 154–164.

- [13] Cacciapuoti C., Carlone R., Figari R. Spin-dependent point potentials in one and three dimensions. *J. Phys. A: Math. Theor.*, 2007, **40**, P. 249–261.
- [14] Kulinskii V.L., Panchenko D.Yu. Point-Like Rashba Interactions as Singular Self-Adjoint Extensions of the Schrödinger Operator in One Dimension. *Front. Phys.*, 2019, **7**, P. 44(1-8).
- [15] Berkolaiko G., Kuchment P. 2012 *Introduction to Quantum Graphs*, (AMS, Providence).
- [16] Lipovsky J. Quantum Graphs And Their Resonance Properties. *Acta Physica Slovaca*, 2016, **66**(4), P. 265–363.
- [17] Exner P., Keating P., Kuchment P. Sunada T., Teplyaev A. *Analysis on graph and its applications*, 2008, AMS, Providence.
- [18] Chatterjee A., Popov I.Y., Smolkina M.O. Persistent current in a chain of two Holstein-Hubbard rings in the presence of Rashba spin-orbit interaction. *Nanosystems: Physics, Chemistry, Mathematics.*, 2019, **10**(1), P. 50–62.
- [19] Monisha P.J., Sankar I.V., Sil S., Chatterjee A. Persistent current in a correlated quantum ring with electron-phonon interaction in the presence of Rashba interaction and Aharonov-Bohm flux. *Scientific Reports*, 2016, **6**, P. 20056.
- [20] Dehghana E., Khoshnouda D.S., Naeimi A.S. Logical spin-filtering in a triangular network of quantum nanorings with a Rashba spin-orbit interaction. *Physica B*, 2018, **529**, P. 21–26.
- [21] Maryam Sabzevar, Mohammad Hossien Ehsani, Mehdi Solaimani. Spin-Polarized wave-packets transport through one-dimensional nonlinear multiple barriers: Rashba and Dresselhaus Spin-Orbit Interactions. *Philosophical Magazine*, 2023, **103**(8), P. 791–811.
- [22] Blinova I.V., Popov I.Y., Smolkina M.O. Scattering, Spectrum and Resonance States Completeness for a Quantum Graph with Rashba Hamiltonian. Operator Theory, Functional Analysis and Applications. *Operator Theory: Advances and Applications*, 2021, **282**, P. 51–62.
- [23] Popov I.Y., Blinova I.V., Shamionova E.A., Smolkina M.O. On the electron transmission control by a direction of magnetic field. *International Journal of Numerical Modelling: Electronic Networks, Devices and Fields*, 2021, **34**(6), P. e2918.
- [24] Blinova I.V., Popov A.I., Bosova A.A. Spectral gaps for star-like quantum graph and for two coupled rings. *Nanosystems: Phys. Chem. Math.*, 2022, **13**(3), P. 245–249.
- [25] Oh J.H., Lee K.-J., Hyun-Woo Lee, Shin M. Effects of Rashba and Dresselhaus spin-orbit interactions on the ground state of two-dimensional localized spins. *J. Phys.: Condens. Matter*, 2014, **26**, P. 196005.
- [26] Umar Farooq M., Lede Xian, Li Huang. Spin Hall effect in two-dimensional InSe: Interplay between Rashba and Dresselhaus spin-orbit couplings. *Phys. Rev. B*, 2022, **105**, P. 245405.
- [27] Tkach Yu.Ya. Determination of the Rashba and Dresselhaus spin-orbit interaction parameters and g-factor from the critical points of the spectrum in a 2D electron gas in an in-plane magnetic field. *Physica Status Solidi (b)*, 2021, **258**(5), P. 2000553.

---

*Submitted 23 May 2023; accepted 27 July 2023*

*Information about the authors:*

*Irina V. Blinova* – Center of Mathematics, ITMO University, Kroverkskiy, 49, St. Petersburg, 197101, Russia; ORCID 0000-0003-2115-2479; irin-a@yandex.ru

*Evgeny N. Grishanov* – Department of Mathematics and IT, Ogarev Mordovia State University Bolshevistskaya Str. 68, Saransk, 430005, Russia; evgeny@mail.ru

*Anton I. Popov* – Center of Mathematics, ITMO University, Kroverkskiy, 49, St. Petersburg, 197101, Russia; ORCID 0000-0001-7137-4067; popov239@gmail.com

*Igor Y. Popov* – Center of Mathematics, ITMO University, Kroverkskiy, 49, St. Petersburg, 197101, Russia; ORCID 0000-0002-5251-5327; popov1955@gmail.com

*Maria O. Smolkina* – Center of Mathematics, ITMO University, Kroverkskiy, 49, St. Petersburg, 197101, Russia; vega14@mail.ru

*Conflict of interest:* the authors declare no conflict of interest.

## A model of charged particle on the flat Möbius strip in a magnetic field

Igor Y. Popov

ITMO University, St. Petersburg, Russia

popov1955@gmail.com

PACS 02.30.Tb, 03.65.-w; 02.30.Jr

**ABSTRACT** The spectral problem for the Schrödinger operator with a magnetic field on the flat Möbius strip is considered. The model construction is described. It is compared with the case of the Laplace operator.

**KEYWORDS** Landau operator, flat Möbius strip, spectrum

**ACKNOWLEDGEMENTS** The author thanks Dr. I. V. Blinova and L. S. Blinov for useful discussions.

**FOR CITATION** Popov I.Y. A model of charged particle on the flat Möbius strip in a magnetic field. *Nanosystems: Phys. Chem. Math.*, 2023, **14** (4), 418–420.

### 1. Introduction

The quantum Hall effect discovered at the end of the twentieth century (see, e.g., [1–5]) is intensively used in nano-electronics. From the mathematical point of view the problem is related to the investigation of two-dimensional magnetic Schrödinger operator  $H_L$  [3–5]. The magnetic Schrödinger operator in a strip on the plane was studied in many papers [6–9]. There are papers devoted to the spectral problem for three-dimensional Hamiltonian with a magnetic field (see, e.g., [10, 11]).

We use the results of work [12] which studied the magnetic Schrödinger operator in an infinite strip on the plane.

Last time, curved nanostructures attract a special attention. Physicists investigate the properties of nanosystems caused by the nanostructure curvature (see, e.g., [13–18]). We can mention also a model based on quantum mechanics in spaces of constant curvature [19, 20]. Hamiltonians on curved manifolds are especially interesting. In the present paper we deal with the Möbius strip. Recently, a work [21] appeared which considers the Dirichlet Laplacian on the Möbius strip. The authors deal with Courant-sharp property for Dirichlet eigenfunctions on the flat Möbius strip. In the present paper we consider the Dirichlet eigenfunctions for the magnetic Schrödinger operator (Landau operator) on the flat Möbius strip.

Let us describe the flat Möbius strip. Usually, it was made by the following way [21]. We start with the infinite strip  $S_\infty = (-a, a) \times (-\infty, \infty)$  with width  $2a$ , equipped with the flat metric  $dx^2 + dy^2$  of  $\mathbb{R}^2$ . Given  $b > 0$ , define the following isometry of  $S_{inf ty}$ :

$$\sigma_b : (x, y) \rightarrow (-x, y + b).$$

Define the groups

$$G = \{\sigma_b^k | k \in \mathbb{Z}\}, \quad G_2 = \{\sigma_b^k | k \in 2\mathbb{Z}\}.$$

The group  $G_2$  is a subgroup of  $G$ , of index 2, generated by  $\sigma_b^2$ . The action of  $G$  on  $S_\infty$  is smooth, isometric, totally discontinuous, without fixed points. Correspondingly, we can consider the quotient manifolds with boundary

$$C_b = S_\infty/G_2, \quad M_b = S_\infty/G,$$

equipped with the flat metric induced from the metric of  $S_\infty$ . Here  $C_b$  is the cylinder and  $M_b$  is the flat Möbius strip.

This construction is convenient for the authors of [21] because they deal with the Laplacian which “doesn’t feel” a direction, i. e. it is invariant in respect to the map  $(x, y) \rightarrow (-x, y)$ . We will deal with the magnetic Schrödinger operator (Landau operator) which “feels” the direction. That is why, we will use another construction of the flat Möbius strip related to gluing of rectangles.

In the present short rapid note we present the main theorem only. Detailed proof, description of the model and analysis of the result will be published in the next paper.

### 2. Flat Möbius strip in the magnetic field

For the case of the magnetic Schrödinger operator (Landau operator), the situation is more complicated than for the Laplace operator. Consider four copies  $\Omega_j, j = 1, 2, 3, 4$ , of the rectangle  $\Omega = (-a, a) \times (-b, b)$ . The initial operator is the orthogonal sum of operators  $H_j^M$  defined in  $L_2(\Omega_j)$ :  $H^M = H_1^M \oplus H_2^M \oplus H_3^M \oplus H_4^M$  where

$$\begin{aligned} H_{1,2}^M &= -\frac{\partial^2}{\partial x^2} - \left(\frac{\partial}{\partial y} - 2i\pi\xi x\right)^2, \\ H_{3,4}^M &= -\frac{\partial^2}{\partial x^2} - \left(\frac{\partial}{\partial y} + 2i\pi\xi x\right)^2. \end{aligned} \tag{1}$$

It is the Hamiltonian of free two-dimensional particle with charge  $e$  in the homogeneous magnetic field  $\mathbf{B}$  orthogonal to the plane of the particle confinement. Here the vector potential of the magnetic field is chosen in the Landau gauge. Let  $\Phi_0 = 2\pi\hbar c/|e|$  be the magnetic flux quantum playing a role of a unit for the magnetic flux in the system,  $\xi = |\mathbf{B}|/\Phi_0$  is the density of the magnetic flux, i.e. the number of the magnetic flux quanta through the unit area on the plane of the system,  $x, y$  are the Cartesian coordinates on the plane. The system of physical units is chosen in such a way that the charge of the particle  $e$ , the speed of light  $c$  and the Planck constant  $\hbar$  equal 1, the mass of the particle is one half.

We include in the domain of  $H^M$  functions  $(u_1, u_2, u_3, u_4) \in \sum_{j=1}^{j=4} \oplus W_2^2(\Omega_j)$ ,  $W_2^2(\Omega_j)$  is the Sobolev space in  $\Omega_j$ , satisfying the following conditions:

$$D(H^M) : \begin{cases} u_j(-a, y) = u_j(a, y) = 0, & j = 1, 2, 3, 4 \\ u_1(x, b) = u_2(-x, b), & \frac{\partial u_1}{\partial y_1}(x, b) = -\frac{\partial u_2}{\partial y_2}(-x, b), \\ u_2(x, -b) = u_3(x, -b), & \frac{\partial u_2}{\partial y_2}(x, -b) = -\frac{\partial u_3}{\partial y_3}(x, -b), \\ u_3(x, b) = u_4(-x, b), & \frac{\partial u_3}{\partial y_3}(x, b) = -\frac{\partial u_4}{\partial y_4}(-x, b), \\ u_4(x, -b) = u_1(x, -b), & \frac{\partial u_4}{\partial y_4}(x, -b) = -\frac{\partial u_1}{\partial y_1}(x, -b). \end{cases} \tag{2}$$

**Remark.** Each rectangle  $\Omega_j$  presents, actually, one side of the rectangular sheet. The magnetic flux is related to the side of the surface. Correspondingly, if the sheet is turned over, then the sign of the flux ( $\xi$ ) changes. That is why, there are different signs in expressions for  $H_{1,2}^M$  and  $H_{3,4}^M$  in (1). There is no change of the sign between  $H_1^M$  and  $H_2^M$  ( $H_3^M$  and  $H_4^M$ ) because when one glues  $\Omega_1$  to  $\Omega_2$  ( $\Omega_3$  to  $\Omega_4$ ) in accordance with (2), there is, simultaneously, a replacement  $x \rightarrow -x$ .

Solving equations  $H^M\Psi = E\Psi$  at each rectangle and satisfying the gluing and boundary conditions (2), one obtains the spectral equation and the eigenfunctions.

The spectral equation is as follows:

$$\begin{vmatrix} \Phi_{1,n}(-a) & \Phi_{2,n}(-a) \\ \Phi_{1,n}(a) & \Phi_{2,n}(a) \end{vmatrix} = 0. \tag{3}$$

Here

$$\Phi_{1,n}(x; \xi) = e^{-\pi|\xi|(x-\frac{n}{T\xi})^2} \Phi\left(-\frac{E}{8\pi|\xi|} + \frac{1}{4}, \frac{1}{2}; \left(x - \frac{n}{T\xi}\right)^2 2\pi|\xi|\right), \tag{4}$$

$$\Phi_{2,n}(x; \xi) = e^{-\pi|\xi|^2\left(x - \frac{n}{T\xi}\right)^2} \sqrt{2\pi|\xi|} \Phi\left(-\frac{E}{8\pi|\xi|} + \frac{3}{4}, \frac{3}{2}; \left(x - \frac{n}{T\xi}\right)^2 2\pi|\xi|\right), \tag{5}$$

where  $T = 8b$ ,  $\Phi(\tilde{a}, \frac{1}{2}; z)$  is the Kummer function:

$$\Phi\left(\tilde{a}, \frac{1}{2}; z\right) = 1 + \sum_{k=1}^{\infty} \frac{(\tilde{a})_k}{(1/2)_k} \frac{z^k}{k!}, \tag{6}$$

$$(\tilde{a})_k = \tilde{a}(\tilde{a} + 1)\dots(\tilde{a} + k - 1), \quad (\tilde{a})_0 = 1.$$

Roots  $E_{n,m}$  of equation (3) gives us the eigenvalues of the operator. It is known [12] that the roots of equation (3) can be ordered increasingly. Correspondingly,  $E_{n,m}$  is the  $m$ -th root of  $n$ -th equation (3).

The main result is the following theorem.

**Theorem 2.1.** *The eigenvalues  $E_{nm}$  of the operator  $H^M$  are the roots of equation (3) with  $T = 8b$ . The corresponding eigenfunctions have the following form:*

$$\left\{ \begin{array}{l} \Psi_{n,m}^{(1)} = A_{n,m} e^{i \frac{\pi n y}{4b}} \phi_{n,m}(x; \xi), \quad (x, y) \in \Omega_1 \\ \Psi_{n,m}^{(2)} = i^n A_{n,m} e^{-i \frac{\pi n y}{4b}} \phi_{n,m}(x; \xi), \quad (x, y) \in \Omega_2, \\ \Psi_{n,m}^{(3)} = (-1)^n A_{n,m} e^{i \frac{\pi n y}{4b}} \phi_{n,m}(x; \xi), \quad (x, y) \in \Omega_3 \\ \Psi_{n,m}^{(2)} = (-i)^n A_{n,m} e^{-i \frac{\pi n y}{4b}} \phi_{n,m}(x; \xi), \quad (x, y) \in \Omega_4, \end{array} \right. \quad (7)$$

where  $A_{n,m}$  is some constant,  $\phi_{n,m}(x; \xi)$  is given by (8).

$$\phi_{n,m}(x; \xi) = \Phi_{2,n,m}(a; \xi) \Phi_{1,n,m}(x; \xi) + \Phi_{1,n,m}(a; \xi) \Phi_{2,n,m}(x; \xi), \quad (8)$$

where  $\Phi_{j,n,m}(x; \xi)$  is  $\Phi_{j,n}(x; \xi)$  for  $E = E_{nm}$ .

Functions  $\Phi_{1,n}(x; \xi)$  and  $\Phi_{2,n}(x; \xi)$  are two linearly independent solutions of the following equation

$$\psi''(x) - \left( (2\pi\xi)^2 \left( x - \frac{n}{T\xi} \right)^2 - E \right) \psi(x) = 0. \quad (9)$$

One can note that function  $\phi_{n,m}(x; \xi)$  satisfies the following property:

$$\phi_{n,m}(-x; \xi) = \phi_{n,m}(x; -\xi) = \phi_{-n,m}(x; \xi). \quad (10)$$

## References

- [1] Wolf S.A., Awschalom D.D., Buhrman R.A., Daughton J.M., S. von Molnar, Roukes M.L., Chtchelkanova A.Y., Treger D.M. Spintronics: A spin-based electronics vision for the future. *Science*, 2001, **294**, P. 1488–1495.
- [2] Nielsen M.A., Chuang I.L. *Quantum Computation and Quantum Information*. Cambridge University Press, Cambridge, 2010.
- [3] von Klitzing K., Dorda G., Pepper M. New method for high-accuracy determination of the fine structure constant based on quantised Hall resistance. *Phys. Rev. Lett.*, 1980, **45**(6), P. 494–497.
- [4] Ando T. Edge states in quantum wires in high magnetic fields. *Phys. Rev. B*, 1990, **42**(9), P. 5626–5634.
- [5] Büttiker M. Transmission probabilities and the quantum Hall effect. *Surface Science*, 1990, **229**, P. 201–208.
- [6] Ekholm T., Kovarik H. Stability of the magnetic Schrödinger operator in a waveguide. *Commun in Part. Diff. Eq.*, 2005, **30**, P. 539–565.
- [7] Exner P., Kovarik H. *Quantum waveguides*. Springer, Berlin, 2015.
- [8] Borisov D., Ekholm T., Kovarik H. Spectrum of the magnetic Schrödinger operator in a waveguide with combined boundary conditions. *Ann. Henri Poincaré*, 2005, **6**, P. 327–342.
- [9] Briet P., Raikov G., Soccorsi E. Spectral Properties of a Magnetic Quantum Hamiltonian on a Strip. *Asymptotic Analysis*, 2008, **58**(3), P. 127–155.
- [10] Bruneau V., Popoff N. On the ground state energy of the Laplacian with a magnetic field created by a rectilinear current. *J. Functional Analysis*, 2015, **268**, P. 1277–1307.
- [11] Geniet P. On a quantum Hamiltonian in a unitary magnetic field with axisymmetric potential. *J. Math. Phys.*, 2020, **61**, P. 082104.
- [12] Geiler V. A., Senatorov M. M. Structure of the spectrum of the Schrodinger operator with magnetic field in a strip and infinite-gap potentials. *Mat. Sb.*, 1997, **188**(5), P. 21–32 (in Russian); English translation: *Sb. Math.*, 1997, **188**(5), P. 657–669.
- [13] Chaplik A.V., Magarill L.I., Romanov D.A. Effect of curvature of a 2D electron sheet on the ballistic conductance and spin-orbit interaction. *Physica B*, 1998, **249-251**, P. 377–382.
- [14] Ouyang G., Wang C. X., Yang G. W. Surface energy of nanostructural materials with negative curvature and related size effects. *Chem. Rev.*, 2009, **109**(9), P. 4221–4247.
- [15] Kaur J., Kant R. Curvature-induced anomalous enhancement in the work function of nanostructures. *J. Phys. Chem. Lett.*, 2015, **6**(15), P. 2870–2874.
- [16] Briet Ph. A model of sheared nanoribbons. *Nanosystems: Phys. Chem. Math.*, 2022, **13**(1), P. 12–16.
- [17] Donnelly C., Hierro-Rodriguez A., Abert C. et al. Complex free-space magnetic field textures induced by three-dimensional magnetic nanostructures. *Nat. Nanotechnol.*, 2022, **17**, P. 136–142.
- [18] Schmidt A.G.M. Exact solutions of Schrödinger equation for a charged particle on a sphere and on a cylinder in uniform electric and magnetic fields. *Physica E: Low-dimensional Systems and Nanostructures*, 2019, **106**, P. 200–207.
- [19] Gritsev V.V., Kurochkin Yu. A. Model of excitations in quantum dots based on quantum mechanics in spaces of constant curvature. *Phys. Rev. B*, 2001, **64**, P. 035308.
- [20] Geyler V.A., Ivanov D.A., Popov I.Yu. Approximation of a point perturbation on a Riemannian manifold. *Theor. Math. Phys.*, 2009, **158**(1), P. 40–47.
- [21] Berard P.H., Helffer B., Kiwan R. Courant-sharp property for Dirichlet eigenfunctions on the Möbius strip. *Portugaliae Mathematica*, 2021, **78**(1), P. 1–41.

---

*Submitted 02 June 2023; revised 05 August 2023; accepted 08 August 2023*

*Information about the author:*

Igor Y. Popov – Center of Mathematics, ITMO University, Kroverkskiy, 49, St. Petersburg, 197101, Russia; ORCID 0000-0002-5251-5327; popov1955@gmail.com

## Fast forward evolution in heat equation: Tunable heat transport in adiabatic regime

Jasur Matrasulov<sup>1,a</sup>, Jambul R. Yusupov<sup>2,b</sup>, Abdulla A. Saidov<sup>3,c</sup>

<sup>1</sup>Faculty of Physics, National University of Uzbekistan, Tashkent, Uzbekistan

<sup>2</sup>Kimyo International University in Tashkent, Tashkent, Uzbekistan

<sup>3</sup>Turin Polytechnic University in Tashkent, Tashkent, Uzbekistan

<sup>a</sup>jasur1362@gmail.com, <sup>b</sup>j.yusupov@kiut.uz, <sup>c</sup>abdullasaidov@gmail.com

Corresponding author: Matrasulov J., jasur1362@gmail.com

PACS 03.65.Ta, 32.80.Qk, 37.90. j, 05.45.Yv

**ABSTRACT** We consider the problem of fast forward evolution of the processes described in terms of the heat equation. The matter is considered on an adiabatically expanding time-dependent box. Attention is paid to acceleration of heat transfer processes. So called shortcuts to adiabaticity, implying fast forwarding of the adiabatic states are studied. Heat flux and temperature profiles are analyzed for standard and fast forwarded regimes.

**KEYWORDS** Heat equation, shortcuts to adiabaticity, heat transport

**FOR CITATION** Matrasulov J., Yusupov J.R., Saidov A.A. Fast forward evolution in heat equation: Tunable heat transport in adiabatic regime. *Nanosystems: Phys. Chem. Math.*, 2023, **14** (4), 421–427.

### 1. Introduction

Controlling the evolution of physical processes is of fundamental and practical importance for modern science and technology. Mathematically, the problem of tunable evolution of a given physical system can be solved by developing realistic and physically acceptable models allowing manipulations in the evolution equations describing the process. Such a task attracted special attention in quantum mechanics, where an effective prescription for acceleration (deceleration) of a quantum evolution in the Schrödinger equation has been proposed earlier in [1]. The advantage of the prescription proposed in [1] is caused by the fact that it allows to speed up the time evolution of a wave function by controlling the driving potential with resultant regulation of the additional phase of the wave-function. Slightly modified version of the prescription was applied also to acceleration of the evolution for nonlinear Schrödinger equation and quantum tunneling dynamics [2]. Later, the method was considerably improved [3, 4] and applied for different systems (see, e.g., Refs. [2, 5–8]). Another important aspect of fast-forward protocol proposed in [1] is the flexibility for the choice of control parameter that allows one to apply it to the broad variety of physical systems described in terms of different evolution equations. In particular, the prescription was quite effective for fast forwarding of the adiabatic evolution [3, 4]. In case of the adiabatic evolution, the central problem is fast forward of the adiabatic dynamics within a given short time-scale, so called “short-cuts” to adiabaticity. Simply, shortcuts to adiabaticity (STA) are the fast control protocols to drive the dynamics of system, which are fast routes to the final results of slow, adiabatic changes of the controlling parameters of a system [9, 10]. In other words, a technique which allows one to control dynamics of the adiabatic processes is called “shortcuts to adiabaticity”. The concept of STA was introduced first in the Ref. [11]. So far, several types of STA control protocols, such as counterdiabatic driving [12], (also known as transitionless quantum driving [13]), inverse engineering [14], local counterdiabatic driving [15] and fast-forward [3, 4] protocols have been developed. Some other approaches to the STA beyond the protocol proposed in [1] are discussed in detail in Ref. [10]. In this paper, we use fast-forward approach STA from Refs. [3, 4] to develop STA protocol for the heat transport processes described in terms of the heat equation. It is important to note that the protocol was found as successful application to the non-equilibrium equation of states for the quantum gas under a rapidly moving piston [7]. Also, it lead to a simple protocol to accelerate the adiabatic quantum dynamics of spin clusters [5] and adiabatic control of tunneling states [6]. The fast-forward theory is also applicable to dynamical construction of classical adiabatic invariant [16] and to classical stochastic Carnot-like heat engine [8]. Here, we will study temperature profile and heat current for fast forward system described in terms of the heat equation on a finite interval with moving boundaries. This paper is organized as follows. In the next section, we will present a brief description of the fast-forward protocol, following Ref [1]. Section 3 presents brief recall of the heat equation on a finite interval, application of fast forward protocol to the heat equation in a time-dependent box. Finally, section 4 presents some concluding remarks.

## 2. Fast forward of adiabatic dynamics described in terms of parabolic evolution equations

Here, following Ref. [1], we will briefly recall description of the fast forward protocol for the Schrödinger equation, which is a parabolic equation. We do this for 1D confined system by focusing on adiabatic dynamics. First, let us define two systems, the so-called standard system,  $\Psi_0$ , whose evolution is to be fast accelerated and the fast forwarded system,  $\Psi_{FF}$  which is just obtained as a result of acceleration of the evolution of the standard system. Our approach can be formulated as follows:

- (1) A given confining potential  $V_0$  is assumed to vary in time adiabatically and to generate a stationary system  $\psi_0$ , which is an eigenstate of the time-independent Schrödinger equation with the instantaneous Hamiltonian. Then, both  $\psi_0$  and  $V_0$  are regularized so that they should satisfy the time-dependent Schrödinger equation (TDSE);
- (2) Taking the regularized system as a standard system (to be fast forwarded), we shall change the time scaling with use of the scaling factor  $\alpha(t)$ , where the mean value  $\bar{\alpha}$  of the infinitely-large time scaling factor,  $\alpha(t)$  will be chosen to compensate the infinitesimally-small growth rate,  $\epsilon$  of the quasi-adiabatic parameter and to satisfy  $\bar{\alpha} \times \epsilon = \text{finite}$ .

Thus, consider the standard dynamics with a “deformable” trapping potential, whose shape is characterized by a slowly-varying control parameter  $R(t)$  given by

$$R(t) = R_0 + \epsilon t, \quad (1)$$

with the growth rate  $\epsilon \ll 1$ , which means that it requires a very long time  $T = O\left(\frac{1}{\epsilon}\right)$ , to see the recognizable change of  $R(t)$ . The dynamics of a charged particle confined in the field of such potential can be described in terms of the following time-dependent 1D Schrödinger equation (1D TDSE):

$$i\hbar \frac{\partial \psi_0}{\partial t} = -\frac{\hbar^2}{2m} \partial_x^2 \psi_0 + V_0(x, R(t)) \psi_0, \quad (2)$$

where the coupling with external electromagnetic field is assumed to be absent. The stationary bound state  $\phi_0$  satisfies the time-independent counterpart given by

$$E \phi_0 = \hat{H}_0 \phi_0 \equiv \left[ -\frac{\hbar^2}{2m} \partial_x^2 + V_0(x, R) \right] \phi_0. \quad (3)$$

Then, using the eigenstate  $\phi_0 = \phi_0(x, R)$ , satisfying Eq.(3), one might conceive the corresponding time-dependent system to be a product of  $\phi_0$  and a dynamical factor as

$$\psi_0 = \phi_0(x, R(t)) e^{-\frac{i}{\hbar} \int_0^t E(R(t')) dt'}. \quad (4)$$

As it stands, however,  $\psi_0$  does not satisfy TDSE (2). Therefore, we introduce a regularized system

$$\begin{aligned} \psi_0^{reg} &\equiv \phi_0(x, R(t)) e^{i\epsilon \theta(x, R(t))} e^{-\frac{i}{\hbar} \int_0^t E(R(t')) dt'} \\ &\equiv \phi_0^{reg}(x, R(t)) e^{-\frac{i}{\hbar} \int_0^t E(R(t')) dt'} \end{aligned} \quad (5)$$

together with a regularized potential

$$V_0^{reg} \equiv V_0(x, R(t)) + \epsilon \tilde{V}(x, R(t)). \quad (6)$$

The unknown  $\theta$  and  $\tilde{V}$  will be determined self-consistently, so that  $\psi_0^{reg}$  should fulfill the TDSE given by

$$i\hbar \frac{\partial \psi_0^{reg}}{\partial t} = -\frac{\hbar^2}{2m} \partial_x^2 \psi_0^{reg} + V_0^{reg} \psi_0^{reg}, \quad (7)$$

up to the order of  $\epsilon$ .

One can rewrite  $\phi_0(x, R(t))$  using the real positive amplitude  $\bar{\phi}_0(x, R(t))$  and phase  $\eta(x, R(t))$  as

$$\phi_0(x, R(t)) = \bar{\phi}_0(x, R(t)) e^{i\eta(x, R(t))}, \quad (8)$$

and see that  $\theta$  and  $\tilde{V}$  satisfy the following relations:

$$\partial_x (\bar{\phi}_0^2 \partial_x \theta) = -\frac{m}{\hbar} \partial_R \bar{\phi}_0^2, \quad (9)$$

$$\frac{\tilde{V}}{\hbar} = -\partial_R \eta - \frac{\hbar}{m} \partial_x \eta \cdot \partial_x \theta. \quad (10)$$

Integrating Eq. (9) over  $x$ , we have

$$\partial_x \theta = -\frac{m}{\hbar} \frac{1}{\bar{\phi}_0^2} \int \partial_R \bar{\phi}_0^2 dx', \quad (11)$$

which is the main equation of the regularization procedure. The problem of singularity due to nodes of  $\bar{\phi}_0$  in Eq. (11) can be overcome, so long as one is concerned with the systems with scale-invariant potentials.

We now accelerate the quasi-adiabatic dynamics of  $\psi_0^{reg}$  in Eq.(5), by applying the external electromagnetic field. To do this, we introduce the fast-forward version of  $\psi_0^{reg}$  as

$$\begin{aligned}\psi_{FF}^{(0)}(x, t) &\equiv \psi_0^{reg}(x, R(\Lambda(t))) \\ &\equiv \phi_0^{reg}(x, R(\Lambda(t)))e^{-\frac{i}{\hbar} \int_0^t E(R(\Lambda(t')))dt'}\end{aligned}\quad (12)$$

with

$$R(\Lambda(t)) = R_0 + \epsilon\Lambda(t), \quad (13)$$

where  $\Lambda(t)$  is the future or advanced time

$$\Lambda(t) = \int_0^t \alpha(t') dt', \quad (14)$$

and  $\alpha(t)$  is a magnification scale factor defined by  $\alpha(0) = 1$ ,  $\alpha(t) > 1$  ( $0 < t < T_{FF}$ ),  $\alpha(t) = 1$  ( $t \geq T_{FF}$ ). Suppose,  $T$  to be a very long time to see a recognizable change of the adiabatic parameter  $R(t)$  in Eq.(1), and then the corresponding change of  $R(\Lambda(t))$  is reached in the shortened or fast-forward time  $T_{FF}$  defined by

$$T = \int_0^{T_{FF}} \alpha(t) dt. \quad (15)$$

The explicit expression for  $\alpha(t)$  in the fast-forward range ( $0 \leq t \leq T_{FF}$ ) can be written as

$$\alpha(t) = \bar{\alpha} - (\bar{\alpha} - 1) \cos\left(\frac{2\pi}{T/\bar{\alpha}}t\right), \quad (16)$$

where  $\bar{\alpha}$  is the mean value of  $\alpha(t)$  and is given by  $\bar{\alpha} = T/T_{FF}$ .

Furthermore, let us assume  $\psi_{FF}^{(0)}$  to be the solution of the TDSE for a charged particle in the presence of gauge potentials,  $A_{FF}^{(0)}(x, t)$  and  $V_{FF}^{(0)}(x, t)$ ,

$$\begin{aligned}i\hbar \frac{\partial \psi_{FF}^{(0)}}{\partial t} &= H_{FF} \psi_{FF}^{(0)} \equiv \\ &\left( \frac{1}{2m} \left( \frac{\hbar}{i} \partial_x - A_{FF}^{(0)} \right)^2 + V_{FF}^{(0)} + V_0^{reg} \right) \psi_{FF}^{(0)},\end{aligned}\quad (17)$$

where, for simplicity, we employ the prescription of a positive unit charge ( $q = 1$ ) and the unit velocity of light ( $c = 1$ ). The driving electric field is given by

$$E_{FF} = -\frac{\partial A_{FF}^{(0)}}{\partial t} - \partial_x V_{FF}^{(0)}. \quad (18)$$

Substituting Eq. (12) into Eq. (17), we find  $\phi_0^{reg}$  to satisfy

$$\begin{aligned}i\hbar \frac{\partial \phi_0^{reg}}{\partial t} &= \frac{1}{2m} \left( \frac{\hbar}{i} \partial_x - A_{FF}^{(0)} \right)^2 \phi_0^{reg} \\ &+ (V_{FF}^{(0)} + V_0^{reg} - E) \phi_0^{reg},\end{aligned}\quad (19)$$

where  $V_0^{reg} \equiv V^{reg}(x, R(\Lambda(t)))$ , i.e. the advanced-time variant of Eq. (6). The dynamical phase in Eq.(12) has led to the energy shift in the potential in Eq. (19).

Rewriting  $\phi_0^{reg}$  in terms of the amplitude  $\bar{\phi}_0$  and phases  $\eta + \epsilon\theta$  as

$$\phi_0^{reg} \equiv \bar{\phi}_0(x, R(\Lambda(t)))e^{i[\eta(x, R(\Lambda(t))) + \epsilon\theta(x, R(\Lambda(t)))]}, \quad (20)$$

and using Eq. (20) in Eq. (19), we find  $A_{FF}^{(0)}$  of  $O(\epsilon\alpha)$  and  $V_{FF}^{(0)}$  consisting of terms of  $O(\epsilon\alpha)$  and  $O((\epsilon\alpha)^2)$ .

Now, taking the limit  $\epsilon \rightarrow 0$  and  $\bar{\alpha} \rightarrow \infty$  with  $\epsilon\bar{\alpha} = \bar{v}$  being kept finite, we obtain (see Ref. [6] for details):

$$\begin{aligned}A_{FF}^{(0)} &= -\hbar v(t) \partial_x \theta, \\ V_{FF}^{(0)} &= -\frac{\hbar^2}{m} v(t) \partial_x \theta \cdot \partial_x \eta \\ &- \frac{\hbar^2}{2m} (v(t))^2 (\partial_x \theta)^2 - \hbar v(t) \partial_R \eta,\end{aligned}\quad (21)$$

where  $T_{FF} \left( = \frac{T}{\bar{\alpha}} = O \left( \frac{1}{\epsilon \bar{\alpha}} \right) \right) = \text{finite}$ . In the same limiting case as above,  $\psi_{FF}^{(0)}$  is explicitly given by

$$\psi_{FF}^{(0)} = \bar{\phi}_0(x, R(\Lambda(t))) e^{i\eta(x, R(\Lambda(t)))} e^{-\frac{i}{\hbar} \int_0^t E(R(\Lambda(t'))) dt'} \quad (22)$$

### 3. Fast forwarding the heat equation based evolution

Our aim is application of fast forward protocol to the heat equation in time-varying interval, to achieve acceleration (deceleration) of the heat transfer process. Before formulating the problem, we will briefly recall the heat equation and its solution considering it on a finite interval,  $(0, l)$ . The heat equation can be written as

$$\frac{\partial u}{\partial t} = \kappa^2 \frac{\partial^2 u}{\partial x^2} \quad (23)$$

where  $u(x, t)$  is the temperature profile,  $\kappa$  is the heat conductivity. The boundary and initial conditions can be imposed as

$$u(0, t) = u(l, t) = 0, \quad (24)$$

and

$$u(x, 0) = f(x). \quad (25)$$

Exact solutions of the problem given by Eqs. (1)-(3) can be obtained by factorizing variables as

$$u(x, t) = X(x)T(t) = C_n \sin \frac{\pi n}{l} x, \quad (26)$$

Applying the principle of superposition, one obtains the general solution of Eq.(23) [17, 18]

$$u(x, t) = \sum_{n=1}^{\infty} C_n e^{-\frac{\pi^2 \kappa^2 n^2}{l^2} t} \sin \frac{\pi n}{l} x \quad (27)$$

where  $C_n$  can be calculated by using initial temperature profile as follows [17, 18]:

$$C_n = \frac{2}{l} \int_0^l f(x) \sin \frac{\pi n}{l} x dx.$$

In what follows we will choose Gaussian type initial temperature profile given by

$$f(x) = \frac{1}{\sqrt{2\pi}\sigma} e^{-\frac{(x-x_0)^2}{\sigma^2}}$$

For such initial temperature profile, the coefficients,  $C_n$  are computed numerically both for standard as well as for fast-forwarded systems.

Now, consider the fast forward evolution in the heat equation. The standard system,  $u^{(0)}$  is given in terms of the following evolution equation:

$$\frac{\partial u^{(0)}}{\partial t} = \kappa^2 \frac{\partial^2 u^{(0)}}{\partial x^2} \quad (28)$$

where  $\kappa$  denotes the thermal conductivity. We consider the heat equation on a finite-interval with time-varying boundary. The time-dependent boundary conditions are imposed as

$$u^{(0)}(x = 0, t) = 0, \quad u^{(0)}(x = L(\Lambda(t)), t) = 0,$$

We consider the case of time-dependence of the boundary given by

$$L(t) = L_0 + \epsilon t.$$

Furthermore, we assume that our physical process is adiabatic, i.e.  $\epsilon \rightarrow 0$ . Then  $t$  can be replaced by future time given as

$$\Lambda(t) = \int_0^t \alpha(\tau) d\tau. \quad \text{This allows us to write } L(t) \text{ as}$$

$$L(t) = L_0 + \epsilon \Lambda(t).$$

It is easy to see that wall's position for fast-forwarded system can have arbitrary time-dependence, since the magnification factor  $\alpha$  can be any function of time. The velocity of the wall, whose value is finite, is given by

$$\dot{L} = \epsilon \alpha = v, \quad \epsilon \rightarrow 0, \quad \alpha \rightarrow \infty.$$

General solution of the heat equation for adiabatically expanding box can be written as

$$u^{(0)}(x) = \sum_{n=1}^{\infty} C_n \sin \left[ \frac{\pi n}{L(\Lambda(t))} x \right], \quad (29)$$

Before applying fast forward protocol of Ref. [1], we will regularize the standard system as it was done in [4]. Then the solution of the regularized standard system can be written as

$$u_n^{(reg)} = u_n^{(0)}(x)e^{-\frac{\pi^2 n^2 \kappa^2}{L(\Lambda(t))^2}t}, \quad (30)$$

and the regularized potential is given by

$$V^{(reg)}(x, t) = \epsilon \tilde{V}(x, L(\Lambda(t))). \quad (31)$$

The dynamical phase  $\theta$  and the potential  $\tilde{V}$  can be obtained from Eq. (39) and (40) of Ref. [4]. In case of the box for  $\theta$  we have:

$$\partial_x \theta = -\frac{1}{u^2} \partial_L \int_0^x u^2 dx.$$

Now, let us consider fast-forwarding of the regularized dynamics. The heat equation for such fast-forwarded system can be written as

$$\frac{\partial u^{(FF)}}{\partial t} = \kappa^2 \frac{\partial^2 u^{(FF)}}{\partial x^2} + V_{FF} u^{(FF)}, \quad (32)$$

where the definition of the fast-forwarded system is given as follows [4]:

$$u_n^{(FF)} = u_n^{(reg)} e^{\epsilon \theta} = u_n^{(0)} e^{\epsilon \theta} e^{-\frac{\pi^2 n^2 \kappa^2}{L^2}t}.$$

Fast-forward ‘‘potential’’ for our case can be found in the form:

$$V_{FF} = -\frac{d\alpha}{dt} \epsilon \theta - \alpha^2 \epsilon^2 \frac{\partial \theta}{\partial L} - \frac{1}{2} \alpha^2 \epsilon^2 (\nabla \theta)^2$$

Figs. 1 (a) and 1 (b) present the plots of the temperature profile for standard and fast forwarded systems, respectively.

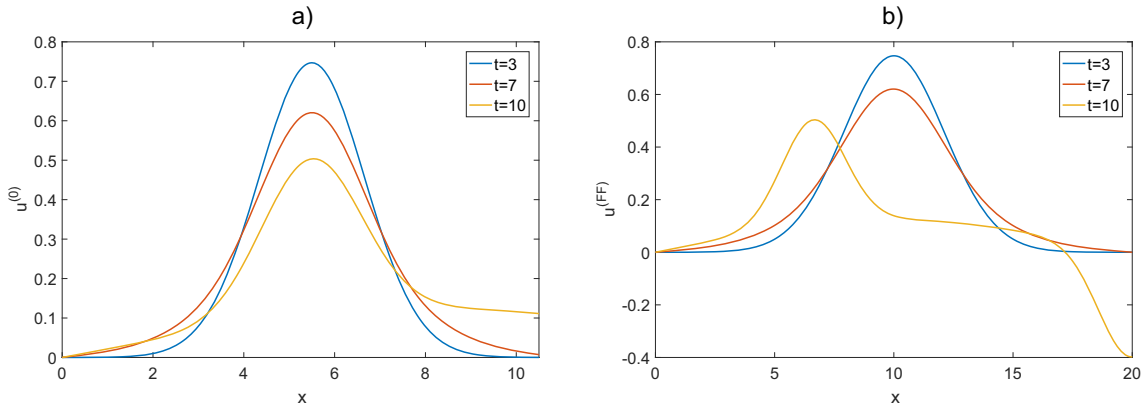


FIG. 1. Temperature profiles of (a) standard and (b) fast forwarded systems. The value of the heat conductance is chosen as  $\kappa = 0.5$ , and parameter  $L_0 = 10$  for both plots,  $\epsilon = 0.04$ ,  $\bar{\alpha} = 100$

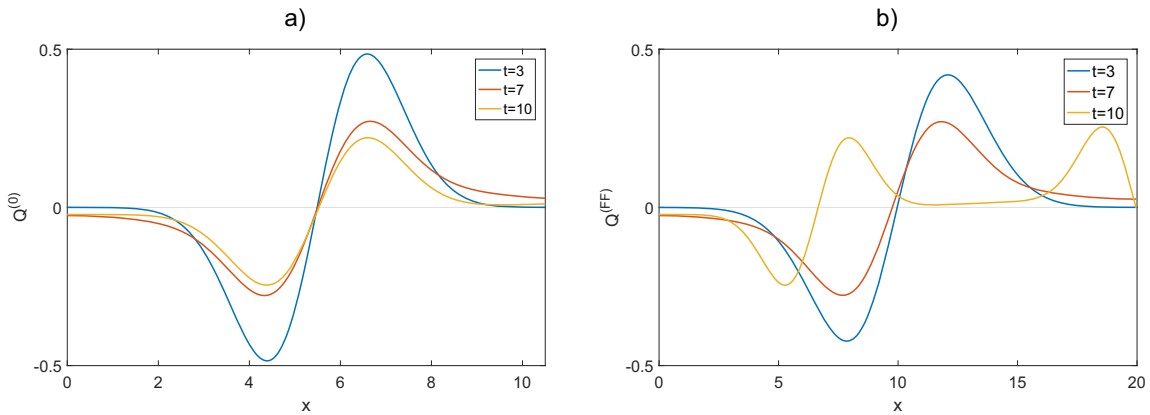


FIG. 2. Heat flux of standard and (b) fast forwarded systems. The value of the heat conductance is chosen as  $\kappa = 0.5$ , and parameter  $L_0 = 10$  for both plots,  $\epsilon = 0.04$ ,  $\bar{\alpha} = 100$

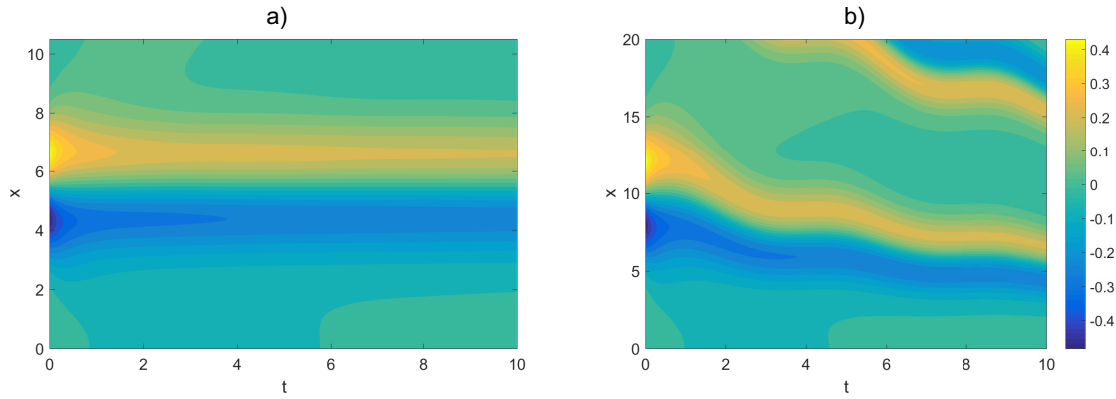


FIG. 3. Heat flux of standard (a) and fast forwarded (b) systems. The value of parameters are chosen as  $\kappa = 0.5$ ,  $L_0 = 10$  and  $\varepsilon = 0.04$ ,  $\bar{\alpha} = 100$  for both plots.

Abrupt qualitative difference between the two curves can be clearly seen. In particular, widening of the profile for fast forwarded state can be observed. Plots of the heat flux for standard and fast forwarded systems, obtained using the explicit solutions given by Eq.(29) and the numerical solution of Eq.(22), are presented in Figs. 2 (a) and 2(b), respectively. Oscillations of the heat flux become more intensive for fast forwarded system. Our analysis of similar plots for much longer (than that shown in the plot) time interval showed more rapid oscillations of fast forwarded state. Figs. 3 (a) and 3 (b) present contour plots of the heat flux for standard and fast forwarded systems vs coordinate and time for the following values of parameters  $\kappa = 0.5$ ,  $L_0 = 10$ ,  $\varepsilon = 0.04$  and  $\bar{\alpha} = 100$ . For standard system, the flux is localized close to the middle of the interval, between 6 and 7, while for fast forwarded system, one can observe certain blurring of the flux, although some weak localization around the points 15 and 16. Finally, one should note that in all the plots, width of the box for fast forwarded case is larger than that for the standard state. This is caused by the fact that for fast forwarded system, we use positive time-magnification factor that causes faster expansion of the interval in fast forwarded case.

#### 4. Conclusions

In this paper, we studied fast forward problem for the heat equation by considering the latter on adiabatically expanding time-dependent box. Masuda-Nakamura fast-forward protocol [1, 3] is applied for acceleration of the evolution of heat transfer process in time-dependent box with slowly moving walls. Physically important characteristics, such as temperature profile and heat flux are computed for standard and fast forwarded regimes. Considerable differences between these characteristics for standard and fast-forwarded regimes are found. In particular, the plots of the temperature profile for standard and fast forwarded states show clear quantitative and qualitative difference of the heat transfer for these two regimes. Breaking of the space-periodicity in heat flux for the fast forwarded system is also found. As the physical realization of the above model, one can consider heat transport in harmonic crystals and in graphene nanoribbon subjected to time-periodic strain. Finally, we note that the above study can be directly extended to the cases of two- and three-dimensional counterparts.

#### References

- [1] Masuda S., Nakamura K. Fast-forward problem in quantum mechanics. *Phys. Rev. A*, 2008, **78**, P. 062108.
- [2] Khujakulov A., Nakamura K. Scheme for accelerating quantum tunneling dynamics. *Phys. Rev. A*, 2016, **93**, P. 022101.
- [3] S. Masuda and K. Nakamura, Fast-forward of adiabatic dynamics in quantum mechanics, *Proc. R. Soc. A* **466**, 1135 (2010).
- [4] Shumpei Masuda and Katsuhiko Nakamura, Acceleration of adiabatic quantum dynamics in electromagnetic fields. *Phys. Rev. A*, 2011, **84**, P. 043434.
- [5] Setiawan I., Bobby Eka Gunara, Masuda S., Nakamura K. Fast forward of the adiabatic spin dynamics of entangled states. *Phys. Rev. A*, 2017, **96**, P. 052106.
- [6] Nakamura K., Khujakulov A., Avazbaev S., Masuda S. Fast forward of adiabatic control of tunneling states. *Phys. Rev. A*, 2017, **95**, P. 062108.
- [7] Babajanova G., Matrasulov J., Nakamura K. Quantum gas in the fast forward scheme of adiabatically expanding cavities: Force and equation of state. *Phys. Rev. E*, 2018, **97**, P. 042104.
- [8] Katsuhiko Nakamura, Jasur Matrasulov, and Yuki Izumida. Fast-forward approach to stochastic heat engine. *Phys. Rev. E*, 2020, **102**, P. 012129.
- [9] Guéry-Odelin D., Ruschhaup A., Kiel A., Torrontegui E., Martínez-Garaot S., Muga J.G. Shortcuts to adiabaticity: Concepts, methods, and applications. *Rev. Mod. Phys.*, 2019, **91**, P. 045001.
- [10] Erik Torrontegui, et al. Chapter 2 - Shortcuts to Adiabaticity, *Advances in atomic, molecular, and optical physics*, 2013, **62**, P. 117.
- [11] Chen X., et al. Fast Optimal Frictionless Atom Cooling in Harmonic Traps: Shortcut to Adiabaticity. *Phys. Rev. Lett.*, 2010, **104**, P. 063002.
- [12] Demirplak M., Rice S.A. Adiabatic Population Transfer with Control Fields. *J. Phys. Chem. A.*, 2003, **107**, P. 9937.
- [13] Berry M.V. Transitionless quantum driving. *Journal of Physics A: Mathematical and Theoretical*, 2009, **42**, P. 365303.
- [14] Martínez-Garaot S., et al. Vibrational Mode Multiplexing of Ultracold Atoms. *Phys. Rev. Lett.*, 2013, **111**, P. 213001.
- [15] A. del Campo. Shortcuts to Adiabaticity by Counterdiabatic Driving. *Phys. Rev. Lett.*, 2013, **111**, P. 100502.
- [16] Christopher Jarzynski, Sebastian Deffner, Ayoti Patra, and Yiğit Subaşı, Fast forward to the classical adiabatic invariant. *Phys. Rev. E*, 2017, **95**, P. 032122.

- [17] Widder D. The Heat Equation. *Academic Press*, 1975.
- [18] Cannon J.R. The One-Dimensional Heat Equation. *Cambridge University Press*, 1984.
- [19] Barbu V. Partial Differential Equations and Boundary Value Problems. *Springer*, 1998.
- [20] Kirkwood J. Mathematical Physics with Partial Differential Equations. *Academic Press*, 2013.
- [21] X-Sh. Yang. Modelling heat transfer of carbon nanotubes, *Modelling Simul. Mater. Sci. Eng.*, 2005, **13**, P. 893.
- [22] H.-D. Wang, B.-Y. Cao, Z.-Y. Guo. Heat flow choking in carbon nanotubes. *Int. J. Heat Mass Transfer*, 2010, **53**, P. 1796.
- [23] Dames C., Chen S., Harris C.T. A hot-wire probe for thermal measurements of nanowires and nanotubes inside a transmission electron microscope. *Rev. Sci. Instrum.*, 2007, **78**, P. 104903.
- [24] Bruns D., Nojeh A., Phani A.S., Rottler J. Heat transport in carbon nanotubes: Length dependence of phononic conductivity from the Boltzmann transport equation and molecular dynamics, *Phys. Rev. Lett. B*, 2020, **101**, P. 195408.

---

*Submitted 17 October 2022; revised 12 June 2023; accepted 25 June 2023*

*Information about the authors:*

*J. Matrasulov* – Faculty of Physics, National University of Uzbekistan, Vuzgorodok, Tashkent 100174, Uzbekistan;  
ORCID 0000-0001-5741-9003; jasur1362@gmail.com

*J. R. Yusupov* – Kimyo International University in Tashkent, 156 Usman Nasyr Str., 100121, Tashkent, Uzbekistan;  
ORCID 0000-0003-1758-6805; j.yusupov@kiut.uz

*A. A. Saidov* – Turin Polytechnic University in Tashkent, 17 Niyazov Str., 100095, Tashkent, Uzbekistan;  
ORCID 0000-0003-3295-4119; abdullasaidov@gmail.com

*Conflict of interest:* the authors declare no conflict of interest.

## The Space Charge Model. A new analytical approximation solution of Poisson–Boltzmann equation: the extended homogeneous approximation

Jalal Dweik<sup>a</sup>, Hassan Farhat<sup>b</sup>, Joumana Younis<sup>c</sup>

Jinan University, Tripoli, Lebanon

<sup>a</sup>jalal.douwayk@jinan.edu.lb, <sup>b</sup>hassan.farhat@jinan.edu.lb, <sup>c</sup>joumana.younis@jinan.edu.lb

Corresponding author: Jalal Dweik, jalal.douwayk@jinan.edu.lb

**ABSTRACT** The validity of different analytical approximations solution is studied using the classical Poisson–Boltzmann (PB) equation based on a mean-field description of ions as ideal point charges in combination with the assumption of fully overlapped electrical double layers in the membrane pores. The electrical conductivity is calculated by numerical and approximate analytical methods in order to explain the process of ion transport. In this paper, a new analytical approximation named the extended homogeneous approximation (EH) is presented, which provides better results than the homogeneous approximation based on Donnan theory. Also, the results show that the electrical conductivity calculated by the EH, is coherent with the numerical method within specific limits.

**KEYWORDS** space charge model, Poisson–Boltzmann (PB) equation, electrical conductivity, extended homogeneous (EH) approximation

**FOR CITATION** Dweik J., Farhat H., Younis J. The Space Charge Model. A new analytical approximation solution of Poisson–Boltzmann equation: the extended homogeneous approximation. *Nanosystems: Phys. Chem. Math.*, 2023, **14** (4), 428–437.

### 1. Introduction

Nanofiltration membranes (NF) are particularly relevant for industrial applications because of their valuable features, such as pore diameters smaller than 2 nm [1–3]. NF has several advantages over other filtration processes, including lower energy consumption, lower operating pressures, and the ability to selectively remove specific components. One of the most interesting applications of these membranes is the separation of ions [4, 5]. The separation of ions in NF occurs due to a combination of size exclusion, charge repulsion, and electrostatic attraction. The selectivity of NF membranes can be further enhanced by adjusting the pH of the solution or using different membrane materials with specific surface charges. However, the mechanism of transport through NF membranes is not yet well-established. To shed light on this topic, numerous researchers have utilized different macro and mesoscopic approaches [6–10] to elucidate the physical and chemical mechanisms underlying membrane transport. The space charge (SC) model, which is based on the Poisson–Boltzmann (PB) equation [11], describes ions as ideal point charges and assumes fully overlapped electrical double layers in the membrane pores. This model is well-suited for studying ion transport through charged nanopores membrane. However, the accuracy of the SC model and other approximations, such as Donnan's theory or the homogeneous theory based on the electroneutrality in the pore, is challenged when applied to NF. In this paper, the SC model is applied to study the limit of effectiveness of different areas that provide a physical idea about the behavior of the salt-nanopore system using analytical approximations (homogeneous approximation, good exclusion of co-ions, and plane approximation) and numerical calculations obtained from the PB equation. In this paper, a new analytical approximation solution, named the extended homogeneous approximation (EH) is presented. This approximation allows the researchers to use only one approximation instead of all other approximations mentioned above within specific limits. Finally, the validity of the EH approximation is studied by calculating the electrical conductivity and depends on three main parameters: pore radius, concentration of ions in the bulk, and surface charge density of the pore. These three parameters play a significant role in the transport through the pores. The remainder of this paper is organized as follows. The description of the models is given in section 2. The results and discussion are presented in section 3. The conclusions and suggestions are given in section 4.

### 2. Space charge model

The space charge model was developed by Osterle and colleagues [12–14]. It is a theoretical framework used to describe the behaviour of charged solutes near charged surfaces, such as nanofiltration membranes. It considers the electrostatic interactions between the charged solutes and the charged membrane surface. This model considers axial and radial variations in pressure, electric potential, and concentration. Assume a simple cylindrical pore of radius  $r_p$  and length  $d \gg r_p$ , filled with an aqueous solution with two ionic species [ $i = 1$  (counter-ion), 2 (co-ion)]. The pore's

electrical properties are defined by an assumed uniform surface charge density that depends on the ionic concentrations and the pore surface pH (Fig. 1).

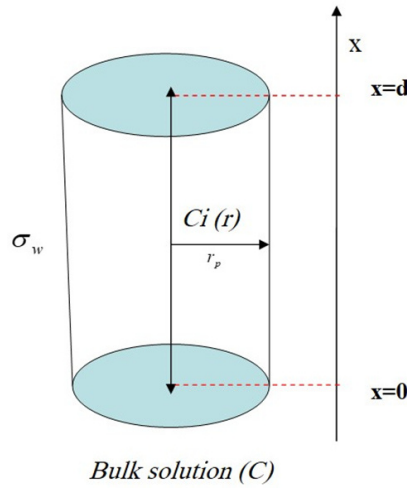


FIG. 1. Description of the model with the important parameters

Suppose that the ionic transport is at the steady state, so that there is no time function in the governing equations. The continuity equation for each ion can be expressed as

$$\nabla \cdot \vec{j}_i = 0, \quad (1)$$

where  $\vec{j}_i$  is the molar flux density of ion  $i$ , described by the extended Nernst–Planck equation

$$\vec{j}_i = -D_i \nabla c_i - \frac{F}{RT} z_i D_i c_i \nabla \Phi + c_i \vec{u}, \quad (2)$$

where  $D_i$  is the local diffusion coefficient of the ion  $i$ ,  $c_i$  is the local concentration of the species considered,  $z_i$  is the ion valence,  $\Phi$  is the total local electric potential,  $F$  is the Faraday constant.

The flow velocity is obtained by the Navier–Stokes equation. Neglecting all inertial terms (“creeping flow approximation”) and the inclusion of electrical forces, the Navier–Stokes equation is expressed by

$$\eta \nabla^2 \vec{u} = \rho \nabla \Phi + \nabla p, \quad (3)$$

where  $p$  is the local pressure applied to the fluid,  $\eta$  is the dynamic viscosity of the solution,  $\rho$  is the ionic charge density, which is defined by the following formula

$$\rho = F \sum_{i=1}^2 z_i c_i. \quad (4)$$

When the density of the fluid is constant, there is, in addition, the incompressibility condition

$$\nabla \cdot \vec{u} = 0. \quad (5)$$

The key of the space charge model is the Poisson–Boltzmann (PB) equation for electric potential and ionic concentration

$$\nabla^2 \Phi = \frac{\rho}{\varepsilon}, \quad (6)$$

$$\nabla^2 \Phi = \frac{\partial^2 \Phi}{\partial x^2} + \frac{1}{r} \frac{\partial \Phi}{\partial r} + \frac{\partial^2 \Phi}{\partial r^2}, \quad (7)$$

where  $\varepsilon = \varepsilon_0 \varepsilon_r$  is the absolute dielectric constant of the solution,  $\varepsilon_0$  is the dielectric constant in vacuum ( $\varepsilon_0 = 8.85 PF/m$ ),  $\varepsilon_r$  is the relative dielectric constant for water ( $\varepsilon_r = 78.54$ ).

The normal component of the molar flux density and velocity is equal to zero at the surface. Thus the boundary condition for Eq. (6) takes the following form:

$$\vec{j}_{i,r} \Big|_{r=r_p} = \frac{\partial c_i}{\partial r} \Big|_{r=r_p} + \frac{z_i F}{RT} c_i \frac{\partial \Phi}{\partial r} \Big|_{r=r_p} = 0. \quad (8)$$

By symmetry, another boundary condition of Eq. (6) which corresponds to the concentration and electric potential at the pore center is fined:

$$\frac{\partial c_i}{\partial r} \Big|_{r=0} = 0, \quad \frac{\partial \Phi}{\partial r} \Big|_{r=0} = 0, \quad (9)$$

and so

$$j_{i,r} \Big|_{r=0} = 0. \quad (10)$$

The global surface charge  $\sigma_w$  is related to the gradient of the potential via the Gaussian equation:

$$\frac{\partial \Phi}{\partial r} \Big|_{r=r_p} = \frac{\sigma_w}{\varepsilon}. \quad (11)$$

If the tangential component of the velocity at the pore surface is zero (no slip), then we can write the boundary condition of the Navier–Stokes equation

$$u_x \Big|_{r=r_p} = 0. \quad (12)$$

By symmetry,

$$\frac{\partial u_x}{\partial r} \Big|_{r=0} = 0. \quad (13)$$

The total local electric potential  $\Phi(x, r)$  can be divided into two parts:

$$\Phi(x, r) = \psi(r) + \varphi(x), \quad (14)$$

where  $\psi(r)$  is the potential due to the electrical double layer at the surface on the radial direction and the potential  $\varphi(x)$  is due to the bulk (outside the pore) along the  $x$  axis. Assume that the variation of  $\varphi(x)$  along  $x$  axis is negligible compared to the variation of the radial component, then Eq. (7) becomes as follows

$$\nabla^2 \Phi \approx \frac{1}{r} \frac{\partial \psi}{\partial r} + \frac{\partial^2 \psi}{\partial r^2}. \quad (15)$$

Assuming that Eqs. (8) and (10) allow the approximation  $j_i(r) = 0$  to be used for any  $r$ , then this equation can be integrated between  $0 < r < r_p$  to find the “radial equilibrium” approximation which gives one the concentration  $c_i(r)$  (Boltzmann distribution)

$$c_i(r) \approx k_i(r) v_i C, \quad (16)$$

where

$$k_i(r) = \exp \left[ -\frac{z_i F \psi(r)}{RT} \right], \quad (17)$$

$C$  is the electrolyte concentration equivalent to the concentration of a bulk solution in equilibrium with the pore at position  $x$  and  $v_i$  (the stoichiometric coefficient) represents the number of ions coming from the dissociated electrolytes. In the case of two ionic species  $i = 1, 2$ , the condition of electroneutrality is described by  $v_1 z_1 + v_2 z_2 = 0$  or  $v_1 |z_1| = v_2 |z_2|$ :

$$(\text{Counter-ion})_{z_1}^{\nu_1} (\text{Co-ion})_{z_2}^{\nu_2} \longrightarrow \nu_1 (\text{Counter-ion})^{z_1} + \nu_2 (\text{Co-ion})^{z_2}$$

The index ( $i = 1$ ) represents the counter ions and the index ( $i = 2$ ) represents the co-ions.

After substitution of Eqs. (15) and (16) in (6), the Poisson–Boltzmann equation which determines the electric potential inside the pore is obtained. It is presented in dimensionless form [14] by the following relation:

$$\frac{2}{\tilde{r}} \frac{\partial}{\partial \tilde{r}} \left( r \frac{\partial \tilde{\psi}}{\partial \tilde{r}} \right) \approx \left( \frac{r_p}{\lambda_c} \right)^2 \left( e^{+\tilde{\psi}} - e^{-\tau \tilde{\psi}} \right), \quad (18)$$

where

$$\tilde{\psi} = -\frac{z_1 F \psi(x, \tilde{r})}{RT} \geq 0, \quad \tilde{r} = \frac{r}{r_p}, \quad \tau = \frac{|z_2|}{|z_1|}, \quad (19)$$

$\lambda_c$  is the Debye length associated with the concentration  $C$  given by:

$$\lambda_c = \left( \frac{RT\varepsilon}{2v_1 z_1^2 F^2 C} \right) \propto C^{-1/2}. \quad (20)$$

The boundary conditions at the center and surface of the pore can be presented in dimensionless form [11–14]:

$$\frac{\partial \tilde{\psi}}{\partial \tilde{r}} \Big|_{\tilde{r}=1} = 4\sigma^*, \quad \frac{\partial \tilde{\psi}}{\partial \tilde{r}} \Big|_{\tilde{r}=0} = 0, \quad (21)$$

where

$$\sigma^* = \frac{1}{4} \left( \frac{r_p}{\lambda_m} \right)^2, \quad (22)$$

$\lambda_m$  is the Debye length associated with the membrane charge density

$$\lambda_m = \left( \frac{2\varepsilon RT}{|z_1| F^2 |X_m|} \right)^{1/2} \propto |X_m|^{-1/2}, \quad (23)$$

and  $R$  is the constant of the ideal gas and  $X_m$  is defined by

$$X_m = \frac{2\sigma_w}{F r_p}. \quad (24)$$

The membrane charge density  $|X_m|$  is expressed in moles per unit volume of the pore. It is proportional to  $|\sigma_w|$  and inversely proportional to the radius of the pore  $r_p$ . The average flux density in the pore can be calculated by integrating the local flux using the formula:

$$\bar{j}_{i,x} = \frac{2}{r_p^2} \int_0^{r_p} j_{i,x} r dr. \quad (25)$$

The average electrolyte flow density is denoted by  $J$ , the volume flow density – by  $J_v$  and the current density – by  $\bar{I}$ . It should be noted that the volume flow rate  $J_v$  is a very good approximation to the barycentric velocity  $U_m$  [13].

$$J = \sum_{i=1}^2 \bar{j}_i, \quad J_v = \bar{u}_x, \quad (26)$$

with the current density given by

$$\bar{I} = F \sum_{i=1}^2 z_i \bar{j}_i. \quad (27)$$

From Eq. (3), using Eqs. (8) and (13) for  $u_x$  and component  $x$  from Eq.(2) and averaging the fluxes over the pore cross-section by Eq. (27), the following system of transport equations is obtained:

$$\begin{aligned} J_v &= -L_{11} \left( \frac{\partial P_0}{\partial x} \right) - L_{12} \left( \frac{\partial \mu}{\partial x} \right) - L_{13} \left( \frac{\partial \varphi}{\partial x} \right), \\ J &= -L_{21} \left( \frac{\partial P_0}{\partial x} \right) - L_{22} \left( \frac{\partial \mu}{\partial x} \right) - L_{23} \left( \frac{\partial \varphi}{\partial x} \right), \\ \bar{I} &= -L_{31} \left( \frac{\partial P_0}{\partial x} \right) - L_{32} \left( \frac{\partial \mu}{\partial x} \right) - L_{33} \left( \frac{\partial \varphi}{\partial x} \right), \end{aligned} \quad (28)$$

where  $\mu$  is the chemical potential given by

$$\mu = RT \ln(C), \quad (29)$$

and  $P_0$  is the effective pressure

$$P_0 = P - \Pi, \quad (30)$$

with  $\Pi$  the osmotic pressure defined according to:

$$\Pi = RT(v_1 + v_2)C. \quad (31)$$

The term of conductivity is given by

$$\kappa = L_{33} = \bar{I} \left( \frac{\partial \varphi}{\partial x} \right)^{-1}, \quad (32)$$

where

$$L_{33} = L'_{33} + L''_{33}, \quad (33)$$

$L_{33} = [\text{diffusive conductivity}] + [\text{convective conductivity}]$  such as

$$\kappa_D = L'_{33} = \left( \frac{C v_1 z_1 F^2}{RT} \right) [D_1 z_1 \bar{k}_1 - D_2 z_2 \bar{k}_2], \quad (34)$$

$$\kappa_c = L''_{33} = \left( (C v_1 z_1 F r_p)^2 \eta^{-1} \right) [\bar{k}_1 g - \bar{k}_2 g]. \quad (35)$$

Using the definition

$$\bar{y} = 2 \int_0^1 y \tilde{r} d\tilde{r}, \quad (36)$$

$\bar{k}_i$  and  $\bar{k}_i g$  can be calculated with the function which is defined [12, 13] by

$$g = \int_{\tilde{r}}^1 \frac{1}{\tilde{r}''} \int_0^{\tilde{r}''} (k_1 - k_2) \tilde{r}' d\tilde{r}' d\tilde{r}'' . \quad (37)$$

The function defined above can be simplified by using the PB equation and Green's theorem to find

$$g(\tilde{r}) = 2 (r_p / \lambda_c)^{-2} [\tilde{\psi}(\tilde{r}) - \tilde{\psi}_w]. \quad (38)$$

The conductivity can therefore be calculated from the electrostatic potential  $\tilde{\psi}(\tilde{r})$  inside the pore. So, in this case, it is necessary to solve the PB equation in dimensionless form to evaluate  $\tilde{\psi}(\tilde{r})$  ( $\tilde{\psi}_w = \tilde{\psi}(\tilde{r}_p)$ ). This potential is a function of the dimensionless parameters  $r_p/\lambda_m$  and  $r_p/\lambda_c$ , which are proportional, respectively, to  $|\sigma_w|^{1/2}$  and  $C_s^{1/2}$

$$\frac{r_p}{\lambda_m} = 7.485 (z_1 r_p \sigma_w)^{1/2}, \quad \frac{r_p}{\lambda_c} = 3.288 (\nu_1 z_1^2 C r_p^2)^{1/2}, \quad (39)$$

with the surface charge density  $\sigma_w$  in  $C/m^2$ , the pore radius  $r_p$  in nm and the bulk concentration  $C$  in moles/l.

### 2.1. Homogeneous analytical approximation (H)

The homogeneous approximation is used to analyze the behaviour of ions inside a cylindrical pore. In a charged pore, ions move through the pore driven by electrostatic forces due to the presence of a fixed charge distribution on the pore surface. The homogeneous approximation assumes that the charge density along the length of the pore is uniformly distributed. By making this approximation, the problem of ion transport in the cylindrical pore can be simplified. This simplification greatly facilitates the mathematical analysis. The homogeneous theory, which assumes a uniform potential, is valid when the pore radius is small and the surface charge density is lower, according to the space charge model [15]. Within the membrane pore, the macroscopic Donnan equilibrium theory can be used in combination with global charge electroneutrality then

$$\sum_{i=1}^2 z_i \bar{c}_i + X_m = 0, \quad (40)$$

with

$$\bar{c}_i = k_i \nu_i C, \quad (41)$$

where

$$k_i = \exp \left[ \frac{z_i}{|z_1|} \tilde{\psi}_0 \right]. \quad (42)$$

The value of the potential  $\tilde{\psi}_0$  is given by Eq. (42) which also allows one to write down:

$$\xi = k_h - k_h^{-\tau} = \frac{|X_m|}{|z_1| \nu_1 C}, \quad (43)$$

with

$$k_h = e^{\tilde{\psi}_0} \quad (44)$$

and  $\xi$  is the normalized membrane charge density in dimensionless form given in terms of  $(r_p/\lambda_m)$  and  $(r_p/\lambda_c)$  by

$$\xi = 4 \frac{(r_p/\lambda_m)^2}{(r_p/\lambda_c)^2}. \quad (45)$$

In the case of the symmetric salt ( $\tau = 1$ ), the solution of the quadratic equation  $k_h^2 - \xi k_h - 1 = 0$  is given by the formula

$$k_h = \frac{1}{2} \left( \xi + \sqrt{\xi^2 + 4} \right). \quad (46)$$

### 2.2. The approximate solutions of the Poisson–Boltzmann equation

**2.2.1. Numerical method.** The simplified Poisson–Boltzmann Eq. (18) is a non-linear partial differential equation and a fundamental equation used to find the electrostatic potential in porous systems [14]. In this work, a numerical approach uses the finite difference method to approximate solutions in one dimension. The proposed numerical method involves discretizing the spatial coordinate, applying suitable boundary conditions, and iteratively updating the electrostatic potential until convergence.

**2.2.2. Analytical solution.** Additionally, the article explores analytical approximations solution for specific scenarios with simplified charge distributions and boundary conditions, providing insights into the behavior of simple systems (*Good Co-Exclusion Approximation, Plane approximation, and Debye–Hückel approximation*). By comparing the numerical and analytical approaches, researchers gain valuable tools to efficiently analyze charged systems in radial direction and better understand their electrostatic behaviour in porous system. However, the validity of the analytical approximations depends on the value of the dimensional electrostatic potential  $\tilde{\psi}(\tilde{r})$ . Therefore, the ranges of validity of different types of analytical approximations vary in function of the parameters  $(r_p/\lambda_m, r_p/\lambda_c)$ .

**2.2.3. Good Co-Exclusion Approximation (GCE).** The concept of ‘‘Co-Exclusion’’ arises from the fact that ions of the same charge have a strong tendency to repel each other, leading to an excluded volume effect. The ‘‘Good Co-Exclusion Approximation’’ is an approach used to simplify the PBE solution by incorporating this excluded volume effect, particularly, for ionic solutions with concentrated charges. In the Good Co-Exclusion Approximation, the ions are treated as hard spheres, and their excluded volume effects are taken into account by modifying the boundary conditions in the PBE. Instead of considering the actual physical boundaries of the ions, the boundary conditions are adjusted to reflect the presence of neighboring ions and their excluded volumes. This approximation assumes that the ions cannot penetrate each other’s excluded volumes and considers their spatial arrangement to account for the effect of ionic crowding. By using the Good Co-Exclusion Approximation, the PBE can be simplified, and the computational cost can be significantly reduced while still providing reasonably accurate results for systems with concentrated ionic solutions. However, it is important to note that this approximation is most applicable to systems with relatively low ion concentration. It is valid for high potential values  $\tilde{\psi} > 1$ , because the second term on the right of Eq. (18) becomes negligible. In this limit, the solution of PB equation [13, 14] between  $0 \leq \tilde{r} \leq 1$  is given by

$$\tilde{\psi}(\tilde{r}) = 2 \ln \left( \frac{\lambda_c}{r_p} \right) + f(\tilde{r}; \sigma^*), \quad (47)$$

with

$$f(\tilde{r}; \sigma^*) = \ln \left[ \frac{16\sigma^*(1 + \sigma^*)}{(1 + \sigma^* - \sigma^*\tilde{r}^2)^2} \right]. \quad (48)$$

By combining Eq. (22) and Eq. (47), the GEC approximation is valid when  $\tilde{\psi}(0) \geq 1$  (minimum value of  $\tilde{\psi}$  at the origin)

$$\left( \frac{r_p}{\lambda_c} \right) \leq 2.426 \left( \frac{r_p}{\lambda_m} \right) \left[ 4 + \left( \frac{r_p}{\lambda_m} \right)^2 \right]^{-1/2}. \quad (49)$$

Staying within the range of validity of the GEC approximation, when the value of  $\sigma^*$  becomes small, the function appearing in Eq. (47) can be simplified. In this case, the homogeneous approximation for the electrostatic potential is valid in the whole range  $0 < \tilde{r} < 1$  with

$$e^{\tilde{\psi}(\tilde{r})} \approx \frac{|X_m|}{|z_1|v_1Cf} = \frac{16\sigma^*}{(r_p/\lambda_c)^2}. \quad (50)$$

The homogeneous GEC approximation is valid when  $(r_p/\lambda_m) < 2$  and inequality (49) simplifies to  $(r_p/\lambda_c) < 1.21 (r_p/\lambda_m)$ .

**2.2.4. Plane and Debye–Hückel approximation.** Solving the Poisson–Boltzmann equation directly in three dimensions can be challenging, especially for complex systems. In some cases, it is possible to simplify the equation and make approximations to make the problem more tractable. One such approximation is the plane approximation or the Debye–Hückel (DH) approximation. The plane approximation assumes that the charge distribution is confined to a single plane, and the system’s behaviour is effectively two-dimensional. This approximation is valid for situations where the charged species are confined to a surface. Solving this simplified one-dimensional Poisson–Boltzmann equation can provide valuable insights into the electrostatic behaviour near the charged plane, making it easier to study systems like charged membranes. The DH approximation is a method to simplify the PB equation under specific conditions related to dilute solutions and weak electrostatic interactions between ions. For a solution containing a symmetric salt at a concentration  $C$ , the nonlinear PB equation can be solved analytically, where the potential  $\tilde{\psi}$  is different from zero only at the pore surface. In this case one has:

$$\frac{1}{\tilde{r}} \frac{\partial \tilde{\psi}}{\partial \tilde{r}} \ll \frac{\partial^2 \tilde{\psi}}{\partial \tilde{r}^2}. \quad (51)$$

Apply the change of variable  $\tilde{r} = 1 - \tilde{t}$ , and consider a uniform potential  $\psi_w$  at the surface, the variation of the potential becomes strong near the surface of the pore, as opposed to inside the pore where its value is close to zero. In this approximation [14], the electrostatic potential at a distance  $\tilde{t}$  from the surface satisfies the plane approximation of the PB equation.

$$\frac{\partial^2 \tilde{\psi}}{\partial \tilde{t}^2} \cong \left( \frac{r_p}{\lambda_c} \right)^2 \sinh(\tilde{\psi}). \quad (52)$$

After integration, the solution of this equation can be found using the boundary condition at the pore surface:

$$\tilde{\psi}(\tilde{t}) = 2 \ln \left[ \frac{1 + u(\tilde{t})}{1 - u(\tilde{t})} \right], \quad (53)$$

where

$$u = \tanh(h) e^{-(r_p/\lambda_c)\tilde{t}}, \quad h = \frac{1}{2} \operatorname{arsinh} \left[ \frac{(r_p/\lambda_m)^2}{2(r_p/\lambda_c)} \right]. \quad (54)$$

At the limit, for a low potential and dilute solution, the solution takes the form of the plane DH approximation.

$$\tilde{\psi}(\tilde{t}) \cong \frac{(r_p/\lambda_m)^2}{(r_p/\lambda_c)} e^{-(r_p/\lambda_c)\tilde{t}}. \quad (55)$$

We observe that the plane approximation is valid when  $r_p/\lambda_c > 11$ . It's important to note that the plane approximation is valid only when the charged particles are distributed primarily along the x-axis and when the distance between the charged particles and the plane is much larger than the characteristic size of the charged particles themselves. In cases where the system deviates significantly from these conditions, the plane approximation may not be accurate.

### 3. Results and discussion

#### 3.1. Extended homogeneous approximation (EH)

EH is a new analytical approximation solution based on the Donnan theory (homogeneous approximation in the pore). It can be studied by adding a small radial variation  $\tilde{\psi}_1(\tilde{r}) \leq 1$ . The potential can be expressed as  $\tilde{\psi}(\tilde{r}) = \tilde{\psi}_0 + \alpha\tilde{\psi}_1(\tilde{r})$ , an approximate analytical solution to Eq. (18) with a development parameter,  $\alpha$ , which depends on  $|\sigma_w|$  and takes the value 1 at the end of the calculation. The expansion of the PB equation to the first order of  $\alpha$  according to the boundary condition given by:

$$2\nabla^2(\tilde{\psi}_1) - W\tilde{\psi}_1 = R, \quad (56)$$

$$\left. \frac{\partial \tilde{\psi}_1}{\partial \tilde{r}} \right|_{\tilde{r}=1} = \left( \frac{r_p}{\lambda_m} \right)^2, \quad (57)$$

$$\left. \frac{\partial \tilde{\psi}_1}{\partial \tilde{r}} \right|_{\tilde{r}=0} = 0, \quad (58)$$

with

$$W = \left( \frac{r_p}{\lambda_c} \right)^2 [k_h + \tau k_h^{-\tau}], \quad R = \left( \frac{r_p}{\lambda_c} \right)^2 [k_h - k_h^{-\tau}]. \quad (59)$$

For a given value of  $\tilde{\psi}_0$ , the analytical solution to Eq. (73) is as follows

$$\tilde{\psi}_1(\tilde{r}) = \frac{(r_p/\lambda_m)^2}{m} \left[ \frac{I_0(m\tilde{r})}{I_1(m)} \right] - 2 \left( \frac{r_p/\lambda_m}{m} \right)^2, \quad (60)$$

with

$$m = (W/2)^{1/2}, \quad (61)$$

$I_0$  and  $I_1$  are the modified Bessel functions of order 0 and 1, respectively.

When the value of  $\tilde{\psi}_0$  is zero, we fall on the Debye–Hückel approximation, for which the approximation is valid if  $\tilde{\psi}_1(1) < 1$  then

$$V > \left( \frac{r_p}{\lambda_m} \right)^2 \left[ \frac{I_0(V)}{I_1(V)} \right], \quad (62)$$

with

$$V = \left( \frac{1 + \tau}{2} \right)^{1/2} \left( \frac{r_p}{\lambda_c} \right). \quad (63)$$

The EH approximation can be represented in the plane ( $r_p/\lambda_m, r_p/\lambda_c$ ) by the inequality  $\tilde{\psi}_1(1) < 1$ . If this radial function tends to 0, it moves to the domain of validity of the homogeneous approximation ( $r_p/\lambda_m < 2$ ). For the GEC zone, the extended homogeneous approximation is valid for  $r_p/\lambda_m < 2.4$ , while outside the GEC zone, the EH zone includes and extends the homogeneous and the Debye–Hückel (DH) zones. Fig. 2 summaries the validity domains of different analytical approximations solution [16].

#### 3.2. Electrical conductivity

The electrical conductivity in charged nanopores is determined by various factors, including the size of the nanopore, the surface charge density (Table 1), the concentration and type of ions presented in the pore (Table 2), and the properties of the surrounding medium. However, the behaviour of electrical conductivity in charged nanopores can be complex and dependent on many factors, and may require detailed computational studies to fully understand. The conductivity is computed by numerical approach using equation (33) and compared to the conductivity calculated by homogeneous and extended homogeneous analytical approximations. Using the EH approximation, the conductivity  $\kappa$  can be calculated analytically and is given by:

$$\kappa = L_{33}^H + \delta L_{33}, \quad (64)$$

where the homogeneous conductivity is given by

$$L_{33}^H = (C\nu_1|z_1|F^2/RT) (D_1|z_1|k_h + D_2|z_2|k_h^{-\tau}) + ((C\nu_1z_1F)^2 L_P^0) \xi^2. \quad (65)$$

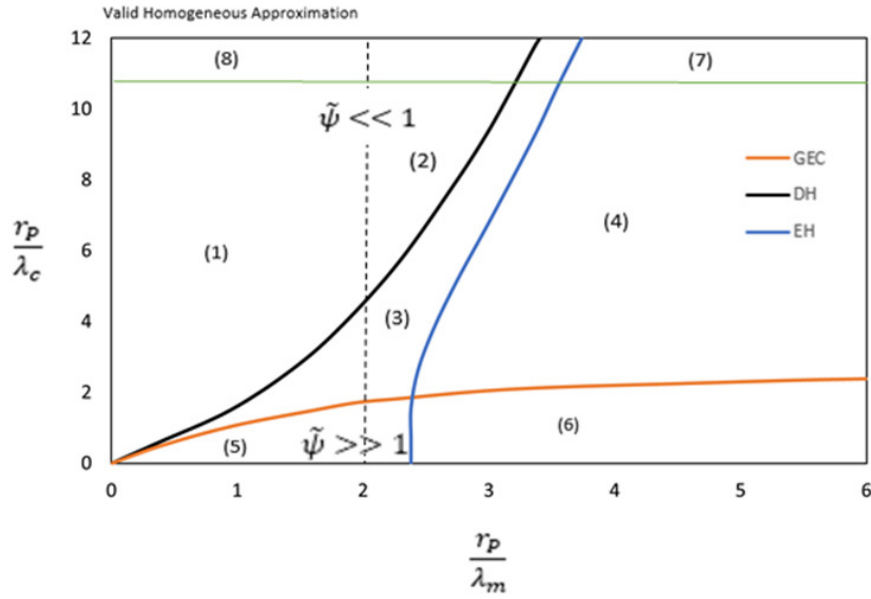


FIG. 2. Representation of the validity domains of different analytical solution approximations [16]. Representation of different zones: (1) and (2) – Validity of the Homogeneous and Debye–Hückel (DH) zone; (1), (2) and (3) – Validity of EH zone; (5) and (6) – Validity of the Homogeneous zone and inhomogeneous GEC; (4) – Intermediate zone; (7) – Validity of the plane approximation; (8) – Validity of the plane Debye–Hückel approximation. The blue curve delimits the area of EH and the dashed line delimits the H area.

The hydraulic permeability of the membrane is given by the following formula

$$L_P^0 = r_p^2/8\eta \tag{66}$$

and the correction term of the homogeneous approximation of order 1 is given by

$$\delta L_{33} = \frac{(C\nu_1 z_1 F r_p)^2 \xi^2}{2\eta} \left[ \frac{1}{4} + \frac{1}{m} \frac{I_0(m)}{I_1(m)} - \frac{1}{2} \left( \frac{I_0(m)}{I_1(m)} \right)^2 \right]. \tag{67}$$

TABLE 1. The Parameter  $r_p/\lambda_m$ , the surface charge density and membrane charge density  $X_m$  for  $r_p = 2$  nm

$r_p/\lambda_m$	$\sigma_w$ (C/m <sup>2</sup> )	$X_m$ (mol/l)
0.18	0.0003	0.0031
4	0.15	1.55
6.4	0.37	3.83
8	0.58	6.01
10.4	0.97	10.05

TABLE 2. Parameter  $r_p/\lambda_c$  and concentration in the bulk for  $r_p = 2$  nm

$r_p/\lambda_c$	$C$ (M)
0.2	$10^{-3}$
0.6	$10^{-1}$
6.5	1
11.4	3

When  $\xi$  tends to 0, then the correction term  $\delta L_{33}$  tends to 0. In this case, the conductivity in the homogeneous zone is attained. Fig. 3 shows that at low surface charge densities, the electrical conductivity is dominated by the properties of the electrolyte solution, and the conductivity decreases as the size of the nanopore decreases due to increased surface effects. At higher surface charge densities, the electrical conductivity may increase due to the formation of ion transport channels or ion hopping mechanisms. At low surface charge density, Fig. 3 shows that the conductivity in a charged pore is proportional to the ionic concentration of the counter ions compensated by the volume charge density of the membrane (contribution of the electrical double layer). It turns out that the SC model predicts very well the experimentally observed conductivity in cylindrical nanopores of radius  $r_p > 3$  nm [16]. This indicates that the model captures the relevant physical phenomena and properties of the nanopores accurately. In this context, the homogeneous approximation is coherent with the numerical method up to  $r_p/\lambda_m \approx 3$ , while the EH remains coherent until  $r_p/\lambda_m \approx 6$ . Indeed, the EH approximations can be valuable analytical methods to calculate physical quantities of certain systems, including membranes for low and high surface charge density  $\sigma_w$ . The issue of the validity of this model for small pore radius  $r_p < 2$  nm remains an open question.

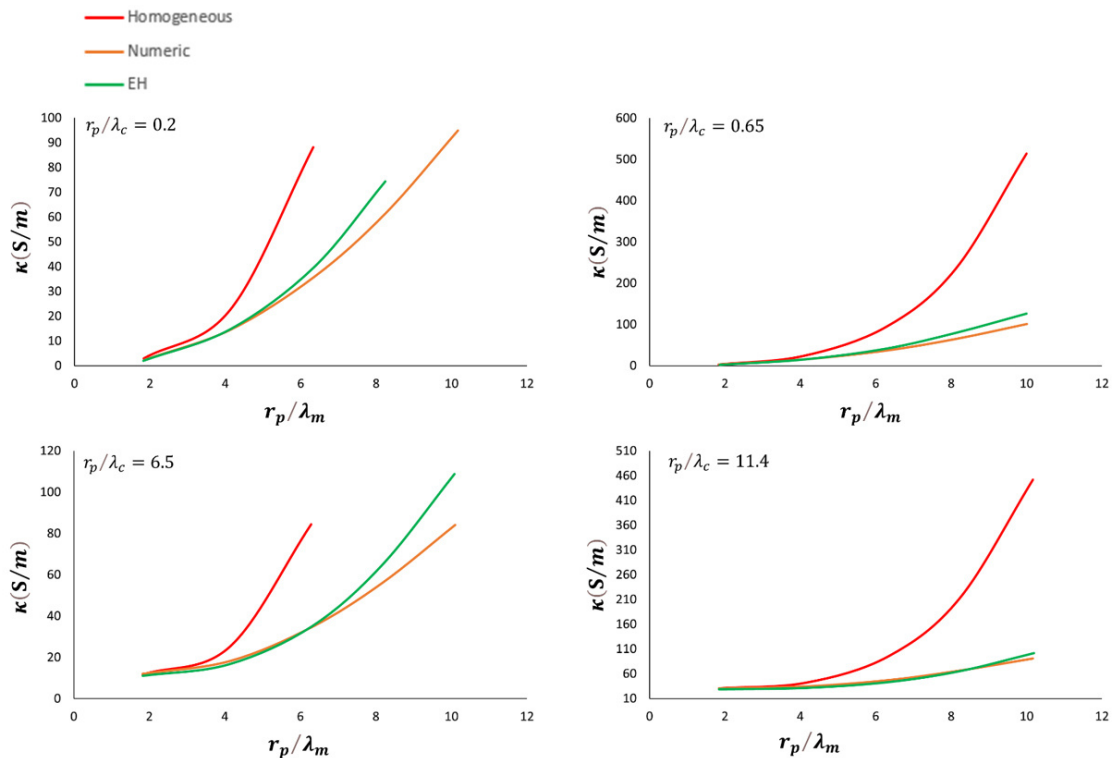


FIG. 3. Conductivity  $\kappa$  as a function of parameter  $r_p/\lambda_m$  in a nanopore of radius  $r_p = 2$  nm containing KCl salt. The conductivity is calculated by numerical, Homogeneous and extended homogeneous approximation

#### 4. Conclusion and perspective

The aim of this paper was to highlight the influence of physical parameters on the ionic transfer, especially the concentration of the bulk and the surface charge density  $\sigma_w$ . Different analytical approximations based on the space charge (SC) model (Homogeneous, Good Co-Ion Exclusion and Planar approximation) is described in this paper. A new analytical approximation named the extended homogeneous approximation is presented. The behavior of the salt-porous system depends mainly on the surface charge density and the concentration in the bulk. The calculation of the conductivity by numerical and approximate analytical methods shows that the Extended Homogeneous approximation (EH) is coherent with the numerical method up to a limit value of  $r_p/\lambda_m \approx 6$ , corresponding to 0.37 value of surface charge density. Then, without going through a heavy numerical method, the EH approximations can be used as simple analytical methods to calculate the physical quantities of the membrane such as electrical conductivity and flow potential within specific limits, help the development of new applications in water treatment, food processing, and the recovery of valuable materials from industrial waste streams.

## References

- [1] Feng X., Peng D., Zhu J., Wang Y., Zhang Y. Recent advances of loose nanofiltration membranes for dye/salt separation. *Separation and Purification Technology*, 2022, **285**, P. 120–228.
- [2] Filippov A.N., Shkirkaya S.A. Theoretical and experimental study of joint osmotic and electroosmotic water transfer through a cation-exchange membrane. *Int. J. of Molecular Sciences*, 2022, **23**, P. 127–178.
- [3] Chen W., Gu Z., Ran G., Li Q. Application of membrane separation technology in the treatment of Leachate in china: A review. *Waste Management*, 2021, **121**, 127.
- [4] Rautenbach R., Groschl A. Separation potential of nanofiltration membranes. *Desalination*, 1990, **77**, P. 73–84.
- [5] Tsuru T., Urairi M., Nakao S., Kimura S. Negative rejection of anions in the loose reverse osmosis separation of mono-and divalent ion mixtures. *Desalination*, 1991, **81**, P. 219–227.
- [6] Yaroshchuk A.E. Osmosis and reverse osmosis in fine-porous charged diaphragms and membranes. *Advances in Colloid and Interface Science*, 1995, **60**, P. 1–93.
- [7] Lefebvre X., Palmeri J., David P. Nanofiltration theory: An analytic approach for single salts. *J. of Physical Chemistry B*, 2004, **108**, P. 16811–16824.
- [8] Lefebvre X., Palmeri J. Nanofiltration (Transport Phenomena). *J. of Physical Chemistry B*, 2005, **109**, P. 5525–5540.
- [9] Szymczyk A., Fievet P. Investigating transport properties of nanofiltration membranes by means of a steric, electric and dielectric exclusion model. *J. of Membrane Science*, 2005, **252**, P. 77–88.
- [10] Chmiel H., Lefebvre X., Mavrov V., Noronha M., Palmeri J. Computer simulation of nanofiltration, membranes and processes. In *Handbook of Theoretical and Computational Nanotechnology – American Scientific Publishers*, 2006, **5**, P. 93–214.
- [11] Peters P.B., van Roij R., Bazant M.Z., Biesheuvel M. Analysis of electrolyte transport through charged nanopores. *Physical Review E*, 2016, **93**, 052801.
- [12] Morrison F.A. Jr., Osterle J.F. Electrokinetic energy conversion in ultrafine capillaries. *J. of Chemical Physics*, 1965, **43**, P. 2111–2115.
- [13] Gross R.J., Osterle J.F. Membrane transport characteristics of ultrafine capillaries. *J. of Chemical Physics*, 1968, **49**, P. 228–234.
- [14] Fair J.C., Osterle J.F. Reverse electrodialysis in charged capillary membranes. *J. of Chemical Physics*, 1971, **54**, P. 3307–3316.
- [15] Dweik J., Koabaz M. Study of ion partitioning in nanoporous materials by analytical approach and molecular modeling. *Nanosystems: Phys. Chem. Math.*, 2023, **14**, P. 172–177.
- [16] Cwirko H.E., Carbonell R.G. Transport of electrolytes in charged pores: Analysis using the method of spatial averaging. *J. of Colloid and Interface Science*, 1989, **129**, P. 513–531.

---

*Submitted 4 July 2023; revised 25 July 2023; accepted 28 July 2023*

### *Information about the authors:*

*Jalal Dweik* – Jinan university, Tripoli Lebanon – Main Campus: Zaytoun Abi-Samra, P. O. Box: 818;  
ORCID 0009-004-2988-0918; jalal.douwayk@jinan.edu.lb

*Hassan Farhat* – Jinan university, Tripoli Lebanon – Main Campus: Zaytoun Abi-Samra, P. O. Box: 818;  
ORCID 0009-0005-4696-9786; hassan.farhat@jinan.edu.lb

*Joumana Younis* – Jinan university, Tripoli Lebanon – Main Campus: Zaytoun Abi-Samra, P. O. Box: 818;  
ORCID 0000-0003-0576-4264; joumana.younis@jinan.edu.lb

*Conflict of interest:* the authors declare no conflict of interest.

## Transport properties of GaAs Co-doped H-passivated low-buckled and high-buckled zigzag silicene nanoribbon two probe devices

Asma N. Naqash<sup>1,2</sup>, Khurshed A. Shah<sup>1,3</sup>, Javid Ahmad Sheikh<sup>2</sup>, Brijesh Kumbhani<sup>4</sup>, Syed Muzaffar Ali Andrabi<sup>5</sup>

<sup>1</sup>Department of Nanotechnology, University of Kashmir, Srinagar, Jammu and Kashmir – 190006, India

<sup>2</sup>Department of Electronics and Instrumentation Technology, University of Kashmir, Srinagar, Jammu and Kashmir – 190006, India

<sup>3</sup>Postgraduate Department of Physics, S. P. College, Cluster University Srinagar, Jammu and Kashmir – 190001, India

<sup>4</sup>Department of Electrical Engineering, Indian Institute of Technology Ropar, Punjab – 140001, India

<sup>5</sup>Department of Applied Sciences, Institute of Technology, Zakura Campus, University of Kashmir, Srinagar, Jammu and Kashmir – 190006, India

Corresponding author: Khurshed A. Shah, [drkhursheda@gmail.com](mailto:drkhursheda@gmail.com)

**ABSTRACT** In this study, we have investigated the transport properties of low buckled (LB) and high buckled (HB) silicene based two probe devices such as I–V characteristics, conductance, transmission spectrum and projected device density of states. Firstly, we have opened a bandgap in both LB and HB zigzag silicene nanoribbon (ZSiNR) by hydrogen passivation and simulated for their transport properties. Further, we have doped the LB and HB ZSiNR structures by gallium (Ga) and arsenide (As) atoms in order to determine their changes in the transport properties. The results show that 4 atom width silicene nanoribbon shows a maximum band gap of 2.76 and 2.72 Å for LB-ZSiNR and HB-ZSiNR, respectively. The 2 atom doped ZSiNR shows good transport characteristics in the voltage range of 0.5 to 1.5 V in comparison with 4 and 6 atom doped models. The obtained results were validated by calculating the transmission spectrum and projected device density of states. It is believed that the modelled devices will find number of futuristic applications in the electronic industry.

**KEYWORDS** zigzag silicene nanoribbons, DFT, I-V characteristics, transmission spectra, PDDoS

**ACKNOWLEDGEMENTS** This work was supported by JKST&IC funded project (Grant No. JKST&IC/SRE/1172-74).

**FOR CITATION** Naqash A.N., Shah K.A., Sheikh J., Kumbhani B., Andrabi S.M.A. Transport properties of GaAs Co-doped H-passivated low-buckled and high-buckled zigzag silicene nanoribbon two probe devices. *Nanosystems: Phys. Chem. Math.*, 2023, **14** (4), 438–446.

### 1. Introduction

The silicene, a honeycomb (hexagonal) structured 2D material exfoliated from silicon monolayer atoms, is exceptionally expedient over graphene due to its sp<sup>3</sup> hybridization. Silicene does not exist in nature and tends to generate larger silicone crystals and silicone compounds [1]. The effective synthesis of this element on metal substrates [2–4] has spurred interest in both theoretical [5, 6] and experimental investigations [7, 8]. The buckled structure of 2D silicene result either from the weak  $\pi$  double bonds due to the parted Si atoms or through the pseudo-Jahn–Teller distortions (PJT) [9]. Due to the zero band gap semimetal character with linearly crossing bands at the Fermi level (EF), the charge carriers move like massless fermions at around 10<sup>6</sup> m/s at the Dirac point. This could be fixed by directing various modulation techniques for recognition of tunable band gaps. A number of such formulations include modeling silicene into nanoribbon (NR) bands of atomic layer width and chemical functionalization [10–13]. In addition, the implementation of strain, the application of an external electrical field [14], vacancy creation [15], surface adsorption, substitution, nano-mesh creation (creating nanoholes on the silicene sheet), etc. could also yield band gap efficiently [16]. There have been some reports proposed by Yao, et al. [17] showing the distinct properties of large spin–orbit coupling (SOC) effect as a result of buckling and the Quantum Spin Hall effect (QSHE) [18], and a valley-polarized metallic phase by Ezawa [19]. Due to such articulations in the silicene material, it finds several device implementations as field effect transistor (FET), tunnel field effect transistor (TFET), spintronics, valleytronics, bandgap engineering, gas sensors etc [16].

The atomic structure of silicene could be perceived into three phases based on the buckling done. The Planar structure (PL) (pristine version), as per the binding energy computations of silicene, has a greater energy than its Low-buckled (LB) and High-buckled (HB) complements. There exist fictitious phonon frequencies in the PL structure for the majority of the Brillouin zone [20] that renders it unstable. The fictitious phonon frequencies are moreover evident in silicene HB structures with significant buckling heights of 2 Å. As a result, HB structures are not consistent to actual local minima over the Born–Oppenheimer surface [21]. Silicene’s LB structures, on the other hand, exhibit phonon dispersion curves with positive coefficients over the whole Brillouin zone, making them dynamically stable [21].

Though the lack of a band gap restricts the material for both electronic and device applications, but optimistically functionalization, strain, or the application of an external electrical field, nano-mesh creation, defect creation, etc. can be implemented to yield a band gap. Another way of solving band gap problem is by slicing silicene into silicene nanoribbons (SiNRs). SiNRs are of two forms viz., Armchair Silicene Nanoribbons (ASiNRs) and Zigzag Silicene Nanoribbons (ZSiNRs) [3]. In the past, several elements like Al, Ga, In, Th, P, As, Sb and Bi have been investigated for various electronic (band structure, density of states (DOS)) and transport properties (transmission spectra and I–V characteristics) of silicene NRs [20]. Likewise, dopants containing Gallium and Arsenic have been implemented for the semiconductor simulation [22, 23].

Gallium belongs to group-III with valency three and arsenic belongs to group-V with valency five in the periodic table. Thus, Gallium atoms are often replaced for doping in p-type semiconductors with majority of the charge carriers as holes and contrast to this arsenic atoms are replaced to dope in n-type semiconductors. Ga and As are mostly used for optoelectronic applications because of their optical properties [24, 25]. Further, the lattice constants of Ga and As are identical [3]. Gallium arsenide is formed by coupling Group III and V elements for implementation as photo detectors, LEDs etc. [26].

The ZSiNRs have been used for various applications such as giant magnetoresistance [27], high hydrogen storage capacity [28], lithium storage [29], spin-filtering [30, 31], magnetic random access memory and digital logic [32], spin polarization [33], etc. In this study, for the first time, we have studied the transport characteristics of GaAs co-doped hydrogen passivated low-buckled (LB) and high-buckled (HB) ZSiNR at various GaAs doping levels. The device is distinctly doped with 2, 4 and 6 GaAs atoms and their transport characteristics are investigated. The studies revealed that doped LB and HB ZSiNR devices have distinct I–V and conductance curves, transmission spectra and device density of states.

## 2. Models and methods

The current study has been carried out utilizing the density functional theory (DFT) and non-equilibrium Green’s Function (NEGF) operations [2], based on the software Atomistic Tool Kit (ATK) software version P-2019.03 and its graphical user interface Virtual Nanolab (VNL) [34]. We project a two-probe device with three zones, the left electrode, the middle scattering region, and the right electrode in order to compute the transport properties. The device is represented in Fig. 1. Electrodes are assimilated into the ZSiNR structure to eliminate the current quantization effects induced by contact regions. The Silicon–Silicon bond length is set at 2.28 Å. The buckling height for the low buckled and the high buckled structures are taken as 0.44 and 0.54 Å, respectively.

Electron density expansion is treated with double zeta polarised basis set that interprets the electron wave function. Also density mesh cut-off is set at 75 Hartree (150 Ry). With a 15 Å vacuum separation along the zigzag silicene nanoribbons (ZSiNR)’s width, the interlayer interactions are circumvented. The Local Density Approximation (LDA) is used to account for the exchange-correlation interactions, which is a basic approximation, whereas Generalized Gradient Approximation (GGA) is an advanced version of LDA and the LDA approximation has been used for the band structure calculations in various structures [2, 38, 39]. The atomic locations and asymmetric lattice constants are relaxed up to a maximum force of 0.01 eV. For sampling during the structure optimization, the Brillouin zone has been sampled at  $1 \times 1 \times 21$  k-points and for the computation of band structure, device density of states and electron transport calculations, a  $1 \times 1 \times 125$  Monkhorst-Pack K-points grid is selected along the ZSiNR growth direction (z-direction). The “limited-memory Broyden–Fletcher–Goldfarb–Shanno” (LBFGS) algorithm has been employed for structure optimization [35]. The electrode temperature of the models has been set to 300K for operation. The current across the electrodes is analyzed by voltage bias of 0 to 2 V. Table 1 below depicts the simulation parameters implemented in the modulation of the two probe device.

## 3. Results and discussions

In order to investigate silicene for device applications, it is important to open the bandgap in the material. In this study, we have H-passivated the ZSiNR and varied its width to investigate the change in band gap in the material as shown in Fig. 2. From the curves, it is clear that for both LB and HB ZSiNR the increase in the width of the nanoribbon results in the decrease of the energy gap which is in agreement with the literature [16, 36] and the 4 atom width LB–H–ZSiNR and HB–H–ZSiNR shows a maximum band gap of 2.76 and 2.72 Å, respectively.

Silicene is a two-dimensional material composed of a single layer of silicon atoms arranged in a honeycomb lattice, similar to graphene. Its atomic structure could be perceived into three phases based on the buckling done. The Planar

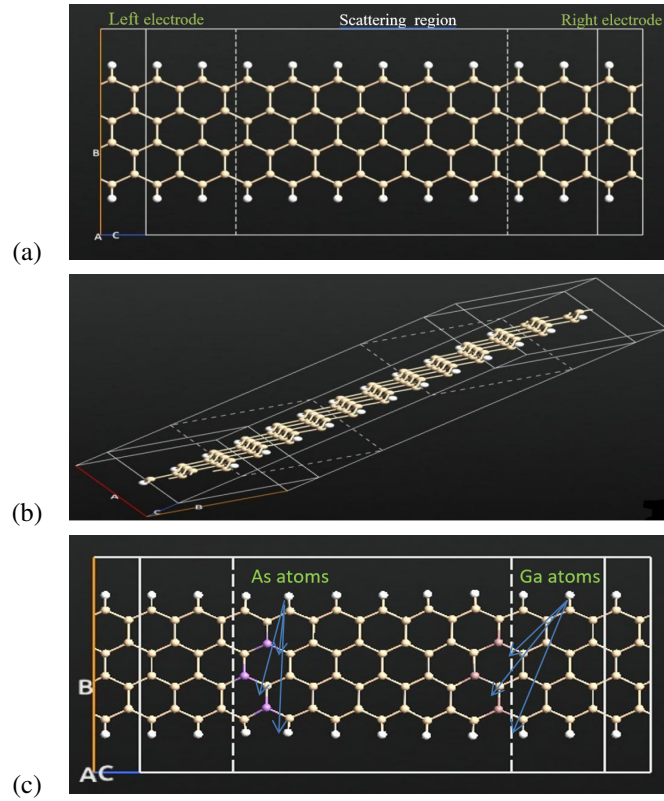


FIG. 1. H-passivated zigzag silicene nanoribbon (ZSiNR) two probe modeled device: (a) – top-view; (b) – side-view; (c) – GaAs co-doped

TABLE 1. The simulation parameters implemented in the modeled two probe devices

Parameter	Value
Calculator	Linear Combination of Atomic Orbitals (LCAO)
Formalism	DFT
Pseudopotential	FHI (Martins–Troullier Type)
Exchange-correlation functional	LDA
Density mesh cut-off Energy	75 Hartree
k-point sampling	1, 1, 125
Basis set	Double- $\zeta$ polarization (DZP)
Electrode Temperature	300 K
Device Algorithm Formalism	Non-equilibrium Green's Function (NEGF)
Poisson Solver	FFT2D

structure (PL) (pristine version), as per the binding energy computations of silicene, has a greater energy than its Low-buckled (LB) and High-buckled (HB) complements. In planar silicene there is no bandgap while the high buckled silicene with buckling height of 2 Å is unstable [16]. The rise in buckling height suggests that silicene's atomic orbitals have a higher concentration of the more stable  $sp^3$  hybridization than  $sp^2$  hybridization. We have inspected two stable buckling heights of 0.44 and 0.54 Å in the middle range of the low buckled silicene, as illustrated in Fig. 2. Consequently, we have labeled them as Low buckle (LB) for 0.44 Å and High buckled (HB) for 0.54 Å, respectively.

In the low buckled (i.e., 0.44 Å) silicene nanoribbon, the silicon atoms are arranged in a planar configuration with minimal vertical displacement (buckling) from the plane of the nanoribbon. This arrangement leads to a relatively large inter-atomic spacing and weaker silicon-silicon bonds. The weak bonding results in a smaller bandgap since the energy required to promote electrons from the valence band to the conduction band is lower. As the width of the low buckled

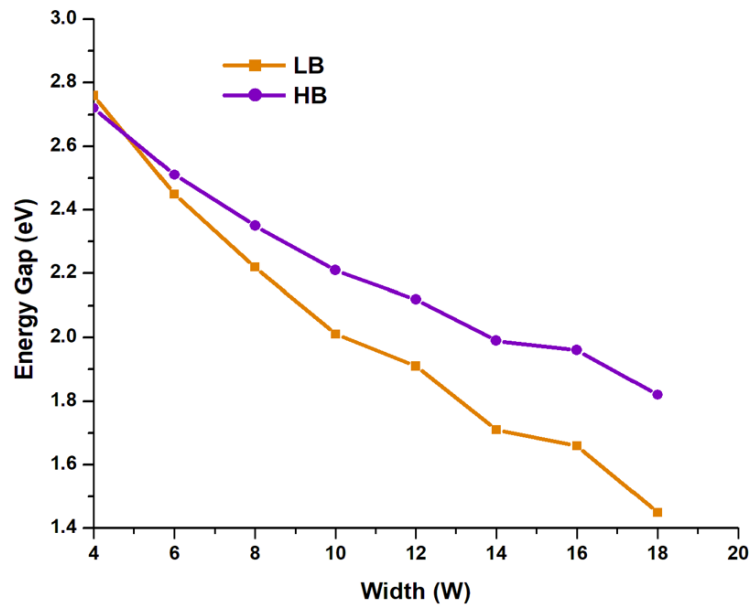


FIG. 2. Variation of bandgap of H-passivated low-buckled (LB) and high-buckled (HB) ZSiNRs with the change in width of the silicene nanoribbon

nanoribbon decreases, the distance between silicon atoms decreases, resulting in strengthening of bonds, and consequently increasing the bandgap. In other words, as the width increases the band gap decreases.

On the other hand, in the high buckled ( $0.54 \text{ \AA}$ ) silicene nanoribbon, the silicon atoms exhibit a more pronounced vertical displacement or buckling from the nanoribbon plane. This buckling causes the atoms to be closer together, leading to stronger silicon-silicon bonds. The stronger bonding results in a larger bandgap since more energy is required to promote electrons across the wider bandgap (wider than the low LB counterpart). As the width of the high buckled nanoribbon decreases, the interatomic spacing remains relatively constant due to the buckling pattern, which keeps the bandgap more stable or possibly even increasing slightly. It's important to note that the exact behavior of the bandgap with respect to decreasing width may also be influenced by the nanoribbon's specific edge configuration, strain effects, and other environmental factors and the quantum confinement effects can play a role in modifying the electronic properties of narrow nanoribbons [16]. Therefore, detailed theoretical calculations or simulations may be necessary to precisely predict the bandgap changes in low and high buckled silicene nanoribbons as their width varies.

The transport characteristics and the impact of various doping levels on the current and conductance of the ZSiNR two-probe systems have been explored. The remaining forces on each atom were reduced to less than  $0.05 \text{ eV/\AA}$  by relaxing each of the structures completely. We have obtained the I-V curves, conductance curves, transmission spectra and projected device density of states (PDDoS) of the LB-ZSiNR and HB-ZSiNR modeled devices. These curves (Figs. 4–6) depict the transport mechanism of the models in the similar manner as does the IV curves [40–43].

The variation in I-V curves of low-buckled and high-buckled ZSiNR modeled devices with different doping levels are shown in Fig. 3(a) and Fig. 3(b) respectively.

From Fig. 3(a) and Fig. 3(b), it is clear that the 2 atoms doped GaAs LB and HB ZSiNR modeled device conducts more as compared to 4 atoms doped GaAs LB and HB ZSiNR devices and the change is significant in the bias range of 0.5 to 1.5 V. However, in LB and HB pristine ZSiNR devices the increase in current is significant in 1.5 to 2 V voltage range which is in agreement with the result reported in the literature [30]. The conductance curves of the modeled devices are depicted in Fig. 4(a) and Fig. 4(b). The conductance of the 2 atoms doped GaAs LB-ZSiNR and HB-ZSiNR modeled devices is higher than the corresponding 4 atoms doped structures particularly in the bias window of 0.5 to 1.5 V which is in agreement with the above observed I-V characteristics.

We further inspected the transmission spectra of the modeled structures to better comprehend the I-V curves at 0.2 V. Fig. 5 and Fig. 6 show the transmission spectra of LB and HB ZSiNR for different doping concentrations. The probability of the occupancy of the states is represented by black, red and green lines for pristine, 2 atoms doped, 4 atoms doped ZSiNRs, respectively. It can be observed from Fig. 5 and Fig. 6 that the transmission peaks with reference to the pristine model are larger than the corresponding peaks of doped models at the applied voltage of 0.2 V. Thus supporting the statement for reduced current in the doped models as compared to the pristine silicene devices. Furthermore, from Fig. 5 and Fig. 6, it is clear that the 2 atoms doped model shows better transmission peaks as compared to the highly doped models. In addition, the transmission is good in the bias range of 0.5 to 1.5 V that is also in agreement with the obtained I-V and conductance curves (refer Fig. 3 and Fig. 4).

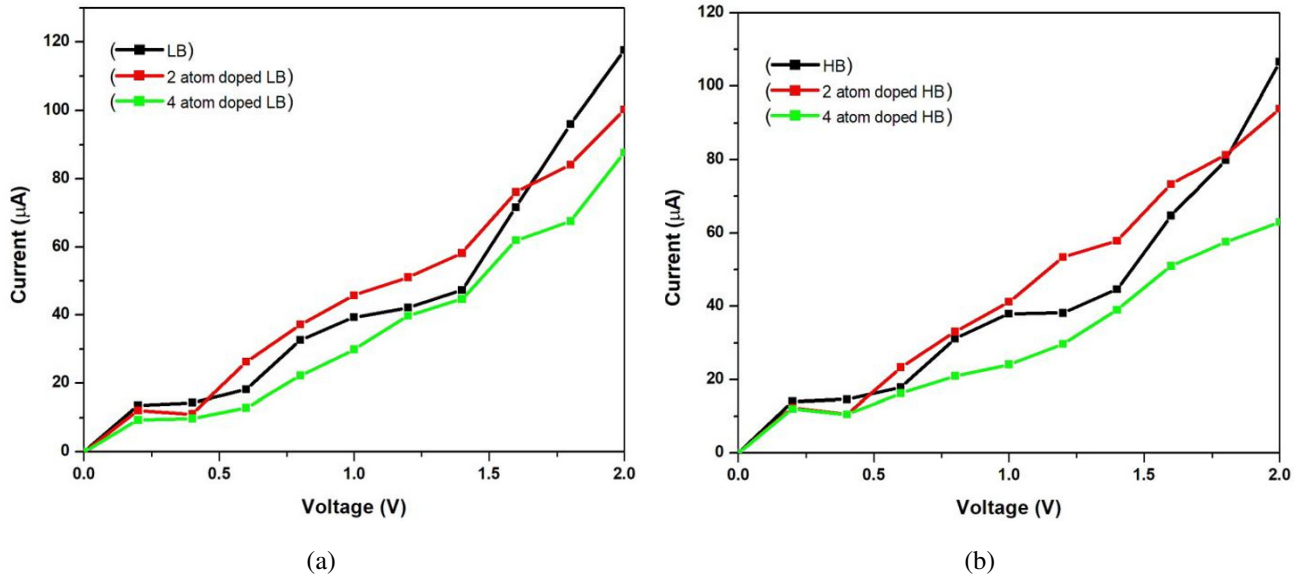


FIG. 3. I–V curves of H-passivated (a) low-buckled (LB) ZSiNR (b) high-buckled (HB) ZSiNR two probe devices

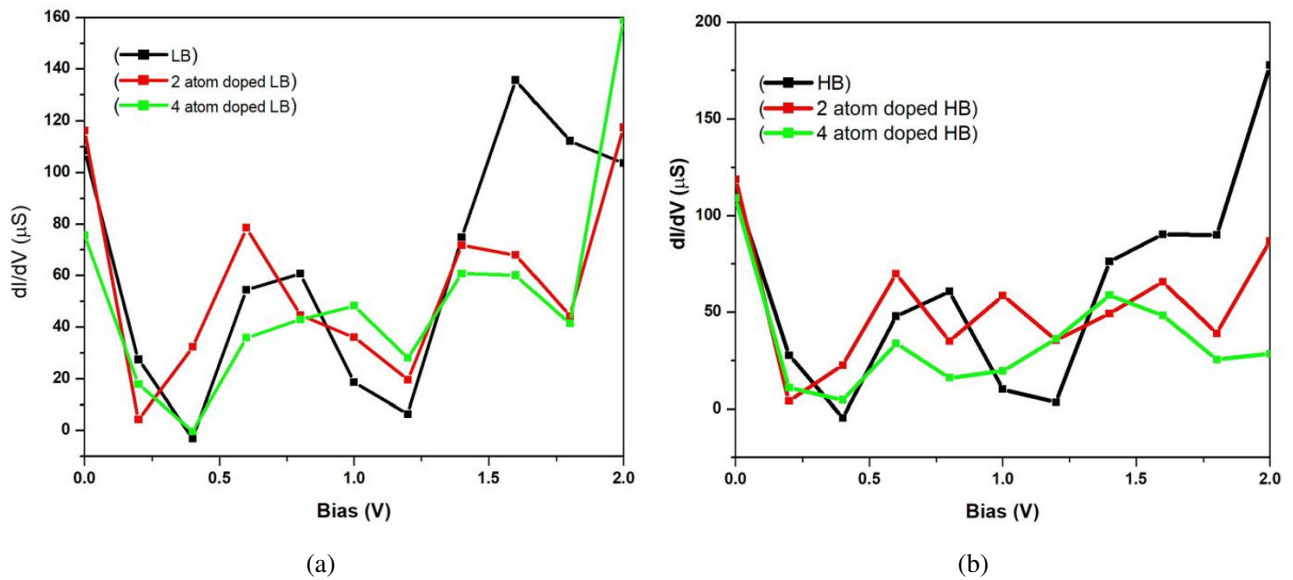


FIG. 4. Conductance curves of H-passivated (a) LB–ZSiNR (b) HB–ZSiNR two probe devices

The PDDoS numerically depicts the density distribution of states. The PDDoS specifies the number of states the quantum carriers are permitted to occupy at a specific energy level.

The ATK software implements the spectral density matrix tool for its computation:

$$\rho(E) = \rho^L(E) + \rho^R(E). \quad (1)$$

Here,  $L$  and  $R$  stand for the corresponding contributions of the left and right electrodes.

The relation for local density of states (LDoS) is given by

$$D(E, r) = \sum_{ij} \rho_{ij}(E) \vartheta_i(r) \vartheta_j(r), \quad (2)$$

where the basis set orbitals  $\vartheta_i(r)$  are real functions in ATK obtained by using the solid harmonics.

Integrating the LDoS over the whole space, PDDoS can be computed as follows;

$$D(E) = \int dr D(E, r) = \sum_{ij} \rho_{ij}(E) S_{ij}, \quad (3)$$

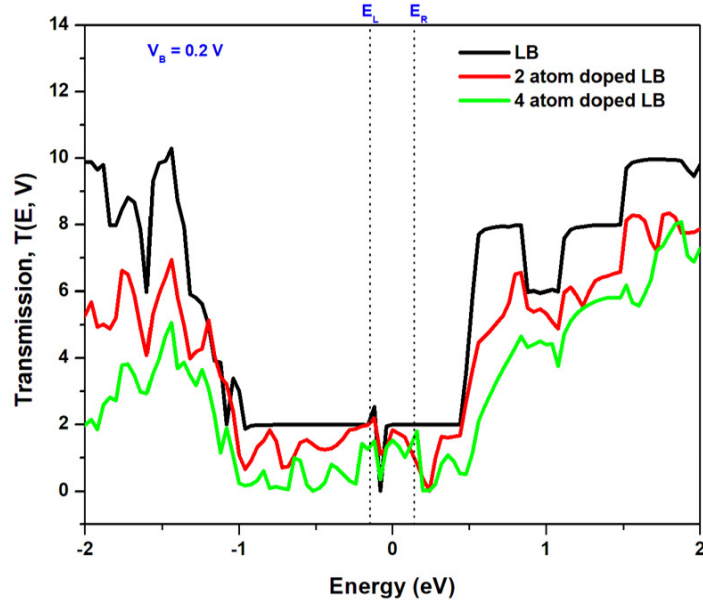


FIG. 5. Transmission spectra of H-passivated LB-ZSiNR for different doping concentrations

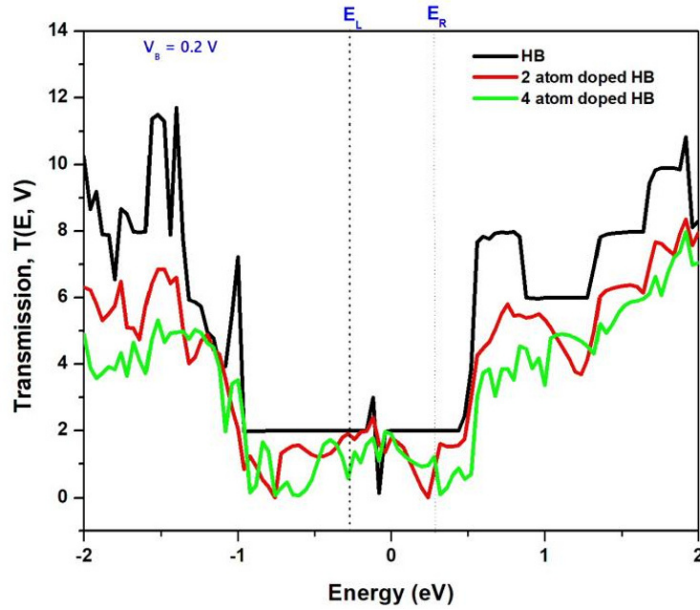


FIG. 6. Transmission spectra of H-passivated HB-ZSiNR for different doping concentrations

where  $S_{ij} = \int \phi_i(r) \phi_j(r) dr$  is the overlap matrix.

The PDDoS of LB and HB H-passivated ZSiNR at different doping levels is shown in Fig. 7. From Fig. 7, it is clear that very small peaks occur below the Fermi level in the pristine and doped ZSiNRs which means that a fewer number of available energy states are presented in the valence band. Furthermore, peaks are also observed above the Fermi level in the conduction band of the both the pristine and the doped ZSiNR models. Thus, the results depict that conductivity is possible for the proposed devices as the occupancy level is sufficient at both the valence and the conduction bands [37].

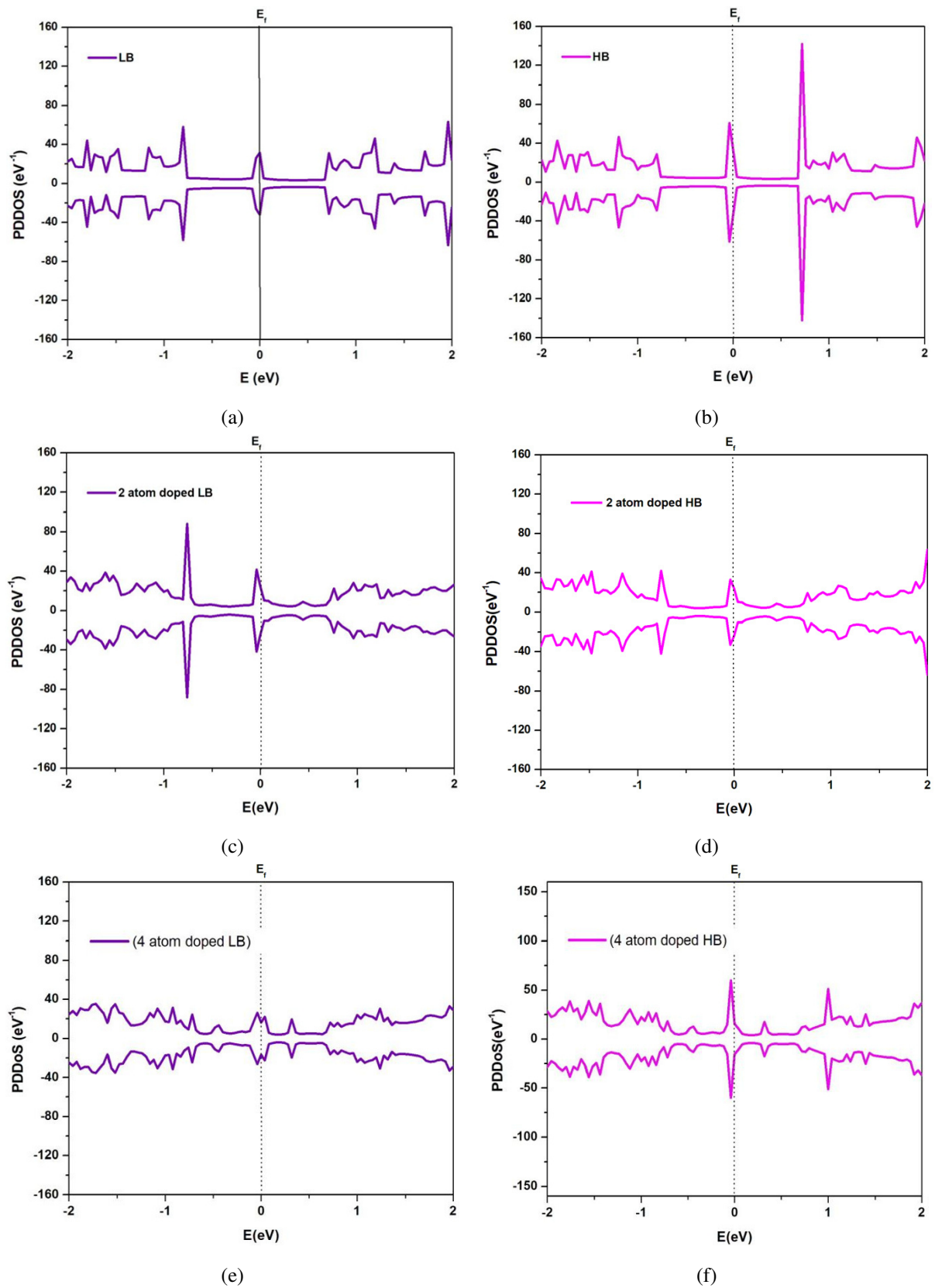


FIG. 7. PDDoS at different doping levels of LB and HB (a) pristine LB, (b) pristine HB, (c) 2 atom doped LB, (d) 2 atom doped HB, (e) 4 atom doped LB, and (f) 4 atom doped HBH-passivated ZSiNR

#### 4. Conclusions

In this study, we have modelled and simulated both pristine and doped low buckled (LB) and high buckled (LB) ZSiNR two probe devices using DFT in combination with NEGF formalism and calculated their I–V characteristics, conductance, transmission spectrum and project device density of states (PDDoS). The results show that the level of buckling in the silicene structures changes the characteristics of the devices which are further dependent on the magnitude of the applied voltage. The doping by gallium and arsenide atoms shows a profound effect on the I–V characteristics and conductance of modelled two probe devices, particularly, in the middle applied voltage range and it is sensitive to the level of doping. The low level doping shows higher magnitude of current than the high level doping. Furthermore, the transmission spectrum and PDDoS completely agree with the I–V and conductance curves. The results are important from both basic and applied points of view.

#### References

- [1] Motamedi M. A space structural mechanics model of silicene. *Proceedings of the Institution of Mechanical Engineers, Part N: J. of Nanomaterials, Nanoengineering and Nanosystems*, 2020, **234** (1–2), P. 3–10.
- [2] Zhao J., Liu H., Yu Z., Quhe R., Zhou S., Wang Y., Liu C.C., et al. Rise of silicene: A competitive 2D material. *Progress in Materials Science*, 2016, **83**, P. 24–151.
- [3] Aufray B., Kara A., Vizzini S., Oughaddou H., Léandri C., Ealet B., Lay G.L. Graphene-like silicon nanoribbons on Ag (110): A possible formation of silicene. *Applied Physics Letters*, 2010, **96** (18), 183102.
- [4] Padova P.D., Quaresima C., Ottaviani C., Sheverdyayeva P.M., Moras P., Carbone C., Topwal D., et al. Evidence of graphene-like electronic signature in silicene nanoribbons. *Applied Physics Letters*, 2010, **96** (26), 261905.
- [5] Lalmi B., Oughaddou H., Enriquez H., Kara A., Vizzini S., Ealet B., Aufray B. Epitaxial growth of a silicene sheet. *Applied Physics Letters*, 2010, **97** (22), 223109.
- [6] Fagan S.B., Baierle R.J., Mota R., da Silva A.J.R., Fazzio A. Ab initio calculations for a hypothetical material: Silicon nanotubes. *Physical Review B*, 2000, **61** (15), 9994.
- [7] Cahangirov S., Topsakal M., Aktürk E., Şahin H., Ciraci S. Two- and one-dimensional honeycomb structures of silicon and germanium. *Physical Review Letters*, 2009, **102** (23), 236804.
- [8] Chen Lan, Liu C.C., Feng B., He X., Cheng P., Ding Z., Meng S., Yao Y., Wu K. Evidence for Dirac fermions in a honeycomb lattice based on silicon. *Physical Review Letters*, 2012, **109** (5), 056804.
- [9] Guzmán-Verri G.G., Lew Yan Voon L.C. Electronic structure of silicon-based nanostructures. *Physical Review B*, 2007, **76** (7), 075131.
- [10] Deepthi Jose, Ayan Datta. Understanding of the buckling distortions in silicene. *J. of Physical Chemistry C*, 2012, **116** (46), P. 24639–24648.
- [11] Ding Yi, Jun Ni. Electronic structures of silicon nanoribbons. *Applied Physics Letters*, 2009, **95** (8), 083115.
- [12] Ding Yi, Yanli Wang. Density functional theory study of the silicene-like SiX and XSi<sub>3</sub> (X= B, C, N, Al, P) honeycomb lattices: the various buckled structures and versatile electronic properties. *J. of Physical Chemistry C*, 2013, **117** (35), P. 18266–18278.
- [13] Ni Zeyuan, Qihang Liu, Kechao Tang, Jiaxin Zheng, Jing Zhou, Rui Qin, Zhengxiang Gao, Dapeng Yu, Jing Lu. Tunable bandgap in silicene and germanene. *Nano Letters*, 2012, **12** (1), P. 113–118.
- [14] Şahin H., Cahangirov S., Topsakal M., Bekaroglu E., Aktürk E., Senger R.T., Ciraci S. Monolayer honeycomb structures of group-IV elements and III-V binary compounds: First-principles calculations. *Physical Review B*, 2009, **80** (15), 155453.
- [15] Iordanidou K., Houssa B., van den Broek B., Pourtois G., Afanas'ev V.V., Stesmans A. Impact of point defects on the electronic and transport properties of silicene nanoribbons. *J. of Physics: Condensed Matter*, 2016, **28** (3), 035302.
- [16] Kharadi M.A., Malik G.F.A., Khanday F.A., Shah K.A., Mittal S., Kaushik B.K. Review – Silicene: From material to device applications. *ECSS J. of Solid State Science and Technology*, 2020, **9** (11), 115031.
- [17] Liu C.C., Hua Jiang, Yugui Yao. Low-energy effective Hamiltonian involving spin-orbit coupling in silicene and two-dimensional germanium and tin. *Physical Review B*, 2011, **84** (19), 195430.
- [18] Liu C.C., Wanxiang Feng, Yugui Yao. Quantum spin Hall effect in silicene and two-dimensional germanium. *Physical Review Letters*, 2011, **107** (7), 076802.
- [19] Motohiko E. Valley-polarized metals and quantum anomalous Hall effect in silicene. *Physical Review Letters*, 2012, **109** (5), 055502.
- [20] Das R., Chowdhury S., Majumdar A., Jana D. Optical properties of P and Al doped silicene: a first principles study. *RSC Advances*, 2015, **5** (1), P. 41–50.
- [21] Saleh Bahaa E.A., Malvin Carl Teich. *Fundamentals of Photonics*. John Wiley & Sons, Inc., Hoboken N.J., 1991.
- [22] Chen Xuanhu, Fangfang Ren, Shulin Gu, Jiandong Ye. Review of gallium-oxide-based solar-blind ultraviolet photodetectors. *Photonics Research*, 2019, **7** (4), P. 381–415.
- [23] Edelman P. Environmental and workplace contamination in the semiconductor industry: implications for future health of the workforce and community. *Environmental Health Perspectives*, 1990, **86**, P. 291–295.
- [24] Shinde S.S., Shinde P.S., Oh Y.W., Haranath D., Bhosale C.H., Rajpure K.Y. Structural, optoelectronic, luminescence and thermal properties of Ga-doped zinc oxide thin films. *Applied Surface Science*, 2012, **258** (24), P. 9969–9976.
- [25] Brodsky M.H. Progress in gallium arsenide semiconductors. *Scientific American*, 1990, **262** (2), P. 68–75.
- [26] Ding He, Hao Hong, Dali Cheng, Zhao Shi, Kaihui Liu, Xing Sheng. Power- and spectral-dependent photon-recycling effects in a double-junction gallium arsenide photodiode. *ACS Photonics*, 2019, **6** (1), P. 59–65.
- [27] Xu Chengyong, Guangfu Luo, Qihang Liu, Jiaxin Zheng, Zhimeng Zhang, Shigeru Nagase, Zhengxiang Gao, Jing Lu. Giant magnetoresistance in silicene nanoribbons. *Nanoscale*, 2012, **4** (10), P. 3111–3117.
- [28] Li Feng, Changwen Zhang, Wei-Xiao Ji, Mingwen Zhao. High hydrogen storage capacity in calcium-decorated silicene nanostructures. *Physica Status Solidi B*, 2015, **252** (9), P. 2072–2078.
- [29] Guo Gang, Yuliang Mao, Jianxin Zhong, Jianmei Yuan, Hongquan Zhao. Design lithium storage materials by lithium adatoms adsorption at the edges of zigzag silicene nanoribbon: a first principle study. *Applied Surface Science*, 2017, **406**, P. 161–169.
- [30] Kharadi M.A., Malik G.F.A., Khanday F.A., Shah K.A. Hydrogenated silicene based magnetic junction with improved tunneling magnetoresistance and spin-filtering efficiency. *Physics Letters A*, 2020, **384** (32), 126826.
- [31] Kharadi M.A., Malik G.F.A., Khanday F.A., Mittal S. Silicene-based spin filter with high spin-polarization. *IEEE Transactions on Electron Devices*, 2021, **68** (10), P. 5095–5100.

- [32] Gani Muzafar, Khurshed Ahmad Shah, Shabir A. Parah. Realization of a sub 10-nm silicene magnetic tunnel junction and its application for magnetic random access memory and digital logic. *IEEE Transactions on Nanotechnology*, 2021, **20**, P. 466–473.
- [33] Kharadi M.A., Malik G.F.A., Mittal S. Electric field tunable spin polarization in functionalized silicene. *Physics Letters A*, 2022, **429**, 127952.
- [34] Quantum ATK version P-2019.03, synopsis quantum ATK. URL: <https://www.synopsys.com/silicon/quantumatk.html>.
- [35] Saputro Dewi Retno Sari, Purnami Widyaningsih. Limited memory Broyden-Fletcher-Goldfarb-Shanno (L-BFGS) method for the parameter estimation on geographically weighted ordinal logistic regression model (GWOLR). *AIP Conference Proceedings*, 2017, **1868** (1), 040009.
- [36] Ding Yi, Jun Ni. Electronic structures of silicon nanoribbons. *Applied Physics Letters*, 2009, **95** (8), 083115.
- [37] Parvaiz Shunaid M., Shah K.A., Dar G.N., Farooq Ahmad Khanday. Electrical doping in single walled carbon nanotube systems: A new technique. *Computational Condensed Matter*, 2020, **25**, e00507.
- [38] Drummond N.D., Zolyomi V., Fal'ko V.I. Electrically tunable band gap in silicene. *Physical Review B*, 2012, **85** (7), 075423.
- [39] Nigam S., Gupta S.K., Majumder C., Pandey R. Modulation of band gap by an applied electric field in silicene-based hetero-bilayers. *Physical Chemistry Chemical Physics*, 2015, **17**, P. 11324–11328.
- [40] Jun K., Wu F., Li J. Symmetry-dependent transport properties and magnetoresistance in zigzag silicene nanoribbons. *Applied Physics Letters*, 2012, **100**, 233122.
- [41] Kaur H., Kaur J., Kumar R. A Comparative Study on Electronic Transport Behavior of Silicene and B40-Nano Onions. *Silicon*, 2022, **14** (15), P. 9479–9487.
- [42] Krishna S.M., Singh S., Kaushik B.K. Edge Modified Stanene Nanoribbons for Potential Nanointerconnects. *IEEE Transactions on Nanotechnology*, 2022, **22**, P. 1–8.
- [43] Showket S., Shah K.A., Dar G.N. Pristine and Modified Silicene based Volatile Organic Compound Toxic Gas Sensor: A First Principles Study. *Physica Scripta*, 2023, **98**, 085937.

---

*Submitted 12 June 2023; revised 18 August 2023; accepted 19 August 2023*

*Information about the authors:*

*Asma N. Naqash* – Department of Nanotechnology and Department of Electronics and Instrumentation Technology, University of Kashmir, Srinagar, Jammu and Kashmir – 190006, India; asma.naqash@gmail.com

*Khurshed A. Shah* – Department of Nanotechnology, University of Kashmir, Srinagar, Jammu and Kashmir – 190006, India; Postgraduate Department of Physics, S. P. College, Cluster University Srinagar, Jammu and Kashmir – 190001, India; ORCID 0000-0002-2694-4515; drkhursheda@gmail.com

*Javid Ahmad Sheikh* – Department of Electronics and Instrumentation Technology, University of Kashmir, Srinagar, Jammu and Kashmir – 190006, India; ORCID 0000-0003-3113-3802; sheikhjavaid@uok.edu.in

*Brijesh Kumbhani* – Department of Electrical Engineering, Indian Institute of Technology Ropar, Punjab – 140001, India; brijesh@iitrpr.ac.in

*Syed Muzaffar Ali Andrabi* – Department of Applied Sciences, Institute of Technology, Zakura Campus, University of Kashmir, Srinagar, Jammu and Kashmir – 190006, India; muzaffar2000@gmail.com

*Conflict of interest:* the authors declare no conflict of interest.

## Induced surface photovoltage in TiO<sub>2</sub> sol-gel nanoparticles

Irina B. Dorosheva<sup>1,2,a</sup>, Alexander S. Vokhmintsev<sup>1,b</sup>, Ilya A. Weinstein<sup>1,2,c</sup>, Andrey A. Rempel<sup>1,2,d</sup>

<sup>1</sup>Ural Federal University, Yekaterinburg, Russia

<sup>2</sup>Institute of Metallurgy of the Ural Branch of the Russian Academy of Sciences, Yekaterinburg, Russia

<sup>a</sup>[i.b.dorosheva@urfu.ru](mailto:i.b.dorosheva@urfu.ru), <sup>b</sup>[a.s.vokhmintsev@urfu.ru](mailto:a.s.vokhmintsev@urfu.ru), <sup>c</sup>[i.a.weinstein@urfu.ru](mailto:i.a.weinstein@urfu.ru), <sup>d</sup>[rempe.imet@mail.ru](mailto:rempe.imet@mail.ru)

Corresponding author: I. B. Dorosheva, [i.b.dorosheva@urfu.ru](mailto:i.b.dorosheva@urfu.ru)

**ABSTRACT** TiO<sub>2</sub> nanoparticles synthesized by the sol-gel method and modified by annealing in air and hydrogen atmospheres were studied by surface photovoltage spectroscopy (SPS). SPS measurements showed that the modified in air TiO<sub>2</sub> nanoparticles have a more intense signal than those treated in hydrogen. A linear correlation was found between the SPS and the diffuse reflectance spectra of the samples.

**KEYWORDS** Titanium dioxide, sol-gel method, nanoparticles, surface photovoltage (SPV).

**ACKNOWLEDGEMENTS** A.S.V. and I.A.W. thank the Ministry of Science and Higher Education of the Russian Federation (research project FEUZ-2023-0014) for support. Part of synthesis of titanium dioxide carried out within the framework of RF State assignment for IMET UB RAS.

**FOR CITATION** Dorosheva I.B., Vokhmintsev A.S., Weinstein I.A., Rempel A.A. Induced surface photovoltage in TiO<sub>2</sub> sol-gel nanoparticles. *Nanosystems: Phys. Chem. Math.*, 2023, **14** (4), 447–453.

### 1. Introduction

Titanium dioxide has attracted the attention of scientists around the world for many years, because it is a chemically stable, non-toxic, and inexpensive material that has functional properties for use as photocatalysts in the decomposition of toxicants [1–4], photosorbents of rare earth elements [5–7], renewable energy sources [8–10], resistive memory elements [11–13], new organic compounds synthesis for medicine [14–16], etc. There are also various ways for the nanosized titanium dioxide synthesis: solvothermal [17–19], hydrothermal [20–22], anodic oxidation [2, 23, 24], chemical vapor deposition [25–27], electrodeposition [28–31], sonochemical [32–35], and microwave methods [36–39]. However, TiO<sub>2</sub> has a wide bandgap of 3.0–3.3 eV [40, 41], which makes it difficult to apply it as a photosorbent and photocatalyst under visible light irradiation. In this regard, the material is modified in various ways: by creating a heterostructure, doping with metal ions, annealing in atmospheres of air, hydrogen, argon, nitrogen, etc. [42–49] to create atomic defects and surface states capable to capture photons with lower energy. One of the instruments for study such states is the surface photovoltage spectroscopy (SPS), which allows a non-contact, non-destructive and highly sensitive way to determine the electronic features in surface of solids and can be used to analyze charges separation and transfer in the mechanisms of photocatalysis, dye sensitization, etc. [50–55]. The method is based on the generation of voltage by a capacitor structure with a sample under study between electrodes upon excitation by light [52] and is a suitable tool for study photophysical processes in nanoscale semiconductors for several reasons. First, the SPS is generated as a result of band-to-band transitions, which makes it possible to estimate the semiconductor bandgap [52]. Second, the method is sensitive to band-to-band transitions due to the surface states of a material, which, as a rule, arise due to impurities or point defects in its structure. Therefore, the aim of this work is to study the titanium dioxide nanoparticles, synthesized by the sol-gel method, via surface photovoltage spectroscopy.

### 2. Samples and experiment

TiO<sub>2</sub> nanoparticles were obtained by the sol-gel method at the initial solution pH of 2, 6, and 8, followed by annealing in air in an SNOL 6.7/1300 muffle furnace at a temperature of 350°C for 4 hours [15, 43, 56, 57]. Also, the sample obtained at pH = 6 was annealed in an MPT-2MR tube furnace in a hydrogen atmosphere at temperatures of 200, 400 and 600°C for 60 minutes [43]. The synthesized TiO<sub>2</sub> nanoparticles were previously studied using X-ray phase analysis, diffuse reflectance spectroscopy, and the Brunauer-Emmett-Teller (BET) method [15, 43, 56, 57] (see Table 1).

The surface photovoltage (SPV) spectra were investigated using the measuring installation based on an LS 55 luminescent spectrometer (Perkin-Elmer, USA) with the developed electroluminescent cell [58] and a PXI-4071 digital multimeter (National Instruments, USA). The SPS measurements were controlled by the original virtual device developed in the LabVIEW programming environment. The studied TiO<sub>2</sub> samples were placed between the transparent ITO glass electrode and the Sn<sub>0.61</sub>Cu<sub>0.39</sub> electrode (Fig. 1).

The distance between the electrodes was  $d \approx 20 \mu\text{m}$ . To generate photovoltage, the sample was excited by monochromatic light from a pulsed Xe lamp in the range of 290–450 nm at a monochromator exit slit of 10 nm and a scanning rate

TABLE 1. Characteristics of titanium dioxide powders [15,43,56,57]

Sample	pH of sol			Annealing temperature in H <sub>2</sub>			Degussa P25	Hombifine
	2	6	8	200°C	400°C	600°C		
Phase composition	Anatase			Amorphous	Anatase		Anatase, rutile	Anatase
Coherent scattering region $\pm 10\%$ , nm	8	9	20	–	46	36	25	15
$S_{BET} \pm 2\%$ , m <sup>2</sup> /g	140	140	90	310	120	40	55	70
$E_g \pm 0.1$ , eV	3.0	3.2	3.2	3.3	3.2	3.2	3.0	3.3

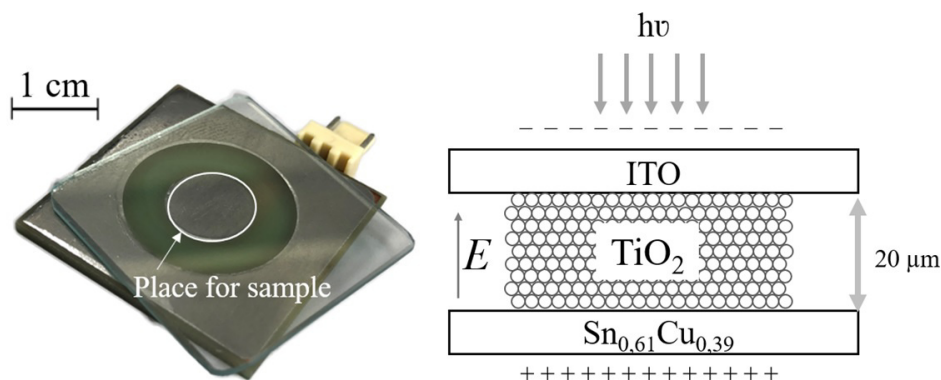


FIG. 1. Image and scheme of a cell for measuring SPV

of 1 nm/s. The SPS signal was recorded by a digital multimeter with a period of 250 ms. Since electrodes with different materials were used, differing in the work function  $A_{out} \approx 4.8$  eV (ITO) and 4.4 eV (Cu, Sn), under the conditions of the induced internal electric field, the background SPS signal was recorded in the dark. Taking into account the emerging contact potential difference of 0.4 eV and the sample thickness  $d$ , the induced electric field was  $E = 2 \cdot 10^6$  V/cm. In this regard, the indicated background SPS signal was subtracted when processing the initial experimental data. The resulting SPS curves were normalized to the ITO transmission spectrum (Fig. 2).

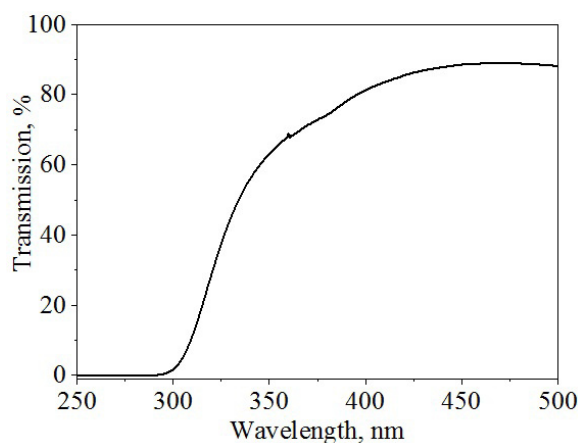


FIG. 2. ITO transmission spectrum

### 3. Results and discussion

The SPS of the studied samples are shown in Figs. 3-4. Hombifine powder was measured for the first time (Fig. 3), there are no data in the literature on measuring its properties by this method. The absolute changes in induced photovoltage  $\Delta U_{max}$  (Fig. 4) depending on the excitation wavelength for samples annealed in air ( $\Delta U_{max} \approx 150$  mV) are almost two times higher than for samples annealed in hydrogen ( $\Delta U_{max} \approx 60 \div 80$  mV).

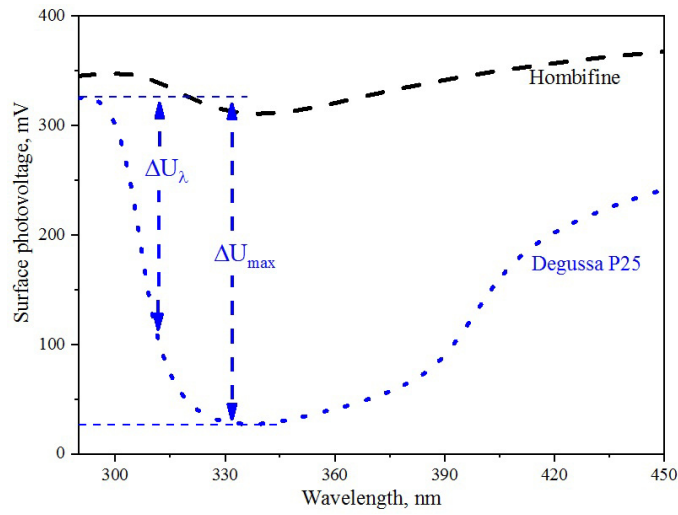


FIG. 3. SPV spectra of Degussa P25 and Hombifine powders

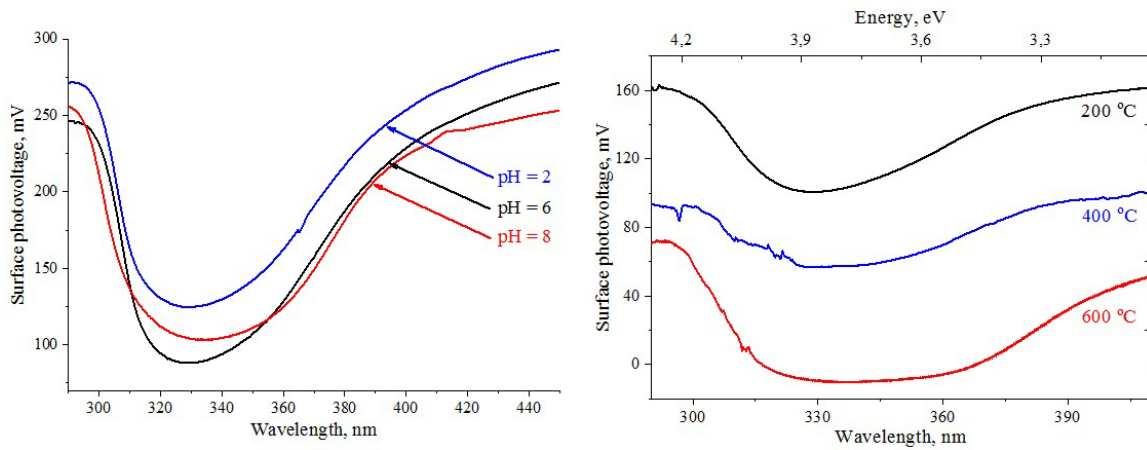


FIG. 4. SPV spectra of TiO<sub>2</sub> samples obtained by the sol-gel method

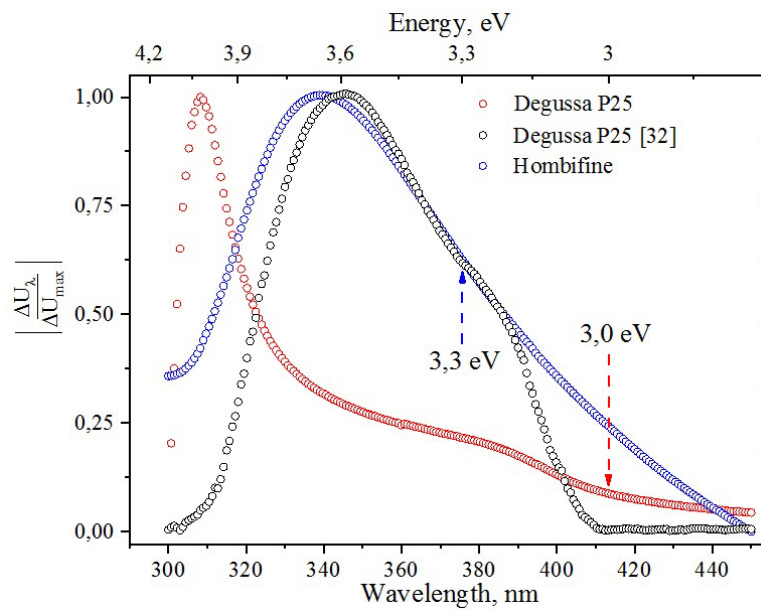


FIG. 5. Normalized surface photovoltage spectra for Degussa P25 and Hombifine powders

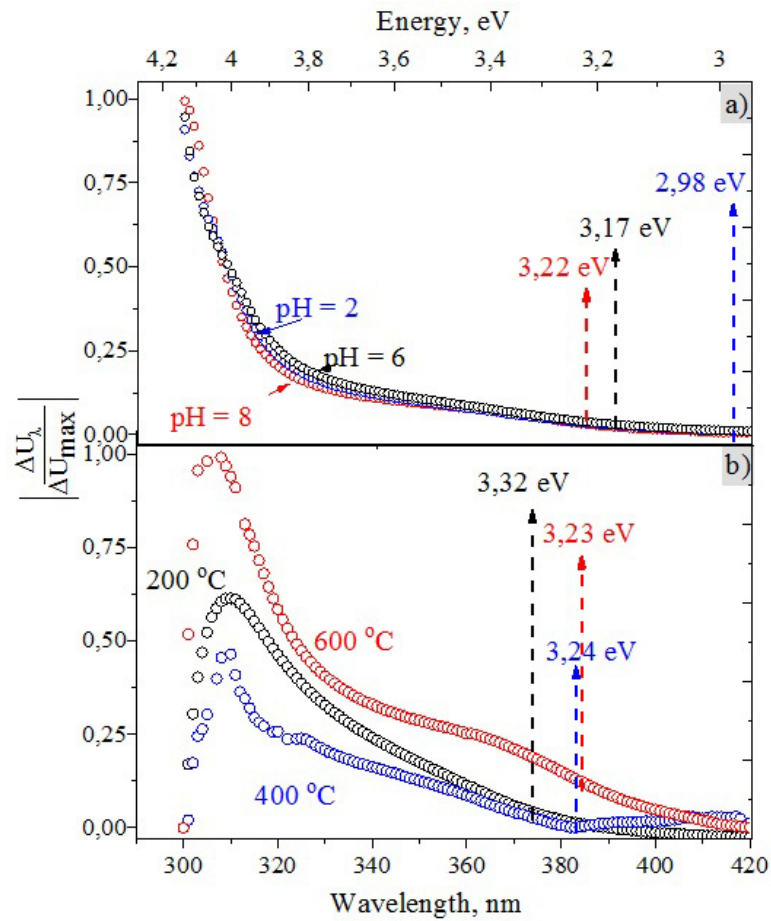


FIG. 6. Normalized surface photovoltage spectra of TiO<sub>2</sub> samples obtained by the sol-gel method

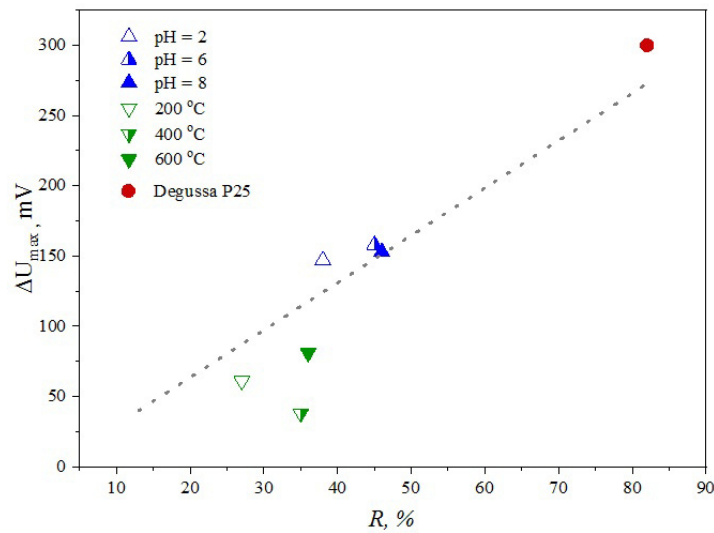


FIG. 7. The dependence of the SPS signal  $\Delta U_{max}$  on the reflectance  $R$  at a 430 nm wavelength

After annealing TiO<sub>2</sub> nanoparticles in air, the SPS spectra have a similar shape, regardless of the sol pH during their synthesis. Comparing the studied samples, it can be noted that the highest value of  $\Delta U_{max}$  appears after annealing in air. This is due to the complete crystallization of the samples to anatase symmetry and a decrease of the vacancies concentration upon annealing in air. Upon annealing in a reducing hydrogen atmosphere, both with partial and complete crystallization, the oxygen vacancies concentration remains high in the sample structure. Charge carriers are localized on these defects, reducing the  $\Delta U_{max}$  value. The highest  $\Delta U_{max}$  among those annealed in hydrogen is demonstrated by the sample treated at 600°C. It is probably due to more efficient separation of electron-hole pairs due to complete crystallization to the anatase phase. A low  $\Delta U_{\lambda}$  value indicates inefficient separation of photoinduced electron-hole pairs or their capture by defect states. Upon annealing at 200°C, the amorphous structure is saved and  $\Delta U_{max} \approx 60$  mV. When the temperature rises to 400°C –  $\Delta U_{max} \approx 40$  mV incomplete crystallization of TiO<sub>2</sub> to anatase occurs at this temperature. As a result of the presence of boundaries in such a two-phase structure, the migration of charge carriers to the surface is hindered; therefore,  $\Delta U_{max}$  is smaller than in amorphous TiO<sub>2</sub>. Annealing at 600°C leads to increase  $\Delta U_{max} \approx 80$  mV. This value is higher than that of amorphous TiO<sub>2</sub> obtained at 200°C. Complete crystallization of the sample to anatase at 600°C leads to the vacancy defects concentration decrease, a more efficient separation of the electron-hole pair and, consequently, a change in the surface charge.

It was found (Fig. 5) that Degussa P25 powder has a maximum photoinduced response in the region of 310 nm, which corresponds to band-to-band optical transitions [59, 60]. The Degussa P25 SPS spectra measured in this work and in [61] differ in the peak position (see Fig. 5). In the cited work, the maximum is shifted to the long wavelength region of 340 nm. This is due to the difference in the materials used for the photovoltaic cell electrodes: two ITO glasses in [61]; in our work, one of the cell electrodes is ITO glass, and the second one is Sn<sub>0.61</sub>Cu<sub>0.39</sub> alloy. The work function of these materials differs by  $\approx 0.4$  eV. Therefore, in our case, additional energy is required to separate the electron-hole pair and release the charge to the surface for signal registration. The corresponding shift in the SPS spectra (Fig. 5) clearly demonstrates this fact. It was also found that Hombifine powder has a maximum photoinduced response in the excitation region of 340 nm. It means that for the separation of electron-hole pairs and the release of charge carriers to the surface, less energy is required than for Degussa P25. This is probably due to the single-phase anatase structure of the sample, i.e. there is no charge carriers scattering at the interphase boundaries of rutile and anatase, which can be characteristic for Degussa P25. The arrows in Figs. 5-6 indicate the bandgap energies of the samples. In addition, a linear relationship was found between the SPS signal and the diffuse reflectance at a wavelength of 430 nm (see Fig. 7) with a Pearson's correlation coefficient of  $r = 0.88$ .

Thus, the structural and phase features of stoichiometric TiO<sub>2</sub> nanoparticles, which are characterized by a single-phase composition, as well as a low concentration of vacancy and surface defects, significantly affect the efficiency of charge carrier separation processes during band-to-band optical excitation and the formation of SPV. Note that a controlled change in the nanostructures surface charge is great importance for optimizing their photovoltaic properties.

#### 4. Conclusions

In this work, we study the photovoltaic properties of titanium dioxide nanoparticles synthesized by the sol-gel method and modified by annealing in air and in hydrogen atmospheres. According to the increment SPV spectra  $\Delta U_{\lambda}$ , it was found that the nanoparticles modified in air have a more intense signal compared to those treated in hydrogen. Due to the high concentration of oxygen vacancies formed as a result of annealing in a reducing atmosphere, defect states appeared, on which excited electrons are localized, which 2 times weakens the SPV signal. A linear correlation of the SPS data with the diffuse reflection spectra (Pearson's correlation coefficient  $r = 0.88$ ) was found, which also confirms the efficiency of electron-hole pairs separation and changes in the surface charge, provided that the structure is stoichiometric and with the least number of defects.

#### References

- [1] Valeeva A.A., Dorosheva I.B., Kozlova E.A., Kamalov R.V., Vokhmintsev A.S., Selishchev D.S., Saraev A.A., Gerasimov E.Y., Weinstein I.A., Rempel A.A. Influence of Calcination on Photocatalytic Properties of Nonstoichiometric Titanium Dioxide Nanotubes. *Journal of Alloys and Compounds*, 2019, **796**, P. 293–299.
- [2] Valeeva A.A., Kozlova E.A., Vokhmintsev A.S., Kamalov R.V., Dorosheva I.B., Saraev A.A., Weinstein I.A., Rempel A.A. Nonstoichiometric Titanium Dioxide Nanotubes with Enhanced Catalytic Activity under Visible Light. *Scientific Reports*, 2018, **8**(1), P. 1–10.
- [3] Sreekantan S., Hazan R., Lockman Z. Photoactivity of Anatase-Rutile TiO<sub>2</sub> Nanotubes Formed by Anodization Method. *Thin Solid Films*, 2009, **518**(1), P. 16–21.
- [4] Camacho-Muñoz D., Lawton L.A., Edwards C. Degradation of Okadaic Acid in Seawater by UV/TiO<sub>2</sub> Photocatalysis – Proof of Concept. *Science of The Total Environment*, 2020, **733**, P. 139346.
- [5] Melchakova O.V., Pechishcheva N.V., Korobitsyna A.D. Mechanically Activated Rutile and Its Sorption Properties with Regard to Gallium and Germanium. *Tsvetnye Metally*, 2019, **1**, P. 32–39.
- [6] Method for obtaining a sorbent based on nanosized titanium dioxide. Method for obtaining a sorbent based on nanosized titanium dioxide: Patent 2790032 Russia B01J20/06 B01J20/30 C02F1/28 C02F1/62 B82B3/00. Dorosheva I.B., Pechishcheva N.V., Rempel A.A., patent holder, N 2790032.
- [7] Miller S.M., Spaulding M.L., Zimmerman J.B. Optimization of Capacity and Kinetics for a Novel Bio-Based Arsenic Sorbent, TiO<sub>2</sub>-Impregnated Chitosan Bead. *Water Research*, 2011, **45**(17), P. 5745–5754.

- [8] Valeeva A.A., Dorosheva I.B., Kozlova E.A., Sushnikova A.A., Kurenkova A.Y., Saraev A., Schroettner H., Rempel A. Solar Photocatalysts Based on Titanium Dioxide Nanotubes for Hydrogen Evolution from Aqueous Solutions of Ethanol. *International Journal of Hydrogen Energy*, 2021, **46**(32), P. 16917–16924.
- [9] Zheng L., Teng F., Ye X., Zheng H., Fang X. Photo/Electrochemical Applications of Metal Sulfide/TiO<sub>2</sub> Heterostructures. *Advanced Energy Materials*, 2020, **10**(1), P. 1902355.
- [10] Kapilashrami M., Zhang Y., Liu Y.S., Hagfeldt A., Guo J. Probing the Optical Property and Electronic Structure of TiO<sub>2</sub> nanomaterials for Renewable Energy Applications. *Chemical Reviews*, 2014, **114**(19), P. 9662–9707.
- [11] Vokhmintsev A.S., Weinstein I.A., Kamalov R.V., Dorosheva I.B. Memristive Effect in a Nanotubular Layer of Anodized Titanium Dioxide. *Bulletin of the Russian Academy of Sciences: Physics*, 2014, **78**(9), P. 932–935.
- [12] Lettieri S., Pavone M., Fioravanti A., Amato L.S., Maddalena P. Charge Carrier Processes and Optical Properties in TiO<sub>2</sub> and TiO<sub>2</sub>-Based Heterojunction Photocatalysts: A Review. *Materials*, 2021, **14**(7), P. 1–57.
- [13] Dash C.S., Sahoo S., Prabaharan S.R.S. Resistive Switching and Impedance Characteristics of M/TiO<sub>2-x</sub>/TiO<sub>2</sub>/M Nano-Ionic Memristor. *Solid State Ionics*, 2018, **324**, P. 218–225.
- [14] Dorosheva I.B., Valeeva A.A., Rempel A.A., Trestsova M.A., Utepova I.A., Chupakhin O.N. Synthesis and Physicochemical Properties of Nanostructured TiO<sub>2</sub> with Enhanced Photocatalytic Activity. *Inorganic Materials*, 2021, **57**(5), P. 503–510.
- [15] Dorosheva I.B., Rempel A.A., Trestsova M.A., Utepova I.A., Chupakhin O.N. Synthesis of a TiO<sub>2</sub> Photocatalyst for Dehydrogenative Cross-Coupling of (Hetero)Arenes. *Inorganic Materials*, 2019, **55**(2), P. 155–161.
- [16] Elsayed D.A., Assy M.G., Mousa S.M., El-Bassyouni G.T., Mouneir S.M., Shehab W.S. TiO<sub>2</sub> Nanoparticle as Catalyst for an Efficient Green One-Pot Synthesis of 1H-3-Indolyl Derivatives as Significant Antiviral Activity. *Bioorganic Chemistry*, 2022, **124**, P. 105805.
- [17] Ye Y., Feng Y., Bruning H., Yntema D., Rijnaarts H.H.M. Photocatalytic Degradation of Metoprolol by TiO<sub>2</sub> Nanotube Arrays and UV-LED: Effects of Catalyst Properties, Operational Parameters, Commonly Present Water Constituents, and Photo-Induced Reactive Species. *Applied Catalysis B: Environmental*, 2018, **220**, P. 171–181.
- [18] Niu B., Wang X., Wu K., He X., Zhang R. Mesoporous Titanium Dioxide: Synthesis and Applications in Photocatalysis, Energy and Biology. *Materials*, 2018, **11**(10), P. 1–23.
- [19] He F., Li J., Li T., Li G. Solvothermal Synthesis of Mesoporous TiO<sub>2</sub>: The Effect of Morphology, Size and Calcination Progress on Photocatalytic Activity in the Degradation of Gaseous Benzene. *Chemical Engineering Journal*, 2014, **237**, P. 312–321.
- [20] Macak J.M., Hildebrand H., Marten-Jahns U., Schmuki P. Mechanistic Aspects and Growth of Large Diameter Self-Organized TiO<sub>2</sub> Nanotubes. *Journal of Electroanalytical Chemistry*, 2008, **621**(2), P. 254–266.
- [21] Tay Q., Liu X., Tang Y., Jiang Z., Sum T.C., Chen Z. Enhanced Photocatalytic Hydrogen Production with Synergistic Two-Phase Anatase/Brookite TiO<sub>2</sub> Nanostructures. *Journal of Physical Chemistry C*, 2013, **117**(29), P. 14973–14982.
- [22] Liu N., Chen X., Zhang J., Schwank J.W. A Review on TiO<sub>2</sub>-Based Nanotubes Synthesized via Hydrothermal Method: Formation Mechanism, Structure Modification, and Photocatalytic Applications. *Catalysis Today*, 2014, **225**, P. 34–51.
- [23] Rempel A.A., Valeeva A.A., Vokhmintsev A.S., Weinstein I.A. Titanium Dioxide Nanotubes: Synthesis, Structure, Properties and Applications. *Russian Chemical Reviews*, 2021, **90**(11), P. 1397–1414.
- [24] Zhou X., Nguyen N.T., Özkan S., Schmuki P. Anodic TiO<sub>2</sub> Nanotube Layers: Why Does Self-Organized Growth Occur—A Mini Review. *Electrochemistry Communications*, 2014, **46**, P. 157–162.
- [25] Sotelo-Vazquez C., Quesada-Cabrera R., Darr J.A., Parkin I.P. Single-Step Synthesis of Doped TiO<sub>2</sub> Stratified Thin-Films by Atmospheric-Pressure Chemical Vapor Deposition. *Journal of Materials Chemistry A*, 2014, **2**(19), P. 7082–7087.
- [26] Byun D., Jin Y., Kim B., Kee Lee J., Park D. Photocatalytic TiO<sub>2</sub> Deposition by Chemical Vapor Deposition. *Journal of Hazardous Materials*, 2000, **73**(2), P. 199–206.
- [27] Pradhan S.K., Reucroft P.J., Yang F., Dozier A. Growth of TiO<sub>2</sub> Nanorods by Metalorganic Chemical Vapor Deposition. *Journal of Crystal Growth*, 2003, **256**(1–2), P. 83–88.
- [28] Baran E., Yazici B. Effect of Different Nano-Structured Ag Doped TiO<sub>2</sub>-NTs Fabricated by Electrodeposition on the Electrocatalytic Hydrogen Production. *International Journal of Hydrogen Energy*, 2016, **41**(4), P. 2498–2511.
- [29] Cheng X., Pan G., Yu X. Visible Light Responsive Photoassisted Electrocatalytic System Based on CdS NCs Decorated TiO<sub>2</sub> Nano-Tube Photoanode and Activated Carbon Containing Cathode for Wastewater Treatment. *Electrochimica Acta*, 2015, **156**, P. 94–101.
- [30] Ishikawa Y., Matsumoto Y. Electrodeposition of TiO<sub>2</sub> Photocatalyst into Nano-Pores of Hard Alumite. *Electrochimica Acta*, 2001, **46**(18), P. 2819–2824.
- [31] Karuppuchamy S., Amalnerkar D.P., Yamaguchi K., Yoshida T., Sugiura T., Minoura H. Cathodic Electrodeposition of TiO<sub>2</sub> Thin Films for Dye-Sensitized Photoelectrochemical Applications. *Chemistry Letters*, 2002, **1**, P. 78–79.
- [32] Ibrahim A., Mekprasart W., Pecharapa W. Anatase/Rutile TiO<sub>2</sub> Composite Prepared via Sonochemical Process and Their Photocatalytic Activity. *Materials Today: Proceedings*, 2017, **4**(5), P. 6159–6165.
- [33] Arami H., Mazloumi M., Khalifehzadeh R., Sadrnezhaad S.K. Sonochemical Preparation of TiO<sub>2</sub> Nanoparticles. *Materials Letters*, 2007, **61**(23–24), P. 4559–4561.
- [34] Guo W., Lin Z., Wang X., Song G. Sonochemical Synthesis of Nanocrystalline TiO<sub>2</sub> by Hydrolysis of Titanium Alkoxides. *Microelectronic Engineering*, 2003, **66**(1–4), P. 95–101.
- [35] Yu J.C., Zhang L., Yu J. Direct Sonochemical Preparation and Characterization of Highly Active Mesoporous TiO<sub>2</sub> with a Bicrystalline Framework. *Chemistry of Materials*, 2002, **14**(11), P. 4647–4653.
- [36] Selvam T.P., Kumar P.V., Saravanan G., Prakash C.R. Microwave-Assisted Synthesis, Characterization and Biological Activity of Novel Pyrazole Derivatives. *Journal of Saudi Chemical Society*, 2014, **18**(6), P. 1015–1021.
- [37] Suwarnkar M.B., Dhabbe R.S., Kadam A.N., Garadkar K.M. Enhanced Photocatalytic Activity of Ag Doped TiO<sub>2</sub> Nanoparticles Synthesized by a Microwave Assisted Method. *Ceramics International*, 2014, **40**(4), P. 5489–5496.
- [38] Magdalane C.M., Priyadharsini G.M.A., Kaviyarasu K., Jothi A.I., Simiyon G.G. Synthesis and Characterization of TiO<sub>2</sub> Doped Cobalt Ferrite Nanoparticles via Microwave Method: Investigation of Photocatalytic Performance of Congo Red Degradation Dye. *Surfaces and Interfaces*, 2021, **25**, P. 101296.
- [39] Pol V.G., Langzam Y., Zaban A. Application of Microwave Superheating for the Synthesis of TiO<sub>2</sub> Rods. *Langmuir*, 2007, **23**(22), P. 11211–11216.
- [40] Haider A.J., Jameel Z.N., Al-Hussaini I.H.M. Review on: Titanium Dioxide Applications. *Energy Procedia*, 2019, **157**, P. 17–29.
- [41] Wang S., Zheng M., Jiang D., - al, Zhu Z., Wei K., Li H., Cai G., Chen Z., Qiang L. Synthesis and UV Detection Characteristics of TiO<sub>2</sub> Thin Film Prepared through Sol Gel Route. *IOP Conference Series: Materials Science and Engineering*, 2018, **360**(1), P. 012056.

- [42] Rempel A.A., Kuznetsova Y.V., Dorosheva I.B., Valeeva A.A., Weinstein I.A., Kozlova E.A., Saraev A.A., Selishchev D.S. High Photocatalytic Activity Under Visible Light of Sandwich Structures Based on Anodic TiO<sub>2</sub>/CdS Nanoparticles/Sol-Gel TiO<sub>2</sub>. *Topics in Catalysis*, 2020, **63**(1–2), P. 130–138.
- [43] Dorosheva I.B., Adiyak E.V., Valeeva A.A., Rempel A.A. Synthesis of Nonstoichiometric Titanium Dioxide in the Hydrogen Flow. *AIP Conference Proceedings*, 2019, **2174**, P. 020019.
- [44] Kamalov R., Vokhmintsev A., Dorosheva I., Kravets N., Weinstein I. Synthesis of Composite Based on Carbon Nanotubes and Anodic Titania. *Advanced Science Letters*, 2016, **22**(3), P. 688–690.
- [45] Rempel A.A., Kozlova E.A., Gorbunova T.I., Cherepanova S.V., Gerasimov E.Y., Kozhevnikova N.S., Valeeva A.A., Korovin E.Y., Kaichev V.V., Shchipunov Y.A. Synthesis and Solar Light Catalytic Properties of Titania-Cadmium Sulfide Hybrid Nanostructures. *Catalysis Communications*, 2015, **68**, P. 61–66.
- [46] Wang Y., He Y., Lai Q., Fan M. Review of the Progress in Preparing Nano TiO<sub>2</sub>: An Important Environmental Engineering Material. *Journal of Environmental Sciences (China)*, 2014, **26**(11), P. 2139–2177.
- [47] El-Bahy Z.M., Ismail A.A., Mohamed R.M. Enhancement of Titania by Doping Rare Earth for Photodegradation of Organic Dye (Direct Blue). *Journal of Hazardous Materials*, 2009, **166**(1), P. 138–143.
- [48] Humayun M., Raziq F., Khan A., Luo W. Modification Strategies of TiO<sub>2</sub> for Potential Applications in Photocatalysis: A Critical Review. *Green Chemistry Letters and Reviews*, 2018, **11**(2), P. 86–102.
- [49] Gupta B., Melvin A.A., Matthews T., Dash S., Tyagi A.K. TiO<sub>2</sub> Modification by Gold (Au) for Photocatalytic Hydrogen (H<sub>2</sub>) Production. *Renewable and Sustainable Energy Reviews*, 2016, **58**, P. 1366–1375.
- [50] Lenzmann F., Krueger J., Burnside S., Brooks K., Gra M., Gal D., Ru S., Cahen D. Surface Photovoltage Spectroscopy of Dye-Sensitized Solar Cells with TiO<sub>2</sub>, Nb<sub>2</sub>O<sub>5</sub>, and SrTiO<sub>3</sub> Nanocrystalline Photoanodes: Indication for Electron Injection. *ACS Publications*, 2001, **105**(27), P. 6347–6352.
- [51] Yanhong L., Dejun W., Qidong Z., Min Y., Qinglin Z. A Study of Quantum Confinement Properties of Photogenerated Charges in ZnO Nanoparticles by Surface Photovoltage Spectroscopy. *Journal of Physical Chemistry B*, 2004, **108**(10), P. 3202–3206.
- [52] Kronik L., Shapira Y. Surface Photovoltage Phenomena: Theory, Experiment, and Applications. *Surface Science Reports*, 1999, **37**(1), P. 1–206.
- [53] Xin B., Jing L., Ren Z., Wang B., Fu H. Effects of Simultaneously Doped and Deposited Ag on the Photocatalytic Activity and Surface States of TiO<sub>2</sub>. *The Journal of Physical Chemistry B*, 2005, **109**(7), P. 2805–2809.
- [54] Liqiang J., Dejun W., Baiqi W., Shudan L., Baifu X., Honggang F., Jiazhong S. Effects of Noble Metal Modification on Surface Oxygen Composition, Charge Separation and Photocatalytic Activity of ZnO Nanoparticles. *Molecular Catalysis*, 2006, **244**(1–2), P. 193–200.
- [55] Chakrabarti S., Ganguli D., Chaudhuri S. Photoluminescence of ZnO Nanocrystallines Confined in Sol-Gel Silica Matrix. *Journal of Physics D: Applied Physics*, 2003, **36**(2), P. 146–151.
- [56] Dorosheva I.B., Valeeva A.A., Rempel A.A. Sol-Gel Synthesis of Nanosized Titanium Dioxide at Various PH of the Initial Solution. *AIP Conference Proceedings*, 2017, **1886**(1), P. 020006.
- [57] Dorosheva I.B., Weinstein I.A., Rempel A.A. Electrochemical and Sol-Gel Synthesis of Nanostructured Titania Photocatalyst Acting under Sunlight, 16TH IUPAC HIGH TEMPERATURE MATERIAL CHEMISTRY CONFERENCE (HTMC-XVI) Yekaterinburg, 2018, 272 p.
- [58] Electroluminescent cell. Electroluminescent cell: patent 151492 Russia H05B 33/20 G01N 21/66. Vokhmintsev A.S., Fedorov M.D., Weinshtein I.A., patent holder. N 151492.59.
- [59] Lu Y., Yuan M., Liu Y., Tu B., Xu C., Liu B., Zhao D., Kong J. Photoelectric Performance of Bacteria Photosynthetic Proteins Entrapped on Tailored Mesoporous WO<sub>3</sub>-TiO<sub>2</sub> Films. *Langmuir*, 2005, **21**(9), P. 4071–4076.
- [60] Liqiang J., Honggang F., Baiqi W., Dejun W., Baifu X., Shudan L., Jiazhong S. Effects of Sn Dopant on the Photoinduced Charge Property and Photocatalytic Activity of TiO<sub>2</sub> Nanoparticles. *Applied Catalysis B: Environmental*, 2006, **62**(3–4), P. 282–291.
- [61] Jing L., Li S., Song S., Xue L., Fu H. Investigation on the Electron Transfer between Anatase and Rutile in Nano-Sized TiO<sub>2</sub> by Means of Surface Photovoltage Technique and Its Effects on the Photocatalytic Activity. *Solar Energy Materials and Solar Cells*, 2008, **92**(9), P. 1030–1036.

---

Submitted 26 May 2023; revised 21 June 2023; accepted 22 June 2023

#### Information about the authors:

*Irina B. Dorosheva* – Ural Federal University, Mira str., 19, Yekaterinburg, 620002, Russia; Institute of Metallurgy of the Ural Branch of the Russian Academy of Sciences, Amundsena str., 101, Yekaterinburg, 620016, Russia; ORCID 0000-0001-9229-6758; i.b.dorosheva@urfu.ru

*Alexander S. Vokhmintsev* – Ural Federal University, Mira str., 19, Yekaterinburg, 620002, Russia; ORCID 0000-0003-2529-3770; a.s.vokhmintsev@urfu.ru

*Ilya A. Weinstein* – Ural Federal University, Mira str., 19, Yekaterinburg, 620002, Russia; Institute of Metallurgy of the Ural Branch of the Russian Academy of Sciences, Amundsena str., 101, Yekaterinburg, 620016, Russia; ORCID 0000-0002-5573-7128; i.a.weinstein@urfu.ru

*Andrey A. Rempel* – Ural Federal University, Mira str., 19, Yekaterinburg, 620002, Russia; Institute of Metallurgy of the Ural Branch of the Russian Academy of Sciences, Amundsena str., 101, Yekaterinburg, 620016, Russia; ORCID 0000-0002-0543-9982; rempel.imet@mail.ru

*Conflict of interest:* the authors declare no conflict of interest.

## Solution processed Ag–In–S nanoparticles as light adsorber in ZnO for photovoltaic application

K. Abinaya<sup>1</sup>, P. Sharvanti<sup>2</sup>, N. Rajeswari Yogamalar<sup>3,a</sup>

<sup>1</sup>London South Bank University, London, UK

<sup>2</sup>Research and Development, Saint Gobain, San Diego, California, USA

<sup>3</sup>Hindustan Institute of Technology and Science, Padur, Kelambakkam, Chennai, India

<sup>a</sup>rajeswariyogamalar.n@gmail.com

Corresponding author: N. Rajeswari Yogamalar, [rajeswariyogamalar.n@gmail.com](mailto:rajeswariyogamalar.n@gmail.com)

**ABSTRACT** Nano-sized indium incorporated silver sulphide (Ag–In–S) nanocomposites were synthesized by simple wet chemical method as an electron transport layer in zinc oxide (ZnO) for high efficient photovoltaic (PV) cell. The inclusion of high conductivity indium ions in Ag<sub>2</sub>S will improve the facile electron transfer and the assembled hetero-structure features the solar light harvesting in PV cell. The powder X-ray diffraction (XRD) studies confirmed the formation of indium incorporated Ag<sub>2</sub>S (A/IS) nanocomposites and ZnO/AIS (ZAIS) compound nanocomposites crystallizing in pure monoclinic phase and mixed wurtzite hexagonal, monoclinic and tertiary phases respectively. The wide particle size distributions in ZAIS clearly revealed the adherence of AIS nanocomposites in ZnO lattice thus, promoting the light adsorption property. In addition, the tuning of the optical bandgap covering the entire solar spectrum (UV, visible, and infra-red regions), multiple-band electron transitions and hence, promoting the fast electron transportation are effectively achieved in ZAIS compound nanocomposites. With this simple positive approach, the PV cell efficiency is pushed forward with the In<sup>3+</sup> metal ion incorporation however; enhanced, enriched solar cell efficiency can be later tuned up with the detailed optimization studies.

**KEYWORDS** Electron transport layer, nanocomposites, hetero-structure, nano-confinement, light adsorption.

**ACKNOWLEDGEMENTS** We acknowledge Hindustan Institute of Technology and Science for the financial assistance through HITS Seed Money Grant 2023 SEED/CRC/HITS/2022-23/0013. We owe a deep sense of gratitude to Prof. Dr. R. Jayavel, Former Dean, ACT campus and all the research scholars, Centre for Nanoscience and Technology, Anna University, Chennai for ensuring the facilities and instruments available in the laboratory.

**FOR CITATION** Abinaya K., Sharvanti P., N. Rajeswari Yogamalar Solution processed Ag–In–S nanoparticles as light adsorber in ZnO for photovoltaic application. *Nanosystems: Phys. Chem. Math.*, 2023, **14** (4), 454–466.

### 1. Introduction

Nanocrystals are increasingly gaining importance in modern technological advances due to their unique properties as well as the efforts to miniaturize the systems [1, 2]. In order to explore the novel physical properties and to realize the potential applications of these nanocrystals, the ability to fabricate and process nanocrystals are the first corner stone in nanotechnology [3, 4]. Silver sulphide (Ag<sub>2</sub>S) is an important I–VI inorganic semiconductor material which finds diverse applications in energy devices [5, 6]. Ag<sub>2</sub>S easily crystallizes in monoclinic phase and exhibits an anisotropic growth with controlled particle size. The Ag<sub>2</sub>S in nano-sized structure appears to be a promising candidate in the conversion of the solar energy to the electrical energy as it has a narrow optical bandgap which can be tuned in the range of 1 eV to 2 eV. Tuning the bandgap and aligning the bandgap with the lattice matched hetero-structures play an important role in sensing and adsorbing the maximum available light energy (visible region and infra-red region) of the solar spectrum [7, 8]. Thus, the influence of above two parameters (nano-size confinement and optical bandgap engineering) on light harvesting is effectively investigated with the incorporation of high conductivity indium (In) metal ion by conventional wet chemical precipitation method into Ag<sub>2</sub>S lattice. The major advantages of wet chemical method are relatively economical, large scale production, low energy consumption, and wide ranges of metals, metal oxides, metal sulphide, and nanocomposites are synthesized with peculiar morphology [9, 10]. The choice of In<sup>3+</sup> metal ion, promotes more electron injections and with high ionic conductivity of  $\sigma = 10^7 \Omega^{-1} \text{m}^{-1}$  enhances the electron transfer process and hence, reduces the electron-hole recombination process.

Mingxia J., et. al. reported the strong emitting photoluminescence properties of silver indium sulphide AgInS<sub>2</sub> quantum dots towards the power conversion efficiency (PCE) and long stability bio-imaging [11]. Highly luminescent AgInS nanoparticles are synthesized by Watcharaporn H., et. al. through two-step injection process [12]. Here, the AgInS

TABLE 1. The photovoltaic performance of Ag<sub>2</sub>S, In<sub>2</sub>S<sub>3</sub>, and silver indium sulphide AgInS<sub>2</sub> as an adsorber and buffer layer in solar cell

Sample	Solar cell	Synthesis method	Photovoltaic Performance			Ref. No.
			V <sub>OC</sub> (V)	J <sub>SC</sub> (mAcm <sup>-2</sup> )	η %	
Ag <sub>2</sub> S as absorber layer	Inverted organic polymer solar cell	Spray pyrolysis Nano-particles	0.52	16.50	5.15	[15]
In <sub>2</sub> S <sub>3</sub> as buffer layer	CIGS	PVD Thin film	0.51	30.83	2.88	[16]
In <sub>2</sub> S <sub>3</sub> as electron transport layer	Perovskite solar cell	Solvent-thermal method Nanosheets	1.06	21.56	15.88	[17]
Cu diffused AgInS <sub>2</sub>	Heterojunction solar cell	Solution method Nano-powder	0.54	6.74	1.13	[18]
AgInS <sub>2</sub> as electron transport layer	Perovskite solar cell	Solution method Nano-powder	1.12	22.20	13.8	[19]

core is coated with the gallium sulphide (GaS<sub>x</sub>) shell and enhanced the photoluminescence quantum efficiency yield. The systematic characterization studies of graphene (Gr) incorporated indium sulphide nano film exhibited significant modifications in structural and opto-electronic properties especially in PV and photocatalyst applications [13]. A review article on tailored indium sulphide based solar materials for solar energy conversion and utilization is systematically summarized and its advancements are highlighted in detailed [14]. Mohammed Hamed S.G. employed silver sulphide nanoparticles as light trapping layer in an inverted solar cell [15]. The literary surveys on silver sulphide and indium sulphide for light harvesting are many in numbers. Despite these improvements, in this paper, an approach is made to integrate the properties of indium sulphide and silver sulphide into indium incorporated silver sulphide as light sensitizers / adsorbers in stable metal oxide ZnO based *pn* junction PV cell. To differentiate and to characterize the significance of the present work, Table 1 is tabulated to show the PV performance of individual chemical compounds Ag<sub>2</sub>S, In<sub>2</sub>S<sub>3</sub> and silver indium sulphide AgInS<sub>2</sub> acting as an adsorber or buffer layer in solar cell [15–19].

Here, a wet chemically synthesized Ag<sub>2</sub>S and In incorporated Ag<sub>2</sub>S are individually added with the ZnO nanorods to form the compound nanocomposites. The so-formed compound nanocomposites are deposited as *n*-type layer in heterojunction PVI and the efficiency of the assembled devices are compared, measured and evaluated by current density – voltage (*J-V*) characterization.

## 2. Experimental

### 2.1. Synthesis

The following reagents – silver nitrate AgNO<sub>3</sub>, sulphur powder, sodium hydroxide pellets (NaOH), indium acetate In(CH<sub>3</sub>COO)<sub>3</sub>, poly-ethylene glycol (PEG), zinc nitrate ZnNO<sub>3</sub>, cetrimide (CTAB), ammonia solution NH<sub>3</sub>OH, were purchased from Merck with high purity and were used without further purifications.

In a typical synthesis of ZnO nanorods, 0.1 M of zinc nitrate was dissolved in 80 mL of deionized water (DW). To establish a controlled and anisotropic growth, 0.1 mM of capping agent namely PEG was added and stirred continuously for 30 min. A clear transparent solution was obtained implying the complete dissolution of crystal. Further, to initiate the precipitation process, 0.2 M of NaOH pellets were added and the transparent solution turned to milky white. Then, the solution mixture was transferred to hot air oven maintained at 90°C for 6 h and finally, the obtained solution was centrifuged repeatedly and vacuum dried at 60°C for 4 h to get crystallized white ZnO nanopowders (“Z”).

The pure and indium incorporated silver sulphide nanocomposites were prepared similarly. For Ag<sub>2</sub>S synthesis, 0.2 M of silver nitrate and 0.2 mM of CTAB were dissolved in 50 mL of EG and pre-heated at 120°C for 30 min. Then a solution mixture of 0.6 M of sulphur powder and 1 M of NaOH pellets were dissolved in another 50 mL of EG and stirred for 30 min. Now, both the solutions were mixed and maintained at 120°C for 8 h in hot air oven. A black precipitate was obtained after centrifugation, vacuum dried at 60°C for 4 h and the sample was named as “AS”. The same methodology was adopted to synthesize indium incorporated Ag<sub>2</sub>S nanocomposites, where 40 mM of indium acetate was added along with the silver precursor and the resulted sample powder was referred as “AIS”.

In the synthesis of compound nanocomposites by in-situ chemical precipitation method, the host material compound “Z” and the light sensitizer were taken in the ratio of 4:1 and were grown simultaneously. The as-synthesized “Z” was dispersed in 30 mL of EG, 10 mL of DW and 10 mL of methanol. The above solvent composition was mainly to promote

the adhesion of light sensitizer to the host compound and further, to establish controlled growth kinetics. Now, the as-synthesized "AS" and "AIS" were individually dispersed in the above solution mixture and maintained at 120°C for 8 h in hot air oven. The obtained precipitates were washed, centrifuged and vacuum dried. The as-synthesized nanocomposites were referred as "ZAS" and "ZAIS".

The entire procedures involved in the nanocomposites synthesis and the photograph of Z, AS, AIS, ZAS, and ZAIS were shown in the Fig. 1 and Fig. 2 respectively. In Fig. 2, the addition of  $\text{In}^{3+}$  metal ion precursor and the formation of nanocomposites resulted in a wide color variations from dirty white (Z) and black (AS) to dark grey (ZAS) and orange brown (AIS and ZAIS) solutions. The color variations might be due to the formation of different crystal structures or unusual optical properties which would be evaluated in the subsequent material characterizations.

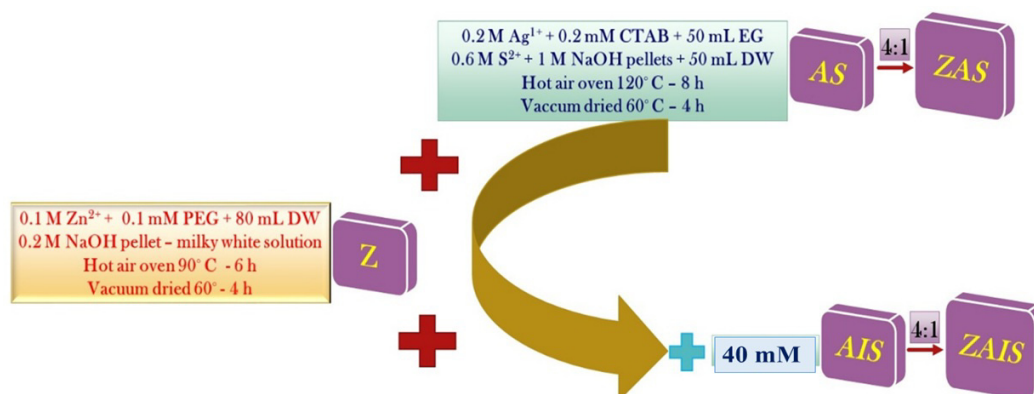


FIG. 1. The entire synthesis procedures of ZnO based compound nanocomposites by wet chemical method

## 2.2. Characterizations

The crystalline phases were verified with Mini Flex II Rigaku X-ray diffractometer (XRD) at a scanning rate of 0.2°/min in the range of 20° to 60° with Cu  $K_{\alpha 1}$  radiation (1.5406Å) operated at 40 kV and 35 mA. The morphological study was carried out using TESCAN Vega III scanning electron microscopy (SEM) at an accelerating voltage of 5 kV to 10 kV. Room temperature UV-visible diffusion reflectance spectroscopy (DRS) data was acquired using T90+ UV/Vis spectrophotometer. Here, BaSO<sub>4</sub> powder was used as reference and the spectrum was recorded at room temperature in the wavelength range of 200 nm to 900 nm with the speed of 0.5 nm/s. The  $J-V$  measurements for the device were measured using a Keithley sourcemeter with 100 mW/cm<sup>2</sup> AM 1.5G of solar spectrum illumination.

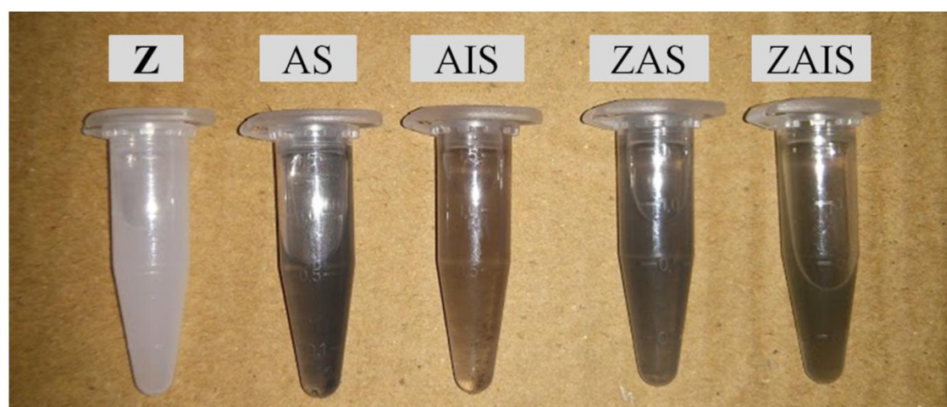


FIG. 2. Photographic view of the as-synthesized samples Z, AS, AIS, ZAS and ZAIS nanocomposites

## 3. Results and discussions

### 3.1. Phase analysis

The Fig. 3 shows the typical XRD pattern of as-synthesized ZnO nanostructures (Z). All the diffraction peaks were referred with standard JCPDS database of 89-1397 and indexed as hexagonal phase wurtzite structure of ZnO. The absence of other secondary diffraction peaks indicates the phase purity of the as-synthesized ZnO nanostructure. The diffraction pattern consists of very narrow and sharp peaks, revealing the improved crystalline with ordered orientation of atoms in the

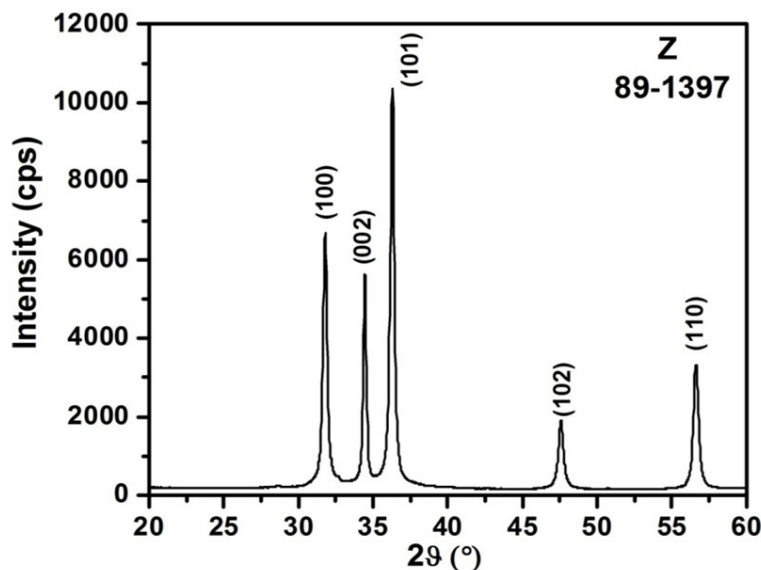


FIG. 3. The XRD pattern of PEG capped ZnO nanostructures (Z)

crystal lattice. For crystallite size analysis, the high intense (101) reflection of the hexagonal phase ZnO was employed. The average crystallite size  $d_{avg}$  was calculated from the instrumental corrected full width half maximum using Scherrer equation  $d_{avg} = \left( \frac{0.9\lambda}{\beta \cos \theta} \right)$  and was found to be 47 nm for Z synthesized by the chemical precipitation method [20].

The XRD patterns of silver sulphide (AS) and transition metal indium incorporated silver sulphide (AIS) nanostructures were shown in the Fig. 4(a) and Fig. 4(b), respectively. All the diffraction peaks of AS were referred, matched

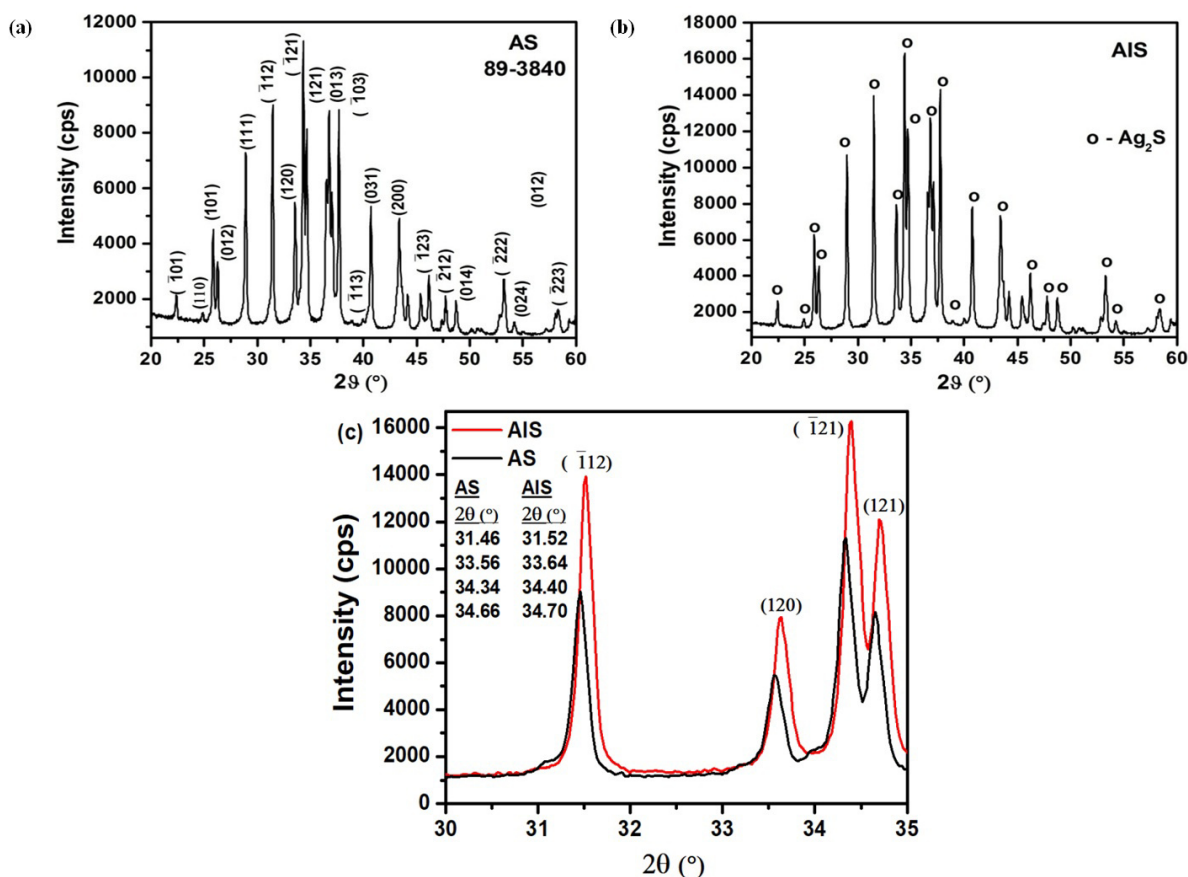


FIG. 4. The XRD patterns of (a) pure, (b) indium incorporated silver sulphide nanoparticles and (c) the peak shift

and indexed with the standard JCPDS data number 89-3840. Here, the sample crystallizes in monoclinic phase and the preferred growth orientation was along the (121) plane at  $34^\circ$ . The *AIS* sample as shown in Fig. 4(b) also exhibits the similar diffraction pattern with increased intensity and slightly broadened in comparison to *AS*. The peaks are matched and indicated by the symbol “o” in the Fig. 4(b). Here, the dominant diffraction peak was slightly shifted towards the higher scattering angle implying the presence of tensile strain originating from the incorporation of  $\text{In}^{3+}$  metal ion in the lattice site of  $\text{Ag}^+$  ion. As the ionic radius of  $\text{In}^{3+}$  (81 pm) was smaller than the  $\text{Ag}^+$  ion (126 pm), the diffraction peak shift was towards the greater angle from  $34.34^\circ$  to  $34.40^\circ$ . The  $\text{In}^{3+}$  ions were well incorporated in the parent lattice and forming a solid solution with no clear demarcation of secondary phase. The secondary phase of  $\text{InS}_2$  might be hidden as they share the common diffraction angle like  $26^\circ$ – $27^\circ$ ,  $38^\circ$ – $39^\circ$  and  $52^\circ$ – $54^\circ$ . The calculated  $d_{avg}$  using Scherrer equation for *AS* and *AIS* samples were 38 nm and 34 nm, respectively.

However, in the preparation of the compound nanocomposites (*ZAS* and *ZAIS*) by in-situ chemical precipitation method, few variations were cited in comparison to the pure sample. In *ZAS* sample, the diffraction peaks corresponding to both the hexagonal phase  $\text{ZnO}$  and monoclinic phase  $\text{Ag}_2\text{S}$  were noticed and represented by the symbol “#” and “o”, respectively, in Fig. 5(a). Here, the  $\text{Ag}_2\text{S}$  nanoparticles formed a compound with the parent matrix material  $\text{ZnO}$  and, hence, a *ZAS* nanocomposite was formed with the second phase (monoclinic). As the composition of  $\text{ZnO}$  and  $\text{Ag}_2\text{S}$  was maintained as 4:1, the growth of  $\text{ZnO}$  nanostructures was predominant. In *ZAS* compound nanocomposites, the XRD peak intensity of (002) at  $\theta = 34^\circ$  was amplified and heightened than (100) plane in comparison to the pure *Z* nanostructure. The observation might be attributed to the superposition of (002) plane of  $\text{ZnO}$  and (121) plane of  $\text{Ag}_2\text{S}$  nanostructures or due to the inclusion of  $\text{Ag}_2\text{S}$  nanoparticles the  $\text{ZnO}$  preferred to grow along the *c*-axis orientation which can be evaluated from SEM study.

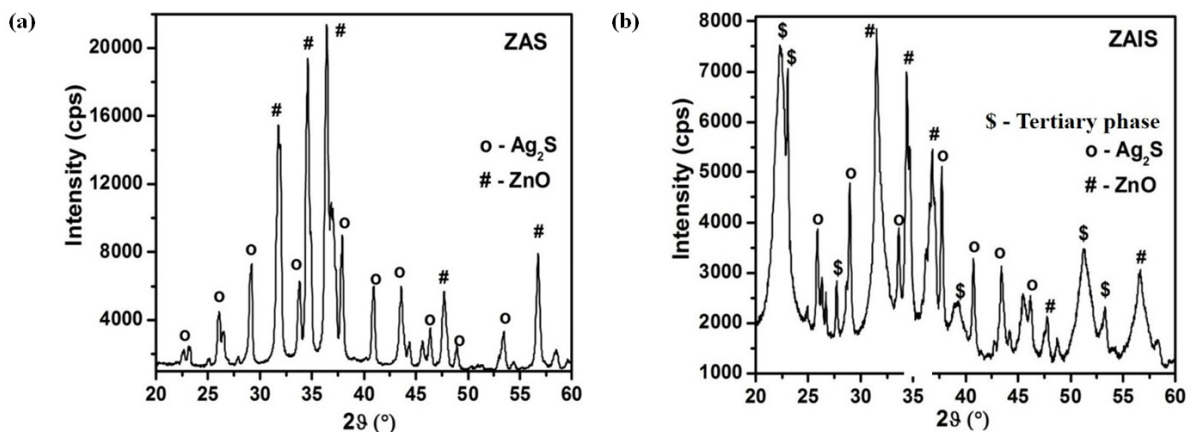


FIG. 5. The XRD patterns of (a) *ZAS* and (b) *ZAIS* compound nanocomposites synthesized by in-situ precipitation method

In *ZAIS* sample (Ref. Fig. 5(b)), apart from the crystal phases of  $\text{ZnO}$  and  $\text{Ag}_2\text{S}$ , a tertiary impurity peaks represented by the “\$” symbol, correspond to the indium hydroxide ( $\text{In}(\text{OH})_3$ ) peaks (200) centered at  $22.4^\circ$  and (400) centered at  $45.5^\circ$  were referred and matched from the standard JCPDS data file number 73-1810 [21, 22]. Fig. 5(b) reflects that the diffraction peak intensities of hexagonal  $\text{ZnO}$  phase were highly suppressed and the growth was well pronounced along (100) plane due to the large distribution of small sized tertiary phase particles on  $\text{ZnO}$  lattice. The above reflections might be ascertained to the rapid nucleation and increased growth rate of tertiary phase in the prescribed synthesis condition. The tertiary phase particles were chemically well-reacted with the host material and strained their lattices to a greater extent. Moreover, the activation energy required for the growth of metal hydroxides  $\text{In}(\text{OH})_3$  ( $\approx 840$  meV) was usually lower than the metal oxide formation  $\text{ZnO}$  ( $\approx 1$  eV) particles and hence, the impurity formation. The SEM studies might support the above establishments.

In both the compound nanocomposites *ZAS* and *ZAIS*, the  $\text{ZnO}$  was strained tensile due to the occupation of other phase materials. From Scherrer equation, a reduced  $d_{avg}$  was obtained for *ZAS* (22 nm) and *ZAIS* (16 nm) compound nanocomposites due to the pure and  $\text{In}^{3+}$  metal ion incorporated  $\text{Ag}_2\text{S}$  light sensitizers.

### 3.2. Particle size distribution

The particle size distribution was collected by MALVERN Zetasizer version 6 and for the measurement, the powder samples were suspended in the water solvent. Here, the *Z*, *AS*, *AIS*, *ZAS*, and *ZAIS* particles exhibited a wide size distribution as depicted in Fig. 6 ranging from 400 nm to  $1.2 \mu\text{m}$ . The wide particle size distributions were ascertained to the inclusion of nano-sized  $\text{In}(\text{OH})_3$ ,  $\text{Ag}_2\text{S}$  and indium incorporated  $\text{Ag}_2\text{S}$  on the high crystalline  $\text{ZnO}$  nanostructures. Approximately 3% of  $\text{InS}_2$  secondary phase is seen in the *AIS* sample which was not identified in the XRD (Ref. Fig. 4(b))

TABLE 2. The Z-average and particle size/phase distribution of Z, AS, AIS, ZAS, and ZAIS nanocomposites

Sample	Z-Average	Peak 1 – ZnO Phase	Peak 2 – Ag <sub>2</sub> S Phase	Peak 3 – Impurity Phase
Z	1967	992 – 100%		
AS	582		367 – 100%	
AIS	466		522 – 97.10%	5049 – 2.90% (InS <sub>2</sub> )
ZAS	1144	2117 – 100%	Hump at 400 nm	
ZAIS	1202	1343 – 89.70%		5376 – 3.30% (InS <sub>2</sub> ) 196 – 7.00% (In(OH) <sub>3</sub> )

due to the peak overlapping. In *ZAIS* compound nanocomposites, the particle distributions were referred in three different segments implying the formation of small percentage of tertiary phase impurities with reduced crystallite size. The Z-average, particle size and phase distribution of all samples are tabulated in Table 2.

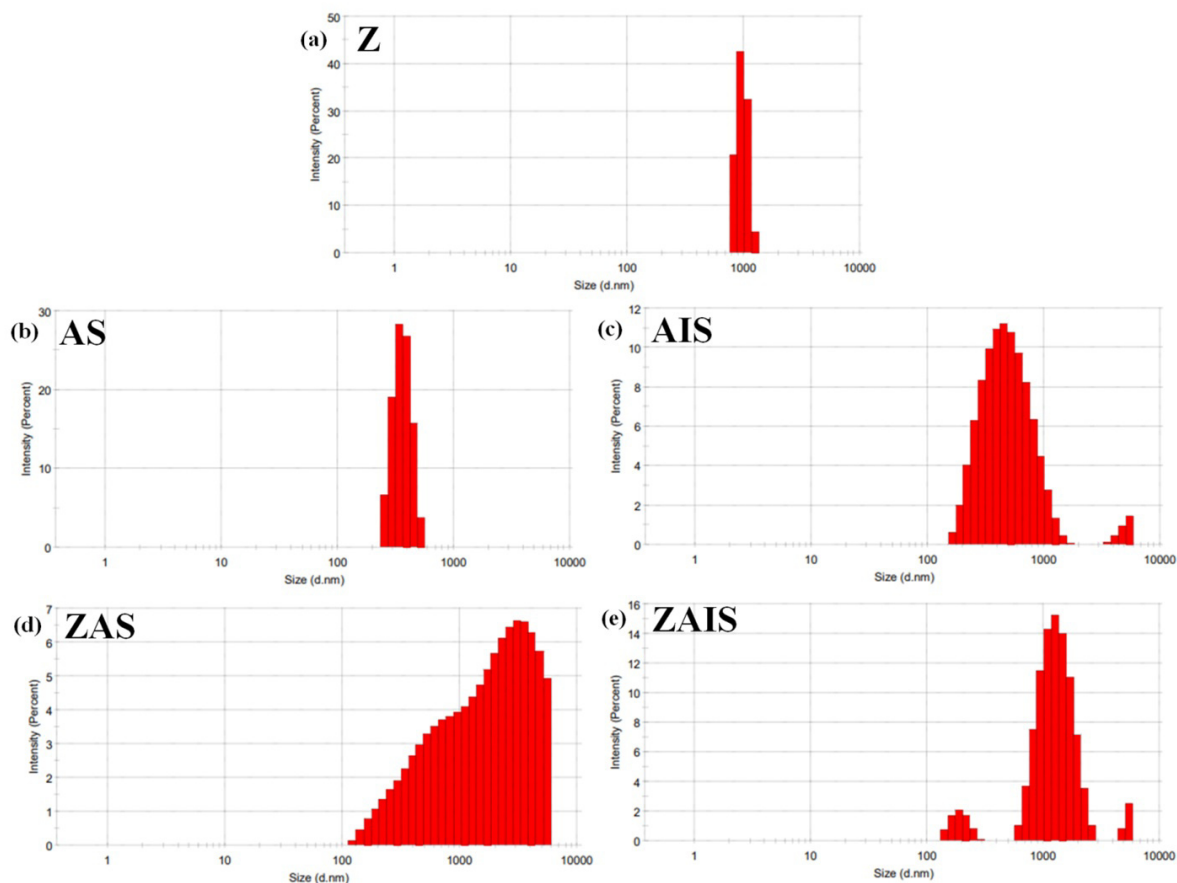


FIG. 6. The particle size distribution of Z, AS, AIS, ZAS, and ZAIS nanocomposites

### 3.3. Heat transfer mechanism

To evaluate the formation of secondary and tertiary phase impurities in the synthesized nanocomposites, the thermal decomposition study was performed by TG/DTA analysis where the samples were heated from room temperature to 800° at constant heating rate of 10°C/min in air and depicted in Fig. 7. All the samples exhibit similarity with host atom and dopant atom decomposition and the weight reduction is found to be low. While the maximum weight reduction of 29% is observed for the *ZAIS* due to the existence of residual phase materials present in the sample. Further, the occurrence of multistage decomposition beyond 400°C implies the process of crystallization and chemisorptions of intermediate molecules as inferred from the DTG curve. The DTG curve of *ZAIS* shows multiple sharp exothermic peaks revealing the thermal instability of as-synthesized samples.

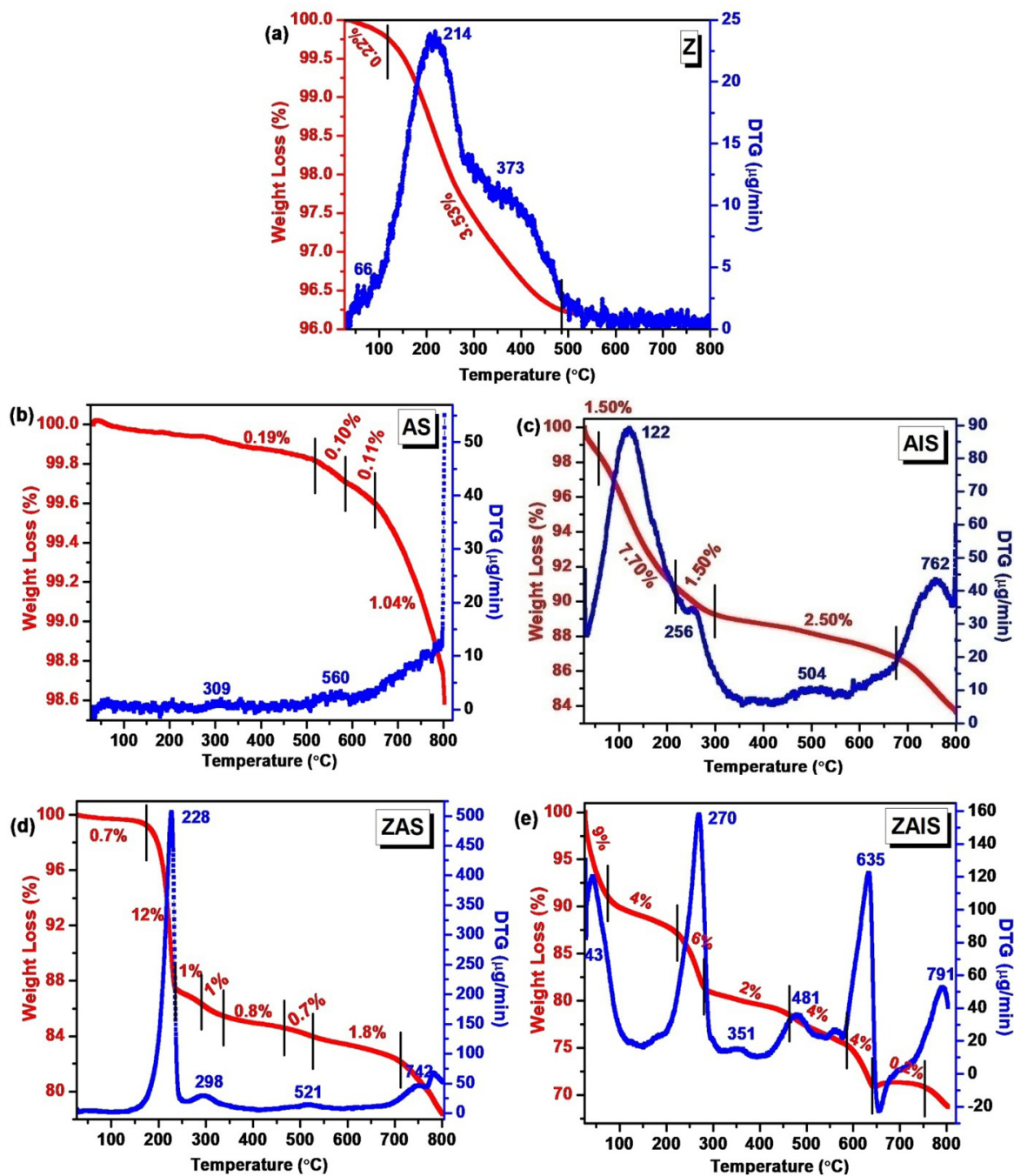


FIG. 7. The TG/DTG plot of (a) Z, (b) AS, (c) AIS, (d) ZAS, and (e) ZAIS nanocomposites

### 3.4. Morphological analysis

The typical SEM images of the ZnO nanoparticles were shown in Fig. 8(a) and Fig. 8(b). From the low and high magnified SEM micrographs, one can visualize the flower-like arrangement of ZnO nanostructures. Each petal of varying dimensions was assembled and architecture to form a flower-like arrangement. In high magnified SEM image shown in Fig. 8(b), the dimension of each petal was measured and was in the range of 400 nm to 720 nm. Few of the petals were immature and unable to form a complete flower-like structure. Here, the capping molecule PEG confine the growth and promote an anisotropic growth and, thus, resulting in unique morphology. The as-synthesized AS and AIS samples were nano-sized and non-homogeneous particle in nature and were displayed in Fig. 9 and Fig. 10. In Fig. 10(a-b), the nano-sized AS come closer to each other due to large surface area and forms an uneven oval, spherical and irregular structure. However, in Fig. 11(a-b), the degree of aggregation and agglomeration of AIS particles were higher than AS and, hence, distinct particle size and definite morphology cannot be assigned.

The SEM micrographs of ZAS and ZAIS compound nanocomposites synthesized by in-situ chemical precipitation method were portrayed in the Fig. 11 and Fig. 12, respectively. The image in Fig. 11(a) and in Fig. 12(a) clearly pictures

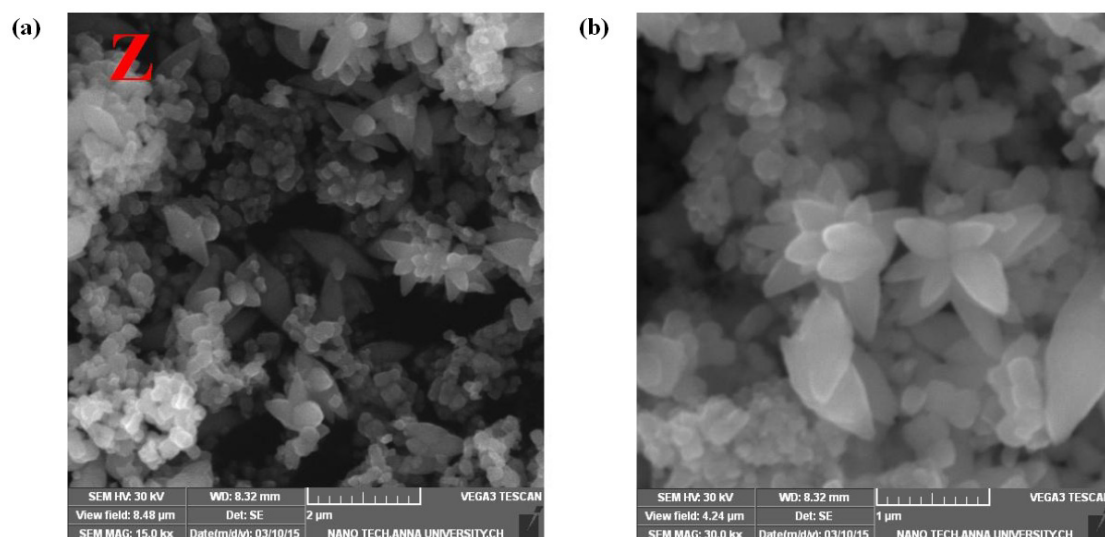


FIG. 8. (a) Low and (b) high magnified SEM micrographs of Z nanostructures

that the samples were composed of both particle and rod like structures implying the formation of blender mixtures. The rods were evolved from the ZnO nanostructures and particles were grown from the AS and AIS nanoparticles. A long solid ZnO nanorods were developed from flower-like ZnO nanostructure (Ref. Fig. 8(b)) and re-crystallized in *c*-axis as inferred from the XRD characterization depicted in the Fig. 5(a). The light sensitizer nano-sized AS particles occupy the ZnO surface, they hinder the multi-dimensional growth and promotes the 1D rod like structure. The AS particles were randomly distributed and aggregated certainly. However, the ZnO nanorods so formed in the ZAIS compound nanocomposites were shortened, flat and broken due to the Oswald ripening process and re-crystallization (Ref. Fig. 12(b)) [23]. As the activation energy of tertiary phase particles were dominant, the growth and formation of solid 1D ZnO nanorod were highly inhibited and, hence, broken, immature, crushed rods with reduced crystallite size  $d_{avg}$  were produced. The promptly nucleated nano-sized AIS particles densely adhere to the broken surface and get adsorb to the rod surface firmly and evenly than AS particles. Thus, an ordered flower-like arrangement was distorted during the formation of compound nanocomposites.

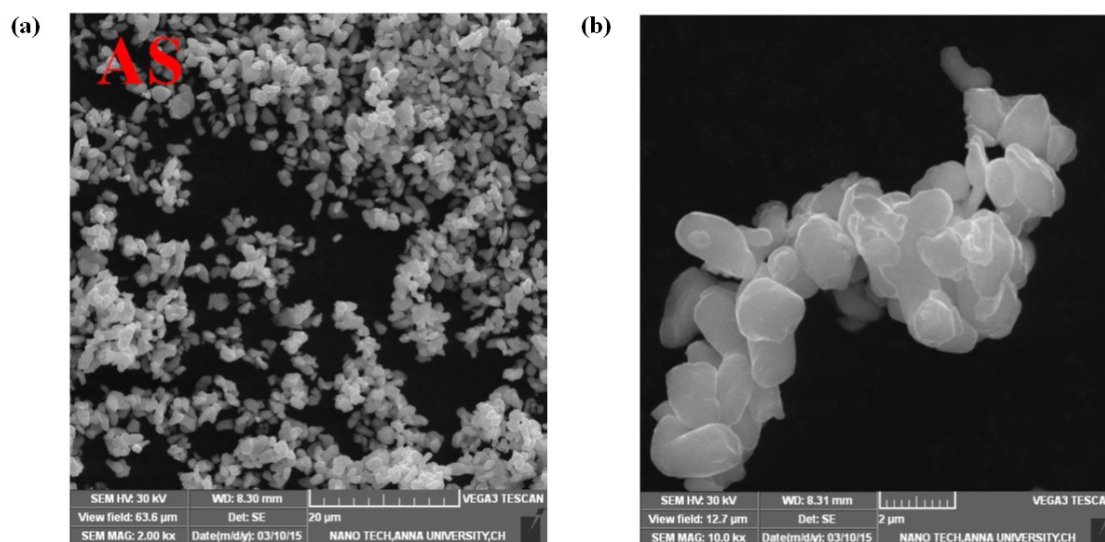


FIG. 9. (a) Low and (b) high magnified SEM micrographs of AS nanostructures

### 3.5. Diffuse Reflectance Spectroscopy

In adsorption study, room temperature UV-visible DRS spectra were recorded for the as-synthesized samples and were shown in Fig. 13. The ZnO nanostructures open a broad reflectance edge around 330 nm of wavelength. The nano-sized AS and AIS samples exhibit a narrowed reflectance with the onset of reflectance was found around 1220 nm. While

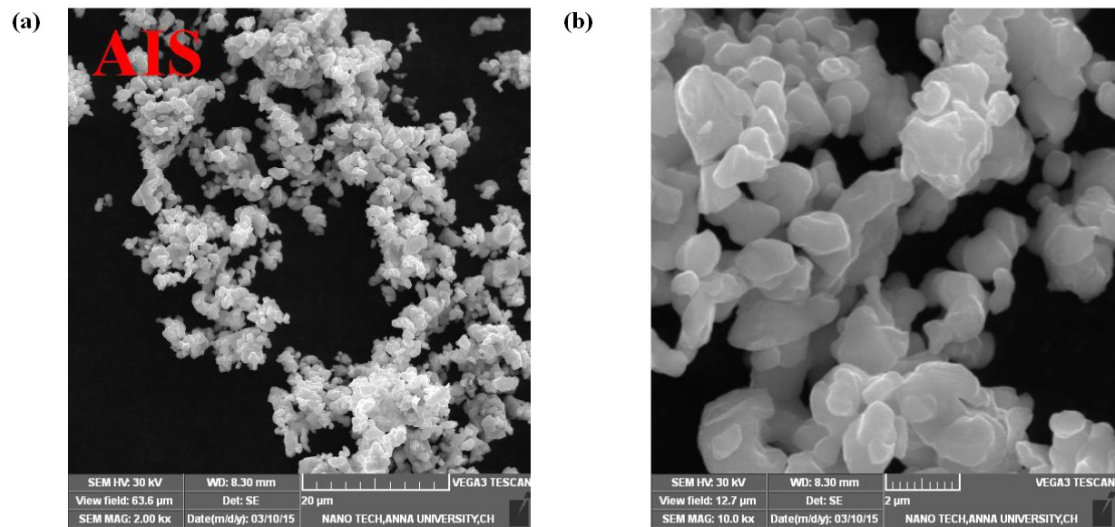


FIG. 10. (a) Low and (b) high magnified SEM micrographs of AIS nanostructures

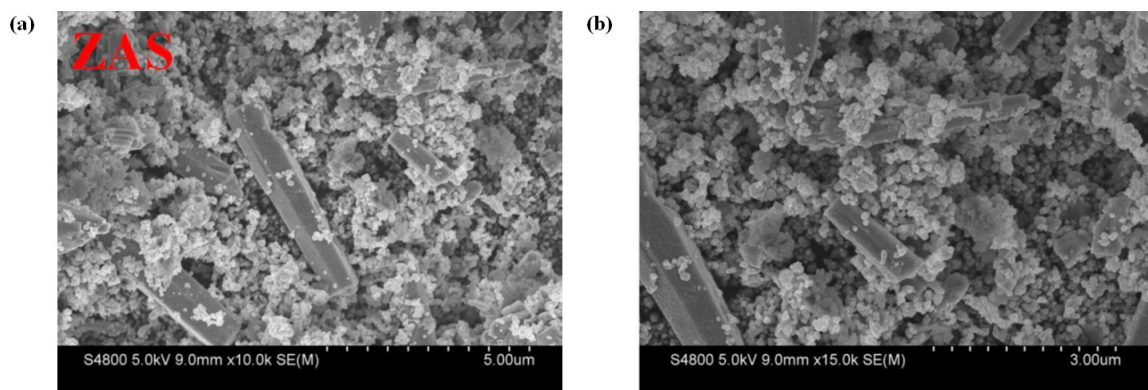


FIG. 11. (a) Low and (b) high magnified SEM micrographs of ZAS compound nanocomposites

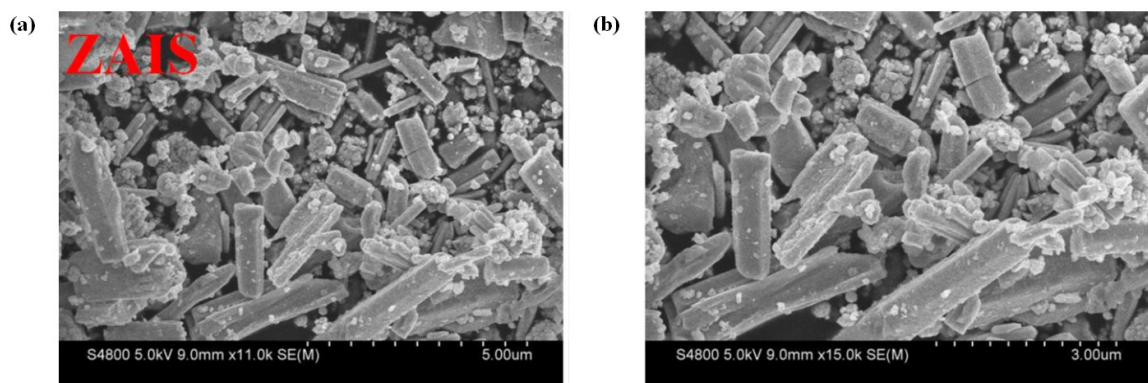


FIG. 12. (a) Low and (b) high magnified SEM micrographs of ZAIS compound nanocomposites

the compound nanocomposites, ZAS and ZAIS shows a reflectance commencing from 1100 nm. The sharp rise in the spectrum reveals the electronic band gap transition between the valence band and the conduction band.

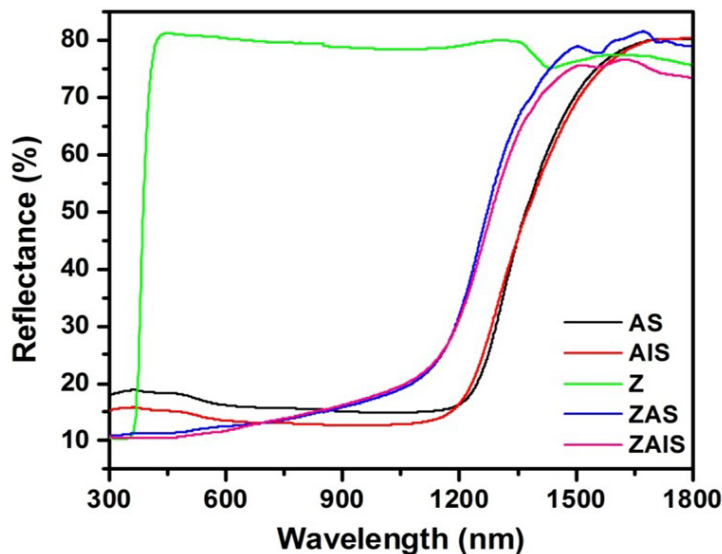


FIG. 13. The DRS spectra of Z, AS, AIS, ZAS and ZAIS nanocomposites

The optical band gap of the samples was derived from the Kubelka-Munk (K-M) function given by the equation  $F(R_{\infty}) = \frac{(1 - R_{\infty})^2}{2R_{\infty}} = \frac{k(\lambda)}{s(\lambda)} = \alpha = \frac{(h\nu - E_g)^{1/2}}{h\nu}$ . Here,  $F(R_{\infty})$  is the K-M function,  $R_{\infty}$  is the diffuse reflectance of an infinitely thick sample,  $k(\lambda)$  is the absorption coefficient,  $s(\lambda)$  is the scattering coefficient, and  $h\nu$  is the photon energy. The optical band gap  $E_g$  was obtained by extrapolating the linear portion of the curve plotted between  $[F(R_{\infty})(h\nu)]^2$  and energy in eV [24]. For pure zinc oxide, the line is extrapolated and intersects at 3.16 eV as seen from Fig. 14(a). While AS and AIS samples exhibit an almost similar optical band gap of 0.82 eV implying that the dopant indium was properly substituted in the host lattice site silver sulphide (Ref. Fig. 14(b)). However, in ZAS and ZAIS, a linear extrapolation appears at 0.91 eV and further, an elemental rise appears around 2.5 to 3 eV involving the convoluted band gap of ZnO. Thus, in the compound nanocomposites, the optical bandgap occupies the intermediate position of Z and light sensitizers and, thus, covering the UV, visible and infra-red regions of solar spectrum. As a result, an optical bandgap tuning required for the photo-excitation of electrons can be accomplished with the ZAS and ZAIS sensitized by AS and AIS light sensitizers for solar cell applications.

#### 4. Photovoltaic cell

The influence of light sensitizers AS and AIS in ZnO and the device performance were evaluated by the density-voltage ( $J$ - $V$ ) characteristics obtained using Keithley sourcemeter with  $100 \text{ mW cm}^{-2}$  AM 1.5 G solar illumination. The

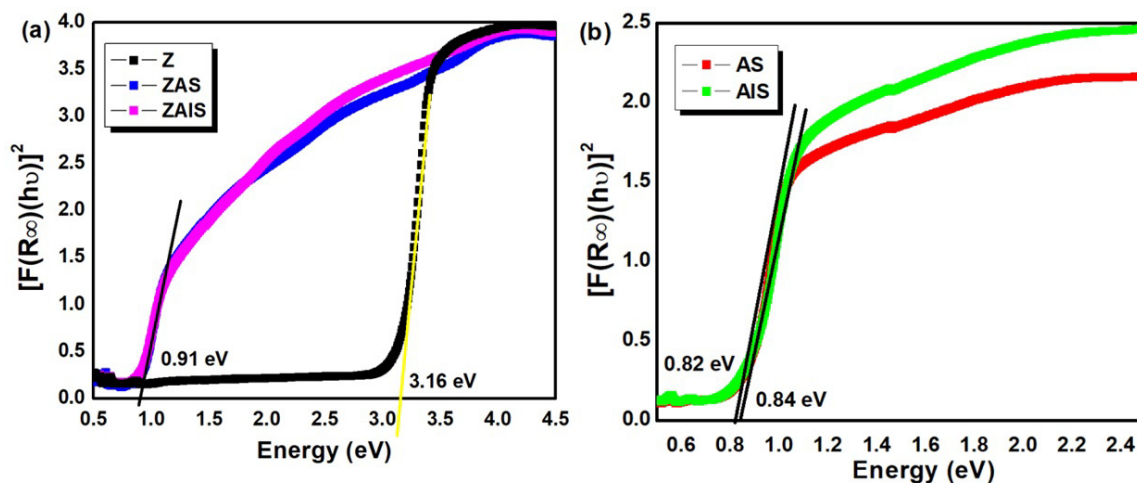


FIG. 14. Energy bandgap of as-synthesized (a) Z, ZAS, ZAIS nanocomposites and (b) AS, AIS samples

PV cell parameters of the devices, including the  $J_{sc}$ ,  $V_{oc}$ , and  $FF$  values were calculated. In assembling the PV cell, sol-gel processed spin coating and successive ionic layer adsorption and reaction (SILAR) method were adopted for the film growth as prescribed in our earlier work [25]. To evaluate the role of light sensitizers and the  $In^{3+}$  metal ion, two different combinations of  $pn$ -junction based PV cells were designed. The first device composed of ZAS and the second with the ZAIS as  $n$ -type layer and Rose Bengal (RB) as  $p$ -type layer. Both the layers were successively spin coated on the ITO coated glass substrate. Finally, a proper Ohmic contact was established on the  $n$ -type material and  $p$ -type material by the selective etching of ITO substrate and DC sputtering of Au electrode respectively. The schematic model of PV device architecture and the device performance for ZAIS was illustrated in Fig. 15. An interface is formed between the RB and ZnO based nanocomposites. When solar light energy was absorbed by the junction, free charge carriers were generated and transported by means of driving force due to in-built electric field. The presence of nano-sized light sensitizers and the energy band matching of RB and nanocomposites, promoted more photons adsorption and transportation and thereby, inducing more current flows.

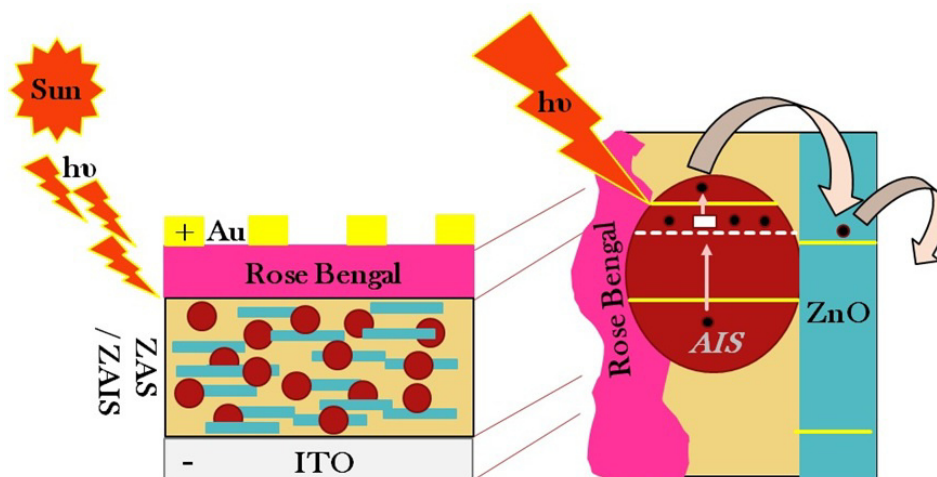


FIG. 15. The schematic model of photovoltaic device and working of ZAIS composed  $pn$  junction PV cell

The coating thickness of the hetero-layer ( $p$ -layer and  $n$ -layer) was visualized and measured from the cross-section SEM images of the ITO coated glass substrate as portrayed in Fig. 16(a) and Fig. 16(b). The chemical coating process resulted in dense overlapped coating with the thickness approaching  $120 \mu\text{m}$  and the individual layer was not recognized.

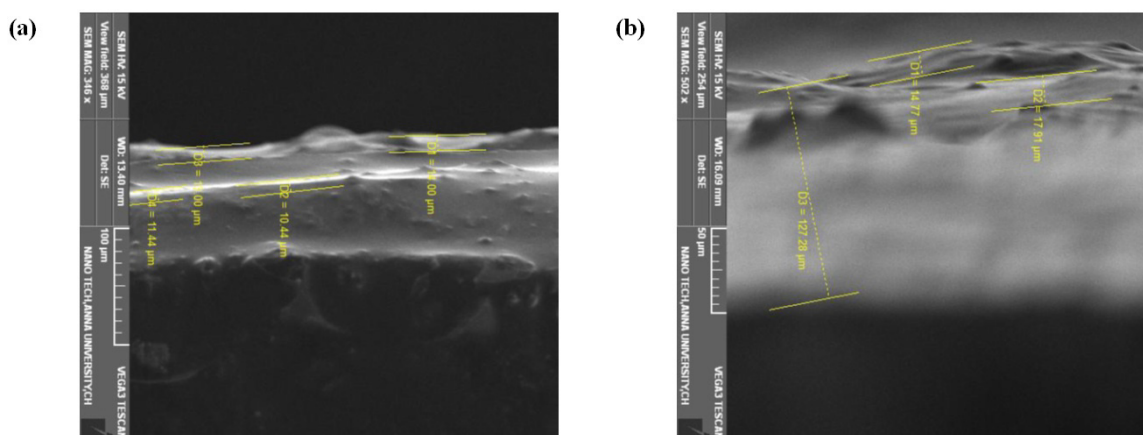


FIG. 16. The (a) cross-sectional images and (b) the approximate thickness measurement of assembled PV cell

#### 4.1. J-V characteristics

The PV cell composed of ZAIS exhibited a higher efficiency of 1.2% evaluated against ZAS of 0.76% as revealed from Fig. 17(a) and Fig. 17(b). For the PV device applications, the  $pn$ -junction should promote facile charge transport which can be achieved by the incorporation of transition metal dopant  $In^{3+}$  ions.

In comparison with ZAS, the obtained results in ZAIS nanocomposites can be addressed by the following causes. In ZAIS, the structure of ZnO was strained and modified by the inclusion of indium incorporated  $Ag_2S$  nanoparticles which

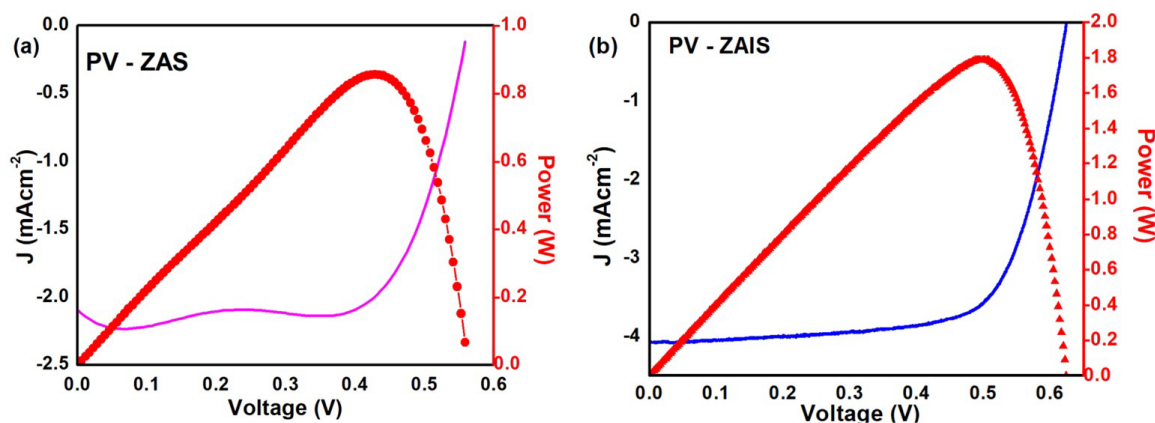


FIG. 17. Current density and voltage characteristics and power calculation of PV cells composed of (a) ZAS and (b) ZAIS compound nanocomposites

TABLE 3. Solar cell parameters of ZAS and ZAIS composed *pn* junction PV devices

PV devices	$V_{OC}$ (V)	$J_{SC}$ (mA/cm <sup>2</sup> )	$FF$ %	$\eta$ (no unit)
RB / ZAS	0.56	2.70	50.00	0.76
RB / ZAIS	0.62	4.00	50.00	1.20

resides either at the lattice sites or on the surface of ZnO and, therefore, leads to the formation of defects (tertiary phase impurities). The strained region of ZnO lattice exhibits higher chemical reactivity and consequently easy displacement of electron density from the lattice plane. This surface alteration and intact adherence of nano-sized indium incorporated Ag<sub>2</sub>S nanoparticles on the ZnO surface render facile and rapid charge transfer within the device. In addition, the size quantized AIS nanoparticles with optical band gap of 0.91 eV was included to absorb wide range of the solar spectrum and the nanoscale mixing of AIS nanoparticles into the ZnO matrix increased the interfacial area and promoted large number of excitons per incident photon. The above factors, thus, simultaneously control the  $J_{sc}$ ,  $V_{oc}$ , and  $\eta$  parameters of the PV device.

Table 3 summarizes the PV cell parameters obtained for the two devices. From the table, the high  $V_{OC}$  and  $J_{SC}$  values were mainly due to the incorporation of In<sup>3+</sup> metal ion with excess electrons and high conductivity respectively. The In<sup>3+</sup> ions occupy beneath the conduction band of Ag<sub>2</sub>S, donating the free electrons with low energy absorption and simultaneously transferring the excited electrons to the stable metal oxide ZnO due to its high conductivity. By this process, long lived more number of free electrons are transferred between the material compounds and, thus, increasing the current density  $J$  value from 2.7 mA/cm<sup>2</sup> in ZAS to 4.0 mA/cm<sup>2</sup> in ZAIS nanocomposites.

Though the choice of materials adopted for PV cell designing were preferable, the calculated efficiency was still not appreciable and the cause might be due to the tertiary phase impurities resulting in higher series resistance existing in the junction. The current-voltage  $I$ - $V$  equation for the *pn* junction is given by  $V_{OC} = \frac{k_B T}{e} \ln \frac{I_{ph}}{I_{sO}}$  [26]. In single junction ZAIS PV cell, the low efficiency was attributed to the defect induced recombination loss due to the existence of tertiary phase material. In addition, the thermalization loss further suppress the efficiency as residual intermediate phase materials were present which was evident from the TGA/DTA curve. In future work, an optimized synthesis method will be followed to furnish the higher efficiency.

## 5. Conclusions

In summary, we have established a simple wet chemical process nano-sized Ag<sub>2</sub>S and In<sup>3+</sup> metal ion incorporated Ag<sub>2</sub>S method to enhance the light adsorption and light energy conversion for PV application. The improvement was attributed to the maximum light absorption in the visible and infra-red regions of the solar spectrum offered by the low optical bandgap Ag<sub>2</sub>S and facile charge transport which arises from the high conductive indium metal ion in Ag<sub>2</sub>S nanoparticles along with the 1D ZnO nanorods. The present work initiates the advantage of nano-sized AS and AIS inclusion in ZnO for PV application and with the proper device organization it would paves the way towards the high efficient PV cell.

## References

- [1] Ahmet Z.S., Mohammed Ayaz U., Bekir S.Y., Abdullah A.S. Performance enhancement of solar energy systems using nanofluids: An updated review. *Renew. Energy*, 2020, **145**, P. 1126–1148.
- [2] Selvakumar P., Muthukumarasamy N., Agilan S., Vijayshankar A., Akila Y., Venkatraman M.R., Senthilarasu S., Dhayalan V. A review on the classification of organic / inorganic / carbonaceous hole transporting materials for perovskite solar cell application. *Arab. J. Chem.*, 2020, **13**, P. 2526–2557.
- [3] Zahra S. Recent progress in development of diverse kinds of hole transport materials for the perovskite solar cells: A review. *Renew. Sust. Energy Rev.*, 2020, **119**, P. 109608–109646.
- [4] Zinab H.B., Qamar W., Azhar F., Lukas Schmidt M., Thomas M., Rajan J. Advances in hole transport materials engineering for stable and efficient perovskite solar cells. *NanoEnergy*, 2017, **34**, P. 271–305.
- [5] Ambalika S., Rahul S., Nishat B., Asha Kumari. Review on synthesis, characterization and applications of silver sulphide quantum dots. *J. Mat. Sci. Res. Rev.*, 2021, **7**(3), P. 42–58.
- [6] Anjana V.N., Majo J., Sijo F., Alex J., Ebey P. Koshy, Beena M. Microwave assisted green synthesis of silver nanoparticles for optical, catalytic, biological and electrochemical applications. *Artif. Cells Nanomed. Biotechnol.*, 2021, **49**, P. 438–449.
- [7] Auttasit T., Kun-Lun W., Hao-Yu T., Ming-Way L., Gou Jen W. Ag<sub>2</sub>S quantum dot-sensitized solar cells. *Electrochem. Commun.*, 2010, **12**, P. 1158–1160.
- [8] Nurul Syafiqah M., Suhaila S., Norasikin Ahmad L., Asri Mat Teridi M., Adib Ibrahim M. Effect of silver sulphide (Ag<sub>2</sub>S) layer towards the performance of copper indium sulphide (CuInS<sub>2</sub>) quantum dots sensitized solar cell. *Int. J. Nanotechnol.*, 2021, **17**, P. 795–806.
- [9] Hanlin H., Mriganka S., Xuejuan W., Jiaoning T., Chih-Wei C., Gang L. Nucleation and crystal growth control for scalable solution-processed organic–inorganic hybrid perovskite solar cells. *J. Mater. Chem. A*, 2020, **8**, P. 1578–1603.
- [10] Yaokang Z., Sze-Wing N., Xi L., Zijian Z. Solution-processed transparent electrodes for emerging thin-film solar cells. *Chem. Rev.*, 2020, **120**, P. 2049–2122.
- [11] Mingxia J., Yun L., Chenxi L., Hao B., Liting G., Peng C., Xiliang L. Strongly emitting and long-lived silver indium sulphide quantum dots for bioimaging: Insight into co-ligand effect on enhanced photoluminescence. *J. Colloid Interface Sci.*, 2020, **565**, P. 35–42.
- [12] Taro U., Kazutaka W., Dharmendar Kumar S., Shuzo H., Takahisa Y., Tatsuya K., Martin V., Tsukasa T., Susumu K. Narrow band-edge photoluminescence from AgInS<sub>2</sub> semiconductor nanoparticles by the formation of amorphous III–VI semiconductor shells. *NPG Asia Mater.*, 2018, **10**, P. 713–726.
- [13] Jilu C.J., Tina S., Sunny M., Shaji S., Augustine S. Investigations on the properties of indium sulphide – Graphene nanocomposites thin films. *Thin Solid Films*, 2020, **695**, P. 137758–137772.
- [14] Jingjing Z., Hou W., Xingzhong Y., Guangming Z., Wenguang Tu Sibow. Tailored indium sulphide-based materials for solar-energy conversion and utilization. *J. Photoch. Photobio. C: Photochem. Rev.*, 2019, **38**, P. 1–26.
- [15] Mohammed Hamed S.G., Michael A.A., Yong Z., Genene Tessema M. Silver sulphide nano-particles enhanced photo-current in polymer solar cells. *Appl. Phys. A*, 2020, **126**, P. 207–214.
- [16] Mohammad Istiaque H. Prospects of CZTS solar cells from the perspective of material properties, fabrication methods and current research challenges. *Chalcogenide Lett.*, 2012, **9**, P. 231–242.
- [17] Zhe X., Jihuai W., Yuqian Y., Zhang L., Jianming L. High-efficiency planar hybrid perovskite solar cells using indium sulphide as electron transport layer. *ACS Appl. Energy Mater.*, 2018, **1**, P. 4050–4056.
- [18] Asim G., Amlan J. Pal. Copper-diffused AgInS<sub>2</sub> ternary nanocrystals in hybrid bulk-heterojunction solar cells: Near-infrared active nanophotovoltaics. *Appl. Mater. Interfaces*, 2013, **5**, P. 4181–4189.
- [19] Anusit K., Pisist K., Takashi S. Silver-indium-sulphide quantum dots in titanium dioxide as electron transport layer for highly efficient and stable perovskite solar cells. *J. Mater. Sci.: Mater. Electron.*, 2019, **30**, P. 4041–4055.
- [20] Dan H., Peng S., Huihui Z., Huihui Y., Qi X., Zhongxi Y., Qi W. Flower-like In<sub>2</sub>O<sub>3</sub> hierarchical nanostructures: synthesis, characterization, and gas sensing properties. *RSC Adv.*, 2014, **4**, P. 50241–50248.
- [21] Jiayong G., Xihong L., Jingheng W., Shilei X., Teng Z., Minghao Y., Zishou Z., Yanchao M., Shing Chi Ian W., Yong S., Yexiang T. Oxygen vacancies promoting photoelectrochemical performance of In<sub>2</sub>O<sub>3</sub> nanocubes. *Sci. Rep.*, 2013, **3**, P. 1–7.
- [22] Mingxia J., Yun L., Chenxi L., Hao B., Liting G., Peng C., Xiliang L. Strongly emitting and long-lived silver indium sulphide quantum dots for bioimaging: Insight into co-ligand effect on enhanced photoluminescence. *J. Colloid Interface Sci.*, 2020, **565**, P. 35–42.
- [23] Yuqiang Y., Jihuai W., Xiaobing W., Qiyao G., Xuping L., Weihai S., Yuelin W., Yunfang H., Zhang L., Miaoliang H., Jianming L., Hongwei C., Zhanhua W. Suppressing vacancy defects and grain boundaries via Oswald ripening for high-performance and stable perovskite solar cells. *Adv. Mater.*, 2020, **32**, P. 1904347.
- [24] Dhanabal R., Chithambararaj A., Velmathi S., Chandra Bose A. Visible light driven degradation of methylene blue dye using Ag<sub>3</sub>PO<sub>4</sub>. *J. Environ. Chem. Engg.*, 2015, **3**, P. 1872–1881.
- [25] Rajeswari Yogamalar N., Sadhanandam K., Chandra Bose A., Jayavel R. Quantum confined CdS inclusion in grapheme oxide for improved electrical conductivity and facile charge transfer in hetero-junction solar cell. *RSC Adv.*, 2015, **5**, P. 16856–16869.
- [26] Markus D., Thathit S., Arif H., Ahmad T., Abdulloh F., Risa S. Shockley's equation fit analyses for solar cell parameters from I-V curves. *Int. J. Photoenergy*, 2018, **2018**, P. 1–7.

---

*Submitted 27 September 2022; revised 17 March 2023; accepted 11 June 2023*

*Information about the authors:*

**K. Abinaya** – Doctoral Researcher, London South Bank University, London SE1 0AA, UK

**P. Sharvanti** – Senior Process Engineer, Research and Development, Saint Gobain, San Diego, California 92123, USA

**N. Rajeswari Yogamalar** – Department of Physics, Hindustan Institute of Technology and Science, Padur, Kelambakkam, Chennai – 603103, India; ORCID 0000-0002-4954-6552; rajeswariyogamalar.n@gmail.com

**Conflict of interest:** the authors declare no conflict of interest.

## Structural, electrical, optical and phase investigation of perovskite barium zirconate (BaZrO<sub>3</sub>) nanoparticles prepared through auto-combustion technique

J. Abimalar<sup>1,2</sup>, V. Anslin Ferby<sup>1,2</sup>

<sup>1</sup>Department of Physics and Research Centre, Scott Christian College (Autonomous), Nagercoil – 629 003, Tamil Nadu, India

<sup>2</sup>Manonmaniam Sundaranar University, Abishekapatti, Tirunelveli – 627 012, Tamil Nadu, India

Corresponding author: J. Abimalar, [jabimalar98@gmail.com](mailto:jabimalar98@gmail.com)

**ABSTRACT** The BaZrO<sub>3</sub> ceramics were prepared via sol-gel auto-combustion technique with three Fuel to Oxidant (F/O) ratios ( $\varphi = 0.5, 1.0$  and  $1.5$ ) and annealed at 1200 °C for 2 hours. X-ray diffraction (XRD) and Rietveld refinement data confirmed the cubic perovskite phase with the Pm $\bar{3}$ m (221) space group. These three samples are well indexed in JCPDS no: 06-0399. The ratio  $F/O = 1.0$  gives one a small crystallite size and very high surface area. The ratio  $F/O = 1.5$  provides a very high crystallite size and very low dislocation density. The oxygen vacancies in the samples were analyzed using Raman spectroscopy. The optical band gap energy value increases from 2.02 to 3.09 eV with increasing  $F/O$  ratio. Using of impedance spectroscopy for BaZrO<sub>3</sub> at room temperature allows us to reveal decreasing ionic conductivity with an increasing  $F/O$  ratio. The Nyquist plot for all samples exhibits a circular arc in the high-frequency zone and nearly a straight line in the low-frequency region. Due to the presence of low grain boundary with high ionic conductivity the BaZrO<sub>3</sub> electrolyte material is used for energy storage in devices.

**KEYWORDS** nanoparticle, combustion synthesis, X-ray diffraction technique, Rietveld refinement analysis, FT-Raman spectroscopy, UV-vis absorption spectrum, impedance

**FOR CITATION** Abimalar J., Anslin Ferby V. Structural, electrical, optical and phase investigation of perovskite barium zirconate (BaZrO<sub>3</sub>) nanoparticles prepared through auto-combustion technique. *Nanosystems: Phys. Chem. Math.*, 2023, **14** (4), 467–478.

### 1. Introduction

BaZrO<sub>3</sub> is a cubic perovskite with a structure ABO<sub>3</sub>. Because of its unusual physical properties, BaZrO<sub>3</sub> is attractive for usage in electro-ceramics [1]. BaZrO<sub>3</sub> (BZO) is an ideal model for a wide range of ABO<sub>3</sub> perovskite. They have different technical applications, including high-temperature materials, electronic ceramics, nonlinear optics, catalysis, superconductors, etc. [2–7]. Barium Zirconate is an alkaline earth perovskite with significant electro-ceramic potential [8–10]. High proton conductivity and green-blue emission are the advantages of a structurally disordered vacancy in the BaZrO<sub>3</sub> semiconductor [8, 11].

The perovskite materials are used for capacitors, nonvolatile memory, actuators, sensors, piezoelectric, ultrasonic, underwater devices, high-temperature heating applications, frequency filters for wireless communications, and other applications [12–15]. Barium zirconate (BaZrO<sub>3</sub>) has significant economic and technological importance because of its properties such as a “high melting point (2920 °C), poor thermal conductivity, remarkable mechanical and structural integrity under intense heat conditions, strong protonic conductivity, etc. [12–17]”. BaZrO<sub>3</sub> is a photoluminescence (PL) material with low cost and good environmental performance that emits light in the visible spectrum [18]. BaZrO<sub>3</sub> ceramics also have exceptional dielectric characteristics, making them a good choice for microwave and wireless communication applications [9, 10]. BaZrO<sub>3</sub> can be formed by several methods: hydrothermal [20], ceramic [21], co-precipitation [22], etc.

Advanced ceramics, catalysts, and nanomaterials are prepared by a simple and practical combustion synthesis process [23]. Based on the propellant chemistry concepts used in this technique [24], a redox reaction involves the interaction of an oxidant and a fuel. Various types of combustion synthesis differ mainly in the reactants or burning method [23, 25–29]. For comparison, conventional techniques like solid-state synthesis and combustion-based methods, nitrate methods may generate monophasic nanopowders with homogeneous microstructure at lower temperatures or faster reaction times [30–33]. A commonly used solution combustion process is called citrate-nitrate auto-combustion synthesis (CNA) [34–36]. Metal nitrates are used as oxidants, and citric acid as fuel. The well-known Pechini approach and the CNA method are similar in many ways [37, 38]. “Sol-gel combustion method” is more efficient [39]. However, the CNA approach varies from the Pechini process in which the nitrates are not first removed as NO<sub>x</sub> but remain with the metal citrates that ignite the auto-combustion.

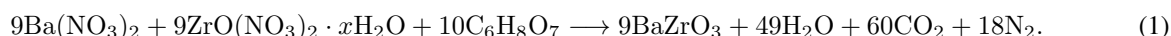
BaZrO<sub>3</sub> nanoparticles obey good electrical properties and high ionic conductivity. Nowadays researchers are mainly focused on developing energy storage devices. To enhance the efficiency of materials, researchers are working on combining transition metal oxides (TMOs) with other transition metals, metal oxides, ABO<sub>3</sub> or BO<sub>2</sub>-type materials, etc. These materials can modify the surface area, pore characteristics, ion intercalation/ deintercalation, conductivity etc. TMO is an efficient electrode material, especially in supercapacitors and solar cell applications. Peng-Jian Wang et al. worked with BaTiO<sub>3</sub>-Bi(Li<sub>0.5</sub>Nb<sub>0.5</sub>)O<sub>3</sub> nanocomposites. From the result, the maximum energy density obtained is 14.2 J/cm<sup>3</sup> at 497 mv/m. This simple filler preparation method provides a universal and best technical approach for high energy density capacitors. It is the successful application of universal nanocomposites [40]. Recently, hexaferrites reported to possess a spontaneous electrical polarization at room temperature [41].

In this research work, citric acid is chosen as fuel, because it has good complexing ability, low ignition temperature (200 – 250 °C) and controlled combustion reaction with nitrates. In this paper, the synthesis and characterization of BaZrO<sub>3</sub> nanoparticles with various *F/O* ratios through the “sol-gel auto-combustion method” was reported.

## 2. Experimental procedure

### 2.1. Synthesis of BaZrO<sub>3</sub> nanoparticles

Citric acid (C<sub>6</sub>H<sub>8</sub>O<sub>7</sub>) was chosen as the fuel, and Ba(NO<sub>3</sub>)<sub>2</sub> (barium nitrate) and ZrO(NO<sub>3</sub>)<sub>2</sub> · *x*H<sub>2</sub>O (zirconium (IV) oxynitrate hydrate) were used as sources of cations and oxidants [42]. Gravimetric analysis revealed that ZrO(NO<sub>3</sub>)<sub>2</sub> · *x*H<sub>2</sub>O has a hydration level (*x*) of 1. Metal-Nitrate solution prepared by dissolving stoichiometric weighed Ba(NO<sub>3</sub>)<sub>2</sub> and ZrO(NO<sub>3</sub>)<sub>2</sub> · *x*H<sub>2</sub>O separately in deionized water. This stage gave rise to a clear solution indicating total dissolution. NH<sub>4</sub>OH was added drop by drop and adjusted the pH 7 using a pH meter. After heating the combination of ammonia and the neutralized solution to 80 °C on a hot plate and continuously stirring, the two components evaporated to dryness. The solution became more viscous as the water evaporated, forming the extremely viscous gel. The gel ignited temperature raised to 100 – 120 °C. The dried gel burned to create a soft powder. The following equation represents the combustion reaction:



For the formation of phase pure Barium Zirconate nanoparticles, the following procedure is used. The resultant ash powder is dried and crushed for annealing purposes. ‘Indfurr furnaces’ were used for annealing. Time profile controllers will allow the feed to a set 1200 °C temperature and hold for two hours at the particular setting temperature. The heating and cooling rate is 10 °C/min and the annealing temperature is 1200 °C. It helps us to reduce the secondary phase of BaCO<sub>3</sub>.

Lattice constant is obtained by the following equation

$$\frac{1}{d_{hkl}^2} = \frac{h^2 + k^2 + l^2}{a^2}. \quad (2)$$

The average lattice constant, determined using the previously mentioned calculation, is  $a = 4.17 \text{ \AA}$ . This estimated lattice constant value agrees well with the reference data,  $a = 4.19 \text{ \AA}$  [43].

Applying Scherer’s formula, the full width at half maximum (FWHM) of the high-intensity peak (110) is used to calculate the crystallite size:

$$D = \frac{k\lambda}{\beta \cos \theta}, \quad (3)$$

where  $D$  denotes the crystallite size in nanometres,  $k$  ( $k = 0.83$ ) is the instrumental constant,  $\lambda$  denotes the wavelength of X-ray radiation in nanometres,  $\theta$  denotes the Bragg angle in radians and  $\beta$  denotes the FWHM in radians. The most fundamental feature of the solid-state structure is the unit cell volume ( $V$ ).

The density of the prepared nanoparticles ( $\rho_x$ ) is calculated using the relation

$$\rho_x = \frac{ZM}{N_A V} \text{ g/cm}^3, \quad (4)$$

where  $Z$  is the number of formula units in the unit cell ( $Z = 1$ ),  $M$  is the molecular mass of the sample and  $N_A$  is Avogadro’s number.

The microstrain of the prepared nanoparticles ( $\varepsilon$ ) is calculated from the equation,

$$\varepsilon = \frac{1}{\sin \theta} \left[ \frac{\lambda}{D} - \beta \cos \theta \right], \quad (5)$$

where  $\beta$  is the full-width at half-maximum of the (110) peak and  $D$  is the average grain size.

The length of the dislocation lines per unit volume of the crystal is called the dislocation density [44]. Dislocations are defects in crystals caused by incorrect lattice registration in the surface area of the crystal. Dislocations are not equilibrium

defects to explain their presence in the measured dislocation densities, unlike vacancies and interstitial atoms [45–47]. In this case, dislocation density ( $\delta$ ) is calculated using the relation [48].

$$\delta = \frac{1}{D^2}, \quad (6)$$

where,  $\delta$  is the dislocation density and  $D$  is the particle size (nm).

The following formula is used to determine the surface area of the nanoparticles [49]:

$$S = \frac{6}{\rho \cdot D} \text{ cm}^2/\text{g}, \quad (7)$$

where  $S$  is the surface area,  $\rho$  is the density and  $D$  is the grain or crystallite size. All the calculated lattice parameters of the BaZrO<sub>3</sub> nanoparticles prepared for three  $F/O$  ratios were listed in Table 1.

TABLE 1. Calculated lattice parameters of BaZrO<sub>3</sub> nanoparticles

Parameters/sample	$F/O = 0.5$	$F/O = 1.0$	$F/O = 1.5$	Standard Values
Lattice constant ( $\text{\AA}$ )	4.1778	4.1642	4.1757	4.19
Unit cell volume $V(\text{\AA}^3)$	72.92	72.21	72.81	73.72
Crystallite size $D$ (nm)	49	47	72	—
Density ( $\rho$ ) $\text{g/cm}^3$	6.296	6.357	6.304	6.22
Dislocation Density ( $\times 10^{14}$ ) Lines/metre	4.21	4.5	1.9	—
Surface area ( $S$ ) $\times 10^6 \text{ cm}^2/\text{g}$	19.56	20.02	13.16	—
Micro strain ( $\varepsilon$ ) $\times 10^{-3}$	2.0	2.1	1.3	—

### 3. Results and discussion

#### 3.1. X-ray diffraction (XRD) analysis

BaZrO<sub>3</sub> sample XRD patterns are displayed in Fig. 1. The sharp spikes indicated the crystallinity of the BaZrO<sub>3</sub> nanoparticles prepared for three  $F/O$  ratios.

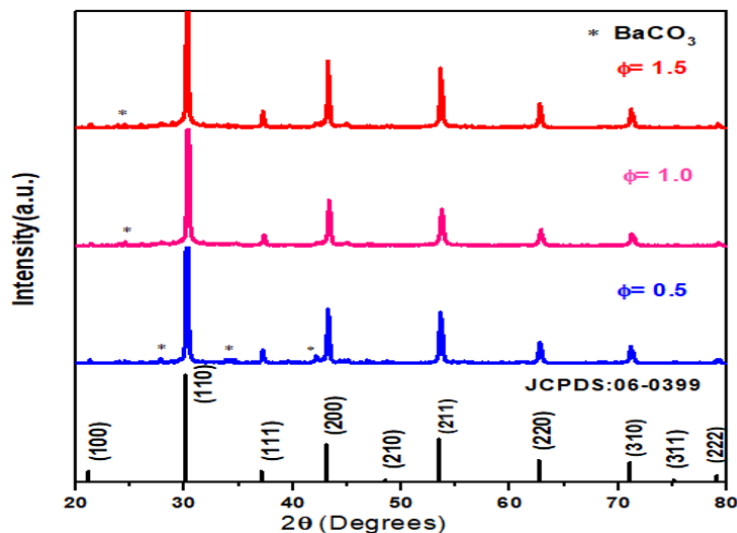


FIG. 1. The XRD pattern of BaZrO<sub>3</sub> samples prepared for three  $F/O$  ratios

These XRD patterns displayed seven main spikes of the BaZrO<sub>3</sub>, such as (110), (111), (200), (210), (211), (220) and (310) well matched with cubic structure (JCPDS-06-0399). Very small amount of BaCO<sub>3</sub> (\*) is presented at  $2\theta = 24, 28, 33, 42^\circ$ . It is due to the dissolution of CO<sub>2</sub> from the air in the water. Mojdeh Azzizi et al. studied yttrium doped barium zirconate using two types of fuel with three different annealing temperatures 900, 1150 and 1300 °C. As a result,

citric acid fuel take lesser time for combustion and 1150 °C annealed sample produces an almost phase pure BAYZ nanopowder [50].

Table 1 illustrates that the calculated average lattice constants  $a$ ,  $b$  and  $c$  values of BaZrO<sub>3</sub> nanoparticles suit the standard value.  $F/O = 1.0$  gives a small crystallite size, its surface area is very high.  $F/O = 1.5$  provides a very high crystallite size and very low dislocation density. FWHM (Full-width half maximum) value plays a major role in crystallite size. If the FWHM value increases, crystallite size should decrease. The unit cell volume and the density depend upon the lattice constant. The variation in the  $F/O$  ratio affects crystallite size. The release of additional gaseous products causes the crystallite size decreases by raising the  $F/O$  ratio from 0.5 to 1.0. High surface-to-volume ratio for grains decreases as excess heat is removed from the system [51]. The crystallite size increases from 41 to 63 with a further increase in the  $F/O$  ratio from 1.0 to 1.5. The increase in flame temperature of combustion that increases particle growth can be related to it [52]. The results indicated that the combustion-produced particle is nanocrystalline and has a size range of 47 – 72 nm.

### 3.2. Rietveld analysis

Every type of crystalline material can be fitted with patterns using the Rietveld refining method, and it is highly efficient but not accessible for single crystals [53, 54]. The technique results in the use of the fact that the peak shape of Bragg reflections can be mathematically defined as well as the fluctuations in their width (FWHM) with the scattering angle  $2\theta$ . The Rietveld method enables least-squares refinement [ $\chi^2$  minimization] of an atomic model (crystal structure parameters) combined with a proper peak shape function, i.e., a simulated powder pattern, directly towards the observed powder pattern without extracting structure factor or integrated intensities once the structure is known and a suitable starting model is discovered. The Rietveld refinements for accurate structural parameters and the profile parameters start once the structural model is complete and the background contribution contains proper starting values. The resulting profile fit and the reliability factor or  $R$ -value values both show the refinement's progress. Up to the fit converges the structure has to be improved. In order to get accurately estimated standard deviations, which may be expressed quantitatively in terms of reliability factors or  $R$ -values, all parameters (profile and structural) must be refined simultaneously [55].

To get precise standard deviation values, Chi-square ( $\chi^2$ ) reduction was used to refine all structural parameters. Diffraction intensity data were taken into consideration for the computation of standard deviations. The intensity values are typically written as  $I_{o,i}$ , where 'o' stands for the observed values and 'i' for the intensity measured at  $2\theta$  value  $2\theta_i$ . A model is fitted to the observed data in Rietveld analysis, and if the model is accurate, it will calculate the "true" intensity levels. The model-derived intensity values will be denoted as  $I_{c,i}$ , where 'c' stands for the computed model. The Rietveld algorithm optimizes the model function to minimize the weighted sum of squared differences between the observed and computed intensity values, i.e., to minimize  $\sum_i w_i [I_{c,i} - I_{o,i}]^2$ , where the weight, labeled as  $w_i$ , is  $1/\sigma^2[I_{o,i}]$  [55] and the expected value of  $\sum_i w_i [I_{c,i} - I_{o,i}]^2$  is one. This "best possible  $R_{wp}$ " quantity is a very useful concept and is called the expected  $R$  factor ( $R_{exp}$ ):

$$R_{wp} = 100 \left[ \frac{\sum_{i=1,n} w_i |I_i - I_{c,i}|^2}{\sum_{i=1,n} w_i I_i^2} \right]^{1/2} \quad (8)$$

The actual  $R_{wp}$  should aim to be close to the statistically expected  $R$  value,  $R_{exp}$ :

$$R_{wp} = 100 \left[ \frac{n - p}{\sum_{i=1,n} w_i I_i^2} \right]^{1/2}, \quad (9)$$

where  $n$  is the number of observations and  $p$  is the number of parameters.  $R_{exp}$  reflects the quality of data. Thus, the ratio between the  $R_{wp}$  and  $R_{exp}$  gives one the result of goodness of fit,

$$\chi^2 = \left[ \frac{R_{wp}}{R_{exp}} \right]^2 \quad (10)$$

The refined BaZrO<sub>3</sub> diffraction pattern is displayed in Fig. 2. It is the result of using various  $F/O$  ratios followed by the EXPO programme. The plots make it very clear that the fitting accuracy is excellent. The calculated patterns are displayed in the same field as a dense line curve. The bottom field displays the variation between the calculated and observed intensity.

The cubic structure of the BaZrO<sub>3</sub> ceramic has a space group (Pm $\bar{3}$ m) and point-group symmetry ( $O_h$ ). Furthermore, Zirconium (Zr) atoms produce [ZrO<sub>6</sub>] clusters with six oxygen (O) atoms, whereas Barium (Ba) atoms (lattice modifiers) make [BaO<sub>12</sub>] clusters with twelve O atoms in a Cuboctahedral shape. Zr atoms are positioned Centro-symmetrically within the octahedron in [ZrO<sub>6</sub>] clusters [56].

Table 2 contains the results for the lattice parameter, crystallite size,  $S$ ,  $\chi^2$  and  $R$ -values.

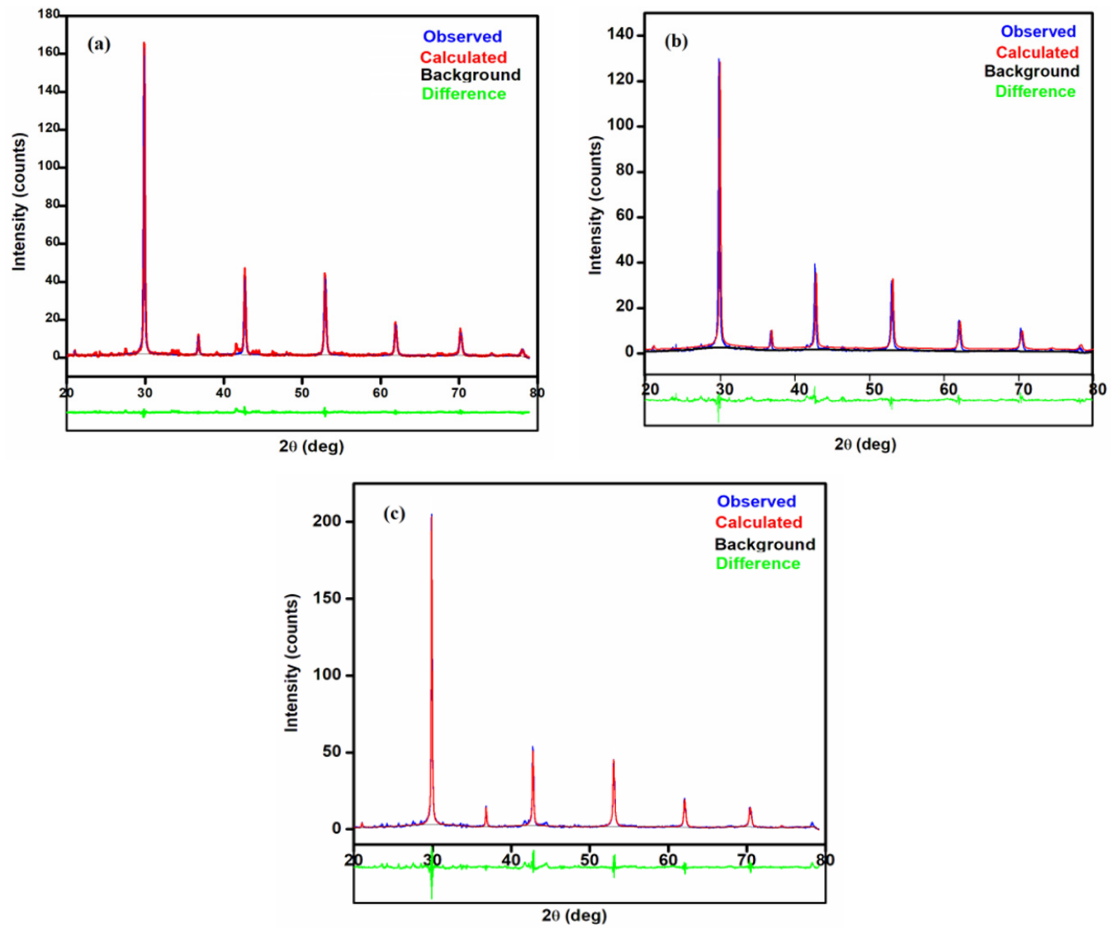


FIG. 2. Rietveld refinement output of the  $\text{BaZrO}_3$  samples for three various  $F/O$  ratios: (a)  $\varphi = 0.5$ , (b)  $\varphi = 1.0$ , (c)  $\varphi = 1.5$

TABLE 2. Rietveld refined data of  $\text{BaZrO}_3$  nanoparticles

$\text{BaZrO}_3$	Lattice Parameters	Crystallite size (nm)	Micro strain (%) ( $\times 10^{-3}$ )	Rietveld Refine Parameters
$\Phi = 0.5$	$a = b = c = 4.18 \text{ \AA}$ $\alpha = \beta = \gamma = 90^\circ$	49.32	0.357	$R_{wp} = 18.69$ $R_p = 12.84$ $R_e = 14.53$ $S = 1.29$
$\Phi = 1.0$	$A = b = c = 4.17 \text{ \AA}$ $\alpha = \beta = \gamma = 90^\circ$	42.73	0.547	$R_{wp} = 16.050$ $R_p = 11.452$ $R_e = 12.38$ $S = 1.30$
$\Phi = 1.5$	$a = b = c = 4.18 \text{ \AA}$ $\alpha = \beta = \gamma = 90^\circ$	58.41	0.129	$R_{wp} = 16.98$ $R_p = 12.57$ $R_e = 14.92$ $S = 1.14$

On comparing the results of crystallite size with the XRD result, after the Rietveld refinement the crystallite size decreases then increases and the microstrain is increased then decreased. It is happened because of the rise in temperature. In the range of 1.14 to 1.30, the fitted pattern's goodness of fit (GoF) values can be found.

### 3.3. Raman spectroscopy analysis

The Raman spectra of BaZrO<sub>3</sub> are shown in Fig. 3. Although the perfect cubic perovskite would be expected to exhibit, all samples showed evidence of numerous vibrational modes. Second-order scattering was responsible for the identification of active vibrational modes in barium zirconate with oxygen vacancies [57, 58]. However, since the band at 200 cm<sup>-1</sup> is connected to the torsional motion of the lattice, Karlsson et al. hypothesized that the spectrum comes from lattice distortions [59].

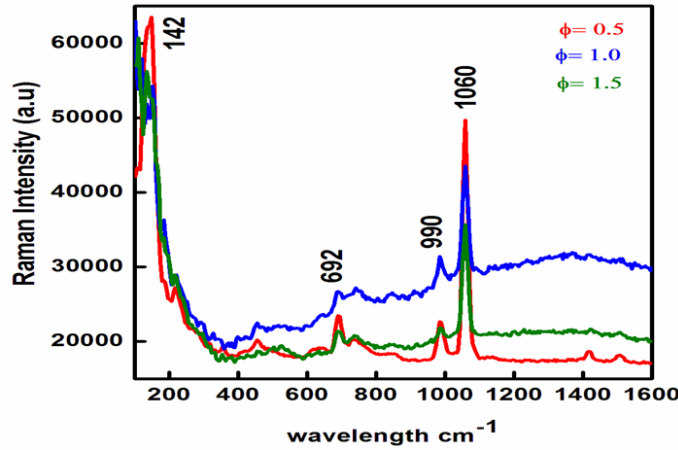


FIG. 3. FT RAMAN spectra of BaZrO<sub>3</sub> samples prepared for different  $F/O$  ratios

It is well known that BaZrO<sub>3</sub> with acceptor impurities, such as trivalent ions, leads to the formation of oxygen vacancies according to:



where  $M$  is the trivalent ion,  $V_{rmo}$  is the oxygen vacancy, and  $3O_o^X$  is the oxygen at oxygen site. Hereafter the Kröger-Vink notation is used for point defects. Nominally pure BaZrO<sub>3</sub> may still contain intrinsic acceptor impurities in the form of Ba-vacancies which naturally occur during sintering at high temperatures due to loss of Ba. When exposed to humid atmosphere, the incorporation of protons occurs in the form of hydroxyl group ( $OH^-$ ) that fills up the oxygen vacancies according to [60, 61]:



From Eq. (12), the two  $OH^-$  groups form after the reaction between water molecules and an oxygen vacancy.

Slodczyk et al. proposed that the active BZ Raman spectra are indicative of nano-domains with local symmetry that differs from that of the cubic structure, given the reality that the spectra include large bands and these distortions are supposed to be very minor [62, 63]. In simple terms, the majority of the bands are liked across all samples, only with some strength shifts or differences depending on composition. The translation oscillation modes from 50 to 250 cm<sup>-1</sup> are produced by the motions of the Ba<sup>2+</sup> network, which are dominated by the Coulomb interactions [62, 63].

While the peaks at higher frequencies indicate the modes of more covalently bonded oxygen octahedra, the peaks between 600 and 900 cm<sup>-1</sup> are explained by the symmetric stretching ( $V$ ) of oxygen bonds [62–64]. Furthermore, the BaCO<sub>3</sub> vibrational peak with the Raman shift of 1060 cm<sup>-1</sup> indicates the creation of carbonate (CO<sub>3</sub>) species [65].

### 3.4. UV-vis spectroscopy analysis

The UV-Vis absorbance spectrum of BaZrO<sub>3</sub> ceramics is shown in Fig. 4. The peak around 220 nm can be attributed to band edge absorption of BaZrO<sub>3</sub>. According to the method outlined by Wood and Tauc [66], the optical band gap energy ( $E_{gap}$ ) was calculated using the following equation:

$$(\alpha h\nu) = B (h\nu - E_{gap})^n, \quad (13)$$

where  $B$  is a band tailoring constant,  $n$  is a constant related to the various types of electronic transitions ( $n = 1/2, 2, 3/2$  or  $3$ ) for direct allowed, indirect allowed, direct forbidden, and indirect forbidden transitions, respectively [67],  $h$  is the Plank constant,  $\nu$  is the frequency,  $E_{gap}$  is the optical band gap, and  $\alpha$  is absorbance. In this instance, the indirect acceptable transition one is taken to be  $n = 2$ .

The Tauc plot of BaZrO<sub>3</sub> is shown in Fig. 5. for three  $F/O$  ratios ( $\varphi = 0.5, 1.0$  and  $1.5$ ). The band gap of the material, if it is a direct transition, as shown by the Tauc plots [68], is obtained by extrapolating the linear component of

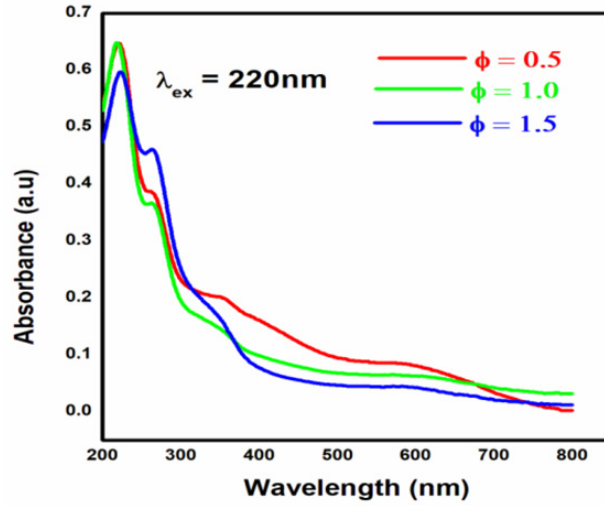


FIG. 4. UV-Vis absorbance spectra of  $\text{BaZrO}_3$  samples prepared for different  $F/O$  ratios

$(\alpha h\nu)^2$  versus  $(hc/\lambda)$ , to obtain the  $E_{gap}$  values. For the respective  $F/O$  ratios of 0.5, 1.0, and 1.5, the band gap of pure  $\text{BaZrO}_3$  at room temperature is determined to be 2.02, 2.96, and 3.09 eV. The excitation wavelength is 220 nm. As the fuel content rises, the band gap of  $\text{BaZrO}_3$  increases.

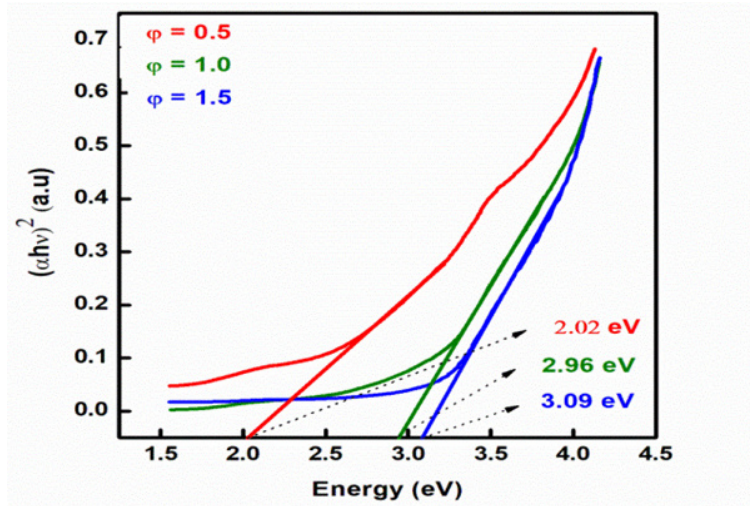


FIG. 5. Tauc plot of  $\text{BaZrO}_3$  samples prepared for different  $F/O$  ratios

### 3.5. Impedance spectroscopy analysis

The electrical and dielectric properties of a polycrystalline  $\text{BaZrO}_3$  ceramic and their interfaces with electronically conducting electrodes have been examined in a wide range of frequencies (100 Hz – 1 MHz) at room temperature using the complex impedance spectroscopy method [69]. The complex dielectric permittivity, abbreviated  $\epsilon^*$ , complex impedance, abbreviated  $Z^*$ , and electric modulus, abbreviated  $M^*$ , which are connected to one another as follows:

$$Z^* = Z' + jZ'' \quad (14)$$

$$M^* = \frac{1}{\epsilon^* \omega} \quad (15)$$

$$\frac{1}{\epsilon^* \omega} = j(\omega C_0) Z^* \quad (16)$$

$$j(\omega C_0) Z^* = M' + jM'' \quad (17)$$

where  $(Z', M')$  and  $(Z'', M'')$  are the real and imaginary compounds of impedance and modulus, respectively,  $j = \sqrt{-1}$  is the imaginary factor and  $\omega$  is the angular frequency,

$$\omega = 2\pi f. \quad (18)$$

There are two parts to the impedance expression: a real part and an imaginary part. A “Nyquist Plot” is created when the real part ( $Z_{real}$ ) is plotted on the X-axis and the imaginary part ( $Z_{imag}$ ) is plotted on the Y-axis (see Fig. 6). The  $Z_{imag}$  is negative, whereas each point on the Nyquist plot represents an impedance value at a certain frequency point. Low frequency impedance is applied to the right side of the plot along the X-axis, and higher frequency impedances are applied to the left. Additionally, impedance can be shown as a vector (arrow) with a length of  $|Z|$  on a Nyquist plot. The “phase angle” is the angle formed by this arrow and the X-axis [70]. A Bode plot is widely used in the engineering community compared to the Nyquist plot. It consists of two different logarithmic plots: frequency vs magnitude and frequency vs phase (Fig. 7). It is another technique to describe the impedance results.

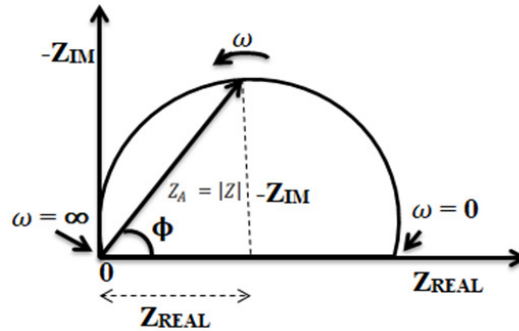


FIG. 6. Nyquist plot with impedance vector

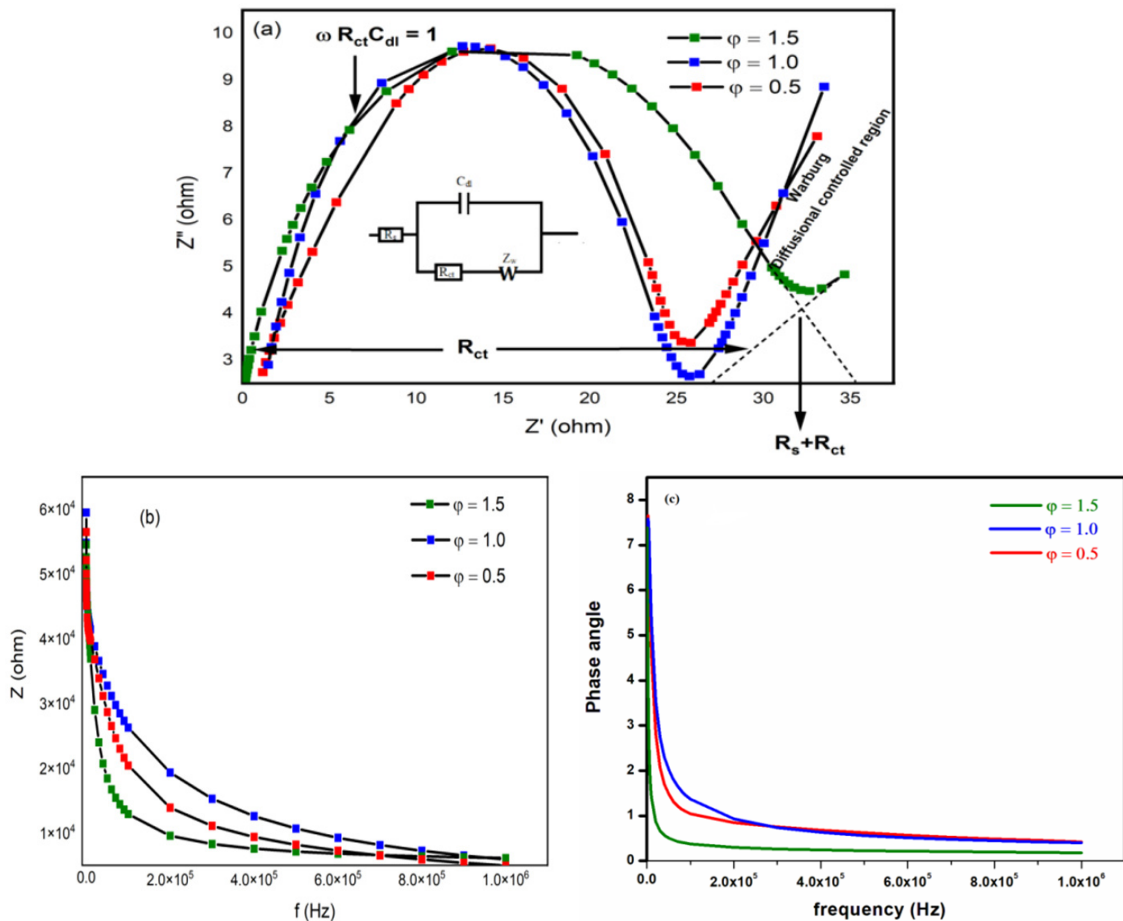


FIG. 7. (a) Nyquist plot for BaZrO<sub>3</sub> with  $\varphi = 0.5, 1.0$  and  $1.5$  at room temperature; (b) frequency vs magnitude (Bode plot); (c) frequency vs phase angle (Bode plot) for BaZrO<sub>3</sub> with  $\varphi = 0.5, 1.0$  and  $1.5$  at room temperature

Impedance is really measured by introducing a potential wave to the working electrode and monitoring the ensuing current wave  $Z$ .  $Z_{real}$ , and  $Z_{imag}$  are taken from these two waves and sketched. These parameters are measured for potential waves with various frequencies to produce the spectrum. In a three-electrode system, an EIS experiment is carried out by fixing an applied voltage [71], according to the initial report on electrochemical impedance spectroscopy that was published in 1975 [72]. The generated Warburg impedance ( $W$ ), charge transfer resistance ( $R_{ct}$ ), and solution resistance ( $R_s$ ) are gathered and shown in the Nyquist plots.

The Warburg impedance ( $W$ ) is an extra resistance that can be produced by the diffusion of molecules or redox species. Frequency affects the manner in which this impedance behaves. In fact, the diffusing reactants do not have to go very far. The Warburg impedance is minimal at high frequencies. The force to diffuse the redox molecules increases the Warburg resistance at low frequencies. The Nyquist plot shows the infinite Warburg impedance as a tilted line with a 45° slope. On the Bode plot, however, the Warburg effect appears as a 45° phase shift.

The Nyquist curve of BaZrO<sub>3</sub> with  $\varphi = 0.5, 1.0, \text{ and } 1.5$  at room temperature is shown in Fig. 7(a). Warburg resistance, which is induced by the frequency dependence of ion diffusion from the electrolyte to the surface, is a phenomenon as all samples exhibit a circular arc in the high-frequency zone and nearly a straight line in the low-frequency region. As the  $F/O$  ratio increases, the semicircle's diameter gradually changes. A Bode curve of the impedance  $Z(\Omega)$  for BaZrO<sub>3</sub> is shown in Fig. 7(b). A Bode plot of the phase angle for BaZrO<sub>3</sub> is shown in Fig. 7(c). For  $\varphi = 0.5, 1.0, \text{ and } 1.5$  ratios, the impedance magnitude  $|Z|$  reduces with increasing  $F/O$  ratio at low frequency and decreases at high frequency. For observing phase margins where the system becomes unstable (violent phase or magnitude changes), the Bode plot offers many advantages. The study of sensors, filters, and transistors in electronic devices can benefit from it as a result [73]. Real and imaginary part of impedance increases with increasing  $F/O$  ratio.

Ionic conductivity is reduced by  $4.833 \times 10^{-3}$  to  $3.327 \times 10^{-3}$ . It introduces significant structural defects to the BaZrO<sub>3</sub> crystal, as evidence by large lattice microstrain. In general, the Oxygen vacancy assisted high ionic conductivity [74].

Bulk resistance of the three various  $F/O$  ratio value, the calculated value of ionic conductivity were listed in Table 3.

TABLE 3. Ionic conductivity data of BaZrO<sub>3</sub> electrolyte

Sample	Sample thickness (cm)	Bulk resistance ( $\Omega$ )	Area of the sample (cm)	Ionic conductivity S/cm
$\varphi = 0.5$	0.1901	25.54	1.54	$4.833 \times 10^{-3}$
$\varphi = 1.0$	0.1762	25.91	1.54	$4.416 \times 10^{-3}$
$\varphi = 1.5$	0.1661	32.42	1.54	$3.327 \times 10^{-3}$

The ionic conductivity was found to be

$$\sigma = \frac{L}{R_b^* A}, \quad (19)$$

where  $L$  is the thickness (cm),  $A$  is the contact area (cm<sup>2</sup>), and  $R_b$  ( $\Omega$ ) is the bulk resistance of the BaZrO<sub>3</sub> electrolyte,  $\sigma$  is the ionic conductivity (S·cm<sup>-1</sup>). The Nyquist plot of the complex impedance readings was used to calculate  $R_b$ . The Ionic conductivity result shows the BaZrO<sub>3</sub> electrolyte material can be used as semiconducting device application.

The EIS approach, a non-destructive investigation tool, can be used to efficiently characterize physical and chemical processes in fuel cells as well as energy storage devices. In order to monitor these materials' and devices' performance and stability, as well as their charge transport characteristics, the EIS can be used [75].

Figure 8 displays the impedances of BaZrO<sub>3</sub> at room temperature. For  $\varphi = 0.5, 1.0, \text{ and } 1.5$  ratios, the real component  $Z'(f)$  of impedance decreases with increasing frequency (Fig. 8(a)). The imaginary portion  $Z''(f)$  of BaZrO<sub>3</sub> is shown in Fig. 8(b), and it increases to a maximum value before it starts to decrease at high frequencies, demonstrating the presence of a relaxation process in the system. The relaxation period for the dielectric-relaxation process is provided by the  $Z''$  peak.

#### 4. Conclusion

The sol-gel auto-combusted method was used to successfully synthesise perovskite Barium Zirconate nanoparticles with various  $F/O$  ratios. XRD was used to examine the crystalline size. The Rietveld refinement verified that the BaZrO<sub>3</sub> phase was unique and clear. Raman spectroscopy was used to confirm the existence of various modes. With an increasing  $F/O$  ratio, it was discovered that the optical band gap increases from 2.02 to 3.09 eV. As the  $F/O$  ratio increased, the impedance and relaxation time of a BaZrO<sub>3</sub> pellet for impedance spectroscopy decreased. For various  $F/O$  ratios (for  $\varphi = 0.5, 1.0, \text{ and } 1.5$ ), the BaZrO<sub>3</sub> electrolyte's ionic conductivity ranged from  $3.327 \times 10^{-3}$  to  $4.833 \times 10^{-3}$ . BaZrO<sub>3</sub> nanoparticles can be used for the development of energy storage devices due to good electrical properties and high ionic conductivity.

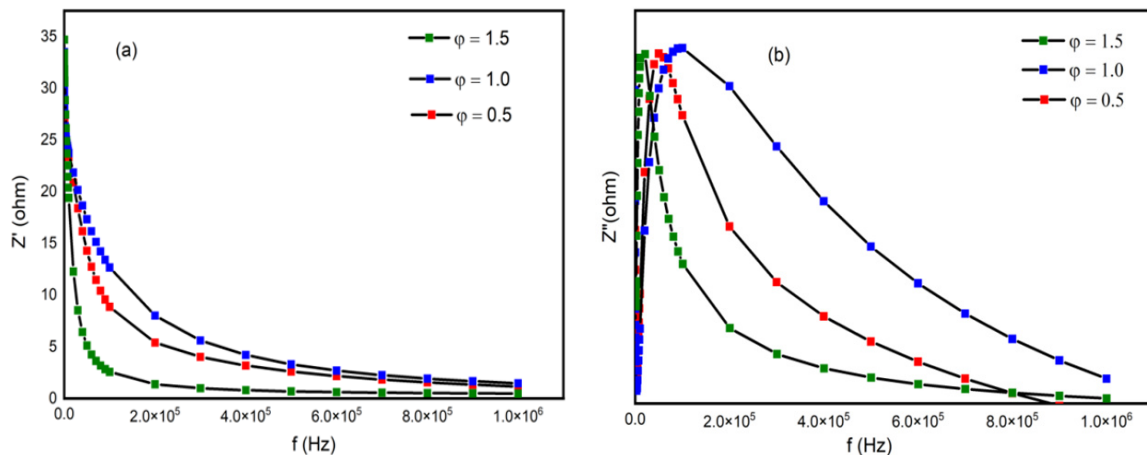


FIG. 8. (a) Real part and (b) imaginary part of impedance as a function of frequency (Bode plot) for BaZrO<sub>3</sub> with  $\varphi = 0.5, 1.0$  and  $1.5$  at room temperature

## References

- [1] Norton F.H. *Fine ceramics: technology and applications*. McGraw-Hill, New York, 1970.
- [2] Boschini F., Rulmont A., Cloots R., Moreno, R. Rheological behaviour of BaZrO<sub>3</sub> suspensions in non-aqueous media. *Ceramics International*, 2009, **35** (3), P. 1007–1013.
- [3] Huang J., Zhou L., Wang Z., Lan Y., Tong Z., Gong F., Li, L. Photoluminescence properties of SrZrO<sub>3</sub>: Eu<sup>3+</sup> and BaZrO<sub>3</sub>: Eu<sup>3+</sup> phosphors with perovskite structure. *J. of Alloys and Compounds*, 2009, **487** (1–2), L5–L7.
- [4] Iwahara H., Asakura Y., Katahira K., Tanaka, M. Prospect of hydrogen technology using proton-conducting ceramics. *Solid State Ionics*, 2004, **168** (3–4), P. 299–310.
- [5] Kreuer K.D. Aspects of the formation and mobility of protonic charge carriers and the stability of perovskite-type oxides. *Solid State Ionics*, 1999, **125** (1–4), P. 285–302.
- [6] Zhou H., Mao Y., Wong S.S. Shape control and spectroscopy of crystalline BaZrO<sub>3</sub> perovskite particles. *J. of Materials Chemistry*, 2007, **17** (17), P. 1707–1713.
- [7] Dong Z., Ye T., Zhao Y., Yu J., Wang F., Zhang L., Guo S. Perovskite BaZrO<sub>3</sub> hollow micro- and nanospheres: controllable fabrication, photoluminescence and adsorption of reactive dyes. *J. of Materials Chemistry*, 2011, **21** (16), P. 5978–5984.
- [8] Cavalcante L.S., Sczancoski J.C., Espinosa J.W.M., Mastelaro V.R., Michalowicz A., Pizani P.S., Longo E. Intense blue and green photoluminescence emissions at room temperature in barium zirconate powders. *J. of Alloys and Compounds*, 2009, **471** (1–2), P. 253–258.
- [9] Parida S., Rout S.K., Cavalcante L.S., Sinha E., Li M.S., Subramanian V., Longo E. Structural refinement, optical and microwave dielectric properties of BaZrO<sub>3</sub>. *Ceramics International*, 2012, **38** (3), P. 2129–2138.
- [10] Choudhury P.R., Krupanidhi S.B. Dielectric response of BaZrO<sub>3</sub>/BaTiO<sub>3</sub> and SrTiO<sub>3</sub>/BaZrO<sub>3</sub> superlattices. *J. of Applied Physics*, 2008, **104** (11), 114105.
- [11] Moreira M.L., Gurgel M.F.C., Mambrini G.P., Leite E.R., Pizani P.S., Varela J.A., Longo E. Photoluminescence of barium titanate and barium zirconate in multilayer disordered thin films at room temperature. *The J. of Physical Chemistry A*, 2008, **112** (38), P. 8938–8942.
- [12] Jia X., Fan H., Lou X., Xu J. Synthesis and gas sensing properties of perovskite CdSnO<sub>3</sub> nanoparticles. *Applied Physics A*, 2009, **94**, P. 837–841.
- [13] LoPinto D.E. *Tunable Piezoelectric Transducers via Custom 3D Printing: Conceptualization, Creation, and Customer Discovery of Acoustic Applications*. Virginia Tech, 2021.
- [14] Yamanaka S., Kurosaki K., Maekawa T., Matsuda T., Kobayashi S.I., Uno M. Thermochemical and thermophysical properties of alkaline-earth perovskites. *J. of Nuclear Materials*, 2005, **344** (1–3), P. 61–66.
- [15] Shirpour M., Rahmati B., Sigle W., van Aken P.A., Merkle, R., Maier J. Dopant segregation and space charge effects in proton-conducting BaZrO<sub>3</sub> perovskites. *The J. of Physical Chemistry C*, 2012, **116** (3), P. 2453–2461.
- [16] Herbert J.M. *Ceramic dielectrics and Capacitors*, 1985, Vol. 6, Philadelphia.
- [17] Sundell P.G., Björketun M.E., Wahnström G. Thermodynamics of doping and vacancy formation in BaZrO<sub>3</sub> perovskite oxide from density functional calculations. *Physical Review B*, 2006, **73** (10), 104112.
- [18] Dhahri K., Bejar M., Dhahri E., Soares M. J., Graça M.F.P., Sousa M.A., Valente M.A. Blue-green photoluminescence in BaZrO<sub>3- $\delta$</sub>  powders. *Chemical Physics Letters*, 2014, **610**, P. 341–344.
- [19] Wan Ali W.F.F., Rejab N.A., Othman M., Ain M.F., Ahmad Z.A. An investigation of dielectric resonator antenna produced from silicon (100) enhanced by strontium doped-barium zirconate films. *J. of sol-gel science and technology*, 2012, **61**, P. 411–420.
- [20] Park J.S., Lee J.H., Lee H.W., Kim B.K. Low temperature sintering of BaZrO<sub>3</sub>-based proton conductors for intermediate temperature solid oxide fuel cells. *Solid State Ionics*, 2010, **181** (3–4), P. 163–167.
- [21] Cullity B.D. *Elements of X-ray Diffraction*, Addison-Wesley Publishing, 1956.
- [22] Kittel C., McEuen P. *Introduction to solid state physics*, John Wiley & Sons, 2018.
- [23] Patil K.C., Aruna S.T., Ekambaram S. Combustion synthesis. *Current opinion in solid state and materials science*, 1997, **2** (2), P. 158–165.
- [24] Jain S.R., Adiga K.C., Verneker V.P. A new approach to thermochemical calculations of condensed fuel-oxidizer mixtures. *Combustion and flame*, 1981, **40**, P. 71–79.
- [25] Hwang C.C., Huang T.H., Tsai J.S., Lin C.S., Peng C.H. Combustion synthesis of nanocrystalline ceria (CeO<sub>2</sub>) powders by a dry route. *Materials Science and Engineering: B*, 2006, **132** (3), P. 229–238.
- [26] Mukasyan A.S., Epstein P., Dinka, P. Solution combustion synthesis of nanomaterials. *Proceedings of the combustion institute*, 2007, **31** (2), P. 1789–1795.

- [27] Tyagi A.K., Chavan S.V., Purohit R.D. Visit to the fascinating world of nano-ceramic powders via solution-combustion. *Indian J. of Pure & Applied Physics*, 2006, **44** (2), P. 113–118.
- [28] Chen W., Li F., Yu J., Liu L. A facile and novel route to high surface area ceria-based nanopowders by salt-assisted solution combustion synthesis. *Materials Science and Engineering: B*, 2006, **133** (1–3), P. 151–156.
- [29] Bedekar V., Grover V., Nair S., Purohit R.D., Tyagi A. K. Nanocrystalline electroceramics by combustion method. *Synthesis and Reactivity in Inorganic, Metal-Organic and Nano-Metal Chemistry*, 2007, **37** (5), P. 321–326.
- [30] Xu Q., Huang D.P., Chen W., Lee J.H., Wang H., Yuan R.Z. Citrate method synthesis, characterization and mixed electronic–ionic conduction properties of La<sub>0.6</sub>Sr<sub>0.4</sub>Co<sub>0.8</sub>Fe<sub>0.2</sub>O<sub>3</sub> perovskite-type complex oxides. *Scripta Materialia*, 2004, **50** (1), P. 165–170.
- [31] Majid A., Tunney J., Argue S., Wang D., Post M., Margeson J. Preparation of SrFeO<sub>~2.85</sub> perovskite using a citric acid assisted Pechini-type method. *J. of alloys and compounds*, 2005, **398** (1–2), P. 48–54.
- [32] Palmisano P., Russo N., Fino P., Fino D., Badini C. High catalytic activity of SCS-synthesized ceria towards diesel soot combustion. *Applied Catalysis B: Environmental*, 2006, **69** (1–2), P. 85–92.
- [33] Carvalho M., Costa F.A., Pereira I.S., Bassat J., Grenier J. New preparation method of La<sub>n+1</sub> Ni<sub>n</sub>O<sub>3n+1-δ</sub> (n = 2, 3). *J. of Materials Chemistry*, 1997, **7** (10), P. 2107–2111.
- [34] Marinšek M., Zupan K., Maek J. Ni–YSZ cermet anodes prepared by citrate/nitrate combustion synthesis. *J. of power sources*, 2002, **106** (1–2), P. 178–188.
- [35] Chakroborty A., Sharma A.D., Maiti B., Maiti H.S. Preparation of low-temperature sinterable BaCe<sub>0.8</sub>Sm<sub>0.2</sub>O<sub>3</sub> powder by autoignition technique. *Materials letters*, 2002, **57** (4), P. 862–867.
- [36] Mali A., Ataie A. Influence of the metal nitrates to citric acid molar ratio on the combustion process and phase constitution of barium hexaferrite particles prepared by sol-gel combustion method. *Ceramics International*, 2004, **30** (7), P. 1979–1983.
- [37] Hernandez T., Bautista M.C. The role of the synthesis route to obtain densified TiO<sub>2</sub>-doped alumina ceramics. *J. of the European Ceramic Society*, 2005, **25** (5), P. 663–672.
- [38] Pechini M.P. US Patent No. 3330697, 1967, July.
- [39] Epifani M., Melissano E., Pace G., Schioppa M. Precursors for the combustion synthesis of metal oxides from the sol-gel processing of metal complexes. *J. of the european ceramic society*, 2007, **27** (1), P. 115–123.
- [40] Wang P.J., Zhou D., Li J., Pang L.X., Liu W.F., Su J.Z., Trukhanov A. Significantly enhanced electrostatic energy storage performance of P(VDF-HFP)/BaTiO<sub>3</sub>–Bi(Li<sub>0.5</sub>Nb<sub>0.5</sub>)O<sub>3</sub> nanocomposites. *Nano Energy*, 2020, **78**, 105247.
- [41] Trukhanov S.V., Trukhanov A.V., Turchenko V.A., Trukhanov A.V., Trukhanova E.L., Tishkevich D.I., Gudkova S.A. Polarization origin and iron positions in indium doped barium hexaferrites. *Ceramics International*, 2018, **44** (1), P. 290–300.
- [42] Kumar D., Singh B. BaZrO<sub>3</sub> and Cs–BaZrO<sub>3</sub> catalysed transesterification of *Milletia Pinnata* oil and optimisation of reaction variables by response surface Box–Behnken design. *Renewable Energy*, 2019, **133**, P. 411–421.
- [43] Borja-Urby R., Díaz-Torres L.A., Salas P., Moctezuma E., Vega M., Ángeles-Chávez C. Structural study, photoluminescence, and photocatalytic activity of semiconducting BaZrO<sub>3</sub>: Bi nanocrystals. *Materials Science and Engineering: B*, 2011, **176** (17), P. 1382–1387.
- [44] Nehru L.C., Swaminathan V., Sanjeeviraja C. Photoluminescence studies on nanocrystalline tin oxide powder for optoelectronic devices. *American J. of Materials Science*, 2012, **2** (2), P. 6–10.
- [45] Beltrán A., Andrés J., Longo E., Leite E.R. Thermodynamic argument about SnO<sub>2</sub> nanoribbon growth. *Applied physics letters*, 2003, **83** (4), P. 635–637.
- [46] Schmalzried H., Kröger F.A. *The Chemistry of Imperfect Crystals*, North-Holland Publishing Company, Amsterdam, 1964.
- [47] Bedir M., Öztaş M., Bakkaloğlu Ö.F., Ormanci R. Investigations on structural, optical and electrical parameters of spray deposited ZnSe thin films with different substrate temperature. *The European Physical J. B-Condensed Matter and Complex Systems*, 2005, **45**, P. 465–471.
- [48] Dhanam M., Balasundaraprabhu R., Jayakumar S., Gopalakrishnan P., Kannan M.D. Preparation and study of structural and optical properties of chemical bath deposited copper indium diselenide thin films. *Physica Status Solidi A*, 2002, **191** (1), P. 149–160.
- [49] Park J.Y., Lee Y.J., Jun K.W., Baeg J.O., Yim, D.J. Chemical synthesis and characterization of highly oil dispersed MgO nanoparticles. *J. of Industrial and engineering chemistry*, 2006, **12** (6), P. 882–887.
- [50] Azizi M., Paydar M.H., Alafzadeh M. Influence of the Calcination Temperature and Fuel Composition on Synthesis of BaZr<sub>0.8</sub>Y<sub>0.2</sub>O<sub>3-δ</sub> by Solution Combustion Method for High Proton conductivity. *Int. J. of Advanced Science and Technology*, 2016, **96**, P. 11–20.
- [51] Elilarassi R., Chandrasekaran G. Synthesis and optical properties of Ni-doped zinc oxide nanoparticles for optoelectronic applications. *Optoelectronics Letters*, 2010, **6** (1), P. 6–10.
- [52] Toniolo J., Takimi A.S., Andrade M.J., Bonadiman R., Bergmann C.P. Synthesis by the solution combustion process and magnetic properties of iron oxide (Fe<sub>3</sub>O<sub>4</sub> and α-Fe<sub>2</sub>O<sub>3</sub>) particles. *J. of Materials Science*, 2007, **42**, P. 4785–4791.
- [53] Rietveld H.M. A profile refinement method for nuclear and magnetic structures. *J. of applied Crystallography*, 1969, **2** (2), P. 65–71.
- [54] Rietveld H.M. Line profiles of neutron powder-diffraction peaks for structure refinement. *Acta Crystallographica*, 1967, **22** (1), P. 151–152.
- [55] Young R.A. The Rietveld method. *Int. Union of Crystallography*, 1993, **5**, P. 1–38.
- [56] Sczancoski J.C., Cavalcante L.S., Badapanda T., Rout S.K., Panigrahi S., Mastelaro, V.R., Longo E. Structure and optical properties of [Ba<sub>1-x</sub>Y<sub>2x/3</sub>](Zr<sub>0.25</sub>Ti<sub>0.75</sub>)O<sub>3</sub> powders. *Solid State Sciences*, 2010, **12** (7), P. 1160–1167.
- [57] Schaufele R.F., Weber M.J. First- and second-order Raman scattering of SrTiO<sub>3</sub>. *The J. of Chemical Physics*, 1967, **46** (7), P. 2859–2861.
- [58] Charrier-Cougoulic I., Pagnier T., Lucazeau G. Raman spectroscopy of perovskite-type BaCe<sub>x</sub>Zr<sub>1-x</sub>O<sub>3</sub> (0 ≤ x ≤ 1). *J. of Solid State Chemistry*, 1999, **142** (1), P. 220–227.
- [59] Karlsson M., Matic A., Knee C.S., Ahmed I., Eriksson S.G., Börjesson L. Short-Range Structure of Proton-Conducting Perovskite BaIn<sub>x</sub>Zr<sub>1-x</sub>O<sub>3-x/2</sub> (x = 0–0.75). *Chemistry of Materials*, 2008, **20** (10), P. 3480–3486.
- [60] Kreuer K. On the development of proton conducting materials for technological applications. *Solid State Ionics*, 1997, **97** (1–4), P. 1–15.
- [61] Norby T., Larring Y. Concentration and transport of protons in oxides. *Current Opinion in Solid State and Materials Science*, 1997, **2** (5), P. 593–599.
- [62] Karlsson M., Ahmed I., Matic A., Eriksson S.G. Short-range structure of proton-conducting BaM<sub>0.10</sub>Zr<sub>0.90</sub>O<sub>2.95</sub> (M= Y, In, Sc and Ga) investigated with vibrational spectroscopy. *Solid State Ionics*, 2010, **181** (3–4), P. 126–129.
- [63] Slodczyk A., Colomban P., Willemin S., Lacroix O., Sala B. Indirect Raman identification of the proton insertion in the high-temperature [Ba/Sr][Zr/Ti]O<sub>3</sub>-modified perovskite protonic conductors. *J. of Raman Spectroscopy: An Int. J. for Original Work in all Aspects of Raman Spectroscopy, Including Higher Order Processes, and also Brillouin and Rayleigh Scattering*, 2009, **40** (5), P. 513–521.
- [64] Slodczyk A., Limage M. H., Colomban P., Zaafrani O., Grasset F., Loricourt J., Sala B. Substitution and proton doping effect on SrZrO<sub>3</sub> behaviour: High-pressure raman study. *J. of Raman Spectroscopy*, 2011, **42** (12), P. 2089–2099.

- [65] Li X., Liu M., Lai S.Y., Ding, D., Gong, M., Lee J.P., Liu M. In situ probing of the mechanisms of coking resistance on catalyst-modified anodes for solid oxide fuel cells. *Chemistry of Materials*, 2015, **27** (3), P. 822–828.
- [66] Wood D.L., Tauc J.S. Weak absorption tails in amorphous semiconductors. *Physical Review B*, 1972, **5** (8), 3144.
- [67] Badapanda T., Rout S.K., Cavalcante L.S., Sczancoski J.C., Panigrahi S., Longo E., Li M.S. Optical and dielectric relaxor behaviour of Ba(Zr<sub>0.25</sub>Ti<sub>0.75</sub>)O<sub>3</sub> ceramic explained by means of distorted clusters. *J. of Physics D: Applied Physics*, 2009, **42** (17), 175414.
- [68] Turton R., Turton R.J. *The quantum dot: A journey into the future of microelectronics*. Oxford University Press, USA, 1996.
- [69] Macdonald J.R. Impedance spectroscopy: Models, data fitting, and analysis. *Solid state ionics*, 2005, **176** (25–28), P. 1961–1969.
- [70] Lvovich V.F. Electrochemical Impedance Spectroscopy (EIS) applications to sensors and diagnostics. *Encyclopedia of Applied Electrochemistry*, Eds.: Kreysa G., Ota K.-i., Savinell R.F., 2014, P. 485–507.
- [71] Orazem M.E., Tribollet B. Electrochemical impedance spectroscopy. *New Jersey*, 2008, **1**, P. 383–389.
- [72] Ha L.D., Park K., Chang B.Y., Hwang S. Implementation of second-generation fourier transform electrochemical impedance spectroscopy with commercial potentiostat and application to time-resolved electrochemical impedance spectroscopy. *Analytical chemistry*, 2019, **91** (22), P. 14208–14213.
- [73] Choi W., Shin H.C., Kim J.M., Choi J.Y., Yoon W.S. Modeling and applications of electrochemical impedance spectroscopy (EIS) for lithium-ion batteries. *J. of Electrochemical Science and Technology*, 2020, **11** (1), P. 1–13.
- [74] Wu H., Li F. Oxygen vacancy-assisted high ionic conductivity in perovskite LaCoO<sub>3-δ</sub> ( $\delta = 1/3$ ) thin film: A first-principles-based study. *Physics Letters A*, 2019, **383** (2–3), P. 210–214.
- [75] Cherian C.T., Zheng M., Reddy M.V., Chowdari B.V.R., Sow C.H. Zn<sub>2</sub>SnO<sub>4</sub> nanowires versus nanoplates, electrochemical performance and morphological evolution during Li-cycling. *ACS Applied Materials and Interfaces*, 2013, **5** (13), P. 6054–6060.

---

*Submitted 29 May 2023; revised 29 July 2023; accepted 21 August 2023*

#### *Information about the authors:*

*J. Abimalar* – Department of Physics and Research Centre, Scott Christian College (Autonomous), Nagercoil – 629003, Tamil Nadu, India; Manonmaniam Sundaranar University, Abishekapatti, Tirunelveli – 627012, Tamil Nadu, India; ORCID 0009-0006-5388-0816; University reg. no. 20213162132017; jabimalar98@gmail.com

*V. Anslin Ferby* – Department of Physics and Research Centre, Scott Christian College (Autonomous), Nagercoil – 629003, Tamil Nadu, India; Manonmaniam Sundaranar University, Abishekapatti, Tirunelveli – 627012, Tamil Nadu, India; ORCID 0000-0001-6298-1498; anslinv@gmail.com

*Conflict of interest:* the authors declare no conflict of interest.

## Optimization of certain synthesis parameters for CdSe quantum dots and synthesis of CdSe–ZnSe nano-tetrapods through facile hot injection method

Boni Samuel<sup>1,2,a</sup>, K. J. Adarsh<sup>1,3,b</sup>, V. P. N. Nampoori<sup>1,c</sup>, A. Mujeeb<sup>1,d</sup>

<sup>1</sup>International School of Photonics, Cochin University of Science and Technology, Kochi-22, India

<sup>2</sup>Nirmala College, Muvattupuzha, Ernakulam, India

<sup>3</sup>Sophisticated Test and Instrumentation Centre, Cochin University of Science and Technology, Kochi-22, India

<sup>a</sup>boni@nirmalacollege.ac.in, <sup>b</sup>adarsh@cusat.ac.in, <sup>c</sup>nampoori@gmail.com, <sup>d</sup>mujeebpoovar@gmail.com

Corresponding author: Boni Samuel, boni@nirmalacollege.ac.in

**ABSTRACT** This paper reports a modified version of hot injection method for the synthesis of CdSe quantum dots and CdSe–ZnSe nano-tetrapod structures. In the present method, certain synthesis parameters such as injection temperature, growth temperature and precursor ratio were tuned to influence the growth kinetics and thereby the optical properties of the prepared CdSe QDs were enhanced. The influences of these parameters were studied and suitable conditions were optimized. Using the optimized parameters, CdSe–ZnSe nanostructures were synthesized with tetrapod morphology and their structural and optical properties were studied. The adopted modified version of synthesis is a facile method without stringent conditions such as inert atmosphere and therefore adaptable for the large-scale synthesis in industry.

**KEYWORDS** Growth kinetics, Hot injection, CdSe, CdSe–ZnSe, Nano-tetrapod.

**ACKNOWLEDGEMENTS** The work was supported by the Department of Science and Technology (DST-FIST), Government of India.

**FOR CITATION** Boni Samuel, Adarsh K.J., Nampoori V.P.N., Mujeeb A. Optimization of certain synthesis parameters for CdSe quantum dots and synthesis of CdSe–ZnSe nano-tetrapods through facile hot injection method. *Nanosystems: Phys. Chem. Math.*, 2023, **14** (4), 479–488.

### 1. Introduction

Quantum dots (QDs) have attracted a great research interest around the globe for the last few decades due to their excellent tunability, versatility and chemical processibility [1–3]. Among II–VI QDs, cadmium selenide (CdSe) is a widely explored material for various applications [4,5]. The quality of CdSe QDs is greatly influenced by the precursor chemicals as well as the capping ligand used in the synthesis and other various synthesis parameters such as precursor ratio, ligand ratio, injection temperature, growth temperature, etc. By understanding the role of these parameters on the growth kinetics of the QDs, it can be optimized to yield highly monodisperse, emissive and smaller QDs suitable for various applications such as fluorescence labelling, light emitting devices, etc.

In the early '90s Murray et. al., reported the synthesis of good quality CdSe QDs using dimethyl cadmium as cadmium (Cd) precursor and trioctylphosphine oxide (TOPO) as capping ligand [5,6]. But the chemicals used in these syntheses such as dimethyl cadmium were pyrophoric, extremely toxic, explosive and unstable at room temperature. Stringent conditions such as inert atmosphere and equipment such as glove box, Schlenk lines etc., were mandatory to conduct these syntheses as the dimethyl cadmium releases a large amount of toxic and explosive gas at high temperatures [7,8]. To overcome this problem, Peng et. al., introduced a “greener” synthesis for CdSe QDs, using less toxic cadmium oxide (CdO) as a precursor of Cd [8]. This synthesis involves heating of Cd precursor upto a temperature around 300 °C under inert atmosphere followed by the injection of selenium (Se) precursor, termed as hot injection method. It is also called as kinetic growth method since the particle size increases with the progress in reaction time. Through this method, CdSe QDs were prepared in various solvents such as fatty acids, phosphonic acids, amines, phosphine oxides, and certain compositions of these solvents [7–10]. Nordell et. al., modified this method to an easier, safe and facile synthesis of CdSe QDs dispensing inert atmosphere [11,12]. This facile method was further modified by our group, in which the large scale synthesis of a particular size of QDs was achieved [13]. This simple, large scale production method combined with the large scale purification process proposed by Lim et.al, can be adopted for industrial and R&D applications of CdSe QDs [13,14].

Various morphologies of nanostructures such as dot, rod, tetrapod, etc., facilitate researchers to further manipulate the optical and electronic properties of nanomaterials. Wang et al. reported the synthesis of CdSe nano-tetrapods by incorporating HCl, MnCl<sub>2</sub>, FeCl<sub>2</sub> and H<sub>2</sub>SO<sub>4</sub> separately into a system of spherical CdSe QDs under inert atmosphere. Wang suggested that the protonic acidity in the precursor medium influences the yield of tetrapods [15]. Synthesis of

CdSe tetrapods were also reported through the addition of halides during the reaction [16]. Alivisatos et. al., synthesized rod, arrow, tetrapod and teardrop shaped CdSe nanocrystals using alkylphosphonic acid as a shape controlling factor [17].

The influence of oleic acid concentration as well as injection temperature on the growth kinetics was studied by Mulvaney et. al., and reported that decrease in oleic acid concentration result smaller dots. The synthesis was carried out under inert atmosphere with two injection temperatures, 275 and 265 °C, out of which smaller initial dot size was obtained at 275 °C [18]. The present work is the detailed study on the role of injection temperature, precursor ratio and growth temperature on the growth kinetics of CdSe QDs synthesized in ambient conditions. The effect of these parameters was studied to optimize the same and to tune the desirable optical properties with good repeatability. With the optimized conditions, CdSe quantum dots and CdSe-ZnSe nano-tetrapods of improved quality were synthesized through the facile hot injection method. In the synthesis of CdSe-ZnSe nano-tetrapods any additional chemicals were not used for shape controlling. This modified and optimized synthesis is a one-pot method excluding inert atmosphere and complex facilities so that the technique is adaptable to industry for the large scale synthesis of nanostructures.

## 2. Experimental

### 2.1. CdSe QDS

Cadmium precursor was prepared by adding CdO powder and oleic acid (OA) into octadecene (ODE). The Cd precursor was heated to a temperature higher than 150 °C to dissolve the brown Cd powder in ODE and to form a clear solution. The Se precursor, prepared by mixing Se powder and trioctylphosphine (TOP) in ODE was then swiftly injected into the Cd precursor at a specific temperature, called injection temperature. Immediately after the Se injection, CdSe QDs nucleate and begin to grow. As the Se precursor was injected, the temperature of the mixture decreases from the injection temperature. The resultant temperature, called growth temperature was maintained at a particular level for each synthesis of QD sample. Aliquots of samples collected at different intervals of time such as 5 s, 20 s, 60 s, and 120 s after the Se injection and it was found that the particle size increased as time progresses. The experiment was repeated under different conditions such as injection temperature, molar precursor ratio and growth temperature in order to optimize and yield good quality CdSe QDs.

### 2.2. CdSe-ZnSe nano-tetrapods

The synthesis of CdSe-ZnSe nano-tetrapods, the same hot injection method was adopted with ZnSe grown over the CdSe core through a single step-continuous chemical reaction. Thus, the extra step for the formation of ZnSe layer was skipped and the complexity of the synthesis was significantly reduced [3]. The only difference in the synthesis was the addition of Zn precursor in continuation to the nucleation of CdSe. The method can be extended to grow different shell layers one over the other to yield core-multishell system [19,20]. The values of parameters such as injection temperature, molar precursor ratio and growth temperature optimized for the synthesis of CdSe QDs were also used in the synthesis of CdSe-ZnSe nano-tetrapods. For this, Zn acetate (1 mmol) is mixed with 3 ml of OA and 6 ml of ODE to form the Zn precursor. For the synthesis of CdSe, the optimum identified value of Cd and Se precursors were selected. Selenium precursor was prepared by mixing 5 mmol Se powder, 4 ml of TOPO and 5 ml of ODE. For the Cd precursor, CdO powder (0.5 mmol), OA (3 ml), and ODE (10 ml) were stirred thoroughly and heated up to 225 °C to obtain a clear solution. At this temperature, the Se precursor was swiftly injected to initiate the nucleation of the CdSe QDs. After 5s of Se precursor injection, drops of Zn precursor were added at a rate of 2 ml per minute up to 4.5 min. In order to restrict the nucleation of ZnSe QDs, the precursor concentration was controlled during the injection process and the reaction was maintained in the kinetic growth regime. CdSe-ZnSe nano-tetrapods of different sizes were synthesized and samples were collected at 10 s, 1 min, 2 min, 5 min, and 8 min after the injection of Se.

For the particle size and morphological studies, TEM images were obtained from the JEOL/JEM 2100 transmission electron microscope. Absorption spectra were recorded using Jasco V-570 UV/Vis/IR spectrophotometer. It consists of two light sources, a Deuterium lamp of wavelength ranges from 190 nm to 350 nm and a Halogen lamp of wavelength ranges between 330 nm to 2500 nm. The monochromator contains two plane gratings of 1200 lines/mm for the UV-Vis region and 300 lines/mm for the NIR region. A Photomultiplier tube and a PbS photocell are the detectors. Fluorescence spectra were recorded using Varian-Cary Eclipse fluorimeter in which a xenon lamp was used as an excitation source. The emission from the sample was collected by a PMT detector.

## 3. Results and discussion

### 3.1. Optimization of injection temperature

The injection temperature was varied from 160 to 240 °C at selected intervals. The temperatures above 240 °C were not considered since the optically clear Cd oleate solution becomes darker due to the high reaction of chemicals with atmospheric oxygen at elevated temperatures. Moreover, at these high temperatures, excess evaporation of the solvent leads to the drying of Cd oleate solute for which inert atmosphere is preferred.

Absorption and fluorescence spectra of the synthesized CdSe QDs at various injection temperatures at 160, 200, 215, 225 and 240 °C were recorded. The molar precursor ratio of Cd:Se was selected as 1:1 and the growth temperatures

were maintained 15 °C lower to the corresponding injection temperatures. The excitation wavelength for recording the fluorescence spectra used was 400 nm in all the experiments.

The CdSe QDs synthesized at injection temperatures of 160 and 200 °C show similar absorption and fluorescence spectra as that of 215 °C represented in Fig. 1(a). In the hot injection method, in general, the particle size increases as the reaction time progresses and results in a redshift in both absorption and fluorescence spectra. But for these samples excitonic absorption peak and spectral redshift with an increase in time are not observed in the absorption spectra. Since at these injection temperatures, the amount of nucleated QDs is found to be low, giving a low concentration of samples. Also, the redshift is not presented in the fluorescence spectra, in which the peak wavelengths for all the samples are around 480 nm, depicts that the particles do not grow as reaction time progresses. Moreover, the fluorescence spectra are very broad with an FWHM around 100 nm, which clearly indicates the low quality of the QDs prepared at these injection temperatures.

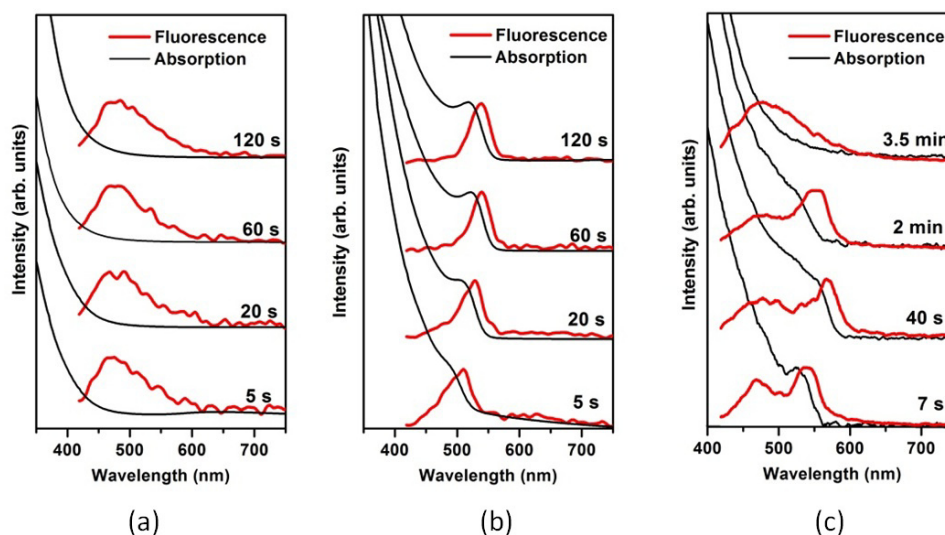


FIG. 1. Normalized absorption and fluorescence spectra of CdSe QDs synthesized at injection temperatures, a) 215 °C and b) 225 °C and c) 240 °C. Excitation wavelength used to record fluorescence emission was 400 nm

In the absorption spectra of QDs synthesized at 225 °C injection temperature, given in Fig. 1(b), prominent excitonic peaks are observed with gradual redshift from 510 nm to 540 nm, with increase in reaction time. This clearly shows that several QDs are nucleated and result a sample of high concentration. Also, the size of the particle increases with reaction time. The fluorescence spectra are narrow with an FWHM in the range of 40 nm to 60 nm in the as-prepared QDs without post-synthesis purifications. Therefore, in this facile hot injection method an injection temperature around 225 °C is suitable for the synthesis of good quality QDs of different sizes.

The synthesis was repeated for the injection temperature of 240 °C and a large amount of QD nucleation and initial growth of particle size were observed similar to the synthesis at 225 °C. But the colour of the QD solution was found to shift from green to red and then back to greenish-yellow as time progresses. The absorption and fluorescence spectra shown in Fig. 1(c) agrees with the observations. The injection temperature at 240 °C results in the nucleation at different time and cause a growth of QDs of two different sizes, which is evident in the fluorescence spectra as two narrow peaks. For the sample at reaction time of 7s, the emission peak at 470 nm has an FWHM of about 60 nm and that at 540 nm has an FWHM of about 45 nm, which clearly shows that these are not a defect induced emission. Generally, in a defect driven emission, the spectrum will be as broad as 100 s of nm [13, 21]. In the case of the sample at reaction time of 3.5 min, the two peaks merge to form a single emission peak around 480 nm. These QDs require severe post-synthesis purification processes and need refinement in their size to obtain narrow fluorescence emission. By analyzing the absorption and fluorescence spectra it was clear that the quality of QDs deteriorated as the temperature increased beyond 225 °C. The sample prepared at 240 °C was compared with that of 225 °C and found that the former is of poor quality with that of the lower temperature and hence it was concluded to maintain facile hot injection method at 225 °C. Thus, good quality QDs having narrow FWHM in the emission spectra even without stringent condition of purification and refinement were obtained.

### 3.2. Optimization of precursor ratio

The influence of Cd:Se molar ratio on the growth kinetics of the CdSe QDs was also studied by synthesizing the QDs at an injection temperature of 225 °C and a growth temperature of 210 °C. The precursor ratio was varied as 2:1, 1:1, 1:5, and 1:10. The absorption spectra of the synthesized samples using these precursor ratios are given in Fig. 2.

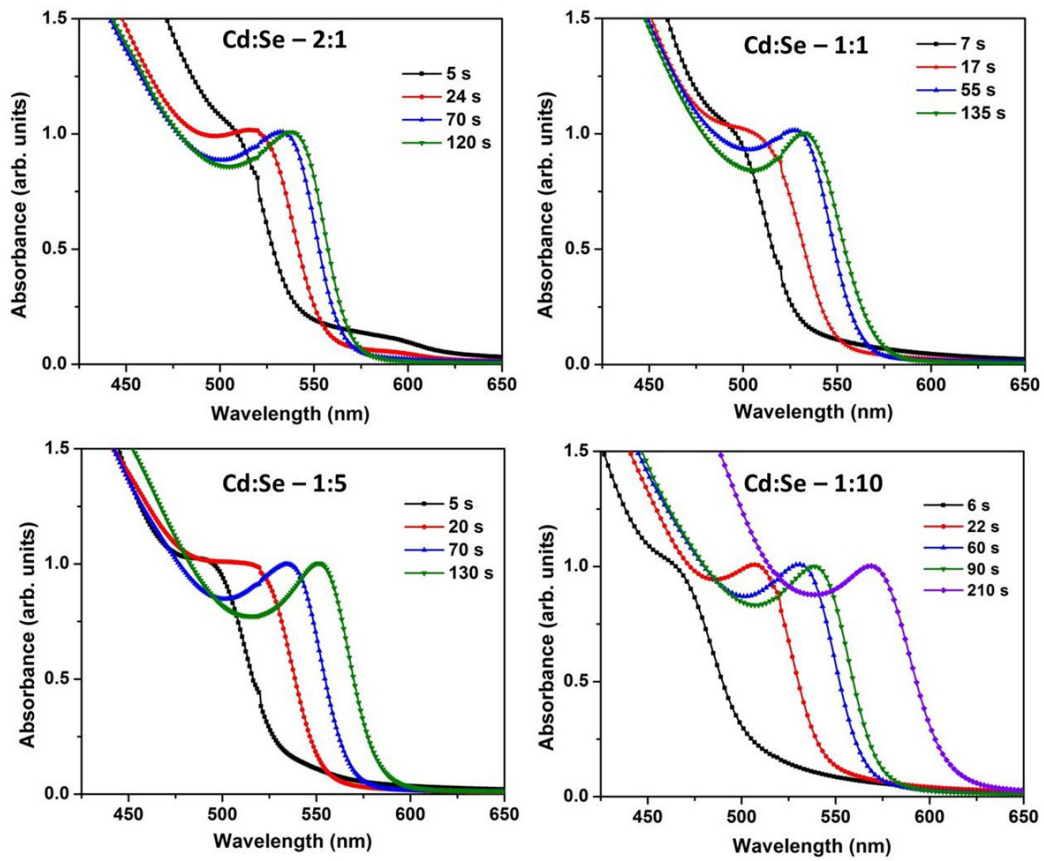


FIG. 2. Absorption spectra of CdSe QDs synthesized using different precursor ratio

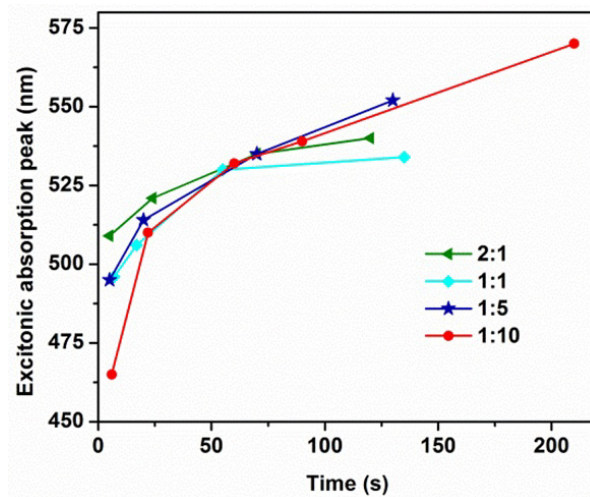


FIG. 3. Variation of excitonic absorption wavelength with increase in reaction time for different precursor molar ratios

The variation of excitonic absorption wavelength with increase in reaction time is presented in Fig. 3. As the reaction progresses, the particle size increases and the excitonic emission undergoes a redshift. In the sample with precursor ratio 2:1, the peak shifts from 510 nm to 540 nm and in samples 1:1 the peak shifts from 495 nm to 535 nm in 120 s and the particle size tends to saturate. For the sample 1:5 the particle size increases beyond 120s and the lowest excitonic peak obtained was around 495 nm. Sample 1:10 gives excitonic absorption peak around 465 nm as the particles are small and further grows similar to the sample 1:5, beyond 120 s. The results show that the presence of excess amount of Se facilitates the nucleation of smaller QDs and growth of different size ranges of QDs. Considering all these facts, for synthesis monodisperse QDs, the precursor ratio was optimized at 1:10.

### 3.3. Optimization of growth temperature

In order to study the influence of growth temperature on the growth kinetics, QDs were synthesized at growth temperatures of 180, 210, 215 and 225 °C. The optimized injection temperature and the molar ratio were fixed at 225 °C and 1:10, respectively, throughout the synthesis. The absorption spectra of the samples are given in Fig. 4. The plot of excitonic absorption peak Vs reaction time is presented in Fig. 5. This graph shows that the rate of particle growth increases with an increase in the growth temperature. The growth temperature below 210 °C the rate of growth is very slow and the particle size tends to saturate. The growth temperature between 210 and 215 °C gives a moderate rate of growth and therefore better control over the particle size. The rate of growth at 225 °C is very high so that the peak wavelength reaches 590 nm in 2 minutes.

CdSe QDs synthesized at 215 °C of growth temperature is selected for further analysis. The absorption and fluorescence spectra of these QDs are given in Fig. 6. Excitonic absorption peak varies from 480 nm to 584 nm during the particle size growth. The three samples with reaction time 2 s, 13 s, 35 s have good quality of fluorescence emission with FWHM of 35 nm, usually termed as colour purity. QDs having high colour purity are useful for labelling and light emitting devices [19, 22]. For the samples with reaction time 80 s and 120 s the FWHM gradually increases to 47 nm and 60 nm, respectively. For the final sample of 200 s, the FWHM is 125 nm broad and centered around 480 nm, due to the particle size broadening effect.

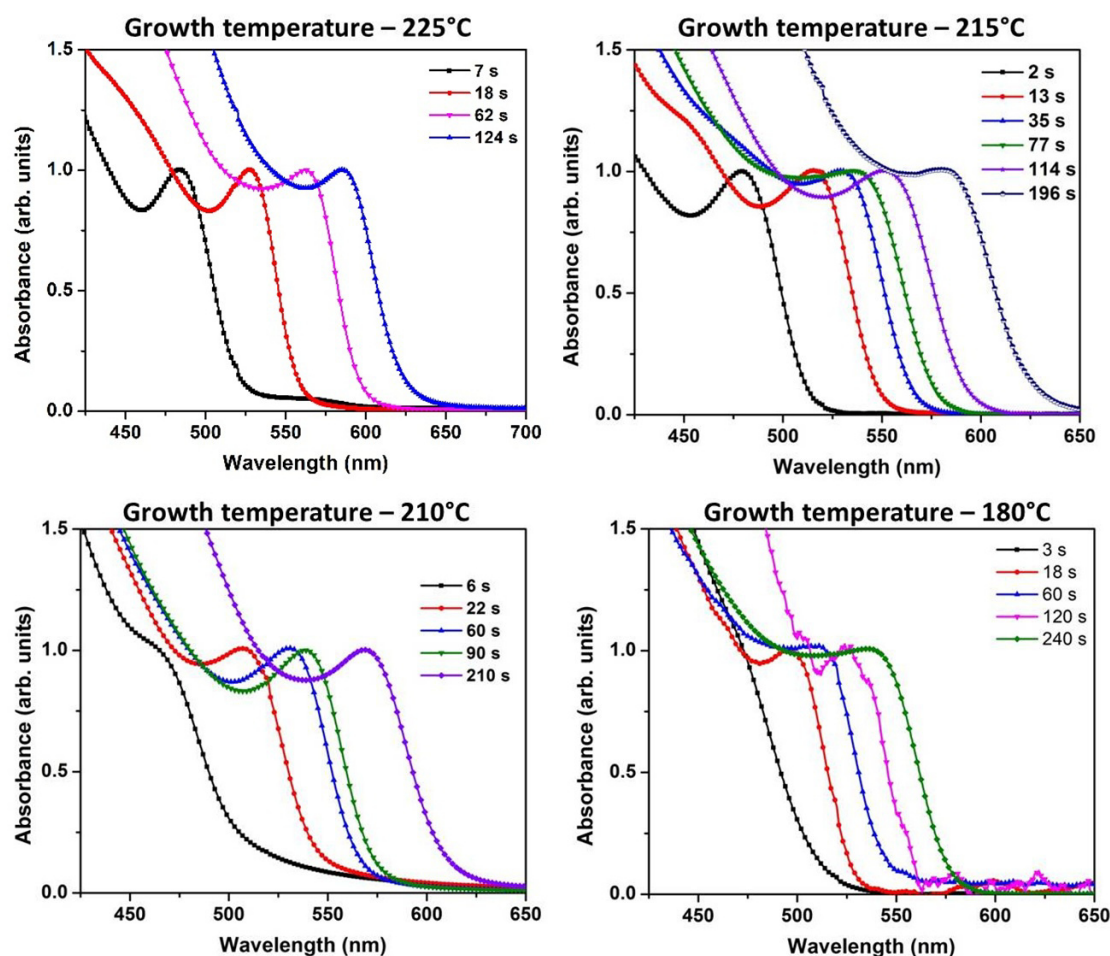


FIG. 4. Absorption spectra of CdSe QDs synthesized at different growth temperature

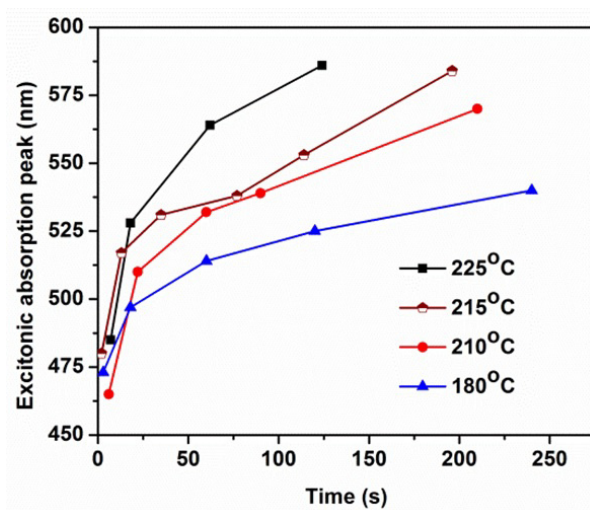


FIG. 5. Variation in excitonic absorption wavelength with reaction time for different growth temperatures

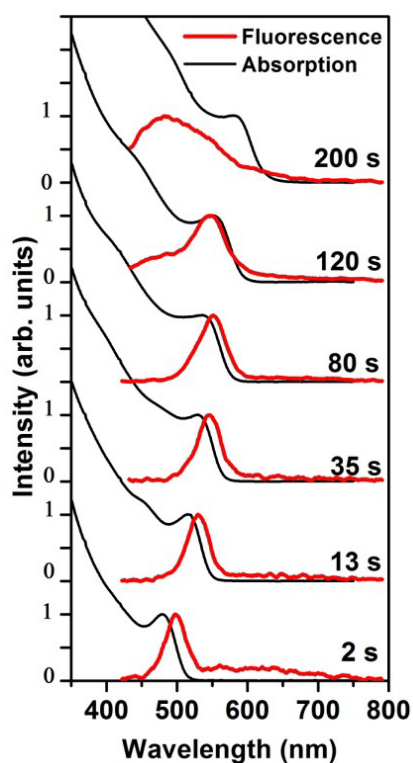


FIG. 6. Normalized absorption and fluorescence spectra of CdSe QDs synthesized at the growth temperature of 215 °C. For recording fluorescence spectra, an excitation wavelength of 400 nm was used

TEM image of one of the samples, taken at 35 s is shown in Fig. 7(a). The particles are nearly monodispersed and spherical in shape. The average particle size is measured to be 2.7 nm and the histogram of the particle size measurement is given in Fig. 7(b). The CdSe QDs synthesized with optimized conditions of injection temperature of 225 °C, precursor ratio 1:10 with growth temperature ranging from 210 to 215 °C have good optical properties.

### 3.4. CdSe–ZnSe nano-tetrapod structure

The optical properties of the CdSe–ZnSe nano-tetrapod was found to be depending significantly on the quality of the CdSe, and hence the same optimized conditions adopted for the CdSe QDs were used for the preparation of CdSe–ZnSe nanotetrapods [3]. With these conditions, CdSe–ZnSe nano-tetrapods of different sizes were synthesized and samples were collected at 10 s, 1 min, 2 min, 5 min, and 8 min after the Se injection time.

TEM images of representative samples at 10 s and 2 min are given in Fig. 8 and Fig. 9. The sample at 10 s consists of QDs with an average size of approximately 3 nm, exhibiting mostly spherical shapes. Some of the QDs exhibit a

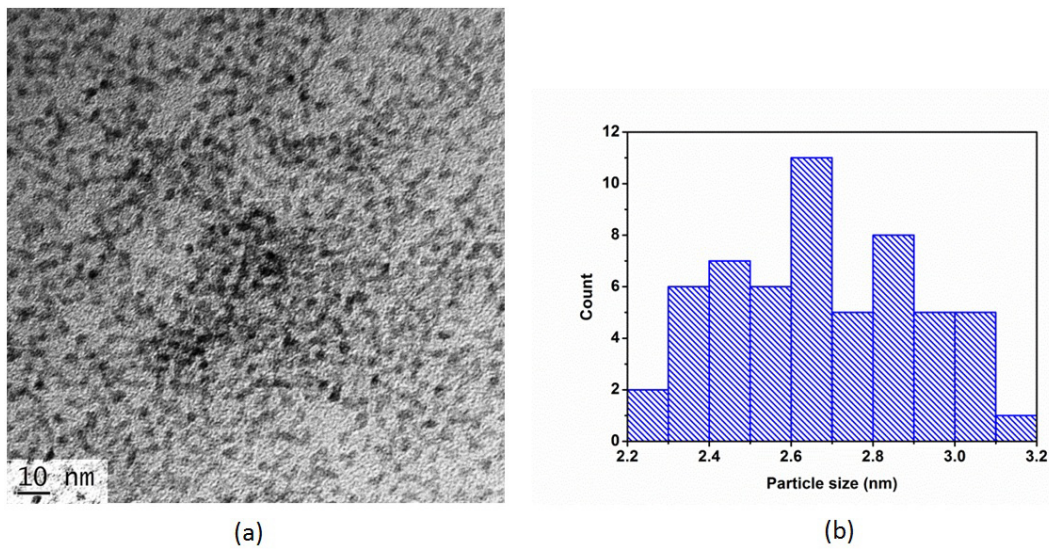


FIG. 7. a) TEM image b) histogram of particle size measurement of CdSe QD sample of 35 s, synthesized at the growth temperature of 215 °C

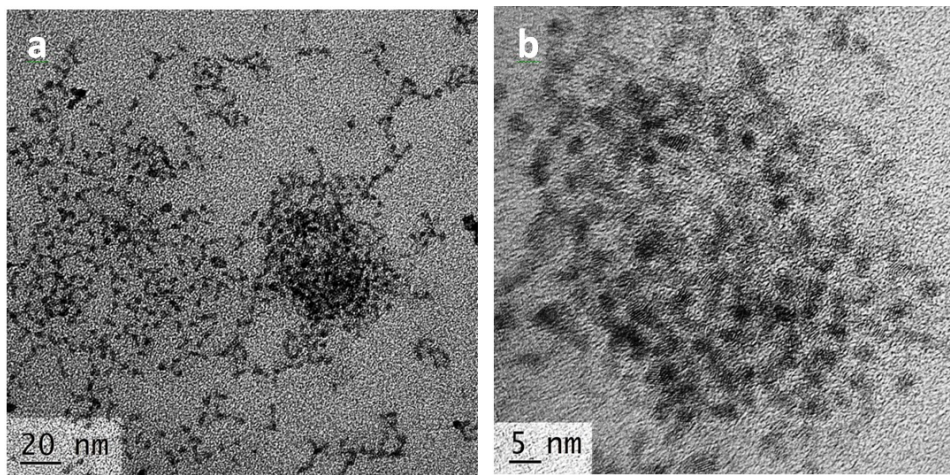


FIG. 8. a) TEM image and b) HRTEM image of sample at 10 s

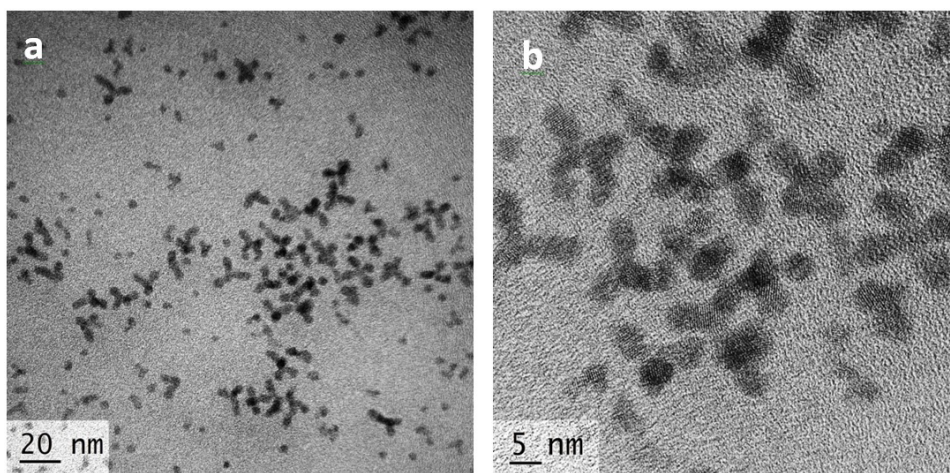


FIG. 9. a) TEM images and b) HRTEM images of sample at 2 min

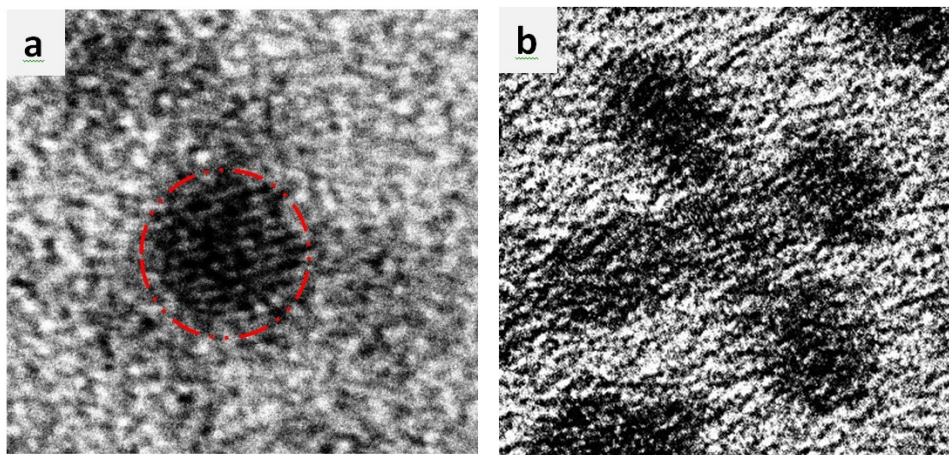


FIG. 10. HRTEM images of a) a single quantum dot from the sample at 10 s and b) a single nanotetrapod from the sample at 2 min

tendency of anisotropic growth. In contrast, sample at 2 min predominantly contains tetrapod structures characterized by a branch-lengths range from 7 nm to 9 nm and widths around 4 nm. The formation of the ZnSe outer layer is evident from the overlapping fringe patterns observed in Fig. 9b.). These patterns arise due to the difference in the d-spacing of CdSe and ZnSe, providing evidence for the presence of the ZnSe outer layer. To facilitate a better comparison, Fig. 10 displays images of a quantum dot from the sample at 10 s and a nanotetrapod from the sample at 2 min. The TEM images reveal a gradual transformation from a spherical to a tetrapod shape, providing clear evidence of the growth process.

Absorption and fluorescence spectra of samples of CdSe–ZnSe nano-tetrapods are given in Fig. 11. In the absorption spectra, second excitonic absorption peaks are clearly visible which indicate the good quality of the tetrapod structure. Fluorescence emissions of samples with 10 s, 1 min and 2 min are in the wavelength ranges from 510 nm to 550 nm, with an FWHM around 35 nm. These samples have colour purity similar to the CdSe QDs discussed in the previous section. Beyond 2 min, new emission at about 470 nm is observed while that at around 550 nm is absent. The tetrapod structures have a CdSe core of zinc blend structure with four wurtzite arms. The slow addition of Zn precursor causes growth of wurtzite structure of CdSe–ZnSe along the four (111) planes of the zinc blend structure [3, 15, 23]. The addition of zinc oleate eliminates the TOP surfactant and triggers an anisotropic growth by introducing a difference in surface energy. Once the surface coverage of ligands is reduced, arms of wurtzite structure are grown along the four (111) faces of the zinc blend CdSe [23]. The four arms are grown through the C-axis of the wurtzite structure [15]. The synthesized CdSe–ZnSe nano-tetrapod structure through this facile hot injection method was completed under ambient conditions with optical properties like significant fluorescence emission.

#### 4. Conclusion

In summary, we have investigated the facile hot injection synthesis method, excluding inert atmosphere and stringent chemical conditions, for the synthesis of CdSe QDs. The synthesis parameters such as injection temperature, precursor molar ratio and growth temperature suitable for the facile method were investigated and optimized. The optimized injection temperature was found to be 225 °C, in which highly monodisperse QDs were synthesized. The molar precursor ratio of 1:10 with excess Selenium was found to be optimum, which gives good quality of QDs in a wide range of particle sizes. The rate of growth of QDs was found to be directly related to the growth temperature. The growth temperature in the range from 210 to 215 °C gives moderate rate of growth, which gives better control over the particle size and improved repeatability. Using these optimized values, the facile method of synthesis of CdSe QDs was employed for the synthesis of CdSe–ZnSe nano-tetrapods of different sizes. Both the synthesized CdSe QDs and CdSe–ZnSe nano-tetrapods under the optimized conditions are exhibiting significant optical properties useful for the applications such as labelling, light emitting devices [19, 22, 24] etc.

#### References

- [1] Alivisatos A.P. Semiconductor Clusters, Nanocrystals, and Quantum Dots. *Science*, 1996, **271**, P. 933-937
- [2] Danek M., Jensen K., Chris B. Murray, Bawendi M.G. Synthesis of luminescent thin-film CdSe/ZnSe quantum dot composites using CdSe quantum dots passivated with an overlayer of ZnSe. *Chemistry of Materials*, 1996, **8**, P. 173–180.
- [3] Guo-Wei Huang, Chun-Yen Chen, Kun-Chan Wu, Moawia O. Ahmed, Pi-Tai Chou. One-pot synthesis and characterization of high-quality CdSe/ZnX (X = S, Se) nanocrystals via the CdO precursor. *Journal of Crystal Growth*, 2004, **265**, P. 250–259.
- [4] Wan Ki Bae, Kookheon Char, Hyuck Hur, Seonghoon Lee. Single-step synthesis of quantum dots with chemical composition gradients. *Chemistry of Materials*, 2008, **20**, P. 531–539.
- [5] Murray C.B., Norris D.J., Bawendi M.G. Synthesis and characterization of nearly monodisperse CdE (E = S, Se, Te) semiconductor nanocrystal-lites. *Journal of American Chemical Society*, 1993, **115**, P. 8706–8715.

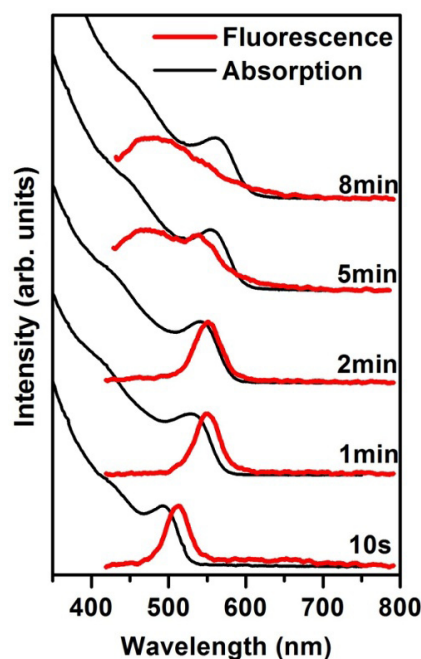


FIG. 11. Normalized absorption and fluorescence spectra of CdSe-ZnSe nano-tetrapod. Excitation wavelength of 400 nm was used for recording fluorescence spectra

- [6] Kalyuzhny G., Murray R.W. Ligand effects on optical properties of CdSe nanocrystals. *Journal of Physical Chemistry B*, 2005, **109**, P. 7012–7021.
- [7] Lianhua Qu, Z. Adam Peng, Xiaogang Peng. Alternative Routes toward High Quality CdSe Nanocrystals. *Nano Letters*, 2001, **1**, P. 333–337.
- [8] Z. Adam Peng, Xiaogang Peng. Formation of high-quality CdTe, CdSe, and CdS nanocrystals using CdO as precursor. *Journal of the American Chemical Society*, 2001, **123**, P. 183–184.
- [9] Lianhua Qu, Xiaogang Peng. Control of photoluminescence properties of CdSe nanocrystals in growth. *Journal of the American Chemical Society*, 2002, **124**, P. 2049–2055.
- [10] Lianhua Qu, Z. Adam Peng, Xiaogang Peng. Alternative routes toward high quality CdSe nanocrystals. *Nano Letters*, 2001, **1**, P. 333–337.
- [11] Karen J. Nordell, Elizabeth M. Boatman, and George C. Lisensky. A safer, easier, faster synthesis for CdSe quantum dot nanocrystals. *Journal of Chemical Education*, 2005, **82**, P. 1697.
- [12] Boni Samuel, Mathew S, V.R. Anand, Adrine Antony Correya, V.P.N. Nampoore, A. Mujeeb. Surface defect assisted broad spectra emission from CdSe quantum dots for white LED application. *Materials Research Express*, 2018, **5**, P. 025009.
- [13] Boni Samuel, Mathew S., V.P.N. Nampoore, A. Mujeeb. Defect passivation introduced through surface reconstruction in TOPO capped CdSe quantum dots for enhancement in quantum yield. *Optical Materials*, 2019, **88**, P. 204–209.
- [14] Hosub Lim, Ju Young Woo, Doh C. Lee, Jinkee Lee, Sohee Jeong, Duckjong Kim. Continuous purification of colloidal quantum dots in large-scale using porous electrodes in flow channel. *Scientific Reports*, 2017, **7**, P. 1–8.
- [15] Pang, Qi Zhao, Lijuan Cai, Yuan Nguyen, Duc Phuong Regnault, Nicolas Wang, Ning Yang, Shihe Ge, Weikun Ferreira, Robson Bastard, Gérald Wang, Jiannong. CdSe Nano-tetrapods: controllable synthesis, structure analysis and electronic and optical properties. *Chemistry of Materials*, 2005, P. 5263–5267.
- [16] Qin Zhang, Chao Nie, Chun Chang, Chenyang Guo, Xiao Jin, Yuancheng Qin, Feng Li, and Qinghua Li. Highly luminescent red emitting CdZnSe/ZnSe quantum dots synthesis and application for quantum dot light emitting diodes. *Optical Materials Express*, 2017, **7**, P. 3875–3884.
- [17] Liberato Manna, Erik C. Scher, and A. Paul Alivisatos. Synthesis of soluble and processable rod-, arrow-, teardrop-, and tetrapod-shaped CdSe nanocrystals. *Journal of the American Chemical Society*, 2000, P. 12700–12706.
- [18] Craig R. Bullen and Paul Mulvaney. Nucleation and growth kinetics of CdSe nanocrystals in octadecene. *Nano Letters*, 2004, **4**, P. 2303–2307.
- [19] Lim J., Jun S., Jang E., Baik H., Kim H., Cho J. Preparation of highly luminescent nanocrystals and their application to light-emitting diodes. *Advanced Materials*, 2007, **19**, P. 1927–1932.
- [20] Ratnesh R.K., Mohan Singh Mehata. Synthesis and optical properties of core-multi-shell CdSe/CdS/ZnS quantum dots: Surface modifications. *Optical Materials*, 2017, **64**, P. 250–256.
- [21] Hsueh Shih Chen; Shian Jy Jassy Wang; Chun Jue Lo; Jim Yong Chi. White-light emission from organics-capped ZnSe quantum dots and application in white-light-emitting diodes. *Applied Physics Letters*, 2005, **86**, P. 131905.
- [22] Jeonghun Kwak, Jaehoon Lim, Myeongjin Park, Seonghoon Lee, Kookheon Char, Changhee Lee. High-power genuine ultraviolet light-emitting diodes based on colloidal nanocrystal quantum dots. *Nano Letters*, 2015, **15**, P. 3793–3799.
- [23] Jaehoon Lim, W. Bae, Ko Un Park, L. Z. Borg, R. Zentel, Seonghoon Lee, K. Char. Synthesis of CdSe tetrapods with high morphological uniformity by the persistent kinetic growth and the halide-mediated phase transformation. *Chemistry of Materials*, 2013, **25**(8) P. 1443–1449.
- [24] Hsueh-Shih Chen; Cheng-Kuo Hsu; Hsin-Yen Hong. InGaN-CdSe-ZnSe quantum dots white LEDs. *IEEE Photonics Technology Letters*, 2006, **18**, P. 193–195.

*Information about the authors:*

*Boni Samuel* – International School of Photonics, Cochin University of Science and Technology, Kochi-22, India; Nirmala College, Muvattupuzha, Ernakulam; ORCID 0000-0003-4743-0692; boni@nirmalacollege.ac.in

*K. J. Adarsh* – International School of Photonics, Cochin University of Science and Technology, Kochi-22, India; Sophisticated Test and Instrumentation Centre, Cochin University of Science and Technology, Kochi -22, India; ORCID 0000-0002-5142-8758; adarsh@cusat.ac.in

*V. P. N. Nampoori* – International School of Photonics, Cochin University of Science and Technology, Kochi-22, India; Nampoori@gmail.com

*A. Mujeeb* – International School of Photonics, Cochin University of Science and Technology, Kochi-22, India; ORCID 0000-0002-5694-0566; mujeebpoovar@gmail.com

*Conflict of interest:* the authors declare no conflict of interest.

## The role and effect of CO<sub>2</sub> flow rate on the structure formation of ultrahigh porous activated carbon from H<sub>3</sub>PO<sub>4</sub>-impregnated waste cotton used as supercapacitor electrode material

Nguyen K. Thach<sup>1,2,a</sup>, Ilya S. Krechetov<sup>1,b</sup>, Valentin V. Berestov<sup>1,c</sup>, Oleg I. Kan<sup>1,d</sup>,  
Ivan A. Maslochenko<sup>1,e</sup>, Tatyana L. Lepkova<sup>1,f</sup>, Svetlana V. Stakhanova<sup>1,3,g</sup>

<sup>1</sup>National University of Science and Technology “MISIS”, Moscow, Russia

<sup>2</sup>College of electromechanical and civil engineering, Vietnam National University of Forestry, Hanoi, Vietnam

<sup>3</sup>Mendeleev University of Chemical Technology of Russia, Moscow, Russia

<sup>a</sup>nguyenkienthach@gmail.com, <sup>b</sup>ilya.krechetov@misis.ru, <sup>c</sup>vberestov97@gmail.com, <sup>d</sup>m2106915@edu.misis.ru,

<sup>e</sup>maslochenko3@mail.ru, <sup>f</sup>lepkova.tl@misis.ru, <sup>g</sup>stakhanova.s.v@muctr.ru

Corresponding author: N. K. Thach, [nguyenkienthach@gmail.com](mailto:nguyenkienthach@gmail.com)

**ABSTRACT** Ultrahigh porosity activated carbon (AC) was made from H<sub>3</sub>PO<sub>4</sub>-impregnated waste cotton precursor by carbonization in Ar and physical activation in variable CO<sub>2</sub> flow rate with ultrahigh heating rate. The presence of CO<sub>2</sub> in the activation plays an important role in the formation of the porous structure of AC. The obtained AC had outstanding physical and electrochemical properties. The specific surface area and micropore volume of AC reached 4800.7 m<sup>2</sup>/g and 2.499 cm<sup>3</sup>/g, respectively. The pore size distribution was mainly in the microporous region. The electrochemical double-layer capacitors (EDLCs) with AC-based active electrode and an electrolyte solution of 1 M 1,1-dimethylpyrrolidinium tetrafluoroborate in acetonitrile were fabricated. The specific capacitance of electrode material degraded less than 10 % with the highest value of 105.7 F/g at 0.05 A/g as the specific current varied from 0.05 A/g – 15 A/g. After 8000 charge-discharge cycles at 1 A/g, the specific capacitance of the AC-base electrode material fabricated at CO<sub>2</sub> flow rate greater than 200 ml/min degraded less than 15 % with the highest value of 101.2 F/g. The optimal CO<sub>2</sub> flow rate for fabricating waste cotton-based AC is 200 ml/min.

**KEYWORDS** activated carbon, porous activated carbon, cellulose, waste cotton, supercapacitor.

**ACKNOWLEDGEMENTS** The authors would like to thank Dr. Alexey Igorevich Salimon, Dean of the Department of Physical Chemistry, the College of New Materials and Nanotechnologies, the University of Science and Technology “MISIS”, Moscow, Russia, for valuable recommendations on the content of the article. The authors would also like to thank The Hierarchically Structured Materials Lab, Center for Digital Engineering, Skoltech, Moscow, Russia, for helping us to conduct the BET and SEM measurements.

**FOR CITATION** Thach N.K., Krechetov I.S., Berestov V.V., Kan O.I., Maslochenko I.A., Lepkova T.L., Stakhanova S.V. The role and effect of CO<sub>2</sub> flow rate on the structure formation of ultrahigh porous activated carbon from H<sub>3</sub>PO<sub>4</sub>-impregnated waste cotton used as supercapacitor electrode material. *Nanosystems: Phys. Chem. Math.*, 2023, **14** (4), 489–497.

### 1. Introduction

Energy has been the crucial issue for the global economy. Currently, the main energy resources for human are fossil resources such as coal, crude oil, and natural gas, etc. The excessive use and depletion of these resources have been causing serious environmental pollution. Therefore, people have been looking for renewable energy sources that are environmentally friendly and can gradually replace fossil fuels such as solar energy, wind energy, tidal energy [1–3], etc. However, these energy sources are intermittent and vary with time of a day, seasons, and years. So, they have been required a highly efficient energy storage and conversion system to maintain continuous operation. Batteries and supercapacitors are main electrical energy storage and conversion devices today.

Batteries store energy in the form of chemical energy based on redox reactions occurring on the electrodes. The stored energy of the battery is large and can meet most of the energy demands of electrical and electronic devices in daily life [4]. The drawbacks of the batteries are low power density, short life-cycle and containing some toxic substances that are harmful to the environment at the end of their life. Meanwhile, EDLCs store energy in the form of static electricity that is formed on the interface of the electrochemical double layer between the electrolyte solution and the electrode material surface [5]. Comparing to batteries, EDLCs have a much lower energy density but have higher power density, energy conversion efficiency, long life-cycle (over 100000 charge-discharge cycles) and can operate in extreme environments

with temperatures ranging from  $-40 - +75$  °C [1, 5]. Therefore, depending on the real life applications, batteries and supercapacitors have been used as stand-alone systems or integrated both into real devices such as lights, maintain and protect the memory of electronic devices, cars, trains, and space devices [6, 7], etc. to take benefit of their advantages and limit their drawbacks.

Recently, high porosity AC (with specific surface area greater than  $1000 \text{ m}^2/\text{g}$ ) has been widely used as electrode materials for both batteries and supercapacitors. Among the materials used to produce porous AC, biomass materials are receiving much attention from researchers because they are available, abundant, renewable, and environmentally friendly. They are often waste products of the agricultural and forest products processing industry such as rice husks [8], corncob [9], olive stones [10], sugarcane bagasse [11], cotton [12–14], and cotton stalk [15], etc. To convert biomass materials into porous AC, two main processes are used: carbonization and activation.

The carbonization process is usually carried out in an inert gas ( $\text{N}_2$  or Ar) at temperatures between 400 and 900 °C. The precursors have been impregnated with substances such as  $\text{ZnCl}_2$  [16], KOH,  $\text{H}_3\text{PO}_4$  [11, 17], etc. with different ratios to increase the carbon yield of the obtained products and create favorable conditions for the growth of pore structures during the activation process. There are two processes of carbon activation: physical activation and chemical activation. The physical activation is carried out in a redox gaseous environment such as  $\text{CO}_2$ ,  $\text{H}_2\text{O}$  [18], etc at a temperature of 700 – 1200 °C. These redox gases diffuse deep into the structure of carbon and react with carbon to form and expand pore structures. As a result, the obtained porous AC has large surface area and good pore size distribution. Meanwhile, chemical activation is carried out at a temperature of 500 – 800 °C in the presence of activating agents. The raw material is impregnated with a given activating agent and there are many selective chemical reactions occurring during activation. The result is AC with an amorphous material and the existence of intercalate ions in the structure.

In this study,  $\text{H}_3\text{PO}_4$ -impregnated waste cotton was used to fabricate porous AC because cotton is a naturally highly porous, high content of cellulose (between 80–97% by weight [15, 19, 20]) and less impurities. The porous AC production was conducted in two processes: carbonization at 600 °C in Ar atmosphere and activation at 900 °C in the absence or presence of  $\text{CO}_2$  with variable gas flow rate.

## 2. Materials and methods

### 2.1. Fabricating porous AC

*2.1.1. Preparing  $\text{H}_3\text{PO}_4$ -impregnated waste cotton.* Waste cotton was supplied by Yartsevo Cotton Mill, LLC (Russia).

85 %  $\text{H}_3\text{PO}_4$  solution according to standard GOST 6552-80 (Russia) was diluted with deionized water to form 5 %  $\text{H}_3\text{PO}_4$  solution.

20 g of cotton was immersed in 600 g of 5%  $\text{H}_3\text{PO}_4$  solution. The mixture was heated to a temperature above 80 °C and maintained for 30 minutes. The cotton was then squeezed out and dried at room temperature for 48 h.

*2.1.2. Carbonization process.* Based on our previous research results on optimizing the temperature of the carbonization process to the properties of activated carbon used as electrode materials for supercapacitors [21], we choose the temperature of 600 °C to conduct the carbonization process of  $\text{H}_3\text{PO}_4$ -impregnated cotton.

To increase the uniformity of the torn cotton compared to our previous experiments, 5 g of  $\text{H}_3\text{PO}_4$ -impregnated cotton was torn up by the tearing machine and then loaded into a horizontal reaction chamber with a length of 60 cm and a diameter of 10 cm. Then, Ar gas was supplied at a flow rate of 800 ml/min for 10 minutes to remove air.

Initially, the furnace was heated to 600 °C with a heating rate of 10 °C/min. After reaching the temperature of 600 °C, the reaction chamber was loaded into furnace and maintained with a flow rate of Ar gas of 800 ml/min. By this method, the heating rate of 585 °C/min  $\pm$  10 % was achieved. The carbonization time was 1 h. After carbonization, the reaction chamber was taken out and cooled to room temperature with an Ar flow rate of 800 ml/min and a cooling system. The product was called black carbon fiber (BCF). The obtained products were weighed and stored in nylon bags to avoid dust.

*2.1.3. Activation process.* 1.5 g BCF was added into the reaction chamber. The Ar gas was supplied at a flow rate of 800 ml/min for 10 minutes to remove air.

Initially, the furnace was heated to 900 °C with a heating rate of 10 °C/min. When the furnace reached 900 °C, the reactor chamber was loaded inside, and an Ar flow rate of 800 ml/min was maintained. The heating rate of 751 °C/min  $\pm$  10 % was achieved. When the system was reached 900 °C again, the Ar supply was cut off and  $\text{CO}_2$  was supplied with a flow rate varying from 100 – 800 ml/min. The activation time was 1 h. When the activation process was complete, the  $\text{CO}_2$  flow was cut off and the reaction chamber was taken out and cooled to room temperature with an Ar flow rate of 800 ml/min and a cooling system. The obtained AC products were labeled as CT0 to sample without  $\text{CO}_2$ , and CT1, CT2, CT4, CT8 corresponding to samples with  $\text{CO}_2$  flow rate of 100, 200, 400 and 800 ml/min. With the CT0 sample, the Ar flow rate of 100 ml/min was maintained to remove volatile derivatives during activation.

## 2.2. Fabricating supercapacitor

**2.2.1. Fabricating carbon electrode.** The AC was crushed by mortar and mixed with polytetrafluoroethylene F4D suspension (Russia) used as the binder and carbon black (CABOT®VULCAN ©XC72) as the conducting agent according to the ratio percentage by mass was 80:10:10. The mixture was then added in a glass flask containing 100 ml of deionized water and stirred at 50 °C for 30 minutes. The slurry was filtered, and the obtained material was rolled on a mechanical roller to form a thin film with a thickness of 150 μm. The films were then cut into square electrodes with dimensions of 2.5×2.5 cm and dried at 120 °C in drying oven for 24 h and weighed to an accuracy of 0.001 g.

**2.2.2. Fabricating supercapacitor.** Two carbon electrodes were selected as active electrodes of a capacitor with a mass difference of less than 0.002 g. These carbon electrodes were pasted on the aluminum foils (OKURA-801, Japan) by RIKON adhesive (Russia). Two complete electrodes were placed opposite and separated by separator TF-40-30 (Japan). The electrode system was placed in an adhesive enclosure and kept under vacuum at 120 °C for 48 h. Next, the enclosure was filled with 1 ml electrolyte solution of 1M 1,1-dimethylpyrrolidinium tetrafluoroborate (DMP·BF<sub>4</sub>) in acetonitrile (ACN) solvent and packed to form a complete capacitor.

## 2.3. Instruments and methods for investigating physical and electrochemical properties of porous AC

The surface morphology of AC was investigated by the scanning electron microscope (SEM) TESCAN MIRA (Czech).

The texture characteristics of AC were investigated by the N<sub>2</sub> adsorption-desorption method at 77 K on the Quantachrome LX<sup>2</sup> machine (Quantachrome, Austria).

X-ray diffraction (XRD) spectra were investigated on XPERT-PRO (Latvia) with the emission spectrum of copper with wavelength Kα = 1.541 Å. The X-ray scanning angle from 5 to 80 ° with a scan step of 0.03 ° and a dwelling time of 0.5 s.

The P20-X potentiostat (Elins, Russia) was used to measure the cyclic voltammetry (CV) characteristics of the supercapacitors.

The galvanostatic charge-discharge (GCD) method was used to test the performance of the supercapacitors by using ASK2.5.10.8 HIT analyzer (Russia).

## 3. Results and discussion

### 3.1. AC yield

According to K. Raveendran et al. [22], the thermal decomposition of cellulose and its derivatives takes place intensely in the temperature range of 350 – 450 °C. By the above carbonization method, the lowest furnace average temperature was reached 555 °C which was much greater than the thermal decomposition temperature range of cellulose. At this temperature, the thermal decomposition of cellulose takes place intensely. The decomposition products are water, CO<sub>2</sub>, volatile compounds that exist in the gaseous state. These substances partially penetrate the cotton fiber to dissolve and break the structure of the cellulose crystals creating micro-swelling and the rest evaporate intensely. As a result, there is the formation of open or sealed porous structures that exist manifold within the structure of the obtained material. The carbon yield in our study was achieved average value of 32.3 %.

According to Peng Fu et al. [23], there are some heavy chemical compounds which exist in the solid carbon structure after carbonization and continue thermal decomposition at temperatures range 500 – 800°C. Therefore, there were some derivatives of the cellulose decomposition existing in the obtained BCF after carbonization. Furthermore, there were a certain amount of water vapor and gases which were adsorbed into BCF structure during the storage. Our carbon activation method described above was achieved the lowest furnace average temperature of 786 °C. At this temperature, the derivatives and gases adsorbed on the surface of BCF were evaporated and ejected by the Ar flow. This created favorable conditions for the contact of CO<sub>2</sub> with BCF surface during the activation and facilitated the formation of porous structures. The main reaction took place in the activation according to the equation CO<sub>2</sub> + C = 2CO. The AC yield was shown in Fig. 1.

As shown in Fig. 1, the AC yield decreased as increasing CO<sub>2</sub> flow rate. With sample CT0, the mass of the obtained AC was decreased when compared with the initial mass of BCF although no CO<sub>2</sub> was used in the activation process. This meant that some cellulose derivatives still existed in the original BCF after carbonization. For the other samples, the presence of CO<sub>2</sub> reacted with the carbon and significantly reduced the mass of the AC. The AC yield decreased as the CO<sub>2</sub> flow rate increased. This indicated that CO<sub>2</sub> burned most of the carbon and drastically reduced the AC yield at a high CO<sub>2</sub> flow rate.

When comparing the CT8 sample with the SP600 sample of the previous study [21] with the same flow rates of Ar and CO<sub>2</sub> for both carbonization and carbon activation processes, we found that the carbon yield after carbonization increase insignificantly (from 31.4% to 32.3%), while the activated carbon yield decreased significantly (from 3.3% to 2.2%). This shows that increasing the uniformity of the cotton before loading into the reaction chamber has increased the contact between the gas environment (Ar, CO<sub>2</sub>) and the surface of the bulk cotton. As a result, in the carbonization, the

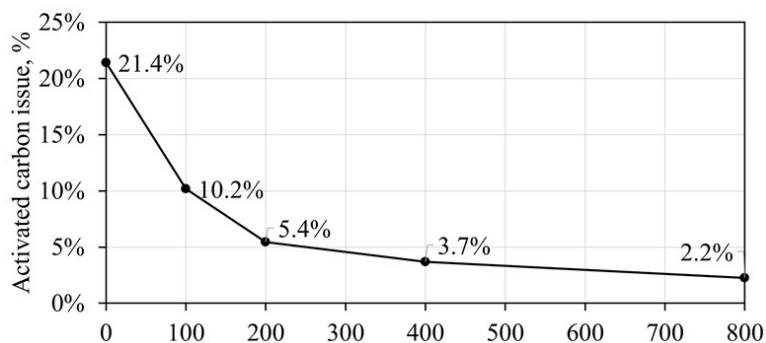


FIG. 1. Activated carbon yield after activation in the absence and presence of  $\text{CO}_2$  at different flow rates

pyrolysis products of cotton will come out easily, the BCF fibers are not sticky. This increases the diffusion ability of  $\text{CO}_2$  during activation into the BCF bulk, increasing the reaction between  $\text{CO}_2$  and carbon leading to the decreasing activated carbon yield.

### 3.2. Physical properties of porous AC

The XRD spectrum of the AC samples were shown in Fig. 2. A broad (002) graphite plane peak at  $2\theta \sim 23.8^\circ$  of sample CT0 was clearer than that of the other samples. This indicated that the CT0 sample was began to graphitize at  $900^\circ\text{C}$  while the rest samples were not. This evidence also demonstrated that  $\text{CO}_2$  reacted with C on the pore wall, destroying the carbon crystal structure and increasing the amorphousness of the obtained porous AC. No obvious (001) graphite plane peak was observed at  $2\theta \sim 44^\circ$ . As a result, the AC was amorphous carbon.

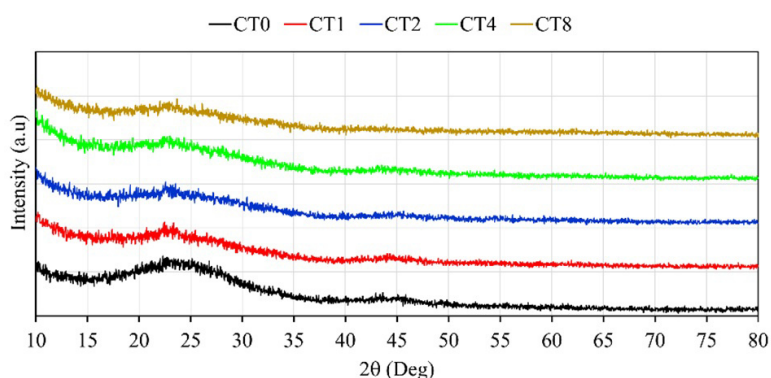


FIG. 2. XRD spectrum of the AC samples fabricated by activation with variable  $\text{CO}_2$  flow rate

The SEM image of the CT2 sample was shown in Fig. 3. As shown in Fig. 3a,b, the obtained AC fiber retained the typical twisted, flattened shape of the original cotton fiber, without impurities adhering to the fiber surface and the fiber size was less than  $10\ \mu\text{m}$ . Fig. 3c showed that there was uniform pore formation, well development of pore structure and pore distribution in the microporous and mesoporous regions.

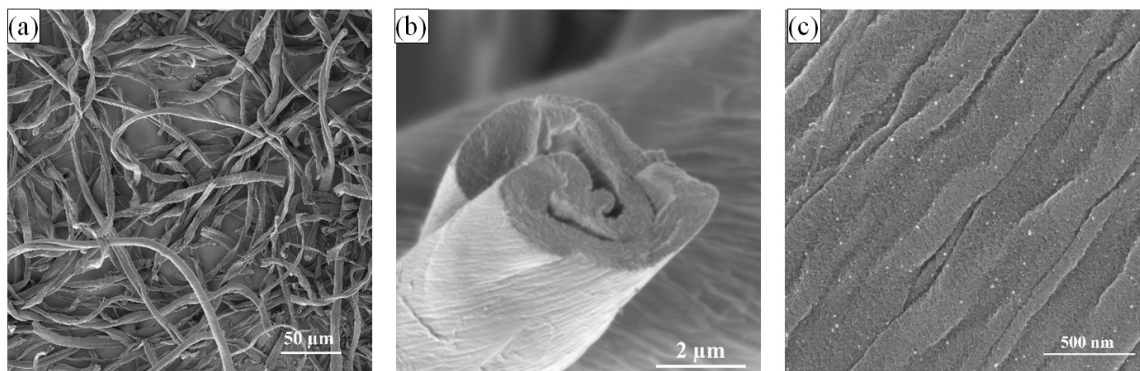


FIG. 3. SEM image of sample CT2

TABLE 1. The surface characteristics of the AC samples

Sample	$S_{BET}$ (m <sup>2</sup> /g)	$S_{mic}$ (m <sup>2</sup> /g)	$S_{mes}$ (m <sup>2</sup> /g)	$V_{mic}$ (cm <sup>3</sup> /g)	$d$ (nm)
CT0	651.2	–	–	0.343	0.52
CT1	1904.4	1220.3	684.1	0.869	1.32
CT2	4800.7	3138.8	1661.9	2.499	1.65
CT4	3557.8	2156.8	1401.0	1.963	1.98
CT8	3863.5	2460.2	1403.3	2.127	1.87

The N<sub>2</sub> adsorption-desorption method at the temperature of 77 K was used to investigate the surface characteristics of the porous AC. The degas process was conducted at 250 °C within 4 h in vacuum. The N<sub>2</sub> adsorption isotherms was conducted with the relative pressure ( $p/p_0$ ) from 0.05 to 0.99 and obtained results as shown in Fig. 4. The N<sub>2</sub> isotherms of all samples had the form corresponding to Type I(b) according to the IUPAC classification [24, 25]. This meant that the pore size was mainly in the microporous region and partly in the mesoporous region with the size less than 2.5 nm. The N<sub>2</sub> adsorption capacity increased rapidly in the presence of CO<sub>2</sub> during the activation process and achieved the highest value at the CO<sub>2</sub> flow rate of 200 ml/min.

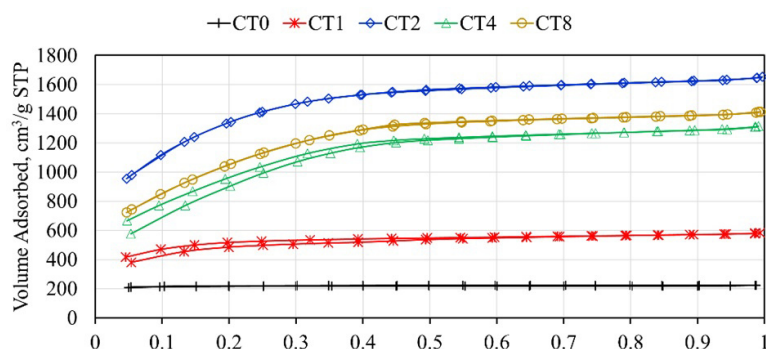


FIG. 4. N<sub>2</sub> adsorption-desorption isotherms of AC prepared in the absence or presence of CO<sub>2</sub> at different CO<sub>2</sub> flow rates

The Brunauer, Emmet, and Teller (BET) method was used to assess the specific surface area of the AC. The specific surface area ( $S_{BET}$ ) was determined in the relative pressure range from 0.05 to 0.3 for the CT0 sample and 0.05 to 0.15 for the rest samples according to IUPAC recommendations for specific surface area assessment of microporous materials. The micropore volume ( $V_{mic}$ ) and pore size ( $d$ ) were determined by the Dubinin–Radushkevich (DR) method. The surface area of the micropore ( $S_{mic}$ ) and pore size distribution were determined by the Density functional theory (DFT) method. The surface area of the mesopore ( $S_{mes}$ ) is the result of the subtraction between  $S_{BET}$  and  $S_{mic}$ . The results were shown in Tables 1 and Fig. 5.

As shown in Table 1, specific surface area ( $S_{BET}$ ), micropore surface area and micropore volume ( $V_{mic}$ ) increased rapidly when the CO<sub>2</sub> flow rate increased from 0 to 200 ml/min and then decreased unevenly when the CO<sub>2</sub> flow rate increased from 200 to 800 ml/min. The highest values of  $S_{BET}$ ,  $S_{mic}$ , and  $V_{mic}$  achieved at the CO<sub>2</sub> flow rate of 200 ml/min were 4800.7 m<sup>2</sup>/g, 3138.8 m<sup>2</sup>/g, and 2.499 cm<sup>3</sup>/g, respectively. This proved that the porous structures developed very well inside the initial BCF and facilitated the development of micropores during activation in the presence of CO<sub>2</sub>. At low CO<sub>2</sub> flow rates, CO<sub>2</sub> molecules have enough time to diffuse deep into the structure of BCF and react with the carbon on the micropore wall to open and enlarge the pores, and thus increase specific surface area, micropore surface area and micropore volume. Meanwhile at high CO<sub>2</sub> flow rates, the amount of CO<sub>2</sub> is larger, the CO<sub>2</sub> molecules move faster and directly participates in the reaction with carbon on the micropore wall on the outer side of BCF more. Consequently, the  $S_{BET}$ ,  $S_{mic}$  and  $V_{mic}$  decrease, and pore size is larger.

As shown in Fig. 5, the pore size distribution peaks of all samples located in the microporous region less than 2 nm and there are no peaks in the mesoporous region. The samples CT0, CT1 had low peaks and small micropore volume. Meanwhile, samples CT2, CT4, and CT8 had three outstandingly high main peaks and were in the microporous region with size less than 1.5 nm. Fig. 5 also showed that there was a shift of the pore size distribution peaks to a larger pore size region as the CO<sub>2</sub> flow rate increased from 200 to 800 ml/min.

When comparing the physical properties of sample CT8 with SP600 of the previous study [21], the obtained activated carbon has an amorphous structure in both cases. However, the specific surface area of the CT8 increased by about 40%

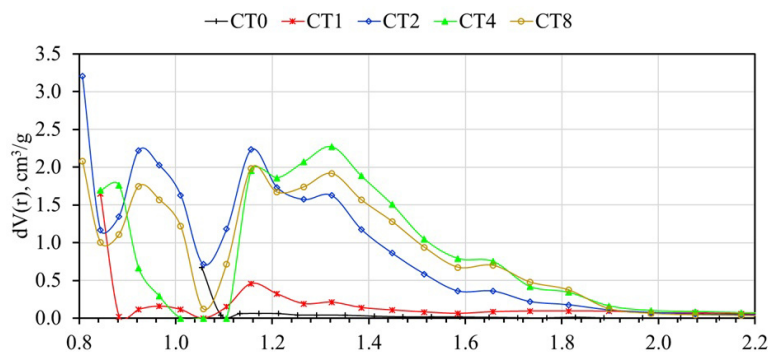


FIG. 5. Pore size distribution of AC materials was determined by the DFT method

compared with that of the SP600 while the pore size decreased from 2.62 nm to 1.87 nm. This again proves that increasing the uniformity of the initial torn impregnated cotton has increased the contact area and increased the diffusivity of  $\text{CO}_2$  into the structure of BCF. Consequently, obtained activated carbon has outstanding physical properties.

### 3.3. Electrochemical properties of porous AC

There are many factors that affect the performance and capacitance of an EDLC such as electrolyte solution, carbon electrodes, collectors, binder [26], etc. Among others, the carbon electrodes and electrolyte solution are the two main factors affecting the performance and specific capacitance value of the EDLCs. The electrolyte adsorption capacity of porous AC materials depends on the surface area and surface functional groups when the carbon electrodes expose to an electrolyte solution. Besides, the matching of the pore size of AC and the electrolyte ion size plays an important role in the diffusion of electrolyte ions deep into the porous structure of carbon electrodes. The electrolyte ions in solution exist in a solvated state when combined with solvent molecules. In ACN solvent, the size of the  $[\text{BF}_4]^-$  ion is about 1.40 nm while the bare ion size is 0.48 nm [27], and the  $[\text{DMP}]^+$  ion has a bare size of 0.44 nm [28]. For microporous AC, when micropore size close to electrolyte ion size, electrolyte ions partly remove the solvent molecular shell and may be deformed during diffusion into micropores [28]. In contrast, the pores will also be deformed during the diffusion of these ions. Consequently, the specific capacitance of the electrode material will change during the continuous operation of the EDLCs.

Figure 6 showed the CV curves of the EDLCs at the potential scan rate of 100 mV/s with the potential varying from 0 to 2.7 V. The CV curve of CT0 was small and highly distorted, while the CV curves of CT1, CT2, CT4, CT8 were a like-rectangular shape. This demonstrated that the surface adsorption property of CT0's carbon electrodes are poor for  $[\text{DMP}]^+$  and  $[\text{BF}_4]^-$  ions. Meanwhile, the CT1, CT2, CT4, CT8 samples had the characteristics of the ideal capacitors, and their carbon electrodes had good reversible electrochemical properties.

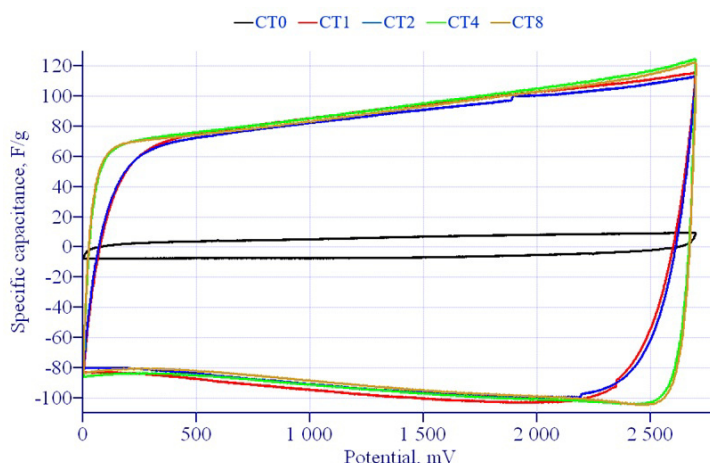


FIG. 6. The CV curves of fabricated supercapacitors at potential scan rate 100 mV/s

Figure 7 showed the dependence of the specific capacitance of electrode material of EDLCs depending on the specific current density varying from 0.05 A/g to 15 A/g and the charge-discharge characteristic of EDLCs at current density of 1 A/g. The specific capacitance of electrode material of CT0 sample was small and decreased quickly with increasing current density up to a value of 10 A/g. Besides, the GCD curve of the CT0 capacitor was asymmetrical and had large IR

drop (Fig. 7b). Therefore, the electrode material of the CT0 capacitor had poor reversibility electrochemical properties and was not suitable as an electrode material for EDLCs. In contrast, the specific capacitance of electrode material of CT1, CT2, CT4, CT8 capacitors were high and degrade less than 10 % as the current density increased up to a value of 15 A/g, and the GCD curves were highly symmetric, and small IR drop. The highest specific capacitance of electrode material reached 105.7 F/g for the CT<sub>4</sub> sample at 0.05 A/g. These proved that the obtained AC when using CO<sub>2</sub> in activation had high stability during the performance of the capacitors, good reversible electrolyte ions adsorption characteristics. The AC materials can be used as electrode materials for high-performance supercapacitors.

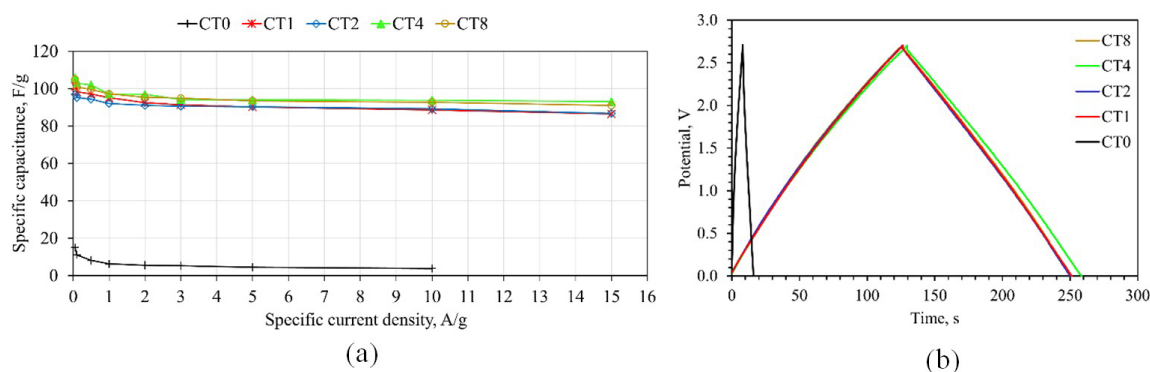


FIG. 7. (a) The dependence of specific capacitance on the current density from 0.05 A/g to 15 A/g and (b) the GCD curves at 1 A/g of the fabricated supercapacitors

When considering the surface area and pore size of AC (Table 1) affect the specific capacitance of electrode material, we found that although  $S_{BET}$ ,  $S_{mic}$  varied greatly, the capacitance of the electrode material did not change much (ca. 5%) between samples CT1, CT2, CT4 and CT8. For the CT2 sample,  $S_{BET}$ ,  $S_{mic}$  were much larger than that of the CT1 sample, but the pore size was mainly distributed in the ultra microporous region, so the electrolyte ions cannot access the inner surface of the pores. Thus, the specific capacitance value of CT2 and CT1 was the same value. The CT4 and CT8 samples had larger pore sizes and thus accessible electrolyte ions had a larger specific capacitance. This demonstrated that the specific capacitance of electrode material depended mainly on the pore size distribution rather than the specific surface area.

The GCD method was used to investigate the life-cycle of the supercapacitors with AC-based electrodes at current density of 1 A/g with potential varied from 0 to 2.7 V and 8000 charge-discharge cycles. We did not conduct GCD testing with the CT0 sample because it was unstable at 1 A/g. The GCD curves of the CT1, CT2, CT4 and CT8 were shown in Fig. 8.

As shown in Fig. 8, the relative capacitance of all capacitors changed rapidly (ca. 10%) during the first 1000 cycles. The CT1 sample was disconnected from the power supply after 4200 cycles. Then it was resumed operation, its relative capacitance recovered a significant value of ca. 90 % and degraded ca. 25% after 8000 cycles. Meanwhile, the specific capacitance of CT2, CT4 and CT8 degraded insignificantly (ca. 5%) from 1000 to 8000 cycles. The capacitance degradation of the CT2, CT4 and CT8 after 8000 cycles were 15%, 15 %, 12 %, respectively. The maximum capacitance value was achieved 101.2 F/g for the CT4 sample. Thus, the obtained activated carbon from activation with CO<sub>2</sub> flow rate greater than 200 ml/min exhibited more stability during the continuous operation of the EDLCs.

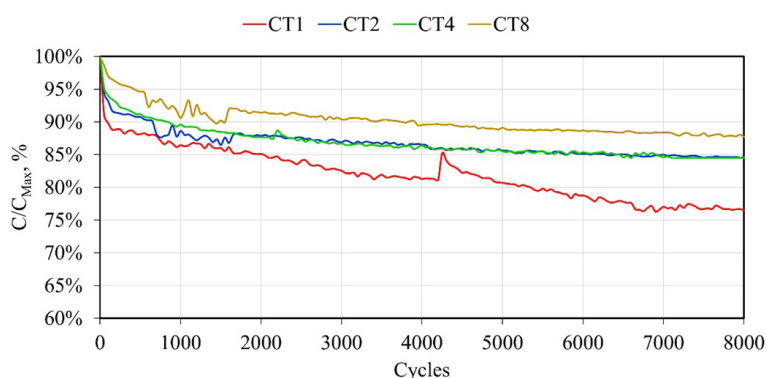


FIG. 8. The dependence of relative capacitance of supercapacitors on the number of charge-discharge cycles at a specific current density of 1 A/g and potential varied from 0 – 2.7 V

#### 4. Conclusion

By carbonization method with extremely heating rate and the temperature of carbonization of  $\text{H}_3\text{PO}_4$ -impregnated waste cotton much higher than that of cellulose, the BCF with abundance of sealed pores inside fiber structure was fabricated. The presence of  $\text{CO}_2$  during the activation with extremely heating rate plays an important role in opening the sealed pores inside BCF structure and facilitating the growth of micropores. The obtained AC was the amorphous carbon and had ultrahigh specific surface area, micropore surface area and micropore volume of  $4800.8 \text{ m}^2/\text{g}$ ,  $3138.8 \text{ m}^2/\text{g}$  and  $2.499 \text{ cm}^3/\text{g}$ , respectively and the pore size distribution was mainly in the microporous region.

The EDLCs with carbon electrodes fabricated from AC obtained by activation in the presence of  $\text{CO}_2$  have high stability and good reversible electrochemical properties to current density up to a value of  $15 \text{ A/g}$ , and the specific capacitance degradation of less than 10 %. The specific capacitance degraded less than 15% with the samples that fabricated at  $\text{CO}_2$  flow rate higher than  $200 \text{ ml/min}$ . The specific capacitance of activated carbon depends strongly on the matching of the average micropore size of AC material and the electrolyte ion size rather than the specific surface area of the material. While the surface area varies greatly and the pore size varies slightly, the specific capacitance of the electrode material changes insignificant. The obtained porous activated carbon material can be used as an electrode material for high-performance supercapacitors. We recommend that the  $\text{CO}_2$  flow rate in the production of activated carbon from  $\text{H}_3\text{PO}_4$ -impregnated waste cotton is  $200 \text{ ml/min}$ .

#### References

- [1] Şahin M., Blaabjerg F., and Sangwongwanich A. A Comprehensive Review on Supercapacitor Applications and Developments. *Energies (Basel)*, 2022, **15**(3), P. 674–699.
- [2] Kumar G.V.B., Kaliannan P., Padmanaban S., Holm-Nielsen J.B., and Blaabjerg F. Effective Management System for Solar PV Using Real-Time Data with Hybrid Energy Storage System. *Applied Sciences*, 2020, **10**(3), P. 1108–1122.
- [3] Yang Y., Han Y., Jiang W., Zhang Y., Xu Y., and Ahmed A.M. Application of the Supercapacitor for Energy Storage in China: Role and Strategy. *Applied Sciences*, 2021, **12**(1), P. 354–372.
- [4] Winter M., Brodd R.J. What Are Batteries, Fuel Cells, and Supercapacitors? *Chem Rev*, 2004, **104**(10), P. 4245–4270.
- [5] Kötz R. and Carlen M. Principles and applications of electrochemical capacitors. *Electrochim Acta*, 2000, **45**(15–16), P. 2483–2498.
- [6] Burke A. Ultracapacitors: why, how, and where is the technology. *J. Power Sources*, 2000, **91**(1), P. 37–50.
- [7] Miller J.R. and Burke A. Electrochemical Capacitors: Challenges and Opportunities for Real-World Applications. *Electrochem Soc Interface*, 2008, **17**(1), P. 53–57.
- [8] Luo Y., Li D., Chen Y., Sun X., Cao Q., and Liu X. The performance of phosphoric acid in the preparation of activated carbon-containing phosphorus species from rice husk residue. *J. Mater. Sci.*, 2019, **54**(6), P. 5008–5021.
- [9] Sych N.V., et al. Porous structure and surface chemistry of phosphoric acid activated carbon from corncob. *Appl. Surf. Sci.*, 2012, **261**, P. 75–82.
- [10] Yakout S.M. and Sharaf El-Deen G. Characterization of activated carbon prepared by phosphoric acid activation of olive stones. *Arabian Journal of Chemistry*, 2016, **9**, P. S1155–S1162.
- [11] Adib M.R.M., et al. Effect of Phosphoric Acid Concentration on the Characteristics of Sugarcane Bagasse Activated Carbon. *IOP Conf. Ser. Mater. Sci. Eng.*, 2016, **136**, P. 012061–012069.
- [12] Nahil M.A. and Williams P.T. Characterisation of Activated Carbons with High Surface Area and Variable Porosity Produced from Agricultural Cotton Waste by Chemical Activation and Co-activation. *Waste Biomass Valorization*, 2012, **3**(2), P. 117–130.
- [13] Sartova K., Omurzak E., Kamarova G., Dzharmaev I., Borkoev B., and Abdullaeva Z. Activated carbon obtained from the cotton processing wastes. *Diam. Relat. Mater.*, 2019, **91**, P. 90–97.
- [14] Ma G. et al. Cotton-based porous activated carbon with a large specific surface area as an electrode material for high-performance supercapacitors. *RSC Adv.*, 2015, **5**(79), P. 64704–64710.
- [15] Nahil M.A. and Williams P.T. Pore characteristics of activated carbons from the phosphoric acid chemical activation of cotton stalks. *Biomass Bioenergy*, 2012, **37**, P. 142–149.
- [16] Liou T.-H. Development of mesoporous structure and high adsorption capacity of biomass-based activated carbon by phosphoric acid and zinc chloride activation. *Chemical Engineering Journal*, 2009, **158**, **2**, P. 129–142.
- [17] Xia M., Shao X., Sun Z., and Xu Z. Conversion of cotton textile wastes into porous carbons by chemical activation with  $\text{ZnCl}_2$ ,  $\text{H}_3\text{PO}_4$ , and  $\text{FeCl}_3$ . *Environmental Science and Pollution Research*, 2020, **27**(20), P. 25186–25196.
- [18] Budinova T. et al. Characterization and application of activated carbon produced by  $\text{H}_3\text{PO}_4$  and water vapor activation. *Fuel Processing Technology*, 2006, **87**(10), P. 899–905.
- [19] Ma G. et al. Cotton-based porous activated carbon with a large specific surface area as an electrode material for high-performance supercapacitors. *RSC Adv.*, 2015, **5**(79), P. 64704–64710.
- [20] Wakelyn P.J. *Cotton Fiber Chemistry and Technology*. CRC Press, 2006.
- [21] Thach N.K., Krechetov I.S., Berestov V.V., Lepkova T.L., and Stakhanova S.V. Optimizing the carbonization temperature in the fabrication of waste cotton based activated carbon used as electrode material for supercapacitor. *Nanosystems: Physics, Chemistry, Mathematics*, 2022, **13**(5), P. 565–573.
- [22] Raveendran K. Pyrolysis characteristics of biomass and biomass components. *Fuel*, 1996, **75**(8), P. 987–998.
- [23] Fu P., Hu S., Xiang J., Sun L., Su S., and An S. Study on the gas evolution and char structural change during pyrolysis of cotton stalk. *J Anal Appl Pyrolysis*, 2012, **97**, P. 130–136.
- [24] Sing K.S.W. Reporting physisorption data for gas/solid systems with special reference to the determination of surface area and porosity (Recommendations 1984). *Pure and Applied Chemistry*, 1985, **57**(4), P. 603–619.
- [25] Thommes M. et al. Physisorption of gases, with special reference to the evaluation of surface area and pore size distribution (IUPAC Technical Report). *Pure and Applied Chemistry*, 2015, **87**(9–10), P. 1051–1069.
- [26] Schütter C., Pohlmann S., and Balducci A. Industrial Requirements of Materials for Electrical Double Layer Capacitors: Impact on Current and Future Applications. *Adv Energy Mater.*, 2019, **9**(25), P. 1900334–1900344.

- [27] Lin R., Taberna P.L., Chmiola J., Guay D., Gogotsi Y., and Simon P. Microelectrode Study of Pore Size, Ion Size, and Solvent Effects on the Charge/Discharge Behavior of Microporous Carbons for Electrical Double-Layer Capacitors. *J. Electrochem. Soc.*, 2009, **156**(1), P. A7–A12.
- [28] Nguyen H.V.T., Kwak K., and Lee K.-K. 1,1-Dimethylpyrrolidinium tetrafluoroborate as novel salt for high-voltage electric double-layer capacitors. *Electrochim Acta*, 2019, **299**, P. 98–106.

---

Submitted 12 January 2023; revised 8 April 2023; accepted 25 June 2023

*Information about the authors:*

*Nguyen K. Thach* – National University of Science and Technology “MISIS”, Leninskiy prospect 4, Moscow, 119049, Russia; College of electromechanical and civil engineering, Vietnam National University of Forestry, Hanoi, Vietnam; ORCID 0000-0003-3749-3198; nguyenkienthach@gmail.com

*Ilya S. Krechetov* – National University of Science and Technology “MISIS”, Leninskiy prospect 4, Moscow, 119049, Russia; ORCID 0000-0002-3879-8017; ilya.krechetov@misis.ru

*Valentin V. Berestov* – National University of Science and Technology “MISIS”, Leninskiy prospect 4, Moscow, 119049, Russia; ORCID 0000-0002-5158-1963; vberestov97@gmail.com

*O. I. Kan* – National University of Science and Technology “MISIS”, Leninskiy prospect 4, Moscow, 119049, Russia; ORCID 0009-0000-6057-6632; m2106915@edu.misis.ru

*Ivan A. Maslochenko* – National University of Science and Technology “MISIS”, Leninskiy prospect 4, Moscow, 119049, Russia; ORCID 0009-0000-2481-2976; maslochenko3@mail.ru

*Tatyana L. Lepkova* – National University of Science and Technology “MISIS”, Leninskiy prospect 4, Moscow, 119049, Russia; ORCID 0000-0002-0648-411X; lepkova.tl@misis.ru

*Svetlana V. Stakhanova* – National University of Science and Technology “MISIS”, Leninskiy prospect 4, Moscow, 119049, Russia; Mendeleev University of Chemical Technology of Russia, Miusskaya square 9, Moscow, 125047, Russia; ORCID 0000-0002-3397-9556; stakhanova.s.v@muctr.ru

*Conflict of interest:* the authors declare no conflict of interest.



# NANOSYSTEMS:

**PHYSICS, CHEMISTRY, MATHEMATICS**

## INFORMATION FOR AUTHORS

The journal publishes research articles and reviews, and also short scientific papers (letters) which are unpublished and have not been accepted for publication in other magazines. Articles should be submitted in English. All articles are reviewed, then if necessary come back to the author to completion.

The journal is indexed in Web of Science Core Collection (Emerging Sources Citation Index), Chemical Abstract Service of the American Chemical Society, Zentralblatt MATH and in Russian Scientific Citation Index.

### Author should submit the following materials:

1. Article file in English, containing article title, the initials and the surname of the authors, Institute (University), postal address, the electronic address, the summary, keywords, MSC or PACS index, article text, the list of references.
2. Files with illustrations, files with tables.
3. The covering letter in English containing the article information (article name, MSC or PACS index, keywords, the summary, the literature) and about all authors (the surname, names, the full name of places of work, the mailing address with the postal code, contact phone number with a city code, the electronic address).
4. The expert judgement on possibility of publication of the article in open press (for authors from Russia).

Authors can submit a paper and the corresponding files to the following addresses: nanojournal.ifmo@gmail.com, popov1955@gmail.com.

### Text requirements

Articles should be prepared with using of text editors MS Word or LaTeX (preferable). It is necessary to submit source file (LaTeX) and a pdf copy. In the name of files the English alphabet is used. The recommended size of short communications (letters) is 4-6 pages, research articles– 6-15 pages, reviews – 30 pages.

#### Recommendations for text in MS Word:

Formulas should be written using Math Type. Figures and tables with captions should be inserted in the text. Additionally, authors present separate files for all figures and Word files of tables.

**Recommendations for text in LaTeX:**

Please, use standard LaTeX without macros and additional style files. The list of references should be included in the main LaTeX file. Source LaTeX file of the paper with the corresponding pdf file and files of figures should be submitted.

References in the article text are given in square brackets. The list of references should be prepared in accordance with the following samples:

- [1] Surname N. *Book Title*. Nauka Publishing House, Saint Petersburg, 2000, 281 pp.
- [2] Surname N., Surname N. Paper title. *Journal Name*, 2010, **1** (5), P. 17-23.
- [3] Surname N., Surname N. Lecture title. In: Abstracts/Proceedings of the Conference, Place and Date, 2000, P. 17-23.
- [4] Surname N., Surname N. Paper title, 2000, URL: <http://books.ifmo.ru/ntv>.
- [5] Surname N., Surname N. Patent Name. Patent No. 11111, 2010, Bul. No. 33, 5 pp.
- [6] Surname N., Surname N. Thesis Title. Thesis for full doctor degree in math. and physics, Saint Petersburg, 2000, 105 pp.

**Requirements to illustrations**

Illustrations should be submitted as separate black-and-white files. Formats of files – jpeg, eps, tiff.



# ***NANOSYSTEMS:***

***PHYSICS, CHEMISTRY, MATHEMATICS***

**Журнал зарегистрирован**

Федеральной службой по надзору в сфере связи, информационных технологий и массовых коммуникаций

(свидетельство ПИ № ФС 77 - 49048 от 22.03.2012 г.)

ISSN 2220-8054

**Учредитель:** федеральное государственное автономное образовательное учреждение высшего образования

«Национальный исследовательский университет ИТМО»

**Издатель:** федеральное государственное автономное образовательное учреждение высшего образования

«Национальный исследовательский университет ИТМО»

**Отпечатано** в Учреждении «Университетские телекоммуникации»

Адрес: 197101, Санкт-Петербург, Кронверкский пр., 49

**Подписка на журнал НФХМ**

На первое полугодие 2024 года подписка осуществляется через

ОАО «АРЗИ», подписной индекс Э57385